Large Eddy Simulation of a Fuel-Rich Turbulent Non-Premixed Reacting Flow with Radiative Heat Transfer

A Thesis Submitted for the Degree
of

Doctor of Philosophy

in the
Faculty of Engineering
of the
University of Glasgow

By

Sreebash Chandra Paul
B. Sc., M. Sc.

Department of Mechanical Engineering
University of Glasgow
Glasgow, UK

March 2008

This work is dedicated to

my mother,

and

in memory of my eldest brother who passed away
during this study.

Declaration

This dissertation is the result of my own work. No part of this dissertation has already been, or is being concurrently submitted for any other degree, diploma or qualification.

.....
Sreebash Chandra Paul
March 6, 2008

Abstract

The aims of this thesis are to apply the Large Eddy Simulation (LES) and beta Probability Density Function (β- PDF) for the simulation of turbulent non-premixed reacting flow, in particularly for the predictions of soot and NO production, and to investigate the radiative heat transfer during combustion process applying Discrete Ordinates Method (DOM). LES seeks the solution by separating the flow field into large-scale eddies, which carry the majority of the energy and are resolved directly, and small-scale eddies, which have been modelled via Smagorinsky model with constant C_s (Smagorinsky model constant) as well as its dynamic calibration. This separation has been made by applying a filtering approach to the governing equations describing the turbulent reacting flow.

Firstly, LES technique is applied to investigate the turbulent flow, temperature and species concentrations during the combustion process within an axi-symmetric model cylindrical combustion chamber. Gaseous propane (C_3H_8) and preheated air of $773K$ are injected into this cylindrical combustion chamber. The non-premixed combustion process is modelled through the conserved scalar approach with the laminar flamelet model. A detailed chemical mechanism is taken into account to generate the flamelet. The turbulent combustion inside the chamber takes place under a fuel-rich condition for which the overall equivalence ratio of 1.6 is used, the same condition was used by Nishida and Mukohara [1] in their experiment.

Secondly, the soot formation in the same flame is investigated by using the LES technique. In this thesis, the soot formation is included through the balance equations for soot mass fraction and soot particle number density with finite rate kinetic source terms to account for soot inception/nucleation, surface growth, agglomeration and oxidation.

Thirdly, the NO formation in the flame is studied by applying the LES. The formation of NO is modelled via the extended Zeldovich (thermal) reaction mechanism. A transport equation for NO mass fraction is coupled with the flow and composition fields.

Finaly, the radiative heat transfer in the flame is investigated. Both the luminous and non-luminous radiations are modelled through the Radiative Transfer Equation (RTE). The RTE is solved using the Discrete Ordinates Method (DOM/S_n) combining with the LES of the flow, temperature, combustion species and soot formation.

The computed results are compared with the available experimental results and the level of agreement between measurements and computations is quite good.

Acknowledgements

Above all, I wish to express my sincere thanks to my supervisor, Dr Manosh Paul, for his invaluable help and steadfast support throughout the period of this research. I am also thankful to him for his wise criticisms and suggestions in preparing and improving of this dissertation. I am also thankful to Dr Donald Ballance for his agreement to become a pastoral supervisor and his help in different ways during my study.

I would like to thank Dr Ian Watson of this Department for his useful discussion on scattering effects. Special thanks to Professor William P. Jones of Department of Mechanical Engineering, Imperial College London for his valuable comments and suggestions on this research. A big thank goes to Dr Kevin Menzies, Senior CFD Specialist in Rolls Royce, Aerothermal and Fluid Systems, Bristol for allowing me to use his generated flamelet results in our computation. I am also thankful to Professor Michael Fairweather of Thermofluids and Combustion, University of Leeds for his valuable discussion on some results.

For the financial support of this study, I thank the Faculty of Engineering of the University of Glasgow. I also like to thank Royal Academy of Engineering, London, UK for awarding an international travel grant to attend the *European Conference on Computational Fluid Dynamics (ECCOMAS CFD)*, The Netherlands.

I would like to thank our IT administrators Mr Kenneth Stevenson and Mr Walter Robinson for their effort to keep the system always running and their support to any problem in the computer systems.

I am delighted to acknowledge the support I have received from all my colleagues in this department. This work could not have been completed in such a peaceful way without their support. I also like to thank all my friends for their encouragements during this research. In particular, many thanks to Mamun, with whom I share my office room, and Suvash in Australia for their help on both scientific and non-scientific matters.

I am grateful to my beloved mother, brothers, and sisters, whose love is more than I can desire. I am also grateful to all of my well-wishers for their inspiration that leads me to go ahead.

Contents

List of Figures

List of Tables

List of Symbols

Roman Symbols

a_i	coefficients in single polynomial
$a_i^{(k)}$	coefficients in piece-wise polynomial
c	constant
c_a	agglomeration rate constant
c_k	Kolmogogov universal subrange constant
c_{min}	number of carbon atoms in the incipient carbon particle
c_p	specific heat of the mixture at constant pressure
c_{pk}	specific heat of species k at constant pressure
C_0	soot absorption constant
C_2	Plank function constant
C_s	Smagorinsky model constant
C_ξ	sub-grid scale scalar flux model parameter
$d_{c(s)}$	soot particle diameter
$d\Omega$	discrete solid angle
D_k	diffusion coefficient of species k
e	internal energy
e_t	total energy
f, f_1, f_2	general flow variables
f_v	soot volume fraction
g	acceleration due to gravity
g_i	body force vector
G	grid filter function
G_r	incident radiation
h	specific enthalpy of the mixture
h_k	specific enthalpy of species k
I	radiative intensity
I_b	black body intensity

I_{bw}	black body intensity at the wall
I_x	incomplete beta function
J_{kj}	diffusion flux of species k
J_j^{sgs}	sub-grid scale scalar flux
k	Boltzmann constant
k_c	cut-off wevenumber used in Fourier cut-off filter
k_1	reaction rate for NO production
k_s	rate constants for soot reaction rates
L_{ij}	Leonard stress
M	total number of species/discrete ordinates
Ma	Mach number
$M_{c(s)}$	molar mass of soot
M_i	molar mass of element i
m_k	mass fraction of species k
M_k	molar mass of species k
N	soot particle number density
N_A	Avogadros' number
N_{grid}	total number of grid nodes
N_t	total number of time steps
p	pressure
P_n	Legendre polynomials
Pr	Prandtl number
$P(\xi)$	β-probability density function
$\mathbf{q}$	radiative heat flux vector
q_j	energy flux
q_{in}	incoming radiative heat flux
$q_j^c/q_j^d/q_j^D$	energy flux by heat conduction/inter-diffusion/Dofour effect
$\mathbf{q_n}$	net wall radiative heat flux vector
Q_{abs}/Q_{sca}	absorption/scattering efficiency factor
$\mathbf{r}$	position vector, (x, y, z)
$\mathbf{r}_w$	position vector of the wall
r_{NO}	production rate for NO
r/s	parameters for beta and gamma functions

r_s	reaction rates for soot formation processes
R	mass based gas constant
Re	Reynolds number
R_o	universal gas constant
$\hat{s}$	discrete direction
s_b	Stefan-Boltzmann constant
S	total number of species
Sc	Schmidt number
S_{ij}	strain rate tensor
S_L	Sutherland's law constant
S_n	approximations of DOM
$S(\phi)$	source terms for scalar equations
t	time
$t^{\#}$	reference time scale
T	flame temperature
T_{ij}	subtest scale stresses
T_{ad}	adiabatic flamelet temperature
T_{ref}	reference temperature in Sutherland's law
T_w	wall temperature
u_i or u, v, w	velocity components in Cartesian coordinate
u_τ	wall friction velocity
w_k	molar rate of formation of species k
x_i or x, y, z	Cartesian coordinate directions
$Y_{c(s)}$	soot mass fraction
Y_{NO}	NO mass fraction
Y_k	mass/mole fraction of species k
Z_i	element mass fraction of element i
Z_{iO}/Z_{iF}	element mass fraction for oxidiser/fuel stream
$W_{c(s)}$	soot concentration

Greek Symbols

α, β, γ	direction cosines
$\beta(r, s)$	beta function

Γ	diffusion coefficient
$\Gamma(r)$	gamma function
Γ_{sgs}	sub-grid scale diffusivity of the scalar
δ_{ij}	kronecker delta
Δh_k	heat of formation of species k
$\Delta x, \Delta y, \Delta z$	mesh specing in the x, y, z directions
Δ	filter width
Δt	numerical time step
Θ	angle between the incident and outgoing beams
ϵ	dissipation rate
ε_w	wall emissivity
κ	thermal conductivity of the mixture
κ_a	absorption coefficient
λ	wave length of light
μ	molecular viscosity
μ^b	bulk viscosity
μ_{ik}	mass proportion of the element i in the species k
μ_{ref}	reference viscosity in Sutherland's law
μ_{sgs}	sub-grid scale eddy viscosity
ν_{sgs}	sub-grid scale kinetic eddy viscosity
ξ	mixture fraction
$\xi_{sgs}^{\prime 2}$	sub-grid scale mixture fraction variance
ρ	fluid density
$\rho_{c(s)}$	soot density
ρ_k	partial mass density of species k
σ	scattering coefficient
σ_{ij}	viscous stress tensor
σ_{sgs}	sub-grid scale Prandtl/Schmidt number
τ_{ij}	subgrid scale stresses
τ_w	wall shear stress
ϕ	general conserved scalar
$\phi^{\prime}_{rms}$	root mean square of turbulent fluctuations
Φ	scattering phase function

ψ	thermochemical variables
Ω	solid angle
ω	quadrature weight
ω_y	vorticity
∇	divergence

Subscripts

m, m'	outgoing and incoming directions

Superscripts

e, w, etc.	surface nodes
E, W, etc.	volume nodes

Mathematical Accents

$\bar{.}$	spatial filtering
$\hat{.}$	test filtering
$\tilde{.}$	density weighted or Favre filtering
$< . >$	time averaging
$< . >_y$	averaging over y direction
$\|.\|$	magnitude
$\|\|.\|\|$	norm of residuals

Chapter 1

Introduction

Combustion or burning is a complex sequence of chemical reactions between a fuel and an oxidiser accompanied by the production of heat in the form of flames. Combustion is basically two types: premixed and non-premixed combustion. In premixed combustion, fuel and oxidiser are completely mixed before combustion takes place. On the other hand, in non-premixed combustion, the reactants are initially seperated, and the reaction occurs only at the interface between the fuel and oxidizer, where the mixing and reaction both take place simultaneously. The mixing of fuel and oxidizer occurs at a molecular level so that chemical reactions can take place. A combined concept of these two combustion categories is called partially premixed combustion.

Turbulent non-premixed combustion occurs in many engineering applications. Understanding of the turbulent combustion process is therefore essential for efficient design of many engineering devices such as gas turbines, internal combustions (IC) engines, furnaces, etc. Moreover, the number of combustion systems used in transformation and transportation industries is rapidly growing and as a result a huge amount of combustion products such as NO_x, CO and unburnt hydrocarbons are produced everyday, which are harmful to human health and a great threat to the global environment. The accurate control and prediction of turbulent flames and an increment of the performance of combustion efficiency, therefore, appear to be a hot and essential topic in engineering.

Soot is mainly unburnt carbon formed usually as a byproduct of incomplete hydrocarbon combustion. In a fuel-rich combustion, enough oxygen is not present to yield a complete conversion of fuel into major combustion products such as carbon dioxide and water vapour. The combustion or pyrolysis of hydrocarbons in high temperature leads to the appearance of soot particles. Other elements such as hy-

drogen and oxygen are usually present in small amount. Soot particles formed during combustion process significantly affect the performance and durability of many engineering systems such as gas turbines and diesel engines. From the environmental point of view, the emission of these nanometer-size soot particles (commonly called smoke) from combustors causes significant human health problems associated with the respiratory system (Vedal [3]). Moreover, it has recently been argued that flame-generated soot might be a major contributor to the global warming.

These important technological and environmental problems motivate advanced research for a complete understanding of the factors governing the complex soot forming process in flames. The detailed study of soot phenomena is also a necessary step towards the development of accurate numerical simulations of practical combustion devices.

In every circumstances where combustion occurs, the formation of Nitrogen Oxides (NO_x) are unavoidable. From a home open fire to a coal fired power plant, NO_x is formed as an undesired product and a contributor to air pollution and health problems. Due to the increasing concerns over the environmental pollution, the understanding of the NO_x formation mechanism during the combustion process and of the development of their reduction technologies is essential for the efficient design of a combustion device.

In most combustion devices, a large portion of the total heat flux/transfer occurs mainly by radiation from the flame. In fuel-rich combustion where fuel/air ratios are high and mixing of fuel and air is inadequate, leads to the production of soot particles. The radiation occurs in both non-luminous and luminous flame. The radiation emitted from non-luminous flame is due to the hot combustion products mainly carbon dioxide (CO_2) and water vapor (H_2O). On the other hand the luminous radiation is mainly due to the appearance of soot particles in the flame. For efficient design of the combustion devices with less pollutant emissions, it is essential to predict the wall temperature accurately which in turn depends on the accurate prediction of the radiative heat transfer. Therefore, an adequate treatment of thermal radiation is essential to develop a mathematical model for the combustion processes.

1.1 Purpose of the Work

The aim of this thesis is to investigate turbulent non-premixed combustion, including species concentrations and temperature, soot formation and growth, NO_x formation, and radiative heat transfer in a model cylindrical combustor. To investigate these, a Large Eddy Simulation (LES) technique is applied. In LES, the non-premixed combustion process is modelled via conserved scalar approach with laminar flamelet model. The soot formation is included into the non-premixed combustion process through the balance equations for soot mass fraction and soot particle number density with finite rate kinetic source terms to account for soot inception/nucleation, surface growth, agglomeration and oxidation. In the NO formation model, the extended Zeldovich (thermal) reaction mechanism is taken into account through a transport equation for NO mass fraction. The radiation is modelled through the Radiative Transfer Equation (RTE), which is the steady state representation of radiative heat transfer/flux. The RTE is solved using the Discrete Ordinates Method (DOM/S_n) which has then been combined with the LES of the flow, temperature, combustion species, soot formation.

The present computational results of temperature distribution, species concentrations and soot concentration are compared with those of the experimental investigation of Nishida and Mukohara [1]. To the best of my knowledge it is the first time that the turbulent flame inside this combustion chamber under the fuel-rich condition is investigated by means of LES technique.

1.2 Thesis Outline

This thesis is organised as follows:

In Chapter 2, a general review of the previous works on non-premixed turbulent combustion, pollutants such as soot and NO_x emissions, and radiative heat transfer have been made.

In Chapter 3, the governing equations of turbulent reacting flow together with the mixture fraction equation are described. Large Eddy Simulation (LES) technique is described to investigate the turbulent non-premixed combustion flow, including species concentrations and temperature, in a cylindrical combustor. The

spatial filtering is introduced and used to the governing equations to separate the flow field into large scale eddies and small scale eddies. The unresolved small scale eddies are modelled using the standard Smagorinsky model as well as its dynamic approach. The filtered values of species mole fractions, temperature and density, which are functions of the mixture fraction, are determined by integration over a beta Probability Density Function (β-PDF). The non-premixed combustion process is modeled based on the conserved scalar approach with laminar flamelet model. The computational results are presented and compared with those of the experimental investigation conducted by Nishida and Mukohara [1].

In Chapter 4, the soot formation mechanism and the modelling of the soot formation are presented. The soot formation is included into the non-premixed combustion process through the balance equations for soot mass fraction and soot particle number density. The filtering of the soot mass fraction and the soot particle number density equations are considered along with the modelling of the subgrid scale soot mass fraction and soot particle number density fluxes. The results from the simulation are presented and compared with those of the experimental investigation conducted by Nishida and Mukohara [1].

In Chapter 5, formation of the nitric oxide (NO) in a model cylindrical combustor is described and modelled through the extended Zeldovich (thermal) reaction mechanism. A transport equation for NO mass fraction is introduced. The subgrid scale NO flux is modelled.

In Chapter 6, the Discrete Ordinates Method (DOM/S_n) with Large Eddy Simulation (LES) is employed to investigate the radiative heat transfer in a three-dimensional model cylindrical combustor. Both the luminous, which is due to the appearance of soot particles in the flame, and non-luminous, which is due to hot products of combustion mainly carbon dioxide (CO_2) and water vapor (H_2O), radiation have been considered in this study. The radiation is modelled through the Radiative Transfer Equation (RTE), which is the steady state representation of radiative heat transfer/flux. The RTE is solved using the DOM/S_n which has then been combined with the LES of the flow, temperature, combustion species and soot formation.

In Chapter A, the computational procedure employed in this thesis is summarised.

In Chapter 7, the findings of the present study have been summarised and some suggestions for the future work are given.

Chapter 2

Review of Previous Works

Abstract: In this chapter a general review of previous works relevant to the thesis has been made. The review works on the turbulent non-premixed combustion, pollutant emissions such as soot formation and NO_x production, and the effects of radiation in turbulent flame are discussed.

2.1 Turbulent Combustion

Combustion remains one of the most complicated phenomena to describe and simulate using numerical tools, mainly because of a practical combustion process is usually associated with the turbulent flows. For more than a century turbulent flows have been investigated but no general approach to the solution of turbulent flow problems exists. The multi-scale character of turbulence makes simulation of such flows a difficult task. In order to account for the full nonlinear multi-scale effect of turbulence in a combustion process, the governing equations must be solved resolving the micro-scale, known as *Kolmogrov scale*, eddies. However, to date this is not a possible task for flows on that technical scale. Thus, depending on the scale of interest, different techniques with different modelling approaches exist in the literature. Large Eddy Simulation (LES) technique is one of them and has recently been shown to be a promising approach for computation of turbulent flows, because of its clear means of overcoming some of the deficiencies which appear in other available approaches such as Reynolds Averaged Navier Stokes (RANS) and Direct Numerical Simulation (DNS), which is restricted to low Reynolds number flows.

The traditional RANS approach involves the use of Reynolds' averaging in

which the long-time average of a quantity f is defined as

$$< f >= \frac{1}{T} \int_{t}^{t+T} f(\tau) d\tau, \tag{2.1}$$

where T is a time interval much longer than all time scales of turbulent flow. The procedure applying to the equations of motions results in the well-known Reynolds-averaged Navier-Stokes (RANS) equations, that describe the evaluation of the mean quantity. The averaging operation defined in (2.1) permits one to decompose any quantity as

$$f =< f > +f', \tag{2.2}$$

where $< f >$ and f' are the mean and fluctuating parts of the original quantity f respectively. But, when this averaging procedure (2.1) is applied to the Navier-Stokes equations, additional terms arise due to the non-linearity of the convection terms. These additional terms, second order moments involving the fluctuations of velocity components about their mean values, have the properties of a stress and also known as Reynolds' stresses since the early work done by Reynolds [4]. These unknown stresses are then modelled to close the system; and a wide range of models, such as two equation $\kappa - \epsilon$ model, for the Reynolds stresses is available in the literature. Transport equations can also be derived for the components of the stress, but these contain unknown third order moments. A hierarchy of equations for the unknown moments can be developed in this way, though, in general, there is no point at which the process can be terminated to give a complete description of turbulence in terms of moments up to some finite order (Branley [5]). Therfore, it is needed to model third order moments in the Reynolds' stress transport equations. However, the flow behavior can not be analysed in detail, because this approach only gives the time-averaged solutions and is unable to simulate the small length scale (known as *Kolmogrov microscale*) and time scale that seem to play an important roles especially in combusting flows.

The Direct Numerical Simulation (DNS) of turbulence is the most straightforward approach to the solution of the equations describing turbulent flows. In DNS, the governing equations are discretised and solved numerically. If the mesh is fine enough to resolve even the small scales of motion, one obtains an accurate three-dimensional time-dependent solution of the governing equations which are com-

pletely free from modelling assumptions. But, as the ratio of the dissipation length scale known as *Kolmogrov microscale,* l_d, to the size of the largest eddies, L, is given by

$$\frac{L}{l_d} \propto Re^{3/4}, \tag{2.3}$$

thus to resolve all scales of motion, the required number of grid nodes, N_{grid}, in a three-dimensional computational domain is

$$N_{grid} \propto Re^{9/4}, \tag{2.4}$$

where Re is the Reynolds number. Therefore, for most natural flows and many practical applications in engineering, Reynolds numbers are so high that it is not possible to represent the whole range of scales in a DNS with todays computer. And, even with rapidly increasing computing power this will remain a work for many years. Thus DNS is restricted to low-Reynolds number turbulent flows due to the necessity of resolving all the spatial scales of motion. A review work dealing the current status of DNS applied to non-premixed combustion is done by Vervisch and Poinsot [6].

In the Large Eddy Simulation (LES) technique, which is considered somewhere between RANS and DNS (Rogallo and Moin [7], Moin [8]), a spatial filtering operation is used to the governing equations to seperate the large scale eddies from the small scale eddies. The large scale eddies carry the majority of the energy and dominate the physical behaviour of any turbulent flow. The filtering is typically taken over the control volume of a numerical simulation with a suitably defined filter function. The resulting equations that describe the space-time evolution of the large scale eddies contain the sub-grid scale (sgs) stresses that describe the effect of the unresolved small scales on the resolved scales. The unresolved sgs stresses are then modelled. The resulting closed equations for large scale fields are then solved numerically on a grid small enough to resolve the smallest of the large eddies.

Regarding the modelling of sgs eddies in LES, a considerable research has been carried out by Smagorinsky [9] and Lilly [10] on an assumption made for the SGS Reynolds stresses. Their ideas were further developed by Deardorff [11] in the area of engineering applications, who simulated the plane Poiseuille flow (channel flow). Since then, LES has been developed and applied to a number of increasingly com-

plex problems by a large number of researchers, such as LES of turbulent confined coannular jets by Akselvoll and Moin [12], LES of a plane jet in a cross-flow by Jones and Wille [13], LES of a round jet in a cross flow by Yuan *et al* [14], and LES of turbulent flow past a swept fence by di Mare and Jones [15]. Comprehansive reviews on Large eddy Simulation of turbulent flows can be found in Lesieur and Metais [16], Moin [17] and Lesieur *et al* [18].

LES application to turbulent combustion with flow came into light as a science in engineering in the 1990s. Since then, number of papers have demonstrated the power of LES method to the flows of turbulent combustion, such as a LES scheme for turbulent reacting flows by Gao and O'Brien [19], LES of a nonpremixed reacting jet by DesJardin and Frankel [20], LES of a turbulent non-premixed flame by Branley and Jones [21], and LES of a model gas turbine combustor by di Mare *et al* [22]. Peters [23], Pitsch [24] and Riley [25] offer comprehensive reviews of Large Eddy Simulation of turbulent combustion.

2.1.1 Turbulence-Chemistry Interation

The chemical reactions that control combustion, however, occur at the smallest scales of the flow and can almost never be fully resolved. As such, modelling approaches are needed in order to predict accurately the chemical behaviour of reacting flows. For non-premixed combustion, most modelling strategies are based on the mixture fraction concept. There are a number of sophisticated modelling approaches can be found in the literature for the coupling between turbulence and chemistry in flames, such as laminer flamelet model (Peters [26], Cook *et al* [27]), conditional moment closure (CMC) model (Klimenko [28], Bilger [29], Smith [30], Kim and Pitsch [31]), linear eddy model (Kerstein [32; 33; 34; 35]), etc. The flamelet model and the conditional moment closure (CMC) model are based on conserved scalar models that account for finite-rate chemistry effects. The β-pdf (Cook and Riley [36], Colucci *et al* [37]) plays a central role in most turbulent-chemistry interation models for non-premixed combustion. In a two-feed system laminer flamelet model along with the β-pdf approach is widely used in the non-premixed combustion.

2.2 Pollutants Emission

As a consequence of turbulent combustion, pollutants such as soot (carbon particles), NO_x, etc, are formed. Some details of review works on soot and NO_x emissions are given in the following subsections.

2.2.1 Soot Emission

The formation of soot particles in a flame is inherently a chemically-controlled phenomena. A great deal of information has come from shock tubes, laminar premixed and non-premixed flames. The previously held views of soot formation process can be divided into four principal sub-processes: (i) soot particle inception or nucleation, (ii) surface growth, (iii) particle coagulation, and (iv) particle oxidation. These sub-processes can occur simultaneously and vary for individual process depending on the specific combustion environment. Although the details of each of these sub-processes are not well known or even not clearly understood but Kennedy [38] offers a good review on these issues.

Zimberg *et al* [39] employed a laminar flamelet state relationship combustion model along with two different soot models to study turbulence, soot chemistry, and radiation interactions for a non-premixed reacting mixture of acetylene and air in a homogeneous box turbulence. The first model involves a direct extension of the laminar flamelet concept to soot using soot volume fraction state relationship. The second soot model involves transport equations for soot mass fraction and soot number density, which include finite rate source terms to account for soot inception (or nucleation), surface growth, agglomeration and oxidation. They used the linear eddy model to simulate turbulent advection.

The soot formation and oxidation with radiative heat loss in confined turbulent jet diffusion has been presented by Brookes and Moss [40]. The soot field has been modelled by two parameters, the soot particles number density and their mass concentration. Their model includes the key process of soot particle nucleation, coagulation, surface growth and oxidation.

Soot volume fraction and number density in a turbulent diffusion flame burning kerosene/air have been predicted by Wen *et al* [41] using two approaches: (i) conventional soot inception model based on the acetylene concentration and is referred

to as the 'acetylene model', (ii) a soot inception model based on the formation rate of three and two ring aromatics and is referred to as the 'PAH inception model'. Their soot model also accounted for inception, surface growth, coagulation and oxidation processes.

Said *et al* [42] proposed a simple two equation model for soot formation that can predict soot volume fraction in a laminar diffusion flame. The model was then coupled with a local Eulerian-Lagrangian model to predict soot formation in a turbulent diffusion flame. In their model, they proposed a set of constants that have been adapted to ethylene-air diffusion flame, although they reported that this model might be applied to any hydrocarbon-air diffusion flame.

Magnussen and Hjertager [43] and Magnussen *et al* [44] incorporated a model for soot formation into an eddy dissipation model for turbulent combustion. They used the kinetic scheme of Tesner *et al* [45] for soot formation in acetylene flames by calculating the mass of soot and the mean particle number density. The gaseous fuel was assumed to be converted into soot via a two-stage mechanism. The first was considered to convert fuel to radical nuclei or soot precursors through fuel cracking, branching, and coagulation steps, with these precursors converted into soot particles in the second stage.

Fairweather *et al* [46] studied the predictions of soot formation and radiative transfer from a turbulent reacting jet in a cross wind. Following this study, Fairweather *et al* [2] also investigated the soot formation in turbulent non-premixed propane flames. In both works, they coupled the soot formation model for laminar premixed flames of Leung *et al* [47] with the $k - \epsilon$ turbulence model. The turbulent, gas-phase, non-premixed combustion process was modelled via the conserved scalar approach with the laminar flamelet concept whereas the soot formation and growth was included in the calculation by the solution of balance equations for soot mass fraction and soot particle number density with the effects of finite-rate kinetic.

Large Eddy Simulation (LES) has been used by Desjardin and Frankel [48] to study the soot formation in two dimensional non-premixed acetylene-air turbulent jet flame. They also employed the soot model of Leung *et al* [47] that involved integration of two additional transport equations for the soot mass fraction and particle number density with finite rate kinetic source terms to account for soot inception/nucleation, surface growth, agglomeration and oxidation. Subgrid correlations

between the soot mass fraction and the particle number density with the velocity field were closed using the Smagorinsky SGS turbulence model. Soot production was determined by the large-scale turbulent advection, SGS turbulent diffusion, and finite rate soot chemistry effects.

2.2.2 NO_x Emission

NO_x is used to refer to the nitric oxide NO and the nitrogen oxide NO_2. The NO_x emission consists of mostly (typically 95% of the total NO_x) the nitric oxide NO which is the primary form in combustion products. The nitric oxide NO is subsequently oxidized to NO_2 in the atmosphere.

There are four different routes or mechanisms in the formation of NO_x, which were identified by Bowman [49]. These are the thermal NO route, the prompt NO route, the N_2O (nitrous oxide) route, and the fuel-bound nitrogen route. But, it is also known that in nonpremixed combustion of hydrocarbon fuels, the first two mechanisms dominate the process of nitric oxide, NO, formation. The thermal NO also well-known as the Zeldovich NO proposed by Zeldovich [50], which dominantly depends on its local temperature and reactants (O_2 and N_2). The prompt or Fenimore NO mechanism proposed by Fenimore [51], is formed through hydrocarbon radical reaction with molecular nitrogen under fuel-rich condition. In most flames, especially those from nitrogen-containing fuels, the prompt mechanism is responsible for only a small fraction of the total NO_x.

Meunier *et al* [52] investigated the NO_x emissions from turbulent propane diffusion flames experimentally as well as numerically. In numerical investigation both the thermal and prompt-NO reaction mechanism were used to predict NO formation. The equations were closed by $k-\epsilon$ turbulence model where as the combustion was modelled using the stretched laminar flamelet model and the probability density function (PDF) method.

Formation characteristics of the nitric oxide in a three-stage air/LPG flame has been investigated both experimentally and numerically by Kim *et al.* [53] including both the thermal and the prompt NO formation mechanism through a conservation equation of NO mass fraction. The computed results were compared with the experimental measurements.

For the hydrogen jet diffusion flame, a prediction method for NO applicable to LES was presented by Taniguchi *et al.* [54]. To model NO production, they considered the extended Zeldovich mechanism with the quasi-steady state approximation of the nitric atom through the balance equation of NO mass fraction. In LES, they neglected the SGS contribution to the NO production.

2.3 Radiation

Several numerical methods such as Zonal Method, Discrete Ordinates Method, Monte Carlo Method, etc., have been developed for predicting radiative heat transfer. In recent years, the Discrete Ordinates Method (DOM) became a popular numerical solution method for the Radiative Heat Transfer Equation (RTE), which shares a computational grid with the control volume approach.

About 5 decades ago, the Discrete Ordinates Method (DOM) was first introduced by Chandrasekhar [55] for investigating radiating heat transfer within a plane parallel medium for astrophysics problems. Carlson and Lathrop [56] have developed the DOM/S_n for solving multi-dimensional neutron transport problems using the finite volume technique. Since then the DOM has extensively been used to analyse the radiative heat transfer in one- and multi-dimensional different types of geometry, e.g., Hyde and Truelove [57], Fiveland [58; 59; 60], Jamaluddin and Smith [61; 62], etc. More recently, Kaplan *et al* [63], Deajardin and Frankel [48], Kayakol *et al* [64] investigated the radiative heat transfer in high teperature combustion devices through the solution of the Radiative Transfer Equation (RTE), which is the steady state representation of the radiative heat transfer, employing DOM/S_n. To predict the radiative heat transfer in high temperature combustion process, it requires a simultaneous solution of the RTE and the governing equations of flow which include the Navier-Stokes equations, the mixture fraction equation, etc., ([63], [48], [65]).

Very few number of works has been done that involves the combination of DOM with LES to solve the radiative heat transfer in a turbulent flame. Deajardin and Frankel [48] have investigated the soot formation in the near-field of a strongly radiating nonpremixed turbulent jet flame using LES in a two dimensional geometry. In their work, they studied luminous radiation from soot formed in the flame by

solving RTE for a non-scattering and grey gas assumption employing the S_4 approximation of DOM. Recently, Jones and Paul [65] combined the DOM with LES of the flow, temperature and combustion species to investigate the radiative heat transfer from non-luminous flame in a three-dimensional model gas turbine combustor, where S_4 approximation of DOM was considered. Later, Paul and Jones [66] and Paul [67] extended their previous work [65] including the lower and higher order approximations i.e., S_2, S_4, S_6, S_8 of DOM.

Chapter 3

Large Eddy Simulation of Fuel-Rich Turbulent Non-Premixed Reacting Flow

Abstract: In this chapter, the turbulent non-premixed combustion flow, including species concentrations and temperature, in a cylindrical combustor has been investigated by using Large Eddy Simulation (LES). In LES a spatial filtering is applied to the governing equations to separate the flow field into large scale eddies and small scale eddies. The large scale eddies which carry most of the turbulent energy are resolved explicitly while the unresolved small scale eddies are modelled using a Smagorinsky model with $C_s = 0.1$ as well as a dynamic model. The filtered values of species mole fractions, temperature and density, which are functions of the mixture fraction (conserved scalar), are determined by integration over a beta Probability Density Function (β-PDF). The computational results are compared with those of the experimental investigation conducted by Nishida and Mukohara [1], where a good agreement is achieved, both quantitatively and qualitatively, for temperature, mixture fraction and most of the combustion species.

3.1 Introduction

In non-premixed combustion an efficient mixing of fuel and air molecules, which is necessary for the chemical reactions of combustion to take place, is one of the basic challenges. Moreover, the number of combustion systems used in the industries are growing rapidly which in turn produce a large amount of combustion

products such as NO_x, CO and unburned hydrocarbons everyday, which are harmful to human heath and a great threat to the global environment. Therefore, an understanding of turbulent non-premixed combustion and its accurate prediction is essential to increase the combustion efficiency of many engineering devices such as gas turbines combustors, internal combustions engines, furnaces, etc, and protect the global worming.

Combustion, usually associated with turbulent flows, remains one of the most complicated phenomena to describe and simulate using numerical tools because of the multi-scale characteristics of turbulence. In order to account for the full non-linear effects of turbulence in a combustion process, the governing equations must be solved numerically so that the smallest scales of turbulence must be resolved. However, to date this is a very difficult and computationally demanding task for practical systems. Thus, depending on the scale of interest, different techniques with different modelling approaches exist in the literature, see Chapter 2 for more details. Large Eddy Simulation (LES) is one of them and has recently been shown to be a promising approach for the computation of turbulent combustion, because of its clear means of overcoming some of the deficiencies which appear in other available approaches such as Reynolds Averaged Navier Stokes (RANS)- only gives the time-averaged solutions, and Direct Numerical Simulation (DNS)- restricted to low Reynolds number flows.

The objective of this chapter is, therefore, to apply the LES for analysing the turbulent flow, species concentrations and temperature arising in the turbulent non-premixed combustion of propane/air in a cylindrical combustor. Gaseous propane (C_3H_8) is injected through a circular nozzle which is attached at the center of the combustor inlet. Preheated air with temperature of $773K$ is supplied through the annulus surrounding of this fuel nozzle. The turbulent combustion inside the chamber takes place under a fuel-rich condition for which the overall equivalence ratio of 1.6 is used, which is the same condition used by Nishida and Mukohara [1] in their experiment. The predicted mean temperature and species concentrations in both the axial and radial directions have been compared with the experimental data obtained by Nishida and Mukohara [1] in the turbulent propane and pre-heated air combustion.

This chapter is structured in the following order. A description of the governing

equations is presented in §3.2. The filtering approach used in LES is presented in §3.3, followed by the filtered governing equations in §3.4. The sgs modelling and the conserved scalar approach to combustion modelling including β-pdf integration are presented in §3.5. In §3.6 the details of the laminar flamelet approach used in the LES is described. Description of the experiment is given in §3.7. Results and discussion are presented in §3.8. Finally, in §3.9 a general conclusion of this chapter is made.

3.2 Governing Equations in LES

3.2.1 The Navier-Stokes (N-S) Equations

In Cartesian coordinates, and making use of tensor notations, the mass conservation or the continuity equation and the transport of momentum are written as
Continuity equation:

$$\frac{\partial \rho}{\partial t} + \frac{\partial (\rho u_j)}{\partial x_j} = 0, \tag{3.1}$$

Momentum equation:

$$\frac{\partial \rho u_i}{\partial t} + \frac{\partial (\rho u_i u_j)}{\partial x_j} = -\frac{\partial p}{\partial x_i} + \frac{\partial \sigma_{ij}}{\partial x_j} + \rho g_i, \tag{3.2}$$

where t is time; x_j is any of the three coordinate directions; u_j is any of the three velocity components; p is the pressure; ρ is the density, which, in reacting flows, varies due to the heat released by the chemical reaction and variations in the chemical composition of the fluid; $g_i = -g\delta_{i3}$, with g being the acceleration of gravity, if the axis corresponding to $i = 3$ is vertical; and the viscous stress tensor can be expressed in terms of molecular viscosity, μ, and local velocity gradient as

$$\sigma_{ij} = 2\mu S_{ij} - \frac{2}{3}\mu S_{kk}\delta_{ij}, \tag{3.3}$$

where $S_{ij} = \frac{1}{2}(\frac{\partial u_i}{\partial x_j} + \frac{\partial u_j}{\partial x_i})$ is the strain rate and δ_{ij} is the kronecker delta i.e., $\delta_{ij} = 0$ for $i \neq j$ and 1 for $i = j$; and $S_{kk} = \frac{\partial u_k}{\partial x_k}$.

Actually, the viscous stress tensor in (3.3) should contain one additional term;

for example equation (3.3) should be

$$\sigma_{ij} = 2\mu S_{ij} - \left[\frac{2}{3}\mu - \mu^b\right] S_{kk}\delta_{ij}$$

in which μ^b is the "bulk viscosity", also known as the dilation viscosity or volume viscosity, which is closely related to the relaxation time[1]. The bulk viscosity is identically zero for low density monotonic gases and is not too important. However, for dense gases and liquids it may be non-zero. Formulas to estimate μ^b may be found in Hirschfelder *et al* [68], although it is a good approximation to neglect it in low densed gaseous mixtures. Throughout the work the Einstein's summation convention has been employed unless stated otherwise.

3.2.2 Species Mass Conservation Equation

In addition to the Navier-Stokes equations, the species mass conservation equation for the fluid mixture is also needed to describe the chemically reacting flow. If m_k are the masses of different species, the density is given by the partial mass density $\rho_k = \rho Y_k$ of species k, where $Y_k = m_k(\sum_k m_k)^{-1}$ is the species mass fraction of species of k. Then the balance equation for species mass conservation becomes,

$$\frac{\partial \rho Y_k}{\partial t} + \frac{\partial(\rho u_j Y_k)}{\partial x_j} + \frac{\partial J_{k,j}}{\partial x_j} = M_k \omega_k, \tag{3.4}$$

where the production term, $M_k\omega_k$, is obtained by the product of the molar mass, M_k, and the molar rate of formation, ω_k, during the chemical reaction. J_{kj} denotes the diffusion flux and using the *Fick's law* it is given by

$$J_{kj} = -\rho D_k \frac{\partial Y_k}{\partial x_j}, \tag{3.5}$$

where D_k is the diffusion coefficient for species k.

The treatment of source term (*i.e.*, chemical reaction rate) in the species conservation equation is usually very difficult in the simulation of turbulent reacting flows. If possible, it is therefore convenient to avoid treatment of this source term

[1] a characteristic time for the transfer of energy from the translational to the internal degrees of freedom.

altogether. As the elements are neither created nor destroyed in chemical reactions, thus it is advantageous to describe the combustion process through strictly conserved quantities which then vanish the source terms in the element conservation equations. The element mass fraction, Z_i, is strictly conserved and can be expressed as the ratio between the mass of an element i and the total mass,

$$Z_i = \sum_{k=1}^{S} \mu_{ik} Y_k \; ; \; i = 1, 2, 3, ..., M. \tag{3.6}$$

where S denotes the number of species, M is the number of different elements in the mixture considered and $\sum_{i=1}^{M} Z_i = 1$. The coefficients, μ_{ik}, denote the mass proportion of the element i in the species k and is given by

$$\mu_{ik} = \frac{M_i}{M_k}, \tag{3.7}$$

where M_i is the molar mass of the element i and M_k is the molar mass of the species k. Since Z_i is strictly conserved, the source term in its transport equation becomes zero,

$$\sum_{k=1}^{S} \mu_{ik} M_k \omega_k = 0; \text{ for } i = 1, 2, 3, ..., M. \tag{3.8}$$

Employing equations (3.6) and (3.8) to equation (3.4) and assuming (as an approximation) all the diffusion coefficients, $D_k = D$, are equal for all species k, the species mass conservation equation reduces to the simple relation for the element mass conservation equation as

$$\frac{\partial(\rho Z_i)}{\partial t} + \frac{\partial(\rho u_j Z_i)}{\partial x_j} = \frac{\partial}{\partial x_j}(\frac{\mu}{Sc}\frac{\partial Z_i}{\partial x_j}), \tag{3.9}$$

where $Sc = \frac{\mu}{\rho D}$ is the Schmidt number.

3.2.3 The Energy Equation

To evaluate the density and the chemical reaction rate, the knowledge of temperature, T, is necessary, which can be obtained by solving the energy transport equation. According to the *first law of thermodynamics*, the gain in total energy is equal

to the heat supplied by the heat conduction to the mass element and the work done by the surface forces on the element. Several forms of this equation exist having either the static temperature, static enthalpy, stagnation enthalpy or internal energy as the principal variable. In terms of the total energy e_t, the equation for energy balance in flow can be expressed as

$$\frac{\partial(\rho e_t)}{\partial t} + \frac{\partial u_j(\rho e_t + p)}{\partial x_j} = -\frac{\partial q_j}{\partial x_j}, \tag{3.10}$$

where the total energy, $e_t = e + \frac{1}{2}u_i u_i$, is the sum of the internal (thermal) energy, e, and the kinetic energy, $\frac{1}{2}u_i u_i$; q_j is the energy flux vector.

This energy transport equation can also be formulated as a balance equation for enthalpy,

$$h = e_t + \frac{p}{\rho}, \tag{3.11}$$

which follows

$$\frac{\partial \rho h}{\partial t} + \frac{\partial u_j \rho h}{\partial x_j} = -\frac{\partial q_j}{\partial x_j} + \frac{\partial p}{\partial t}. \tag{3.12}$$

The enthalpy of the mixture in equation (3.12) is related to the temperature by its definition in terms of the species enthalpy,

$$h = \sum_k h_k Y_k, \tag{3.13}$$

where Y_k is the mass fraction of species k and h_k is the specific enthalpy of species k which is approximated by

$$h_k = c_{pk} T + \Delta h_k, \tag{3.14}$$

where c_{pk} is the specific heat at constant pressure of species k and Δh_k is the heat of formation of species k. Both quantities are constant and selected to approximate the actual $h_k(T)$ variation in the temperature range of interest and the heat liberated in chemical reaction.

Therefore, combining equations (3.13) and (3.14), the enthalpy, h, can be ex-

pressed as a function of T as

$$h = c_p T + \sum_k Y_k \Delta h_k, \tag{3.15}$$

where $c_p = \sum_k Y_k c_{pk}$ is the specific heat for the mixture at constant pressure.

The energy flux vector, q_j, is given by the three different parts (Warnatz *et al* [69]) as

$$q_j = q_j^c + q_j^d + q_j^D, \tag{3.16}$$

where q_j^c denotes flux by *heat conduction* and according to the *Fourier's law* it is given by

$$q_j^c = -\kappa \frac{\partial T}{\partial x_j}, \tag{3.17}$$

where κ is the thermal conductivity of the mixture; q_j^d denotes flux caused by *inter-diffusion* of the species and is given by

$$q_j^d = \sum_k h_k J_{kj} = -\frac{\mu}{Sc} \sum_k h_k \frac{\partial Y_k}{\partial x_j}, \tag{3.18}$$

where equal diffusivities have been assumed; and q_j^D denotes the flux caused by *Dofour effect*. The importance of the *Dofour effect* is negligible (Warnatz *et al* [69], page 158) in chemically reacting flows and has been neglected here.

We can then write the energy flux vector as

$$q_j = -\kappa \frac{\partial T}{\partial x_j} - \frac{\mu}{Sc} \sum_k h_k \frac{\partial Y_k}{\partial x_j}. \tag{3.19}$$

As $h = h(T, Y_k)$, the temperature gradient can be converted to enthalpy gradient, yielding

$$\begin{aligned} \frac{\partial h}{\partial x_j} &= \frac{\partial h}{\partial T}\frac{\partial T}{\partial x_j} + \sum \frac{\partial h}{\partial Y_k}\frac{\partial Y_k}{\partial x_j} \\ &= C_p \frac{\partial T}{\partial x_j} + \sum h_k \frac{\partial Y_k}{\partial x_j}. \end{aligned} \tag{3.20}$$

Using this equation (3.20) to equation (3.19), the energy flux vector becomes,

$$q_j = -\frac{\mu}{Pr}\frac{\partial h}{\partial x_j} + \mu\left(\frac{1}{Pr} - \frac{1}{Sc}\right)\sum_k h_k \frac{\partial Y_k}{\partial x_j}, \tag{3.21}$$

where $Pr = \frac{C_p \mu}{\kappa}$ is the Prandtl number.

The energy transport equation in terms of enthalpy of the mixture can now be written as

$$\frac{\partial(\rho h)}{\partial t} + \frac{\partial(\rho u_j h)}{\partial x_j} = -\frac{\partial}{\partial x_j}\left[-\frac{\mu}{Pr}\frac{\partial h}{\partial x_j} + \mu\left(\frac{1}{Pr} - \frac{1}{Sc}\right)\sum_k h_k \frac{\partial Y_k}{\partial x_j}\right] + \frac{\partial p}{\partial t}. \tag{3.22}$$

This equation can be significantly simplified by introducing some assumptions as follows:

1. If the rate of heat transfer is same as the mass transfer, the ratio of the Schmidt number and Prandtl number, known as the *Lewis number*, is unity i.e., $Le = \frac{Sc}{Pr} = 1$.
2. For low speed flows i.e., flows with small Mach number, Ma, the term $\frac{\partial p}{\partial t}$ is negligible (Branley [5]).

Applying these approximations to equation (3.22), the enthalpy equation further simplifies to

$$\frac{\partial(\rho h)}{\partial t} + \frac{\partial(\rho u_j h)}{\partial x_j} = \frac{\partial}{\partial x_j}\left[\frac{\mu}{Pr}\frac{\partial h}{\partial x_j}\right], \tag{3.23}$$

which is the identical form to the element mass transport equation (3.9).

3.2.4 The Equation of State

In order to make the system of governing equations close completely, the equation of state for density is also needed, which is given as

$$p = \rho R_0 T \sum_k \frac{Y_k}{M_k}, \tag{3.24}$$

where R_0 is the universal gas constant, e.g., $82\ atoms.cm^3 mole^{-1} K^{-1}$ and T is the mixture temperature in Kelvin (K).

If the molar masses of the various species do not greatly differ from one another, an approximate form of equation (3.24) is appropriate, namely

$$p = \rho RT, \tag{3.25}$$

where R is the mass-based gas constant.

3.2.5 The Mixture Fraction and Mixing Patterns

In a two feeded problem, a schematic of a two-feed mixing problem is shown in Fig. 3.1, the element mass fraction can be normalised in the form of $(Z_i - Z_{iO})/(Z_{iF} - Z_{iO})$ and the boundary conditions become identical for all i. So, we may define

$$\xi = \frac{Z_i - Z_{iO}}{Z_{iF} - Z_{iO}}, \tag{3.26}$$

which is called the *mixture fraction* and is used to evaluate the thermochemical variables such as density, temperature and species concentrations of the mixture. The subscripts O and F refer to as oxidiser and fuel stream respectively. As mixing proceeds it is seen that $\xi = 0$ in oxidiser feed and 1 in fuel feed, and that ξ may be physically interpreted as the mass fraction of the material in the mixture which originated from fuel feed, with $1 - \xi$ originating from oxidiser feed. Thus the result of turbulent interdiffusion on the composition at a point is the same as if we take a mass ξ of fuel feed and mix it with a mass $1 - \xi$ of oxidiser feed and let reaction occur. For this reason ξ is referred to as the *mixture fraction*.

In terms of this mixture fraction, the equation (3.9) becomes,

$$\frac{\partial(\rho\xi)}{\partial t} + \frac{\partial(\rho u_j \xi)}{\partial x_j} = \frac{\partial}{\partial x_j}\left(\Gamma \frac{\partial \xi}{\partial x_j}\right), \tag{3.27}$$

where $\Gamma = \frac{\mu}{Pr} = \frac{\mu}{Sc}$ is the diffusion coefficient.

The molecular viscosity μ is strongly affected by the fluid temperature, and its dependence can be expressed through the *Sutherland's Law* (in White [70], page 28-29) as

$$\mu = \mu_{ref}\left(\frac{T}{T_{ref}}\right)^{3/2} \frac{T_{ref}+S_L}{T+S_L}, \tag{3.28}$$

where S_L is the Sutherland's law constant, which is a characteristic of gas; μ_{ref}

and T_{ref} are the reference viscosity and temperature respectively. For example, for air: the Sutherland's law constant (S_L) is 111K, the reference temperature (T_{ref}) is 273K, and the reference viscosity (μ_{ref}) is $1.716 \times 10^{-}5$ N.s/m^2.

3.3 The Filtering Operation

3.3.1 The Spatial Filtering

To obtain the LES equations the governing equations are filtered. A spatial filtering operation is used to separate the large scale (resolved scale) flow field from the small scale (sub-grid scale). If $f(x_j, t)$ is a generic instantaneous variable at a location, x_j, the corresponding filtered variable, known as the resolvable component of $f(x_j, t)$ and denoted by $\bar{f}(x_j, t)$, is defined as the convolution of $f(x_j, t)$ with a filter function G, Leonard [71], according to:

$$\bar{f}(x_j, t) = \int_D f(x'_j, t) G(x_j - x'_j, \Delta(x_j)) dx'_j, \tag{3.29}$$

where D is the entire domain; $\Delta(x_j)$ is the filter width which in LES practice is generally related to the mesh size, e.g., $\Delta = (\delta x \delta y \delta z)^{1/3}$ and G is the suitably defined filter function which must satisfy the normalisation condition:

$$\int_D G(x_j - x'_j, \Delta(x_j)) dx'_j = 1. \tag{3.30}$$

It is important to note that this filter function determines the size and structure of the smallest resolvable eddies. Various distributions of the filter function are available in the literature, for example, see Leonard [71], Germano [72], and Ghosal and Moin [73]. The most commonly used filter functions are given below:

the "top hat" filter,

$$G[x_j - x'_j, \Delta(x_j)] = \begin{cases} \frac{1}{\Delta(x_j)} & \text{if} \quad |x_j - x'_j| \leq \frac{\Delta(x_j)}{2} \\ 0 & \text{otherwise} \end{cases} \tag{3.31}$$

the Gaussian filter,

$$G[x_j - x'_j, \Delta(x_j)] = \sqrt{\frac{6}{\pi\{\Delta(x_j)\}^2} exp\left[-\frac{6(x_j - x'_j)^2}{\{\Delta(x_j)\}}\right]} \tag{3.32}$$

and the Fourier cut-off filter,

$$G[x_j - x'_j, \Delta(x_j)] = \frac{sin(k_c(x_j - x'_j))}{\pi(x_j - x'_j)} \; ; \; k_c = \frac{\pi}{\Delta(x_j)}. \tag{3.33}$$

In practical use, the Gaussian filter and the Fourier cut-off filter are usually applied only in homogeneous directions whereas a top hat filter is applied in inhomogeneous directions. In our simulation we have used the "top hat" filter given in equation (3.31) suggested by Germano [72] as it fits naturally into a finite volume formulation, di Mare and Jones [15].

At the time of applying the spatial filter to the Navier-Stokes (N-S) and mixture fraction equations, some rules for the manipulation of filtered quantities must be known. The following rules as with Reynolds averages, apply for the spatial filtering:

$$\overline{cf} = c\bar{f}, \tag{3.34}$$

where c is a constant and $f(x_j, t)$ is a spatial function. For two functions, $f_1(x_j, t)$ and $f_2(x_j, t)$, it is clear that

$$\overline{f_1 + f_2} = \bar{f}_1 + \bar{f}_2 \tag{3.35}$$

unlike the rules for Reynolds averages however,

$$\overline{f_1.f_2} \neq \bar{f}_1.\bar{f}_2, \tag{3.36}$$

and in general,

$$\bar{\bar{f}} \neq \bar{f}, \tag{3.37}$$

But, it can be seen from the definition of the Fourier cut-off filter that

$$\bar{\bar{f}} = \bar{f}. \tag{3.38}$$

In this case, the spatial filtering commutes with the temporal differentiation as,

$$\overline{\frac{\partial f}{\partial t}} = \frac{\partial \bar{f}}{\partial t}. \tag{3.39}$$

As the filter width must be a function of space, the spatial filtering and spatial differentiation do not commute, i.e.,

$$\overline{\frac{\partial f}{\partial x_j}} \neq \frac{\partial \bar{f}}{\partial x_j}. \tag{3.40}$$

The difference between the term on each side of (3.40) i.e., $\left(\overline{\frac{\partial f}{\partial x_j}} - \frac{\partial \bar{f}}{\partial x_j}\right)$ is referred to as commutation error. Moin *et al* [74] demonstrated this commutation error for one dimensional case. Considering the filter function G as the top hat filter (3.31), the filtering operation was defined as

$$\bar{f}(y) = \frac{1}{\Delta_+(y) + \Delta_-(y)} \int_{y-\Delta_-(y)}^{y+\Delta_+(y)} f(y')dy', \tag{3.41}$$

where $\Delta_+(y)$ and $\Delta_-(y)$ are positive functions and $\Delta_+(y) + \Delta_-(y)$ is the effective filter width at a location y. With the definition (3.41), the commutation error is given by Moin *et al* [74] as,

$$\begin{aligned}\overline{\frac{\partial f}{\partial x_j}} - \frac{\partial \bar{f}}{\partial x_j} = & \frac{\frac{d}{dy}\left(\Delta_+(y) + \Delta_-(y)\right)}{\Delta_+(y) + \Delta_-(y)} \bar{f} - \frac{1}{\Delta_+(y) + \Delta_-(y)} \\ & \times \left[f(y + \Delta_+(y)) \frac{d\Delta_+(y)}{dy} + f(y - \Delta_-(y)) \frac{d\Delta_-(y)}{dy} \right]\end{aligned} \tag{3.42}$$

This lack of commutativity between filtering and differentiation causes every spatial derivative operator in the governing equations to generate terms that can not be expressed solely in terms of the filtered fields. Therefore, a closure problem is introduced not only for the nonlinear terms but also for the linear terms. To remedy this situation, Ghosal and Moin [73] proposed an alternate definition for filtering operation by introducing a mapping, which transforms the computational space of non-uniform filter width into an alternate coordinate system where this filter width is constant. Ghosal and Moin [73] also pointed out that, in LES the grid spacing is approximately equal to the filter width which is of $O(\Delta)$. If a second-order nu-

merical scheme is used to represent the derivatives, the finite differencing error is then of the same order as the error due to the lack of commutativity of the spatial differentiation and the filtering operations. Therefore, in a LES of an inhomogeneous turbulent flow using a second-order finite differencing scheme, the filtering operation can be assumed to commute with the spatial differentiation operation to within the accuracy of the numerical approximation. In this work, this commutation error has been neglected, keeping similarity with the vast majority of the numerical simulations reported in the literature.

3.3.2 Favre Filtering

For the flow with large density variations, like in combustion, it is useful to introduce another filtering approach, namely density weighted filtering, analogous to that suggested by Favre [75]. With density weighted filtering all fluid mechanical quantities except the pressure are mass weighted. The density weighted-filter function is denoted by $\tilde{f}$ and defined as:

$$\tilde{f} = \frac{\overline{\rho f}}{\bar{\rho}}. \tag{3.43}$$

This approach has been used extensively in LES studies of compressible turbulence (Moin *et al* [76], Erlebacher *et al* [77]) and reacting flows (Branley and Jones [21], di Mare *et al* [22], Steiner and Bushe [78], Bushe and Steiner [79]).

3.4 Filtered Governing Equations

Applying the density weighted-filtered function (equation 3.43) to the continuity, Navier-Stokes and mixture fraction equations gives:

$$\frac{\partial \bar{\rho}}{\partial t} + \frac{\partial (\bar{\rho}\tilde{u}_j)}{\partial x_j} = 0, \tag{3.44}$$

$$\frac{\partial (\bar{\rho}\tilde{u}_i)}{\partial t} + \frac{\partial (\bar{\rho}\widetilde{u_i u_j})}{\partial x_j} = -\frac{\partial \bar{p}}{\partial x_i} + \frac{\partial}{\partial x_j}\left[2\mu \bar{S}_{ij} - \frac{2}{3}\mu \bar{S}_{kk}\delta_{ij}\right], \tag{3.45}$$

$$\frac{\partial \bar{\rho}\tilde{\xi}}{\partial t} + \frac{\partial \bar{\rho}\widetilde{u_j \xi}}{\partial x_j} = \frac{\partial}{\partial x_j}\left(\Gamma \frac{\partial \tilde{\xi}}{\partial x_j}\right), \tag{3.46}$$

where the unknown terms $\bar{\rho}\widetilde{u_i}u_j$ and $\bar{\rho}\widetilde{u_j\xi}$ are introduced and need to be modelled. The filtered strain rate, $\bar{S}_{ij}$, is defined by

$$\bar{S}_{ij} = \tfrac{1}{2}(\frac{\partial \bar{u}_i}{\partial x_j} + \frac{\partial \bar{u}_j}{\partial x_i}). \tag{3.47}$$

3.5 Mathematical Modelling

3.5.1 Sub-Grid Scale Modelling

An application of the density weighted filter to the nonlinear convective terms in the system of governing equations introduces the unknown terms, $\bar{\rho}\widetilde{u_i}u_j$ and $\bar{\rho}\widetilde{u_j\xi}$ in equations (3.45) and (3.46) respectively, leaving the equations unclosed. These unknown terms are defined, Germano [80], by

$$\bar{\rho}\widetilde{u_i}u_j = \bar{\rho}\tilde{u}_i\tilde{u}_j + \tau_{ij}, \tag{3.48}$$

and

$$\bar{\rho}\widetilde{u_j\xi} = \bar{\rho}\tilde{u}_j\tilde{\xi} + J_j^{sgs}, \tag{3.49}$$

where τ_{ij} and J_j^{sgs} are unknown terms and referred to as sub-grid scale stresses and sub-grid scale scalar fluxes respectively. These unknowns must be modelled.

The most famous and still widely used model of Smagorinsky [9] and its dynamically calibrated version of Germano *et al* [81], described in the following subsections, have been used for the sub-grid scale stresses, τ_{ij}, modelling in the present work.

For the sub-grid scale scalar fluxes a gradient model, Schmidt and Schumann [82], is applied:

$$J_j^{sgs} = -\bar{\rho}\Gamma_{sgs}\frac{\partial \tilde{\xi}}{\partial x_j} = -\frac{\mu_{sgs}}{\sigma_{sgs}}\frac{\partial \tilde{\xi}}{\partial x_j}, \tag{3.50}$$

where σ_{sgs} is a constant sub-grid scale Prandtl/Schmidt number which is here assigned a value of 0.7.

3.5.2 The Smagorinsky Model

The Smagorinsky model [9], named in honour of J. Smagorinsky, is the most famous and still widely used model for the sub-grid scale stresses. The model is based on eddy viscosity assumption of the form:

$$\tau_{ij} - \frac{1}{3}\delta_{ij}\tau_{kk} = -2\mu_{sgs}\bar{S}_{ij}. \tag{3.51}$$

The reason for carring $\frac{1}{3}\delta_{ij}\tau_{kk}$ in (3.51) is to permit the left hand side of (3.51) to become zero at each point as does the right hand side, when the indices are contracted (Hinze [83]). The sub-grid dynamic eddy viscosity, μ_{sgs}, related to the sub-grid kinetic eddy viscosity, ν_{sgs}, as

$$\mu_{sgs} = \rho\nu_{sgs},$$

is obtained by assuming that the turbulent dissipation is in equilibrium with turbulent energy production which yields an expression of

$$\mu_{sgs} = \bar{\rho}(C_s\Delta)^2|\bar{S}|, \tag{3.52}$$

where C_S is the Smagorinsky model constant and $|\bar{S}| = \sqrt{2\bar{S}_{ij}\bar{S}_{ij}}$ is the magnitude of the resolved scale strain rate tensor $\bar{S}_{ij}$ defined in equation (3.47).

Thus, the Smagorinsky model takes the form of

$$\tau_{ij} - \frac{1}{3}\delta_{ij}\tau_{kk} = -2\bar{\rho}(C_s\Delta)^2|\bar{S}|\bar{S}_{ij}. \tag{3.53}$$

The value of Smagorinsky model constant, C_s in (3.53) is to be assigned. Lilly [10] suggested that the model can be analytically calibrated with an inertial subrange in order to obtain an approximation for the residual stress dissipation. Following Lilly [10]'s work, a relation between the Smagorinsky model constant, C_s, and the Kolmogorov universal subrange constant, C_k, is established by Schmidt and Schumann [82] and Wille [84] in the following way:

$$C_s \approx \frac{1}{\pi}\left(\frac{2}{3C_k}\right)^{\frac{3}{4}}. \tag{3.54}$$

With the Kolmogorov constant $C_k \approx 1.6$, used by Wille [84], the value of the Smagorinsky constant, C_s, was found as 0.165 whereas Lilly [10] found it as $C_s = 0.23$. In most calculations, this value for the Smagorinsky constant is found too large which results in excessive attenuation of small scales. In successful simulations of channel flow (e.g., Deardorff [11]), the value of C_s, for instance, vary around 0.07 while the values $0.081 - 0.1$ were used successfully in mixing layers (e.g., Yoshizawa [85]). In this simulation, $C_s = 0.1$ has been used as suggested by Branly and Jones [21]. Together with this constant C_s, we have also used a dynamically calibrated C_s which is described in the following subsection.

The dissipation rate can be calculated from,

$$\epsilon = 2\nu \bar{S}_{ij} \bar{S}_{ij}, \tag{3.55}$$

Substitution of equation (3.52) into equation (3.55) gives the dissipation rate by means of Smagorinsky model as,

$$\epsilon = (C_s \Delta)^2 |\bar{S}|^3. \tag{3.56}$$

3.5.3 The Dynamic Model for the Smagorinsky Constant

Dynamic calibration of the Smagorinsky model constant is proposed by Germano *et al* [81]. According to Germano *et al* [81], a test filter function $\hat{G}$ having width $\hat{\Delta} > \Delta$ is considered to compute the Smagorinsky model constant C_s in equation (3.53). The hat $(\hat{.})$ will denote a test filtered quantity and which is given by

$$\hat{f}(x_j, t) = \int_D f(x'_j, t) \hat{G}(x_j - x'_j, \hat{\Delta}(x_j)) dx'_j. \tag{3.57}$$

According to this test filter, the Favre-filtered momentum conservation equation becomes

$$\frac{\partial \widehat{\bar{\rho}\tilde{u}_j}}{\partial t} + \frac{\partial}{\partial x_j} \left(\frac{\widehat{\bar{\rho}\tilde{u}_i} \widehat{\bar{\rho}\tilde{u}_j}}{\hat{\bar{\rho}}} \right) = -\frac{\partial \hat{\bar{p}}}{\partial x_i} + \frac{\partial \hat{\bar{\sigma}}_{ij}}{\partial x_j} - \frac{\partial T_{ij}}{\partial x_j}, \tag{3.58}$$

where the subtest scale stresses, T_{ij}, is

$$T_{ij} = \widehat{\bar{\rho}\widetilde{u_i u_j}} - \left(\frac{\widehat{\bar{\rho}\widetilde{u}_i}\widehat{\bar{\rho}\widetilde{u}_j}}{\hat{\bar{\rho}}} \right). \tag{3.59}$$

Now consider the resolved turbulent stresses, L_{ij}, also known as *Leonard stress*, defined as

$$L_{ij} = \widehat{\bar{\rho}\widetilde{u}_i\widetilde{u}_j} - \left(\frac{\widehat{\bar{\rho}\widetilde{u}_i}\widehat{\bar{\rho}\widetilde{u}_j}}{\hat{\bar{\rho}}} \right), \tag{3.60}$$

which is computable from large scale eddy.

The resolved turbulent stresses are representative of the contribution to the Reynolds stresses by the scales whose length is intermediate between the grid filter width and the test filter width i.e., the small resolved scales. Therefore, the quantities given in equations (3.59) and (3.60) are related to the Germano identity [72] as

$$L_{ij} = T_{ij} - \hat{\tau}_{ij}, \tag{3.61}$$

where $\hat{\tau}_{ij} = \widehat{\bar{\rho}\widetilde{u_i u_j}} - \widehat{\bar{\rho}\widetilde{u}_i\widetilde{u}_j}$ is the test filter average of the sub-grid scale stresses, τ_{ij}.

The identity (3.61) can be used to derive more accurate form of the sub-grid scale stress models by determining the value of Smagorinsky constant which is the most appropriate to the instantaneous state of the flow. To utilize this identity, it is assumed that the same functional form can be used to model both T_{ij} and τ_{ij}. In this case the Smagorinsky model is employed, so that

$$T_{ij} - \frac{1}{3}\delta_{ij}T_{kk} = -2\hat{\bar{\rho}}(C_s\hat{\Delta})^2|\hat{\bar{S}}|\hat{\bar{S}}_{ij}, \tag{3.62}$$

$$\tau_{ij} - \frac{1}{3}\delta_{ij}\tau_{kk} = -2\bar{\rho}(C_s\Delta)^2|\bar{S}|\bar{S}_{ij}, \tag{3.63}$$

where

$$\hat{\bar{S}}_{ij} = \frac{1}{2}\left(\frac{\partial\hat{\bar{u}}_i}{\partial x_j} + \frac{\partial\hat{\bar{u}}_j}{\partial x_i} \right) \qquad \text{and} \qquad |\hat{\bar{S}}| = \sqrt{2\hat{\bar{S}}_{ij}\hat{\bar{S}}_{ij}}.$$

Substitution of (3.62) and (3.63) into the Germano identity (3.61) gives

$$L_{ij} - \frac{1}{3}L_{kk}\delta_{ij} = -C\alpha_{ij} + \widehat{C\beta}_{ij}, \tag{3.64}$$

where

$$\alpha_{ij} = 2\hat{\bar{\rho}}\hat{\Delta}^2|\hat{\bar{S}}_{ij}|\hat{\bar{S}}_{ij} \qquad ; \qquad \beta_{ij} = 2\bar{\rho}\Delta^2\bar{S}_{ij}\bar{S}_{ij} \qquad \text{and} \qquad C = C_s^2.$$

In equation (3.64), since the constant C appears inside the test filtering operation, we can not use this equation directly for determining the constant C. In order to continue modelling, Germano *et al* [81] and Moin *et al* [76] ignored the fact that C is a function of position and took C out of the test filtering operation as if it were a constant. This approximation gives

$$L_{ij} - \frac{1}{3}L_{kk}\delta_{ij} = -C(\alpha_{ij} - \hat{\beta}_{ij}). \tag{3.65}$$

In order to obtain a scalar equation for C, the equation (3.65) can be constructed with $\bar{S}_{ij}$ as

$$C = -\frac{L^a_{ij}\bar{S}_{ij}}{M_{ij}\bar{S}_{ij}}, \tag{3.66}$$

where $L^a_{ij} = L_{ij} - \frac{1}{3}L_{kk}\delta_{ij}$ is the anisotropic part of the resolved stress and $M_{ij} = (\alpha_{ij} - \hat{\beta}_{ij})$.

The obtained value of C from expression (3.66) can either be negative or positive. Ghosal *et al* [86] pointed out that a negative value of C implies locally negative eddy viscosity, which in turn implies a flow of energy from small scale to the resolved scales which is known as backscatter and using expression (3.66) in LES, the computation is found to become unstable. But the only adjustable parameter in the model is the ratio of the test filter width to the grid filter width, $\frac{\hat{\Delta}}{\Delta}$. From *a priori test*, Germano *et al* [81] reports that the optimal value for this adjustable parameter to be 2. However, they pointed out that the actual large eddy simulation with the dynamic model appeared to be very intensive to this ratio. In this test using data from direct simulations in turbulent channel flows, Germano *et al* [81] also found that the denominator of (3.66) could vanish or become so small as to lead a computationally unstable value of C. To overcome this unstable situation, C was approximated as only a function of y, the normal direction to wall, and t. To make the expression (3.66) consistent with this assumption, they proposed to average of

both the numerator and denominator over that homogeneous direction, y, to yield

$$C(y,t) = -\frac{\left\langle L_{ij}^a \bar{S}_{ij} \right\rangle_y}{\left\langle M_{ij} \bar{S}_{ij} \right\rangle_y}. \tag{3.67}$$

However, the above procedure perhaps losing some of the conceptual advantages of their formulations.

Lilly [87] reported that, since equation (3.65) represents five independent equation with only one unknown, no value of C can be chosen to satisfy each of them simultaneously. Therefore, Lilly proposed a modification to the Germano's model. Instead of constructing L_{ij} with $\bar{S}_{ij}$, he suggested to minimise the error by applying a least square approach. According to his modification, Q to be the square of the error in (3.64) as

$$Q = \left[L_{ij} - \frac{1}{3} L_{kk} \delta_{ij} + C M_{ij} \right]^2. \tag{3.68}$$

Upon setting $\frac{\partial Q}{\partial C} = 0$, C can be calculated as

$$C = -\frac{L_{ij}^a M_{ij}}{M_{ij}^2} \tag{3.69}$$

It can easily be shown that $\frac{\partial^2 Q}{\partial C^2} > 0$, thus this value of C represents a local minimum of Q. By contrast, the denominator of (3.69) can vanish only if each of the five independent components of M_{ij} vanish separately, that is if the test scale strain vanishes completely. In this case, the numerator also vanishes.

The mean value of the dynamic $C_s = \sqrt{C}$ obtained from the relation (3.69) is presented in Fig. 3.5. The distribution of the dynamic C_s on the horizontal midplane of the combustor is shown in frame (a), while its variations along the axial and radial directions are presented in frames (b) and (c) respectively. These results of C_s show that it is higher in the region of high turbulent intensity i.e., near the inlet. The value then decreases towards the downstream and vanishes at the outlet.

3.5.4 Combustion Modelling: Conserved Scalar Approach

In the conserved scalar modelling approach chemical reaction rates are assumed to be fast compared to the rate at which reactants mix. The mixing is described by

a strictly conserved scalar also known as the mixture fraction. The instantaneous species concentrations are then considered to be a unique function of this conserved scalar. As the functional dependence is highly nonlinear, mean or filtered values are obtained via the probability density function of the conserved scalar (Bilger [88]). Once the density weighted mixture fraction, $\tilde{\xi}$, and its sub-grid scale variance, $\tilde{\xi}''^2_{sgs}$, are known, the filtered density ($\bar{\rho}$) and density weighted thermochemical variables ($\tilde{\psi}$) are obtained from the following:

$$\bar{\rho}(\tilde{\xi}) = \left(\int_0^1 \frac{\tilde{P}(\xi)}{\rho(\xi)} d\xi \right)^{-1}, \tag{3.70}$$

and

$$\tilde{\psi}(\tilde{\xi}) = \int_0^1 \psi(\xi) \tilde{P}(\xi) d\xi, \tag{3.71}$$

where $\tilde{P}(\xi)$ is the density weighted β-pdf, which satisfies the following normalisation condition,

$$\int_0^1 \tilde{P}(\xi) d\xi = 1, \tag{3.72}$$

and is defined as

$$\tilde{P}(\xi) = \frac{\xi^{r-1}(1-\xi)^{s-1}}{\beta(r,s)}, \tag{3.73}$$

where

$$r = \tilde{\xi} \left(\frac{\tilde{\xi}(1-\tilde{\xi})}{\widetilde{\xi''^2_{sgs}}} - 1 \right) \quad , \quad s = \frac{1-\tilde{\xi}}{\tilde{\xi}} r \tag{3.74}$$

and

$$\beta(r,s) = \int_0^1 \xi^{r-1}(1-\xi)^{s-1} d\xi \tag{3.75}$$

is the beta function.

The filtered value of ξ is obtained from the solution of equation (3.46) while various approaches to the modelling of the sub-grid scalar variance, $\widetilde{\xi''^2_{sgs}}$, which appeared in relation (3.74) are available in the literature (Girimaji and Zhou [89], Pierce and Moin [90], Cook and Riley [91]). In this computation, an equilibrium

model for $\widetilde{\xi'^2_{sgs}}$ is adopted as follows:

$$\widetilde{\xi'^2_{sgs}} = C_\xi \Delta^2 \left| \frac{\partial \tilde{\xi}}{\partial x_j} \frac{\partial \tilde{\xi}}{\partial x_j} \right|, \tag{3.76}$$

where C_ξ is a model parameter which has been derived analytically by di Mare [92] and Branly and Jones [21] as 0.2 according to the early works of Lilly [10] and Schmidt and Schumann [82]. But Branly and Jones [21] replaced the value of $C_\xi = 0.2$ with a smaller value of $C_\xi = 0.1$ and found an improved predictions of scalars in LES of a hydrogen flame. As Branly and Jones [21], $C_\xi = 0.1$ is used for the present simulation. However, a dynamic calibration of the model is also possible, as discussed by Pierce and Moin [93], though this has not been considered in the present work.

3.5.5 Integration of the Sub-grid β-pdf

The relationship between the thermochemical variables, ψ, and the mixture fraction, ξ, are expressed as a polynomial of degree n in the conserved scalar:

$$\psi(\xi) = \sum_{i=0}^{n} a_i \xi^i. \tag{3.77}$$

Substituting the polynomial relation (3.77) and the $\beta - pdf$ (3.73) into equation (3.71), the Favre-filtered thermochemical variables may now be rewritten as

$$\tilde{\psi}(\tilde{\xi}) = \int_0^1 \sum_{i=0}^{n} a_i \xi^i \frac{\xi^{r-1}(1-\xi)^{s-1}}{\beta(r,s)} d\xi. \tag{3.78}$$

Making use of the beta function given in (3.75) and the Gamma (Γ) function defined as

$$\Gamma(r) = \int_0^\infty e^{-x} x^{r-1} dx, \tag{3.79}$$

with the relationship between β and Γ functions as,

$$\beta(r,s) = \frac{\Gamma(r)\Gamma(s)}{\Gamma(r+s)}, \tag{3.80}$$

the filtered scalar quantities are finally computed through the following series,

$$\tilde{\psi}(\tilde{\xi}) = \sum_{i=0}^{n} \frac{a_i(r+i-1)!(r+s-1)!}{(r+s+i-1)!(r-1)!}, \tag{3.81}$$

where the coefficients a_0, a_1, ..., a_n are obtained from the polynomial fitting of the flamelet data against the mixture fraction shown in Fig. 3.3.

3.6 Laminar Flamelet Approach

In the laminar flamelet approach the turbulent flame is presumed to comprise an ensemble of laminar flames. Each element of the flame front can then be viewed as a small laminar flame which is also called flamelet (Poinsot and Veynante [94], Williams [95]). The formulation is restricted to 'thin' flame burning where the thickness of the burning zone is less than the Kolmogorov length scale - this fundamental requirement for the existence of flamelets (i.e., laminar-like burning zones in a turbulent medium) is referred to as the Klimov-Williams criterion. Since the chemical time scale is short, the chemistry is more active within this thin layer also known as the fuel consumption region. If this layer is thin compared to the size of Kolmogrov eddies, it is embedded within the quasi-laminar and turbulent flames of such an eddy and the application of the laminar flamelet structure to a turbulent flame is justified. For a more detailed review of the theory Williams [96] and Peters [26; 97] may be consulted.

In the flamelet calculation, the equations for energy and species conservation are usually transformed from the physical co-ordinate system to the mixture fraction and scalar dissipation rate space, where the chemical reaction is assumed to be fast and the scalar dissipation rate (strain rate) accounts for the effects of non-equilibrium. The chemical species, flame temperature and density all can be described only by the two variables, mixture fraction and scalar dissipation rate. Computationally a massive advantage is achieved in the application of laminar flamelet to a turbulent flame as the conservation equations for individual species concentrations and energy are decoupled from the flow calculation. Full details of the mathematical formulations of the flamelet generation are skipped in this thesis but the readers are referred to Peters [26; 97] where a comprehensive review of the

formulation of the laminar flamelet and its application to a turbulent non-premixed flame can be found.

In steady laminar counterflow flames the composition depends on the mixture fraction and the rate of strain, with extinction occurring at high strain rates. However the incorporation of strain or flame stretch effects into LES is problematic and knowledge of the local rate of strain or the scalar dissipation rate - often used in RANS approaches - is insufficient to characterise local extinction. For this reason a flamelet at a single strain rate is selected in the present work.

3.7 Description of Experiment

A schematic of the cylindrical combustor with the computational domain is shown in Fig. 3.2, which is the same configuration as the experimental investigation performed by Nishida and Mukohara [1]. This configuration was chosen on the model basis so the theoretical results could be compared with those obtained experimentally. Gaseous propane (C_3H_8) is injected through a circular nozzle of an internal diameter of $2mm$ at the centre of the combustor inlet while the preheated air with an averaged velocity of $0.96ms^{-1}$ and temperature of $773K$ is supplied through the circular inlet of $115mm$ internal diameter into the $1m$ long combustion chamber. The average fuel velocity measured at the inlet is $30ms^{-1}$, which corresponds to a flow Reynolds number of $13,000$ in the computation. The overall equivalence ratio is 1.6 so that burning occurs in a fuel-rich nonpremixed combustion mode, which produces various forms of hydrocarbons in the combustion products. One of them is acetylene, C_2H_2, which contributes to the formation and growth of soots (solid carbon particles, solid emissions) in the combustion process.

3.8 Results and Discussion

In this section we begin with the presentation of the results obtained from the flamelet computations and this is followed by the presentation of the LES results including the flame temperature, density, mixture fraction and species concentrations. Scatter plots of the thermochemical variables are presented thereafter. Results of the velocity field, turbulent fluctuating and sgs quantities are also presented. The

Table 3.1: Sub-grid scale models used in the computation.

Case		Sub-grid scale models	Legend
1	τ_{ij}	: Smagorinsky model, $C_s = 0.1$	Solid line
	J_j^{sgs}	: Sub-grid scale Schmidt/Prandtl number, $\sigma_{sgs} = 0.7$	
	$\tilde{\xi}_{sgs}^{\prime 2}$	: Equilibrium model, $C_\xi = 0.1$	
2	τ_{ij}	: Dynamic model for C_s	Dashed line
	J_j^{sgs}	: Sub-grid scale Schmidt/Prandtl number, $\sigma_{sgs} = 0.7$	
	$\tilde{\xi}_{sgs}^{\prime 2}$	: Equilibrium model, $C_\xi = 0.1$	

LES results are obtained for two different sgs cases, Case1: Smagorinsky model constant, $C_s = 0.1$, and Case2: dynamically calibrated C_s. The solid lines represent Case1, while the dashed lines indicate Case2. The model parameters are summarised in Table 3.1. The time mean (average) values, defined as

$$< \tilde{\phi} >= \frac{1}{N_t} \sum_{n=1}^{N_t} \tilde{\phi}(x_i, t), \tag{3.82}$$

have been accumulated over a total of 3×10^5 time steps.

The sub-grid contributions to the root mean square (rms) values are negligible and are ignored with the consequence that the rms of turbulence fluctuations in $\tilde{\phi}$ is obtained from:

$$\phi'_{rms} = \left(\frac{1}{N_t} \sum_{n=1}^{N_t} \left(\tilde{\phi} - < \tilde{\phi} > \right)^2 \right)^{1/2}. \tag{3.83}$$

The details of the numerical methods and boundary conditions are discussed in Chapter A.

3.8.1 Laminar Flamelet Results

The dependencies of temperature, density and species mole fractions on the mixture fraction (ξ) resulting from the laminar flamelet computations used in the combustion model are plotted in Fig. 3.3. The flamelet is generated at a strain rate of $15 s^{-1}$ and the boundary conditions are taken to comply with the experimental pre-heated conditions for the air. A detailed reaction mechanism consisting of 87 species and 466

reactions has been used to generate the flamelet data. Further details of the reaction mechanism can be found in Leung [98]. The flamelet calculation was performed under adiabatic condition. To account for radiative heat loss to the combustor walls the flamelet temperature is adjusted using the following relation, Fairweather *et al* [2]:

$$T(\xi) = T_{ad}(\xi)\left[1 - \chi\left(\frac{T_{ad}(\xi)}{T_{ad,max}}\right)^4\right], \tag{3.84}$$

where the radiative fraction, χ, is taken as 0.2 and where T_{ad} represents the adiabatic flamelet temperature.

The flamelet results are shown in Fig. 3.3 where the temperature, density and compositions as a function of mixture fraction are plotted. At a mixture fraction $\xi = 0$ the temperature, $T = 773K$ corresponds to that of the pre-heated air stream whereas the temperature, $T = 298K$ at $\xi = 1$, is that of the propane. At stoichiometric condition (ξ_{stoich}), which is at about $\xi_{stoich} = 0.06$, the oxygen and fuel stream curves meet together and react, see Fig. 3.3 (iii), and a maximum temperature of $T = 1896K$ is achieved, Fig. 3.3 (i). The corresponding density has a minimum value at stoichiometric as expected. The concentrations of CO_2 and H_2O have maximum values close to stoichiometric condition whereas other products have maximum values under fuel-rich conditions.

A polynomial of degree $n = 20$, as described in §3.5.5, was fitted to each flamelet data set shown in Fig. 3.3 in order to determine the power coefficients, a_i, of equation (3.81). These power coefficient data were used as an input in the computation. Once the instantaneous results of the mixture fraction and the variance of the mixture fraction were computed, the power coefficient data was used to evaluate the filtered flame temperature, density and species mole fractions using the relation given in (3.81).

Look-Up tables for the flamelets of (a) density, ρ, (b) temperature, $T(K)$, (c) C_3H_8, (d) N_2, (e) O_2, (f) CO, (g) CO_2, (h) H_2, (i) H_2O, (j) C_2H_2 and (e) CH_4 as a function of mixture fraction, ξ, and mixture fraction variance, ξ'^2, are also presented in Fig. 3.4. The Look-Up tables are generated using the β-PDF integration. From these Look-Up tables, it can be seen that how the value of flamelet changes with the change of mixture fraction variance, ξ'^2.

3.8.2 Temperature, Density and Mixture Fraction results

In Fig. 3.6 some instantaneous snapshots of the flame temperature, $\tilde{T}$, on the horizontal midplane of the combustor are obtained in Case1 and plotted at different simulation times. The purposes of this figure are to visualise the flame and its structure by means of the temperature distributions and also to show how the structure of the flame temperature varies with time.

At the inlet, when the fuel gets first contact with the air, the combustion takes place and the flame temperature rises. Vortices are initially generated near the fuel nozzle and they then diffuse and propagate towards the downstream region of the combustor as seen. A higher colour contour level is seen around the centreline where the combustion occurs around the stoichiometric condition. From the figure it is clear that no combustion occurs near the wall close to the inlet zone where the temperature remains the same as that of the pre-heated air.

The mean values of the (a) flame temperature, $< \tilde{T}(K) >$, (b) density, $< \tilde{\rho} >$, and (c) mixture fraction, $< \tilde{\xi} >$, on the horizontal midplane of the combustion chamber, obtained in Case1, are shown in Fig. 3.7. The solid curve in the contour plot of $< \tilde{T}(K) >$ represents the locus of the stoichiometric mixture fraction, $< \tilde{\xi} >= 0.06$, where the maximum temperature is achieved. The contour levels show that at the centre of the combustor the flame temperature increases along the axial direction, and before it reaches to the half way through the flame temperature drops gradually. This can be seen clearly in Fig. 3.8(a). This contour plot also shows clearly the flame spreading/diffusing in the radial direction which causes a rise in the temperature of the walls at about $y > 0.25m$. The contour plot of the mean density in frame (b) shows that the density is minimum at the region where maximum temperature is achieved which can also be seen in Fig. 3.8(a). From the frame (c), the contour plot of the mean mixture fraction, it can be seen that at the center of the inlet the value of the mean mixture fraction is maximum as this region is dominated by the fuel stream. It is then decreasing towards the downstream and wall having the minimum value at the outlet, which can be seen clearly from the axial and radial profiles of the mixture fraction presented in Fig. 3.9(a)-(b).

In Fig. 3.8 the computationally predicted mean temperatures, $< \tilde{T} >$, are compared against the measurements of Nishida and Mukohara [1]. The corresponding mean density results are also presented. The results in Fig. 3.8(a) are the axial pro-

files on the centreline of the combustor, while the radial distributions of temperature at four different cross-sectional positions are plotted in Fig. 3.8(b-e) respectively. The predicted temperature along the radial direction at different cross-sectional positions are also compared with the results obtained by Fairweather *et al* [2] applying a κ-ϵ turbulence model.

In Fig. 3.8(a), the predicted mean axial temperature on the centreline initially starts with the fuel temperature at the inlet. As the combustion takes place the flame temperature increases and achieves a maximum value of $1696K$ (Case1) and $1730K$ (Case2) at about $y = 0.35m$. The flame temperature then drops gradually with increasing downstream distance with a value of about $1200K$ (Case1) and $1329K$ (Case2) arising at the outlet of the combustor. The maximum temperature in the experiments was recorded as $1778K$ at $y = 0.39m$ which is bit further downstream from the prediction and is slightly under-predicted in this computation. It can be observed that the peak level of mean temperature is predicted better in Case2. The experimental results also show a concave like shape around $y = 0.2m$, not evident in the predictions, where a slight over-prediction in both the cases is evident. However, overall a good agreement is achieved and the decaying trend of temperature along the downstream is well predicted in Case1. As expected, the mean density decreases from the inlet as the temperature rises and is minimum at the point where a maximum temperature occurs. The density then rises very slowly towards the downstream end of the combustor, consistent with the falling temperature.

The radial distribution of the mean temperature, in frames (b-e), shows that the peak value is slightly under-predicted in the computation for both the cases and near the inlet (frames (b) and (c)) this peak temperature is shifted towards the wall of the combustor and the temperature at the centre shows slight over-prediction in both the Case1 and Case2. In the most downstream stations, in frames (d) and (e), a slight under-prediction of temperature occurs at the centre but better prediction is found in Case2. Despite the slight over and under-prediction of temperature comparing with the experiment, it is clear that the trends of increasing and decaying the temperature in the radial direction are matched reasonably well with the experimental data and qualitatively their agreement is very good. The radial distributions of the mean temperature predicted by Fairweather *et al* [2] show an under-prediction near the inlet (in frame (b) and (c)) and an over-prediction at the further downstream (in frame (d)

and (e)). But comparing both the radial temperature profiles against experimental measurements, it can be seen that our predicted results have some better agreement.

We will now make some quantitative assessments of the maximum flame temperatures plotted at each downstream location and the possible consequences with respect to 'diffusion' will be discussed. At $y = 0.1m$ the maximum measured flame temperature was $1774K$ at a radial distance of about $r = 0.012m$, while it is $1683K$ (Case1) and $1714K$ (Case2) at about $r = \pm 0.018m$ in the computation. This is a somewhat larger radius than the experiment and is closer to the wall of the combustor, as mentioned earlier, indicating that the predicted flame diffuses slightly more than was evident in the experiments. This is shown clearly in (c) and (d) where the maxima occur at a radius slightly beyond those of the experiment. In (c) the predicted maximum temperature of $1715K$ (Case1) and $1720K$ (Case2) at $r = \pm 0.021m$ compared with the experimental value of $1762K$ at $r = 0.02m$. The predicted maximum temperature in (d) is $1705K$ (Case1) and $1733K$ (Case2) at $r = \pm 0.017m$ while the experimental maximum is 1773 at $r = 0.016m$. At the furthermost downstream location both the predicted and experimental maximum temperatures occur at the centre of the combustor where the corresponding values are $1689K$ (Case1) and $1724K$ (Case2); and $1768K$ respectively. These slight quantitative discrepancies may be linked with the relatively crude treatment of the radiative heat transfer adopted in the simulations, suggesting the use of a fully coupled and detailed radiation model.

Corresponding to the radial plots of the mean temperature at every cross-sectional positions, the mean density, $< \bar{\rho} >$, are also plotted in the same figure. Two equal minimum values of $< \bar{\rho} >$ are predicted at the locations of the two maximum temperatures, see (a)-(d), and a minimum at the maximum temperature in (e), which are expected as the density of mixture is always inversely proportional to the temperature.

It might be interesting to see how the above results presented in Fig. 3.8 are linked with the mixture fraction and its variance, given the fact that they are function of these two variables. Keeping these in mind, in Fig. 3.9 the mean results of the mixture fraction and the sub-grid scale mixture fraction variance are plotted along the axial direction as well as the radial directions at which we have presented the temperature and density results in the previous figure. The axial profile of the mean

mixture fraction is also compared with the experimental measurement by Nishida and Mukohara [1]. The dotted straight line in (a) and (b) indicate where the stoichiometric level of the mixture fraction occurs in the computation.

The axial mixture fraction profile on the centreline decays rapidly in the upstream region, $y < 0.2m$, and then decays slowly to the outlet of the combustor. The rapid decay in the mixture fraction means the mixing is 'fast'. The mixture fraction is highest at the inlet, consistent with the mixture fraction boundary conditions (see equation (A.1) in Chapter A). The fuel injected through the centre of the combustor inlet reacts with the supplied air and produces the combustion products (shown in Figs. 3.10-3.14), therefore, the mixture fraction is expected to decay in the axial direction as well as the radial direction (see frame (b)) where the air stream dominates. The results in both Case1 and Case2 are found same at the upstream but at the downstream of the combustor the mean mixture fraction is predicted slightly higher in Case2. However, in both the cases, an excellent agreement is achieved in comparing with the experimental data. The magnitude of the sub-grid scale variance of the mixture fraction is predicted to be small and it behaves in the similar way as the mixture fraction, i.e., a rapid decay at $y < 0.2m$ and then slowly to zero as $y > 0.2m$.

The radial profiles of the mixture fraction also show clearly that the curve drops gradually with y and that it spreads and diffuses to the wall of the combustor, which again confirms our comments made earlier. Slightly higher prediction of the mixture fraction at the downstream in Case2 can also be seen from these radial profiles. The sgs mixture fraction variance shows again a similar behaviour of decaying with y but spreading towards the walls and the magnitude is very small. At the locations where the stoichiometric mixture fraction line intersects the mixture fraction curves, and the corresponding values for the mixture fraction variance at those locations can easily be found from (a) and (c).

3.8.3 Mole Fractions of the Combustion Species

The instantaneous and mean values of the mole fractions of the combustion species on the horizontal midplane of the combustor are obtained in Case1 and depicted in Figs. 3.10 and 3.11. The mole fractions of the three reactants, C_3H_8, N_2 and O_2

are plotted respectively in frame (a), (b) and (c) while the mole fractions of all the combustion products CO, CO_2, H_2, H_2O, C_2H_2 and CH_4 are depicted in (d)-(i) respectively. The figures show the distributions of the instantaneous as well as mean values of combustion species on the horizontal midplane of the combustor.

In Fig. 3.12 comparisons of the predicted axial profile of the species mean mole fractions, $< \tilde{Y}_k >$, with those of the experiments are presented. Axial profiles of $< \tilde{Y}_{O_2} >$ and $< \tilde{Y}_{C_2H_2} >$ are also compared with the results obtained by Fairweather *et al* [2]. The axial profiles are taken on the centreline of the combustor, which correspond to the temperature result shown in (a) of Fig. 3.8 and the mixture fraction and its variance results shown in Fig. 3.9(a). In the first three frames, (a)-(c), the mean mole fractions of the three reactants, C_3H_8, N_2 and O_2 are plotted respectively, while the mean mole fractions of all the combustion products, CO, CO_2, H_2, H_2O, C_2H_2 and CH_4 are presented respectively in (d)-(i).

The mean mole fraction of C_3H_8 decays rapidly consistent with that the fast decay of the mixture fraction profile shown in Fig. 3.9(a) and again this corresponds to a fast mixing. Comparing with the experimental data, $< \tilde{Y}_{C_3H_8} >$ is predicted excellently. In (b), the mole fraction of N_2 is predicted very well except in the region $y < 0.3m$ where this value is slightly over-predicted. Reactant $< \tilde{Y}_{O_2} >$ is well predicted against the experiment at the upstream zone but an over-prediction is seen at the downstream region. At the inlet $< \tilde{Y}_{O_2} >$ is zero as expected. Both the experimental and computational results show that $< \tilde{Y}_{O_2} >$ increases from the inlet with the axial distance and they have the same trend up to the mid-location of the combustor. However, the experimental results show hardly variation and nearly constant values of $< \tilde{Y}_{O_2} >$ from the mid-location to the outlet while the simulations show that $< \tilde{Y}_{O_2} >$ increases continuously with downstream distance, a result that is consistent with the simulated mixture fraction decay (see Fig. 3.9) and the flamelet data shown in Fig. 3.3. Axial mean $\tilde{Y}_{O_2}$ mole fraction predicted by Fairweather shows an under-prediction throughout the centerline. This result also confirms that the present model is more capable than the model used by Fairweather *et al* [2].

In Figs. 3.12(d) and (f), the maxima of the combustion products $< \tilde{Y}_{CO} >$ and $< \tilde{Y}_{H_2} >$ are over-predicted compared with the experiment but the trends are well reproduced. The mole fraction of CO_2 plotted in (e) is well-predicted up to

$y = 0.3m$ and shows an under-prediction beyond this region. The mole fraction of H_2O depicted in (g) is over-predicted in the region $0.28m < y < 0.7m$ and under-predicted near the inlet and outlet regions. The products of unburned hydrocarbons shown in (h) and (i), where the maximum of $< \tilde{Y}_{C_2H_2} >$ shows an under-prediction compared with the experiment, however, the flamelet data in Fig. 3.3 clearly shows that the maximum value of $< \tilde{Y}_{C_2H_2} >$ would not exceed the maximum limit of about 0.025 when the mixture fraction variance is close to zero. The peak level of the axial profile of mean $\tilde{Y}_{C_2H_2}$ mole fraction obtained by Fairweather *et al* [2] is also under-predicted but comparatively higher than the prediction by the present model. Fig. 3.12(i) shows $\tilde{Y}_{CH_4}$ is slightly over-predicted up to $y = 0.1m$ but well-predicted in the rest of the domain.

From these axial profiles, it is found that the prediction in the most of the mean mole fractions, $< \tilde{Y}_k >$, except the reactant $< \tilde{Y}_{O_2} >$ and its related mole fractions, such as $< \tilde{Y}_{CO_2} >$ and $< \tilde{Y}_{H_2O} >$, is uninfluenced by the choice of the sub-grid scale model. Comparing with the measurements, it is worth to point out here that the reactant $< \tilde{Y}_{O_2} >$ is predicted better in Case2 which in turn leads to a slightly higher prediction in $< \tilde{Y}_{CO_2} >$ and $< \tilde{Y}_{H_2O} >$ mole fractions by Case2.

The comparisons against experiment for the radial distribution of the mean mole fractions, $< \tilde{Y}_k >$, which are taken at the two cross-sectional positions, $y = 0.1m$ and $y = 0.3m$, are now presented in Figs. 3.13 and 3.14 respectively. The combustion species results again correspond to the temperature results shown in (b) and (d) of Fig. 3.8 and to the mixture fraction results shown in Fig. 3.9(b). In Figs. 3.13 and 3.14, the reactants, $< \tilde{Y}_{C_3H_8} >$, $< \tilde{Y}_{N_2} >$ and $< \tilde{Y}_{O_2} >$ are plotted in (a)-(c); and the combustion products, $< \tilde{Y}_{CO} >$, $< \tilde{Y}_{CO_2} >$, $< \tilde{Y}_{H_2} >$, $< \tilde{Y}_{H_2O} >$, $< \tilde{Y}_{C_2H_2} >$ and $< \tilde{Y}_{CH_4} >$ are presented in (d)-(i), respectively.

The radial plot of $< \tilde{Y}_{C_3H_8} >$ at $y = 0.1m$ shows a very good agreement with the experimental data, while no comparison is possible at $y = 0.3m$ due to the absence of experimental data at that location. Figs. 3.13(b) and 3.14(b) show that $< \tilde{Y}_{N_2} >$ is slightly over-predicted in the vicinity of the centreline but overall the prediction agrees very well with the experiment - as we have already seen in Fig. 3.12(b). The radial profile of $< \tilde{Y}_{O_2} >$ shows that at the cross sectional position, $y = 0.1m$, it is well-predicted around the centreline as well as near the wall of the combustor, but at $y = 0.3m$ this is slightly over-predicted around the centreline and near the wall.

The combustion product, $< \tilde{Y}_{CO} >$, in Figs. 3.13(d) and 3.14(d), shows an over-prediction in the radial direction, while the maxima of $< \tilde{Y}_{CO_2} >$ in (e) are under-predicted. $< \tilde{Y}_{H_2} >$ at $y = 0.1m$ shows an over-prediction, but at $y = 0.3m$ it is under-predicted in the centre region and over-predicted in the flame front region. Another major combustion product, $< \tilde{Y}_{H_2O} >$, which is compared very well with the experiment at $y = 0.3m$. The maxima of $< \tilde{Y}_{C_2H_2} >$ are under-predicted at both cross-sectional positions as we have already noticed in the previous figure, however $< \tilde{Y}_{CH_4} >$ is predicted very well in the radial direction.

Radial profiles of the mole fractions, $< \tilde{Y}_k >$, at location $y = 0.1m$ show that the influence of the choice of the sub-grid scale model is negligible but at position $y = 0.3m$ the predictions of $< \tilde{Y}_{O_2} >$, $< \tilde{Y}_{CO_2} >$ and $< \tilde{Y}_{H_2O} >$ shown respectively in frames (c), (e) and (g) are found slightly better in the center region by Case2.

Despite the slight over and under-prediction in some of the simulated results, the qualitative agreement with the measurements is good and the quantitative agreement for most species is also satisfactory, given that the uncertainties in the current reaction mechanism (Leung *et al* [47]) used to generate the flamelets, which particularly concerns the formation of a number of minor species in the propane flame. The trends in which the species curves grow or decay along the axial and radial directions again compared well with the experiment and the predicted results comply well with the flamelet data. For instance, the predicted values of the major combustion products, $< \tilde{Y}_{CO_2} >$ and $< \tilde{Y}_{H_2O} >$, on the centre line and at the axial location of $y = 0.2m$ are about 0.039 and 0.097 respectively. The corresponding value of the mixture fraction at the same location is predicted about $\tilde{\xi} = 0.11$, and the mixture fraction variance is close to zero there - see Fig. 3.9. The flamelet data for Y_{CO_2} and Y_{H_2O} with $\xi = 0.11$ are about 0.04 and 0.098 respectively, which are very close to the computation data.

It might be argued again, as was done for the temperature, that including the flame radiation and coupling this with the LES model might lead to an improved prediction of the combustion species, as in such case the prediction of the mixture fraction and its sgs variance would also change. The experimental paper of Nishida and Mukohara [1] also reported that they used a small amount of fuel for the pilot flame, which has been ignored in the present simulation as no details were given in their paper. Fairweather *et al* [2] also ignored the pilot flame in their computation.

Although the adiabatic flamelet temperature is adjusted through a simplistic way to determine the heat loss from the flame. But the effects of heat loss on the species concentrations have been ignored. This ignorance should have significant impact on the prediction of combustion products. So, the errors might occur in the predictions are of the same order as the uncertainties associated with the simplified treatment of heat loss from the flame i.e., non-adiabaticity.

3.8.4 Scatter Plots of the Thermochemical Variables

Scatter plots of mixture fraction variance, density and all the thermochemical variables against the mixture fraction on the horizontal midplane and different cross-sectional positions of the combustor are obtained in Case1 and depicted in Figs. 3.15-3.20. These figures are plotted by collecting the results of the mixture fraction and each thermochemical variables at every grid node in the computational domain. In Fig. 3.15 scatter plots of the instantaneous values of (a) mixture fraction variance, $\tilde{\xi}''^2$, (b) temperature, $\tilde{T}(K)$, (c) density, $\tilde{\rho}$, (d) $\tilde{Y}_{C_3H_8}$, (e) $\tilde{Y}_{N_2}$, (f) $\tilde{Y}_{O_2}$, (g) $\tilde{Y}_{CO}$, (h) $\tilde{Y}_{CO_2}$, (i) $\tilde{Y}_{H_2}$, (j) $\tilde{Y}_{H_2O}$, (k) $\tilde{Y}_{C_2H_2}$ and (l) $\tilde{Y}_{CH_4}$ against the instantaneous values of the mixture fraction, $\tilde{\xi}$, on the horizontal midplane of the combustor are presented. The mean values of the corresponding thermochemical variables are plotted in Fig. 3.16. The instantaneous and mean values of these thermochemical variables are also plotted respectively in Figs. 3.17 and 3.18 on the cross-sectional plane at $y = 0.1m$, while at $y = 0.3m$ these results are presented in Figs. 3.19 and 3.20.

In the first frame of all figures shows the variation of the mixture fraction variance against the mixture fraction. From all other frames it can be seen that all the thermochemical variables deviate more from the corresponding flamelet results presented in Fig. 3.3 in the region where the values of the mixture fraction variance are concentrated. The scatter plots of the instantaneous values of the combustion products, $\tilde{Y}_{C_3H_8}$, $\tilde{Y}_{C_2H_2}$ and $\tilde{Y}_{CH_4}$ plotted respectively in the frames (d), (k) and (l) of Fig. 3.19, show some fluctuations for low value of the mixture fraction. These fluctuations, whose magnitude are very low indeed, occur due to the single polynomial fitting on these flamelet data.

3.8.5 Velocity Field and Flow Vortices

The centreline profiles of the mean velocity components, $< \tilde{u} >$, $< \tilde{v} >$ and $< \tilde{w} >$; and pressure, $< \tilde{p} >$, along with their density weighted instantaneous values, are presented in Fig. 3.21(a-d) respectively. No comparison with experiment is made here as no suitable data is available for the velocity field and for the turbulent fluctuating quantities, which will be presented in the next section.

Fig. 3.21(b) shows that the axial velocity component, $< \tilde{v} >$, is maximum near at the inlet and then decays towards the downstream. A similar pattern but lower in magnitude is observed in the radial velocity components, $< \tilde{u} >$ and $< \tilde{w} >$, shown in frames (a) and (c) respectively. The higher level of fluctuations is evident at the downstream of the inlet for the density weighted instantaneous values of the axial velocity as well as radial velocity components, which indicates that the level of turbulence at this zone is higher compared to the rest of domain as it can be seen that the fluctuation slowly disappears towards the downstream. The flow visualisation plots in Fig. 3.23 would also show some forms of the turbulent behaviour in the flow and some quantitative assessments of the turbulent stresses will follow in the next section.

The mean axial velocity, $< \tilde{v} >$, on the centreline varies a little with y as $y > 0.3m$, which can also be seen in Fig. 3.22(g-h), and behaves like a fully developed, self-preserving, flow established from about at the one third horizontal position of the combustion chamber where the gradient of the centreline velocity, $\frac{\partial < \tilde{v} >}{\partial y}$, tends to zero. That is why, for this figure and the rest of figures where the axial results are plotted, the data are plotted up to the maximum axial location of $y = 0.35m$, which again gives us a clear view of the results of the velocity and turbulent characteristics that are dominant mostly at the upstream region, as already seen in Fig. 3.21 for the velocity.

The power law profile for the centreline mean axial velocity of an axisymmetric turbulent fully developed flow can usually be approximated using Tennekes and Lumley [99], $\frac{< \tilde{v} >}{< \tilde{v} >_{y=0}} = 6.4 \left(\frac{y}{D}\right)^{-n}$, where the index n takes a value of unity and D is the internal diameter of the fuel nozzle. This data has been plotted in Fig. 3.21(b) as a solid line with circles in order to get a qualitative feeling of the mean axial velocity we achieved in our simulation. It clearly shows that the trend is the same, though we don't expect that these results would match perfectly with the power law

fittings, this is simply due to the case of combustion where the results are affected by the many factors such as the density field which varies in the simulation and the pressure which is coupled with the combustion temperature.

The instant pressure plot in Fig. 3.21(d) shows a high level of fluctuation at the upstream, which caused a high level of fluctuation in the velocity components seen in Fig. 3.21(a-c). When the fuel mixes with the air and the combustion takes place, the flame becomes unstable with a high density variation due to the high temperature difference between the fuel and air, which has caused a deep pressure drop near the inlet.

The diffusive nature of the flow can again be seen in Fig. 3.22 where the axial velocity component is plotted in the radial direction taking some of the random cross section points. The maximum level of the velocity at the upstream is high, it drops gradually with y, as we have seen in Fig. 3.21(b), but diffuses towards the wall of the combustor.

Comparing the results obtained in Case1 and Case2, it seems both the centerline and radial profiles of velocity components and pressure are uninfluenced by the choice of the sub-grid scale models.

In Fig. 3.23 we have plotted the instantaneous streamlines, computed in Case1, using the radial velocity components $\tilde{u}$ and $\tilde{w}$ at different cross sections of the combustor; (a) $y = 0.1m$, (b) $y = 0.2m$, (c) $y = 0.3m$, (d) $y = 0.4m$, (e) $y = 0.5m$ and (f) $y = 0.6m$, in order to show the turbulent flow field, rotations and flow structure inside the combustor chamber. Looking at the profiles we can conclude immediately how intensive and chaotic the flow is inside the combustor and the instantaneous flow is clearly asymmetric. Near the inlet some vortical eddies initially develop, which are close to the centre of the combustor, see (a), and these again led to create the fluctuations in the velocity field. Further downstream the vortices spread towards the boundary and they are distributed throughout the flow. The quantitative assessment of these turbulent eddies will now be made in Fig. 3.24 where we have shown the instantaneous results of the vorticity, $\tilde{\omega}_y = \frac{1}{2}\left(\frac{\partial \tilde{u}}{\partial z} - \frac{\partial \tilde{w}}{\partial x}\right)$, at the same cross-sectional positions. In Fig. 3.24 a total number of 10 equal contour levels are plotted between the maximum (10^3) and minimum (-10^3) values of $\tilde{\omega}_y$, where the dashed lines indicate the negative contours. In (a), which is taken near at the inlet, the vortex cells produced with a high level of contours indicates the level

of turbulence is high, and initially they are concentrated at the central zone of the combustor as we have already seen these in the flow recirculation in the previous figure. Towards the downstream the vortex strength decreases with the decreasing of turbulence, and the vortex cells also spread towards the boundary as the flow diffuses. It is also clear from all the figures that the strength of the small-scale eddies is very much larger than that of the large-scale motion.

3.8.6 Turbulent Fluctuating and Sub-grid Scale Quantities

In Fig. 3.25(a-c), the centreline profiles for the mean turbulent shear stresses, $< u'v' >$, $< u'w' >$ and $< v'w' >$, are presented respectively. The radial profiles of these stresses are also presented at the two cross-sectional positions, $y = 0.1m$ (left column) and $y = 0.3m$ (right column) in Fig. 3.26(a-c), which correspond to the velocity results shown in (c) and (g) of Fig. 3.22 respectively. The centreline profiles show that the turbulent shear stresses are high at the upstream because of the high turbulence produced in this region, where a high level of fluctuations in the velocity and pressure was already seen. These high levels of turbulent shear stress play an important role determining the mean flow as they contribute to a large amount of momentum transfer. Further downstream the turbulence intensity decreases which in turn decreases the values of the shear stresses. There is a very little variation of the stresses seen with y as $y > 0.2m$ which again confirms the self-preservative nature of the flow in the downstream region. The radial profiles also show that the shear stresses are high in the upstream region (left column of Fig. 3.26) and then they decay with y (right column of Fig. 3.26). Near the combustor wall these values are close to zero as expected. Furthermore, comparing between Case1 and Case2, some variations in the stress results are seen, but they are small.

In Fig. 3.27(a-c), profiles of the root mean square (rms) of the fluctuating components u', v' and w' are plotted along the axial direction respectively, while these results are presented along the radial direction at $y = 0.1m$ (left column) and $y = 0.3m$ (right column) in Fig. 3.28(a-c). All the rms values rise very fast from the inlet, and the locations of their maxima are close to where the turbulent shear stresses were predicted high. Again, this indicates the high level of fluctuations in the flow at the upstream. The maxima then drop gradually to the downstream due

to the low-level fluctuations produced there. In addition, the maximum of v'_{rms} is found higher than those of the other two, because of the high axial velocity component, $\tilde{v}$, at the inlet, which is about 33% of the centreline mean velocity, $< \tilde{v} >$. Although the maxima of u'_{rms} and w'_{rms} are predicted at about the same level probably due to the axisymmetric nature of the mean flow, the three rms values are not equal, consistent with the anisotropic nature of the turbulent flow. The radial plots show that the rms values are maximum in the vicinity of the centreline and decrease to zero towards the wall, hence the production of the turbulence kinetic energy would be high at the centre zone, see Fig. 3.29(b-c).

The centreline and radial profiles of the mean kinetic energy, $< KE >= \frac{1}{2}(< \tilde{u}^2 > + < \tilde{v}^2 > + < \tilde{w}^2 >)$, and the turbulent kinetic energy, $< ke >= \frac{1}{2}(< u'^2 > + < v'^2 > + < w'^2 >)$, are now plotted in Fig. 3.29. The results of $< KE >$ have the similar trends as $< \tilde{v} >$, which is expected as the mean kinetic energy is dominated by the mean axial velocity component. The maximum value of the turbulent kinetic energy is achieved near at the location where the rms of the fluctuating components have their maximum values (see Fig. 3.27 and 3.28), and the turbulence contributes a maximum of about 8% kinetic energy to the total kinetic energy. Again, the two sub-grid models have produced about the same results for the rms and kinetic energy.

The mean mixture fraction fluxes, $< u'\xi' >$, $< v'\xi' >$ and $< w'\xi' >$, and the rms of the mixture fraction fluctuation, ξ'_{rms}, are depicted along the centreline respectively in Fig. 3.30(a-d) and these results are shown along the radial direction at $y = 0.1m$ (left column) and $y = 0.3m$ (right column) in Fig. 3.31(a-d). In Fig. 3.30 the levels of the centreline mixture fraction fluxes are high at the upstream because of the turbulence and the high level of fluctuation achieved in the mixture fraction. In this region, the mixture fraction is predicted to be greater than the stoichiometric level (see Fig. 3.9(a)). In the downstream of the inlet, where the fuel gets its first contact with the air, combustion takes place and the flow becomes highly turbulent, which leads to the high level of the mixture fraction fluxes. These fluxes play a dominant role in the mixing of air and fuel and also contribute to the scalar transports. Moreover, the mixture fraction flux with the axial velocity component, $< v'\xi' >$, has the largest value compared to the other two, this is expected as the axial velocity is higher than that of the radial components. The magnitudes of all the fluxes

decrease towards the downstream region where the mixture fraction fluctuation as well as the turbulence are seen to be low. The radial profiles (Fig. 3.31(a-c)) show the mixture fraction fluxes are higher around the centreline and disappear near the combustor wall like the turbulent shear stresses. The maximum of ξ'_{rms} is found near at the inlet where the mixture fraction value is high and this maximum is about one-third magnitude of the mean mixture fraction. Again both the sub-grid models agree quite well in these predictions.

In the Figs. 3.32 and 3.33, the mean values of the sub-grid scale shear stresses, $< \tau_{uv} >$, $< \tau_{uw} >$ and $< \tau_{vw} >$; and in the Figs. 3.34 and 3.35, the sub-grid scale mixture fraction fluxes, $< \tau_{u\xi} >$, $< \tau_{v\xi} >$ and $< \tau_{w\xi} >$ are plotted. Like previously, (a-c) in Figs. 3.32 and 3.34, shows the results on the centreline, while (a-c) in Figs. 3.33 and 3.35 are the radial results at $y = 0.1m$ (left column) and $y = 0.3m$ (right column). In the upstream region the turbulent intensity was found high, hence the sub-grid scale contributions to the shear stresses and the mixture fraction fluxes are predicted to be maximum. These contributions are negligible and almost vanish beyond the region $y = 0.1m$ of the combustor. On the centreline the sub-grid scale shear stresses, $< \tau_{uv} >$ and $< \tau_{vw} >$, have similar magnitudes that differ in the radial direction. The magnitude of sub-grid scale mixture fraction fluxes, $< \tau_{u\xi} >$ and $< \tau_{w\xi} >$, on the centreline are also very similar as was the case for the centreline sub-grid scale shear stresses, but their ratio varies in the radial direction. As is to be expected, the levels of both the sub-grid scale shear stresses and the sub-grid scale mixture fraction fluxes are very much lower than those of the resolved scale stresses and fluxes.

Comparing the results of all the resolved scale turbulent quantities, presented in Figs. 3.25-3.31, between Case1 and Case2, it has been found that they are almost unaffected by the choice of the sub-grid scale models. However, this is not the same for their sub-grid scale contributions presented in Figs. 3.32-3.35, showing that Case2 produces higher values in the upstream where the dynamic value of C_s (see Fig. 3.5) is found higher than 0.1 used in Case1. Towards the downstream, say at $y = 0.1m$ (left columns of Figs. 3.33 and 3.35), it is observed that the sub-grid scale quantities are predicted higher in Case1 which is due to the higher value of C_s in Case1 at this region. Towards the further downstream (right columns of Figs. 3.33 and 3.35), these quantities completely vanish in Case2 as C_s approaches

to zero, while in Case1 these quantities are predicted very small even negligible.

3.9 Conclusion

Large Eddy Simulation technique has been applied to analyse the turbulent flow, species concentrations and temperature arising in the turbulent non-premixed combustion of propane/air in a cylindrical combustor. The conserved scalar approach with the laminar flamelet model is used to the modelling of the combustion process. The LES results are obtained by employing the Smagorinsky model with a constant C_s of 0.1 as well as the dynamically calibrated C_s.

The predicted mean temperature and species concentrations in both the axial and radial directions have been compared with the experimental data obtained by Nishida and Mukohara [1] in the turbulent propane and pre-heated air combustion. Good agreement is achieved both quantitatively and qualitatively, although there is some disagreement with the experimental results at some locations. The possible reasons of these have been discussed in the results and discussion section which involves some of the uncertainties in the reaction mechanism used to generate flamelets for this study (Leung *et al* [47]). In the experimental study [1], a small part of the fuel was injected through the annular surroundings of the fuel nozzel to form a pilot flame. This was neglected in our computations as no detailed information was available on the pilot flame nozzle and the fuel flow rate through it. It is possible that including the pilot flame in the simulations might have resulted in some of the species and temperature profiles being in closer agreement with the experimental data. Moreover, the present simulation excluded a detailed treatment of the flame radiation loss/gain. The inclusion of radiative heat losses is likely to reduce the flame temperatures and the chemical heat release, which in turn will cause the flame to shrink (Kaplan *et al* [63]). A shrinking of the flame is likely to result in a change to the overall temperature distribution which would then change the species concentrations. In order to achieve this, the model needs to be further developed coupling the flame radiation with the current version of the LES code. In Chapter 6, we have applied the Discrete Ordinates Method (DOM), which is coupled with the LES, for investigating the radiative heat transfer from the flame.

The adiabatic flamelet temperature has been adjusted through a simplistic way

to determine the heat loss from the flame but ignored the effects of heat loss on the species concentrations. Because of this ignorance, the errors might occur in our predictions which may be the same order as the uncertainties associated with the simplified treatment of non-adiabaticity.

Most of the results are almost uninfluenced by the choice of the sub-grid scale models, whether it is a Smagorinsky model with constant C_s of 0.1 or a dynamic model. However, the mole fraction, $< \tilde{Y}_{O_2} >$, is predicted better in a dynamic model which in turn leads to a slightly better prediction in $< \tilde{Y}_{CO_2} >$ and $< \tilde{Y}_{H_2O} >$ by this model. It is also observed that the sub-grid scale quantities are predicted higher by the dynamic model in the upstream region where the value of dynamic C_s is found higher than the constant C_s of 0.1.

In the combustor, combustion occurs under fuel-rich conditions where the overall equivalence ratio was 1.6 which produces various forms of hydrocarbons in the combustion products. One of them is acetylene, C_2H_2, which contributes to the formation and growth of soots (solid carbon particles, solid emissions) in the combustion process. In order to predict soot formation and growth in the same flame it will be necessary, at a minimum, to add two conservation equations, one for the soot mass fraction and another for the soot particle number density to the formulation. Details on this are presented in Chapter 4.

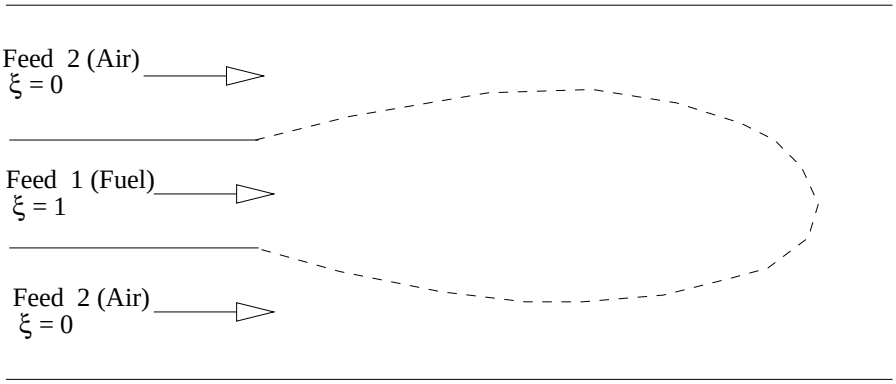

Figure 3.1: A schematic of the two-feed mixing problem.

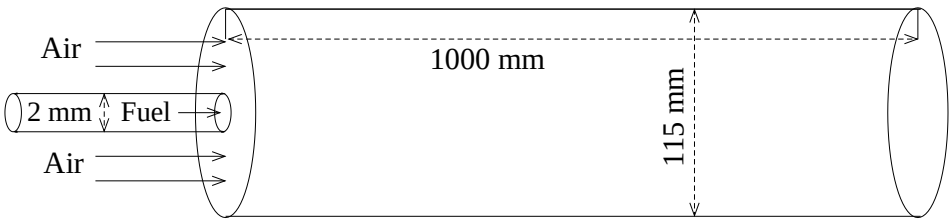

Figure 3.2: A schematic of the cylindrical combustor with computational domain.

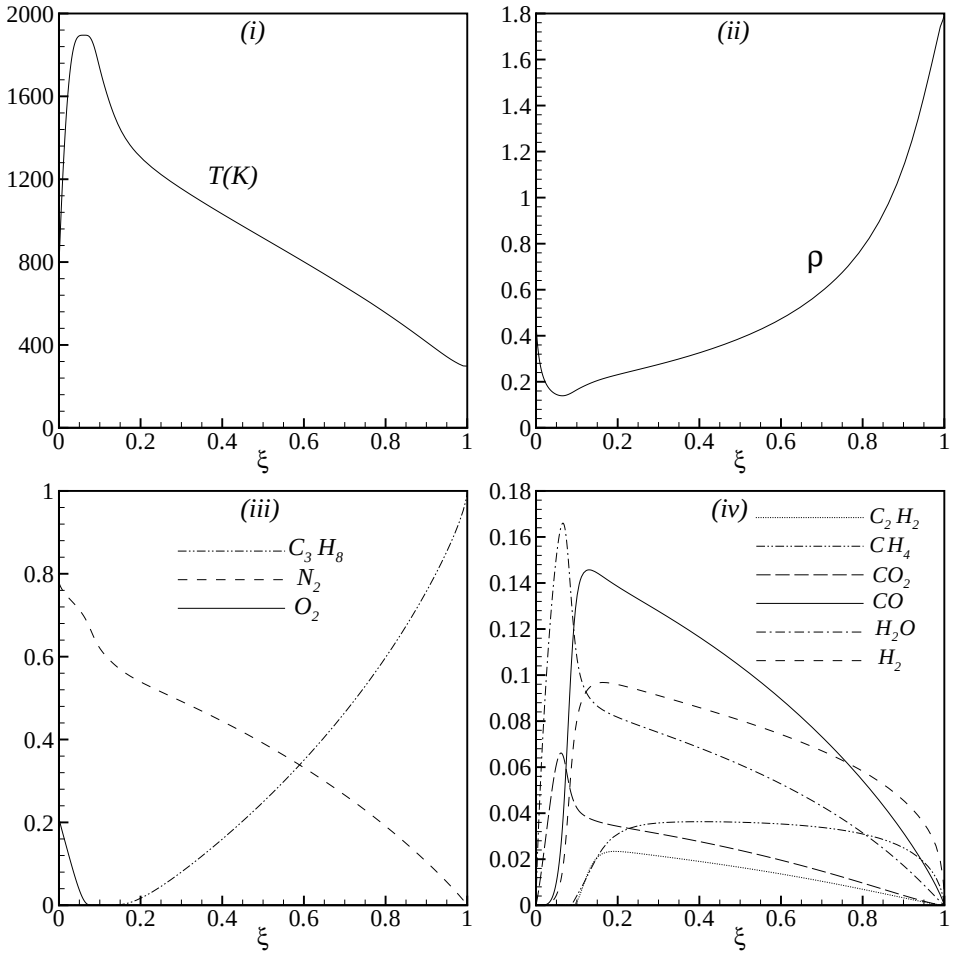

Figure 3.3: Laminar flamelet calculation with the strain rate of $15s^{-1}$ showing the dependence of the (i) temperature, (ii) density and (iii)-(iv) species mole fractions on the mixture fraction, ξ.

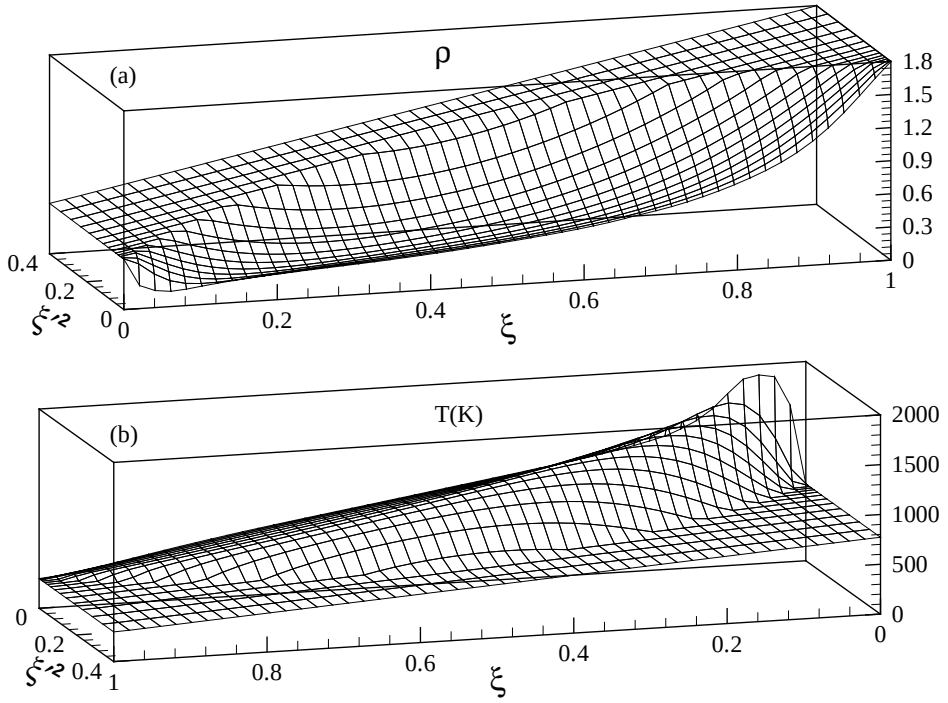

Figure 3.4: Look-Up tables for the laminar flamelets.

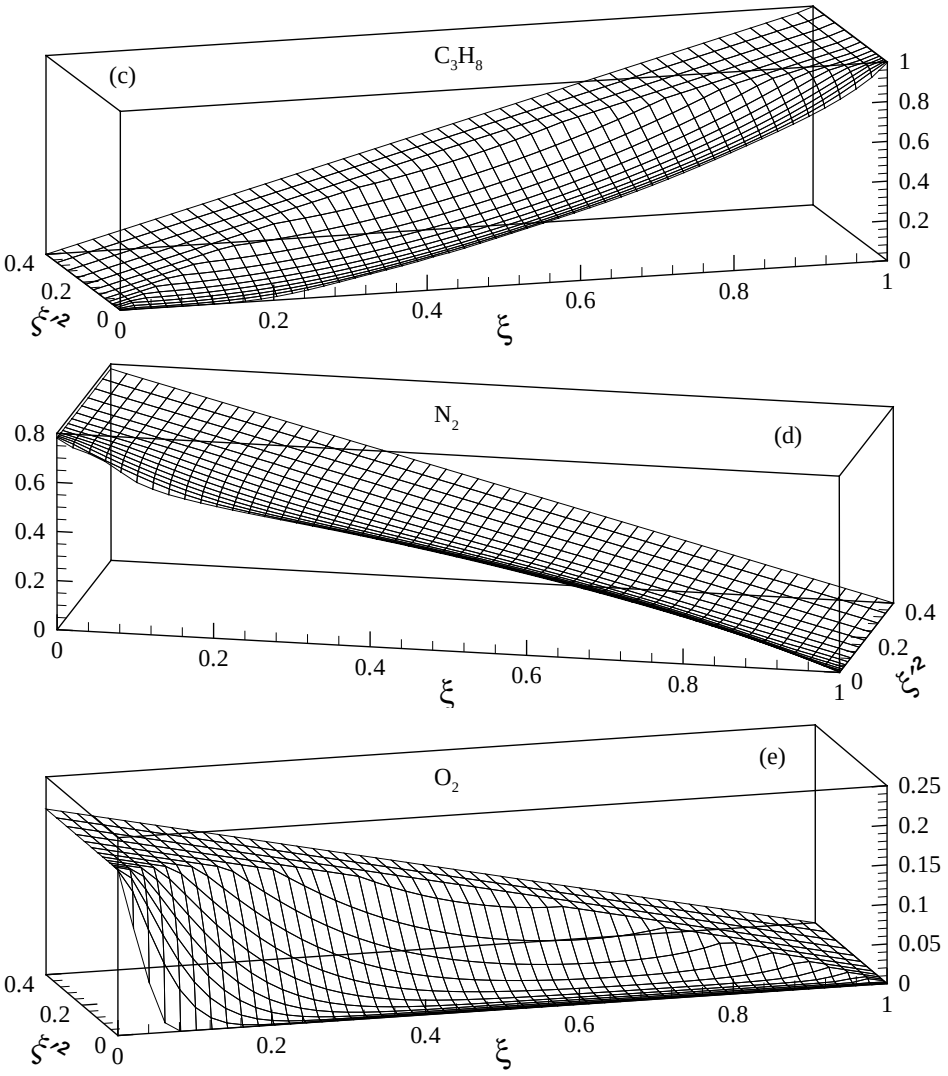

Figure 3.4: (continued)

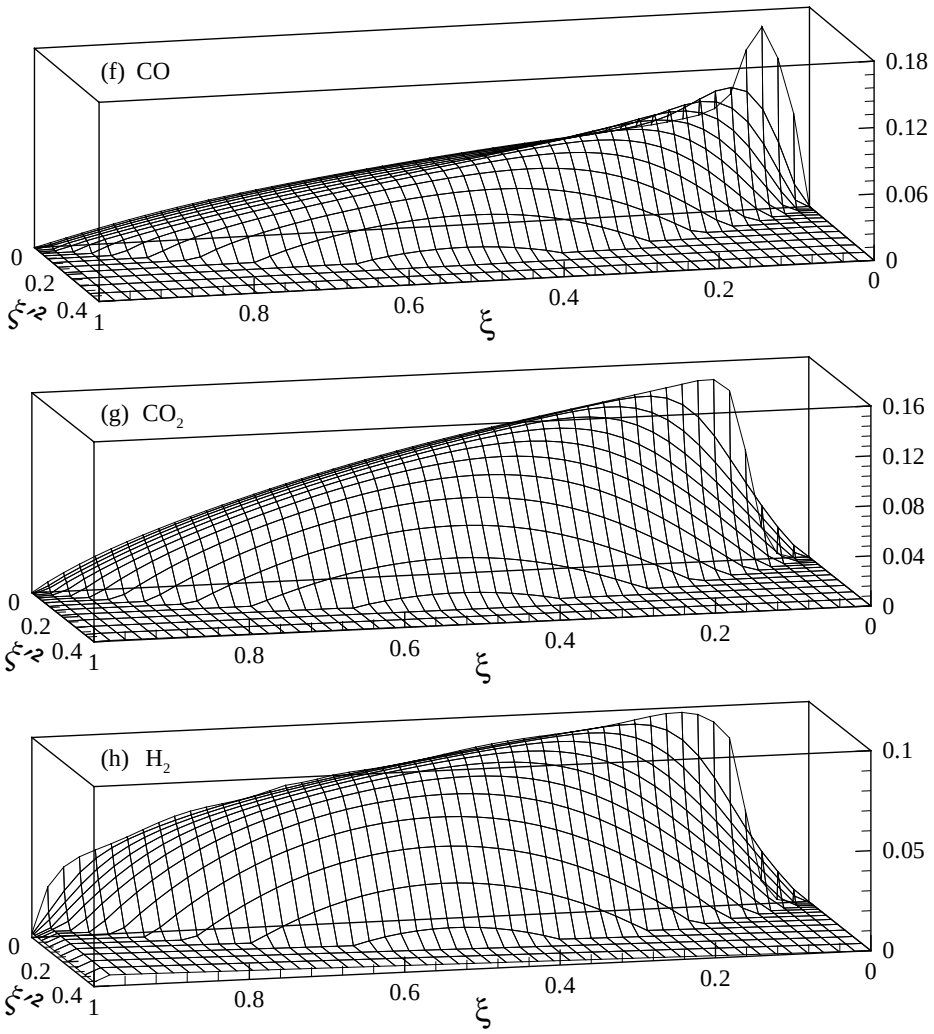

Figure 3.4: (continued)

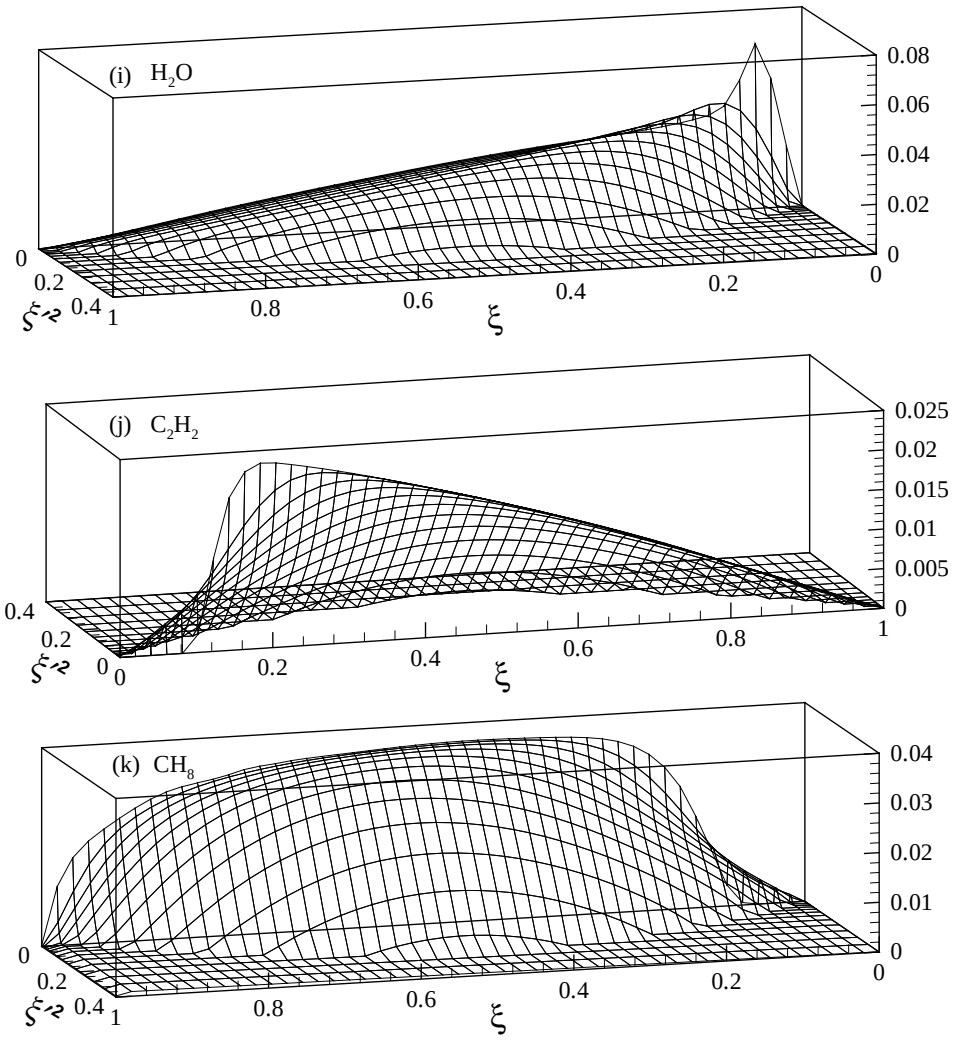

Figure 3.4: (continued)

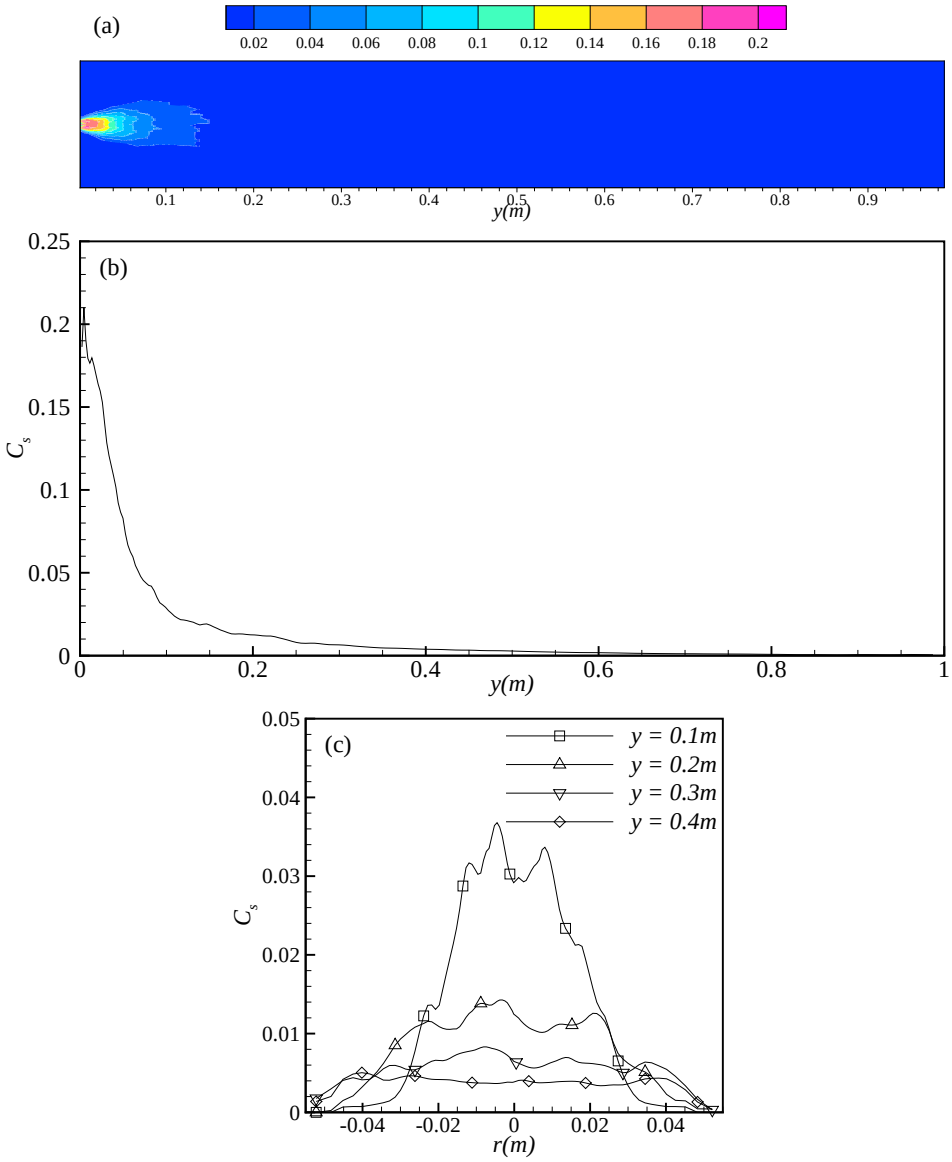

Figure 3.5: Variation of dynamic C_s: (a) on the horizontal midplane, (b) along the axial direction on the centerline and (c) along the radial direction at the different cross-section positions, $y = 0.1m$, $y = 0.2m$, $y = 0.3m$ and $y = 0.4m$.

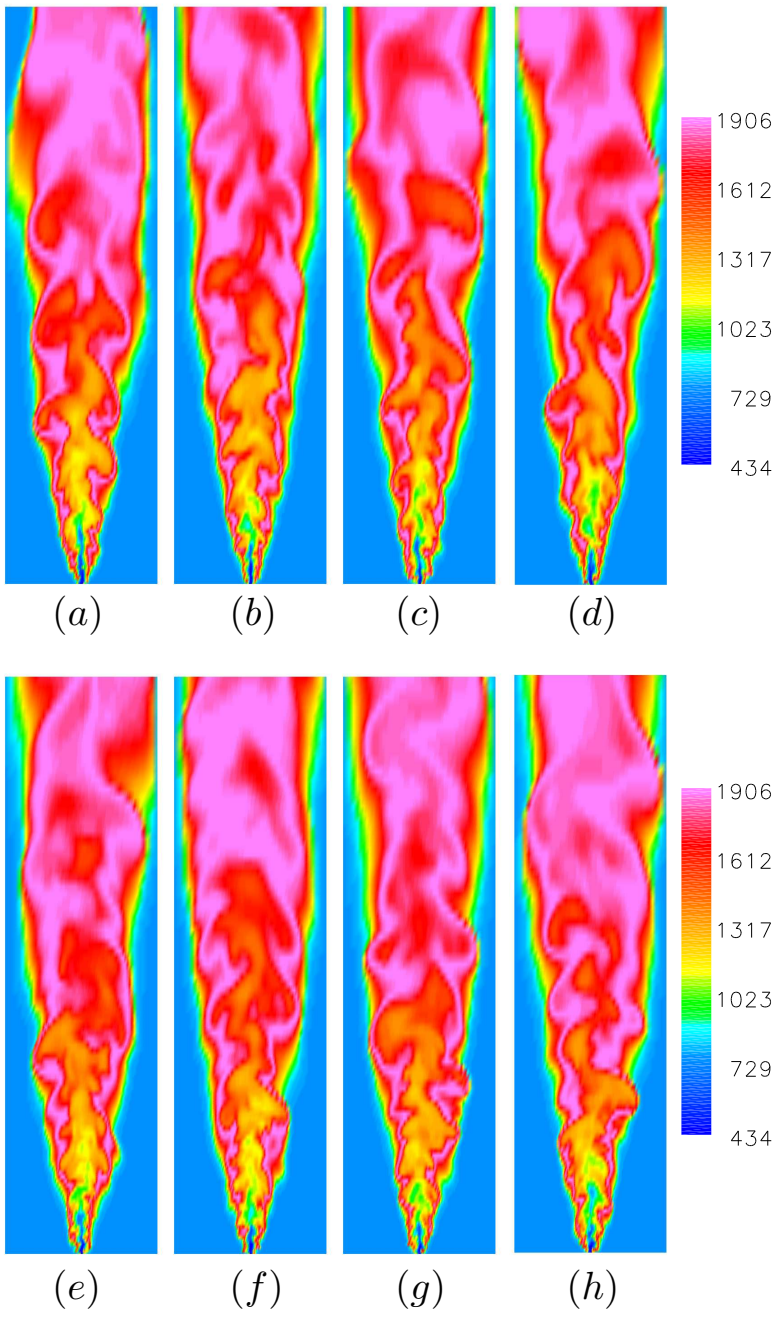

Figure 3.6: Instantaneous temperature, $\tilde{T}(K)$, plot for Case1 on the horizontal midplane of the combustor at different simulation times: (a) $t = 0.1535$ sec, (b) $t = 0.2061$ sec, (c) $t = 0.2737$ sec, (d) $t = 0.3360$ sec, (e) $t = 0.4012$ sec, (f) $t = 0.4613$ sec, (g) $t = 0.5213$ sec, and (h) $t = 0.5714$ sec. Note that the results are zoomed in at the upstream to see the flame structure clearly.

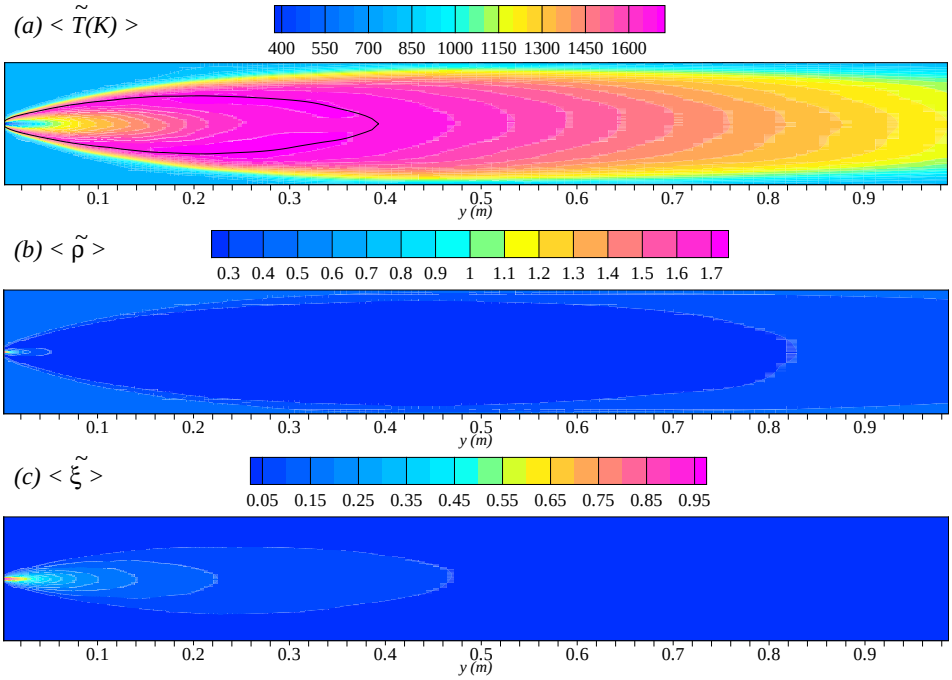

Figure 3.7: Mean (a) temperature, $< \tilde{T}(K) >$, (b) density, $< \tilde{\rho} >$, and (c) mixture fraction, $< \tilde{\xi} >$, plots on the horizontal midplane of the combustor for Case1; the solid line in frame (a) represents the locus of stoichiometric mixture fraction.

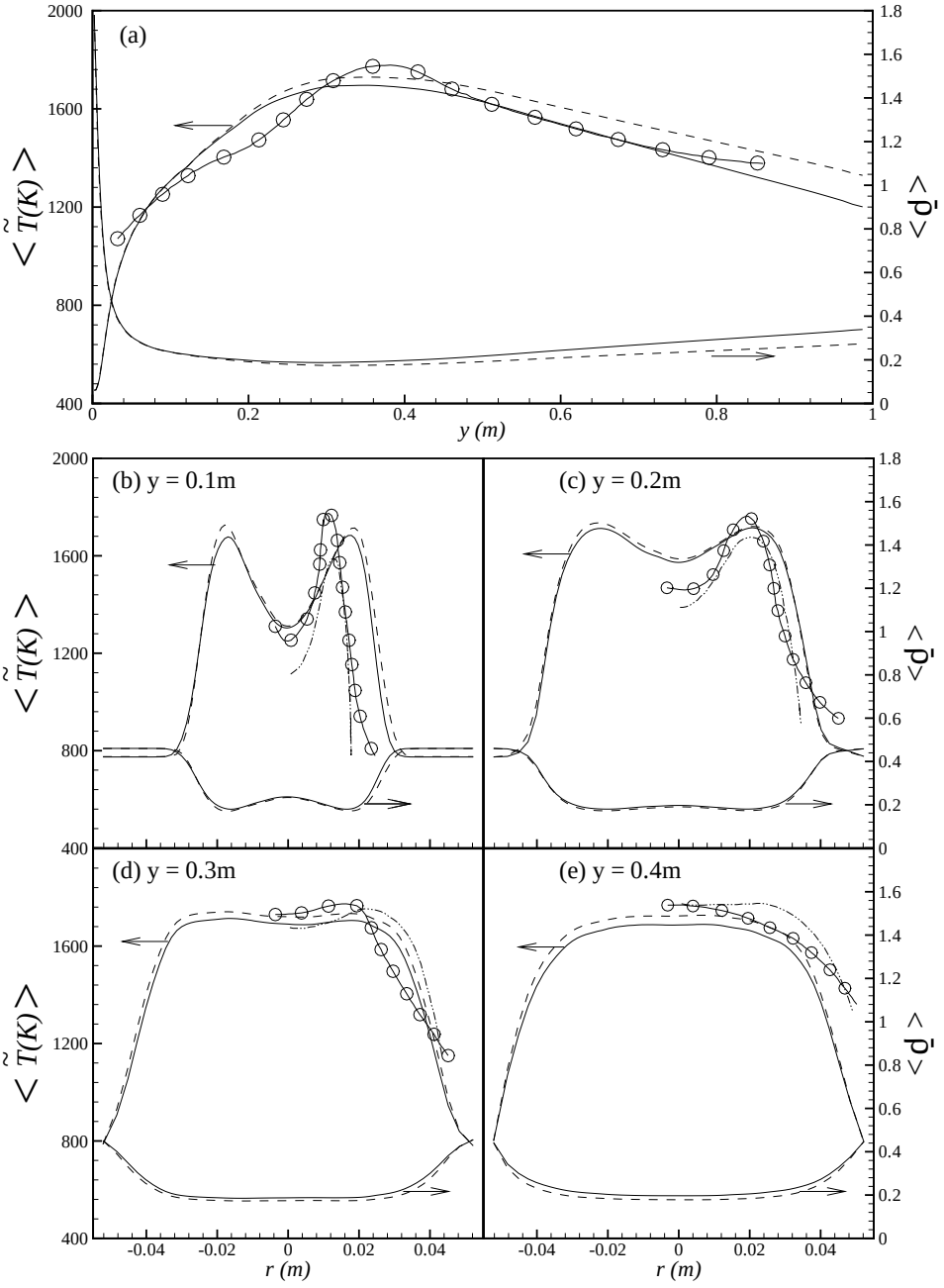

Figure 3.8: Comparisons of the mean temperature, $< \tilde{T}(K) >$, with those of the experimental data along the (a) axial direction, and the radial direction at different cross-sectional positions: (b) $y = 0.1m$, (c) $y = 0.2m$, (d) $y = 0.3m$ and (e) $y = 0.4m$; Solid line, Case1; Dashed line, Case2; Solid line with circle, experimental; Dash dot dot line, Fairweather *et al* [2].

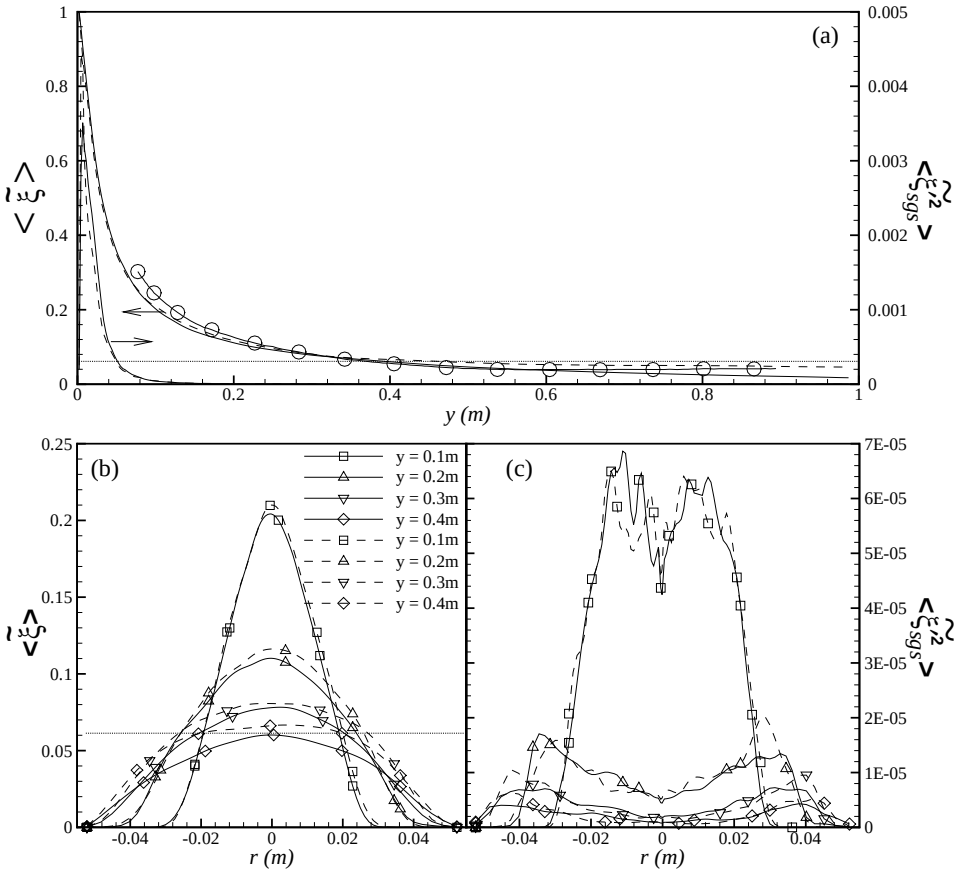

Figure 3.9: Profiles of the mixture fraction and its variance along (a) the axial direction, and (b) the radial direction at various cross sections. Solid line, Case1; Dashed line, Case2; Solid line with circle, experimental; Horizontal dotted line in frame (a) and (b) indicates the position of the stoichiometric mixture fraction.

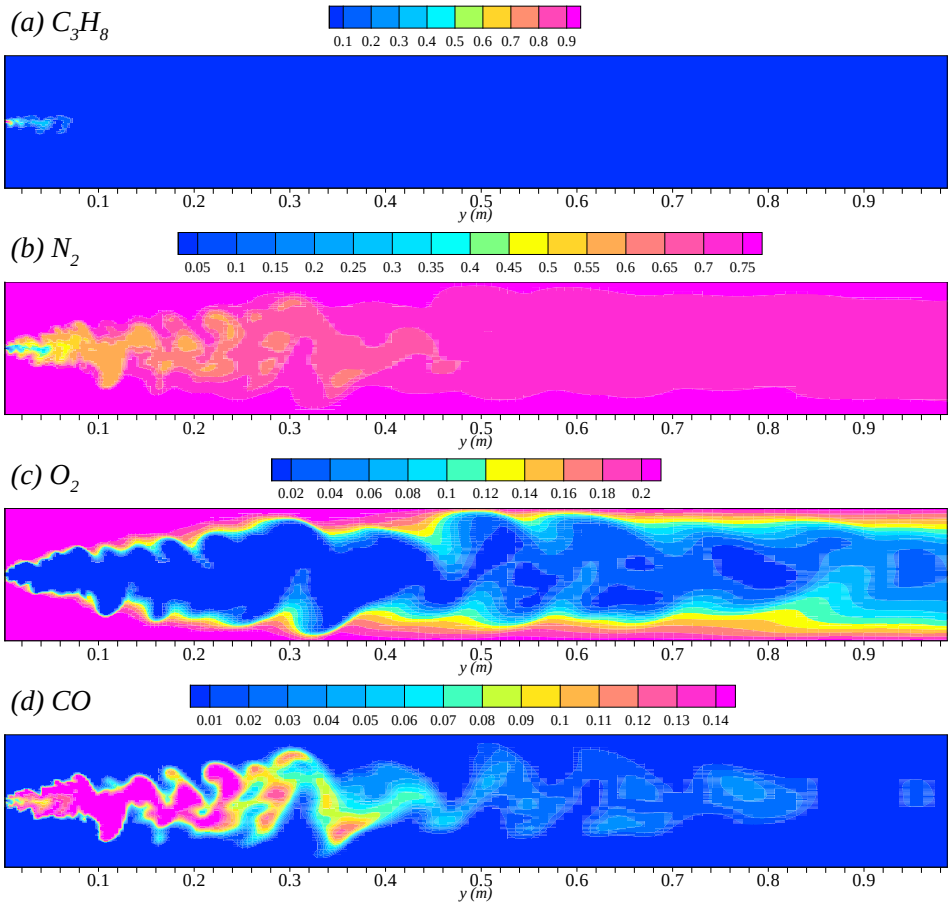

Figure 3.10: Instantaneous mole fractions: (a) $\tilde{Y}_{C_3H_8}$, (b)$\tilde{Y}_{N_2}$, (c) $\tilde{Y}_{O_2}$, (d) $\tilde{Y}_{CO}$, (e) $\tilde{Y}_{CO_2}$, (f) $\tilde{Y}_{H_2}$, (g) $\tilde{Y}_{H_2O}$, (h) $\tilde{Y}_{C_2H_2}$ and (i) $\tilde{Y}_{CH_4}$ on the horizontal midplane of the combustor for Case1.

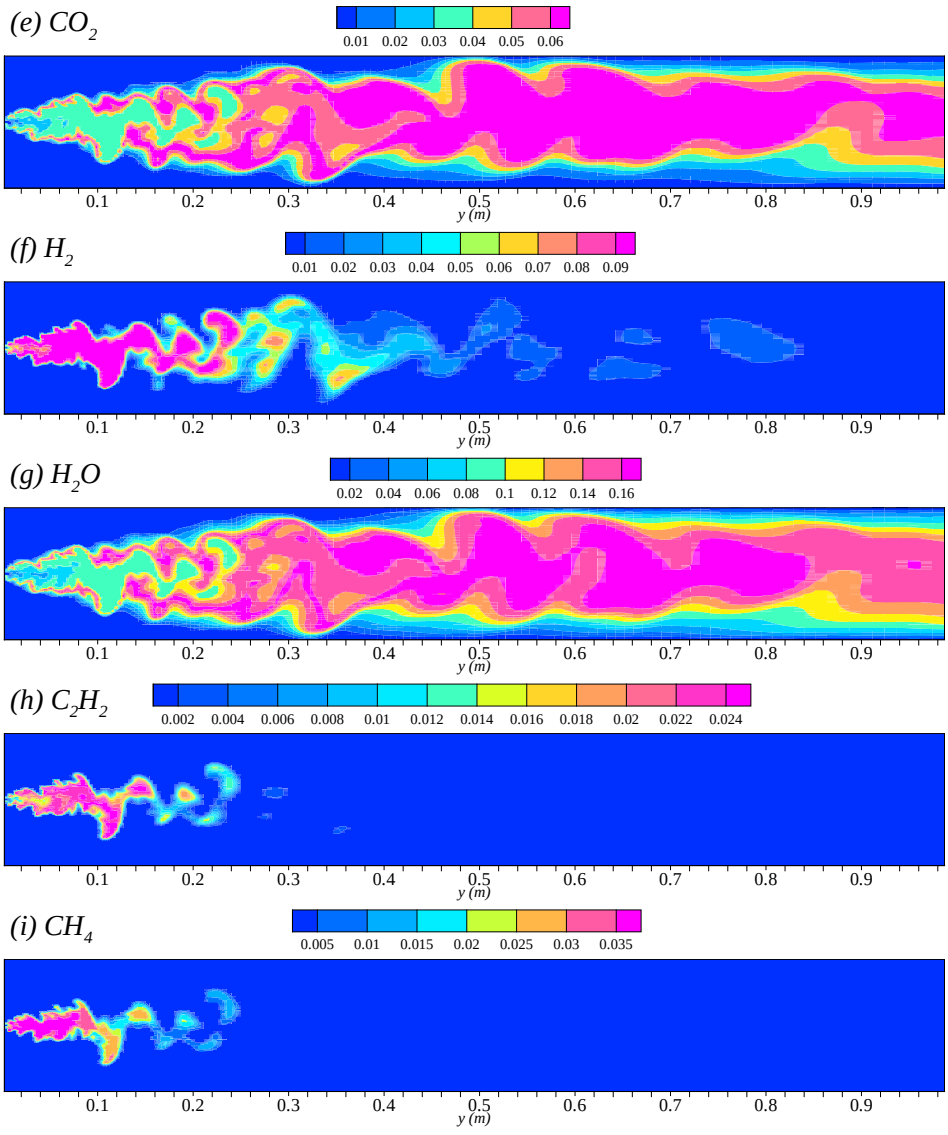

Figure 3.10: (continued)

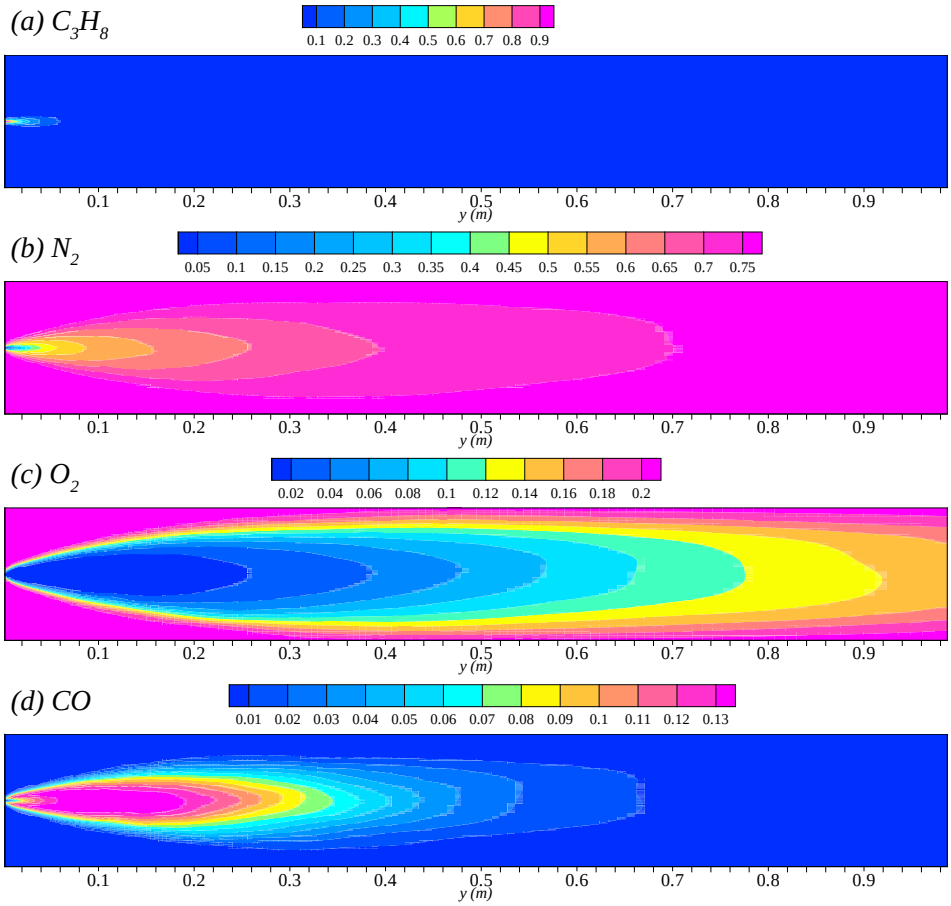

Figure 3.11: Mean mole fractions: (a) $< \tilde{Y}_{C_3H_8} >$, (b)$< \tilde{Y}_{N_2} >$, (c) $< \tilde{Y}_{O_2} >$, (d) $< \tilde{Y}_{CO} >$, (e) $< \tilde{Y}_{CO_2} >$, (f) $< \tilde{Y}_{H_2} >$, (g) $< \tilde{Y}_{H_2O} >$, (h) $< \tilde{Y}_{C_2H_2} >$ and (i) $< \tilde{Y}_{CH_4} >$ on the horizontal midplane of the combustor for Case1.

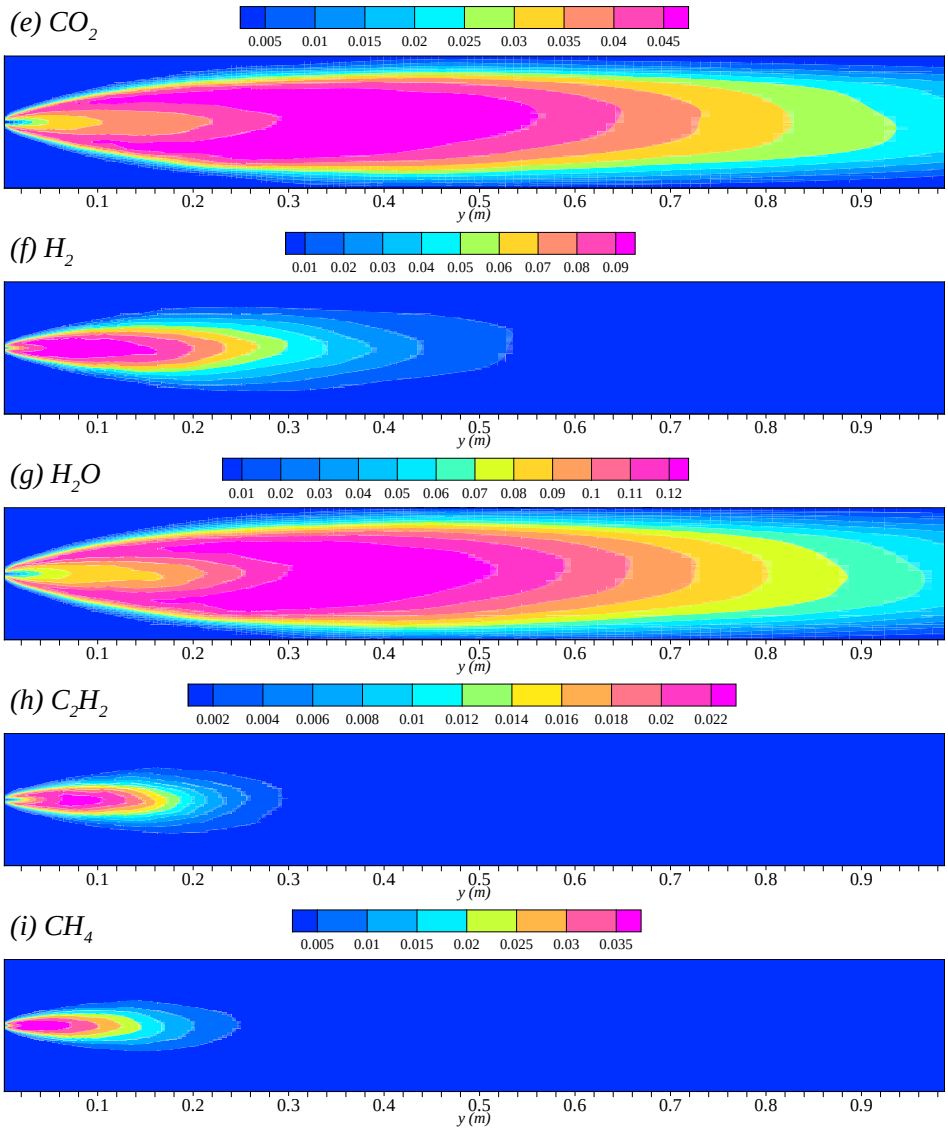

Figure 3.11: (continued)

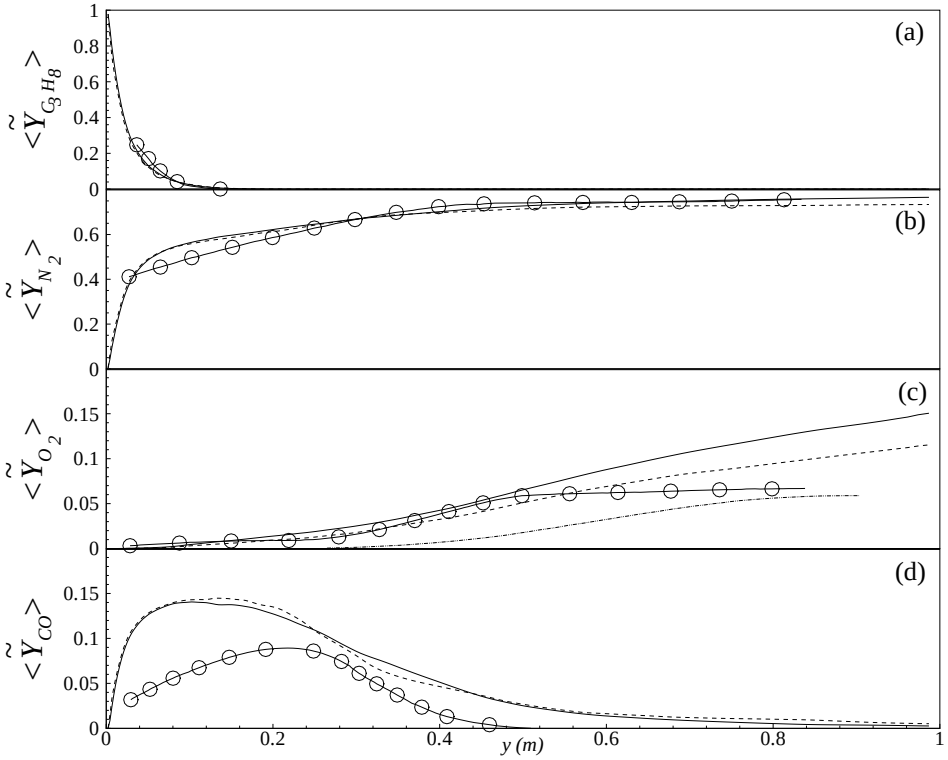

Figure 3.12: Mean mole fractions: (a) $< \tilde{Y}_{C_3H_8} >$, (b)$< \tilde{Y}_{N_2} >$, (c) $< \tilde{Y}_{O_2} >$, (d) $< \tilde{Y}_{CO} >$, (e) $< \tilde{Y}_{CO_2} >$, (f) $< \tilde{Y}_{H_2} >$, (g) $< \tilde{Y}_{H_2O} >$, (h) $< \tilde{Y}_{C_2H_2} >$ and (i) $< \tilde{Y}_{CH_4} >$ along the axial direction; Solid line, Case1; Dashed line, Case2; Solid line with circle, experiment; Dash dot dot line, Fairweather *et al* [2].

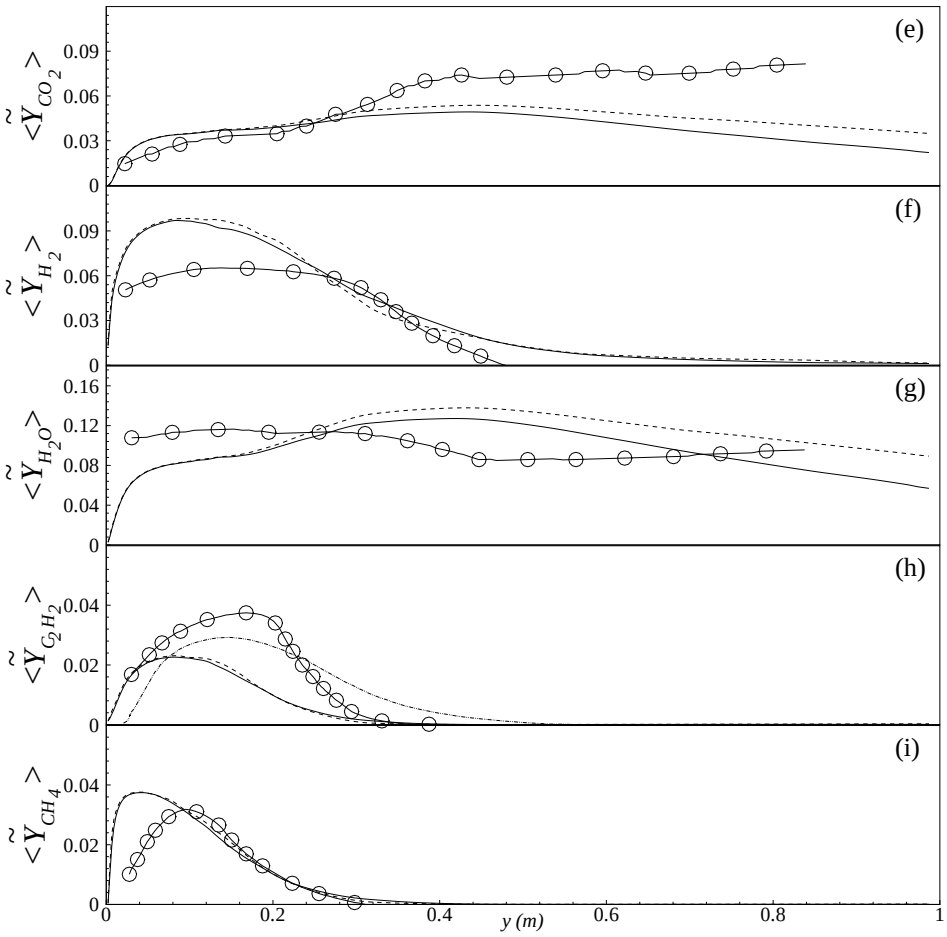

Figure 3.12: (continued)

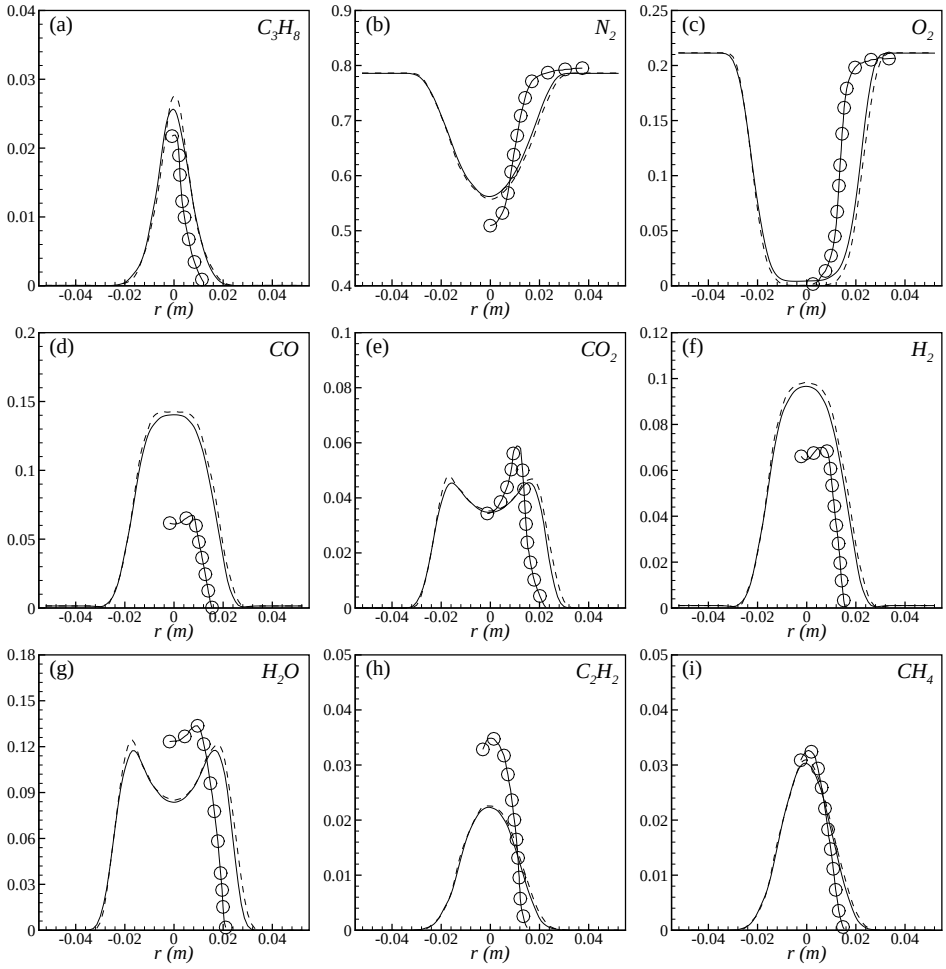

Figure 3.13: Mean mole fractions: (a) $< \tilde{Y}_{C_3H_8} >$, (b)$< \tilde{Y}_{N_2} >$, (c) $< \tilde{Y}_{O_2} >$, (d) $< \tilde{Y}_{CO} >$, (e) $< \tilde{Y}_{CO_2} >$, (f) $< \tilde{Y}_{H_2} >$, (g) $< \tilde{Y}_{H_2O} >$, (h) $< \tilde{Y}_{C_2H_2} >$ and (i) $< \tilde{Y}_{CH_4} >$ along the radial direction at $y = 0.1m$; Solid line, Case1; Dashed line, Case2; Solid line with circle, experiment.

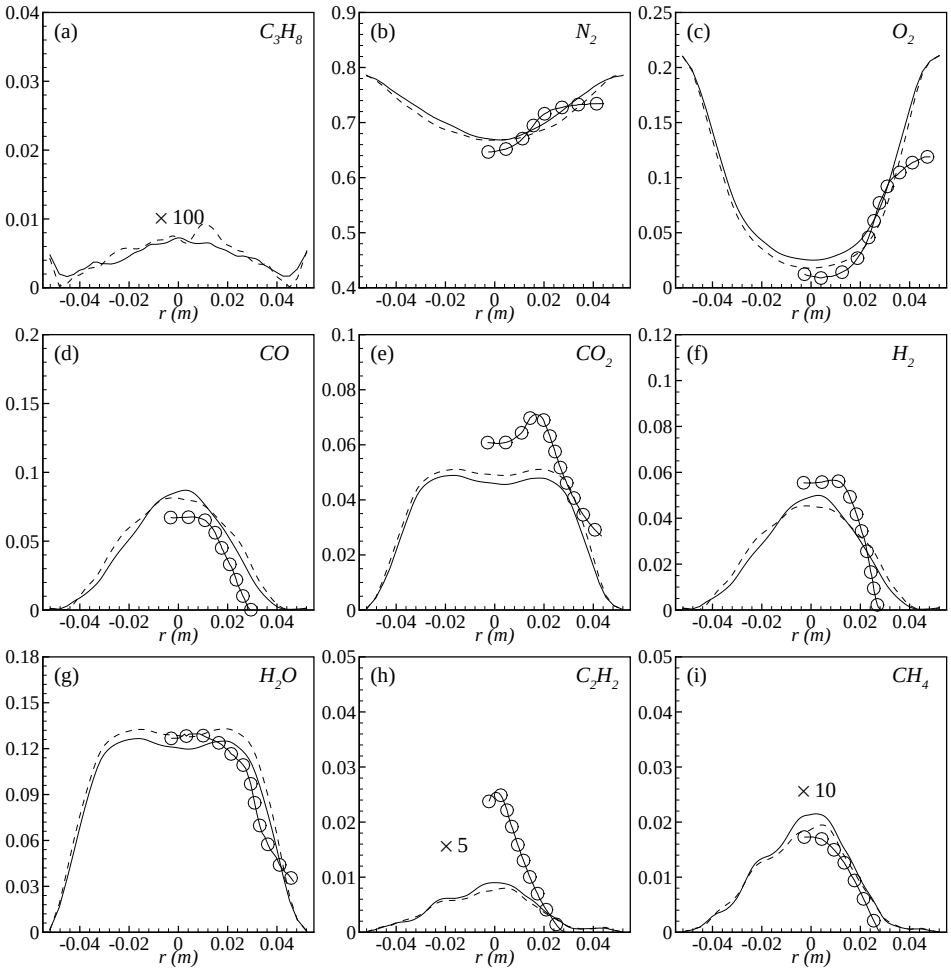

Figure 3.14: Mean mole fractions: (a) $< \tilde{Y}_{C_3H_8} >$, (b)$< \tilde{Y}_{N_2} >$, (c) $< \tilde{Y}_{O_2} >$, (d) $< \tilde{Y}_{CO} >$, (e) $< \tilde{Y}_{CO_2} >$, (f) $< \tilde{Y}_{H_2} >$, (g) $< \tilde{Y}_{H_2O} >$, (h) $< \tilde{Y}_{C_2H_2} >$ and (i) $< \tilde{Y}_{CH_4} >$ along the radial direction at $y = 0.3m$; Solid line, Case1; Dashed line, Case2; Solid line with circle, experiment.

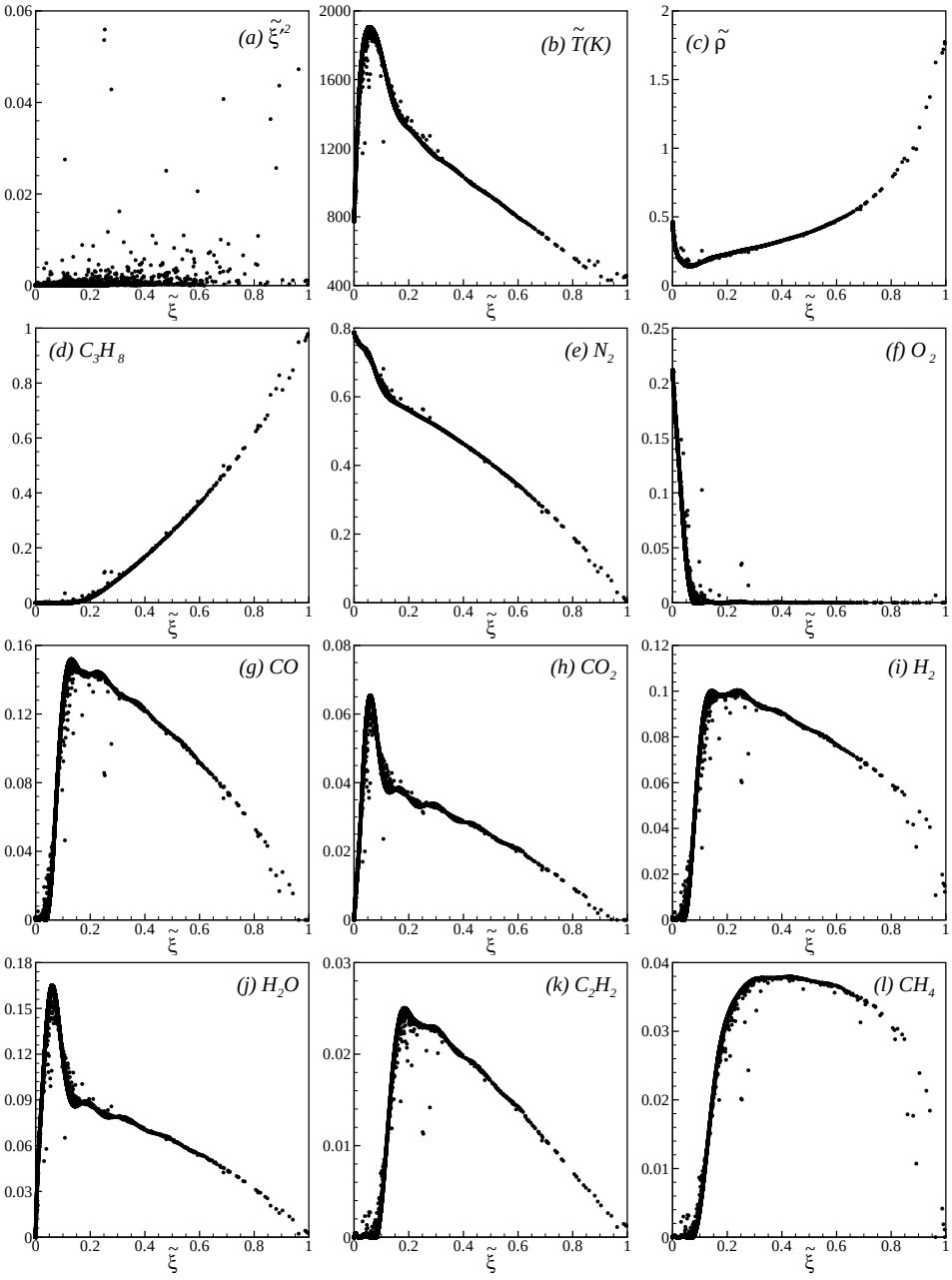

Figure 3.15: Scatter plots of the instantaneous values of (a) $\tilde{\xi}''^2$, (b) $\tilde{T}(K)$, (c) $\tilde{\rho}$, (d) $\tilde{Y}_{C_3H_8}$, (e)$\tilde{Y}_{N_2}$, (f) $\tilde{Y}_{O_2}$, (g) $\tilde{Y}_{CO}$, (h) $\tilde{Y}_{CO_2}$, (i) $\tilde{Y}_{H_2}$, (j) $\tilde{Y}_{H_2O}$, (k) $\tilde{Y}_{C_2H_2}$ and (l) $\tilde{Y}_{CH_4}$ on the horizontal midplane of the combustor for Case1.

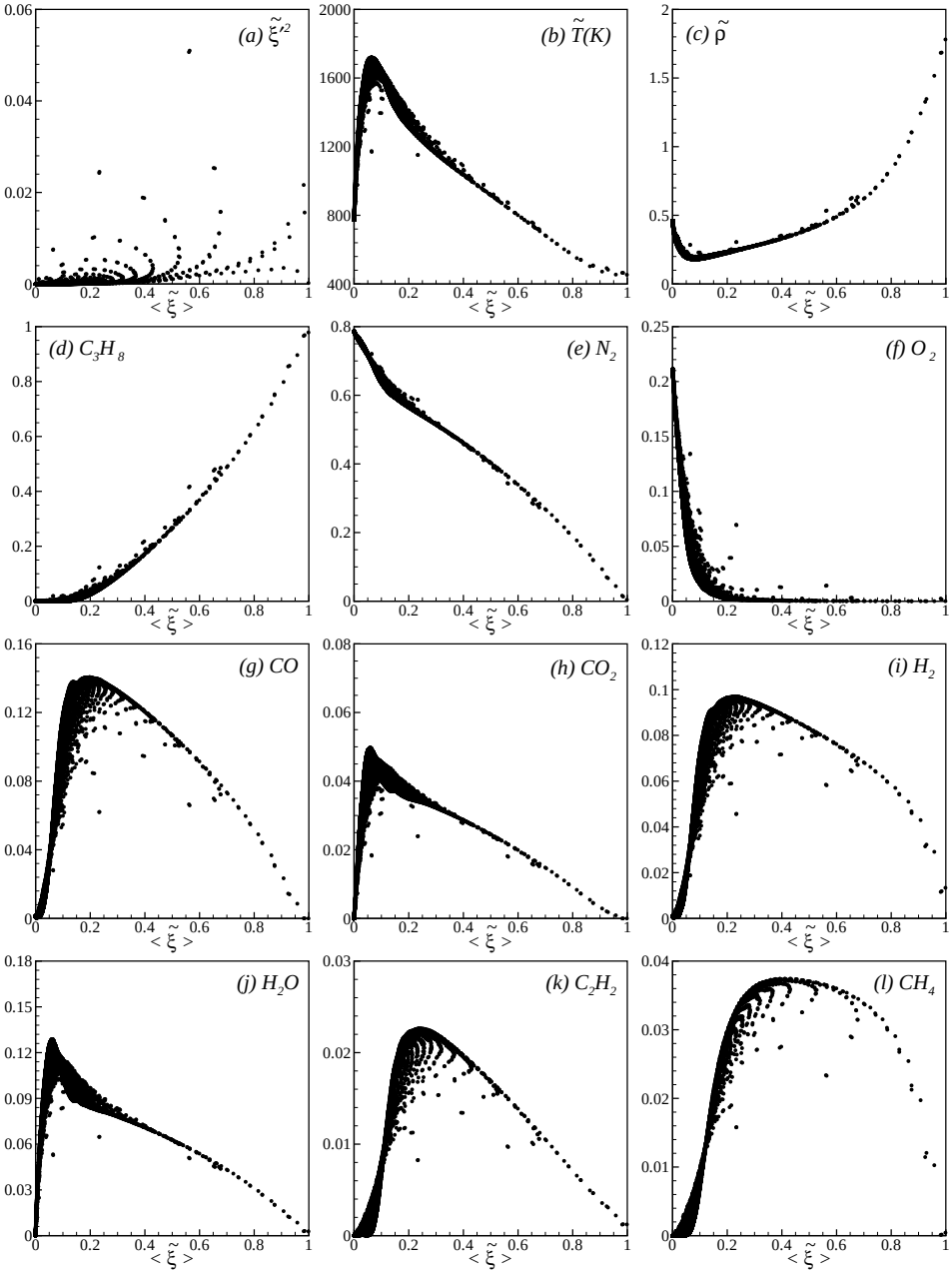

Figure 3.16: Scatter plots of the mean values of (a) $< \tilde{\xi}''^2 >$, (b) $< \tilde{T}(K) >$, (c) $< \tilde{\rho} >$, (d) $< \tilde{Y}_{C_3H_8} >$, (e)$< \tilde{Y}_{N_2} >$, (f) $< \tilde{Y}_{O_2} >$, (g) $< \tilde{Y}_{CO} >$, (h) $< \tilde{Y}_{CO_2} >$, (i) $< \tilde{Y}_{H_2} >$, (j) $< \tilde{Y}_{H_2O} >$, (k) $< \tilde{Y}_{C_2H_2} >$ and (l) $< \tilde{Y}_{CH_4} >$ on the horizontal midplane of the combustor for Case1.

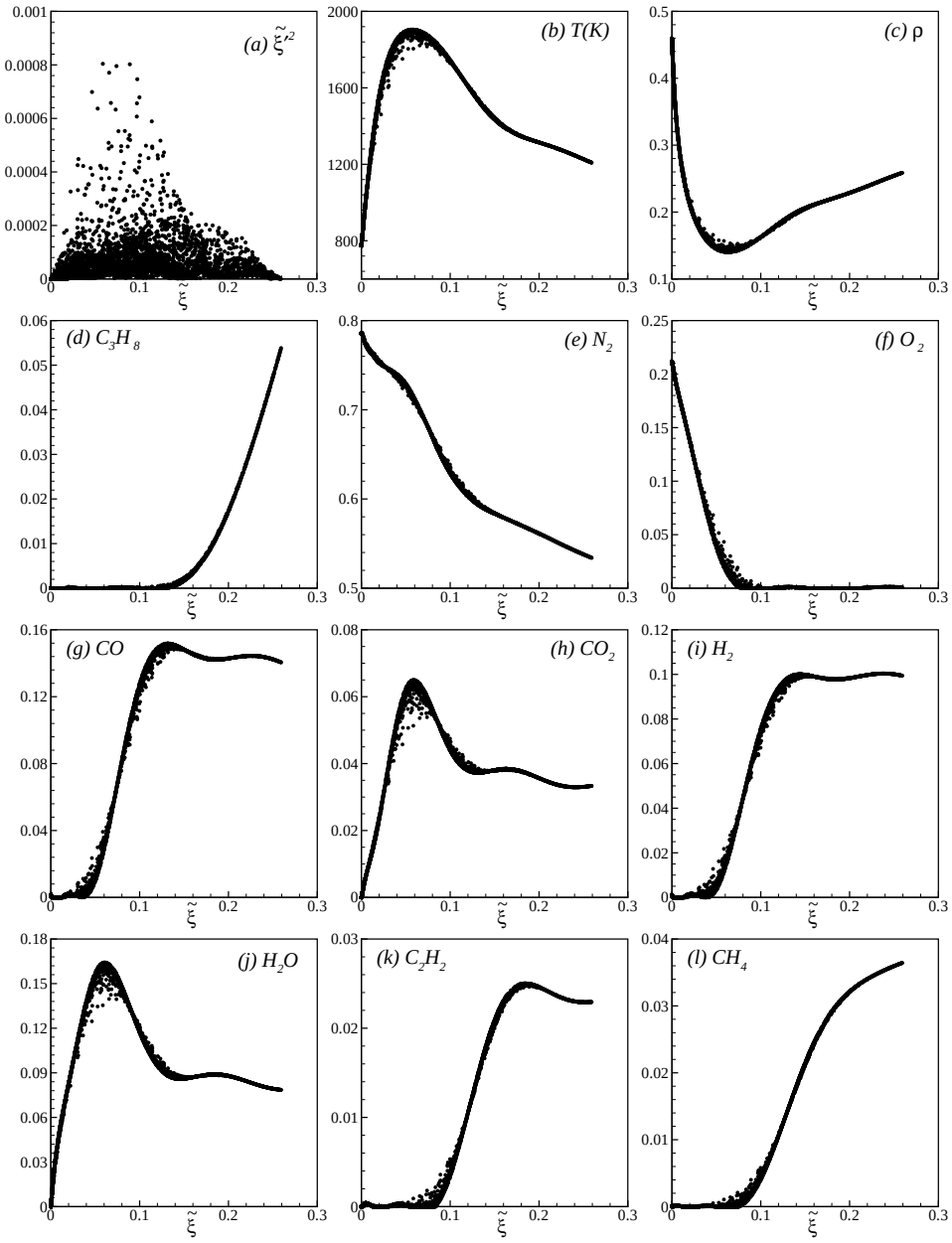

Figure 3.17: Scatter plots of the instantaneous values of (a) $\tilde{\xi}''^2$, (b) $\tilde{T}(K)$, (c) $\tilde{\rho}$, (d) $\tilde{Y}_{C_3H_8}$, (e)$\tilde{Y}_{N_2}$, (f) $\tilde{Y}_{O_2}$, (g) $\tilde{Y}_{CO}$, (h) $\tilde{Y}_{CO_2}$, (i) $\tilde{Y}_{H_2}$, (j) $\tilde{Y}_{H_2O}$, (k) $\tilde{Y}_{C_2H_2}$ and (l) $\tilde{Y}_{CH_4}$ on the cross-sectional plane at $y = 0.1m$ for Case1.

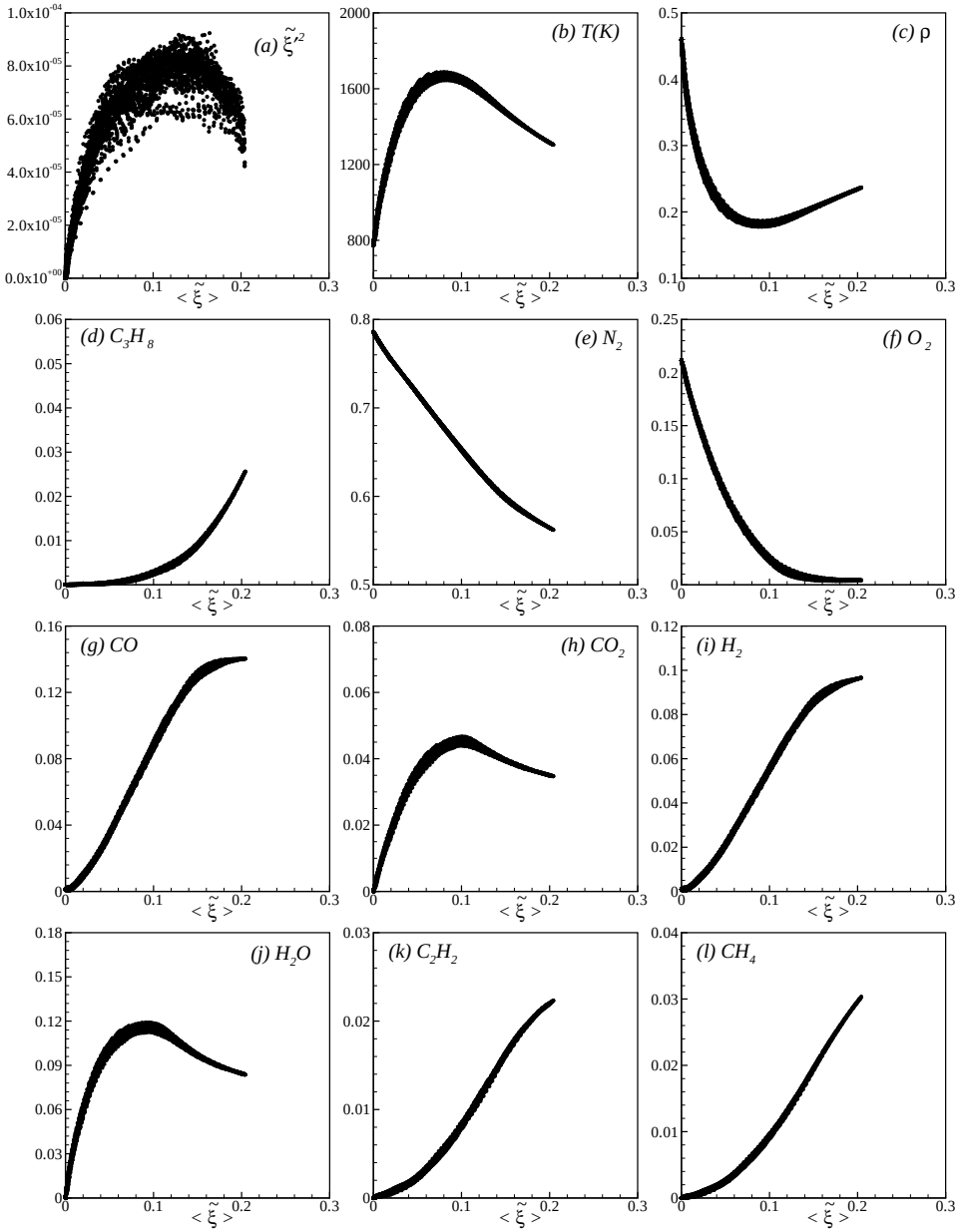

Figure 3.18: Scatter plots of the mean values of (a) $< \tilde{\xi}''^2 >$, (b) $< \tilde{T}(K) >$, (c) $< \tilde{\rho} >$, (d) $< \tilde{Y}_{C_3H_8} >$, (e)$< \tilde{Y}_{N_2} >$, (f) $< \tilde{Y}_{O_2} >$, (g) $< \tilde{Y}_{CO} >$, (h) $< \tilde{Y}_{CO_2} >$, (i) $< \tilde{Y}_{H_2} >$, (j) $< \tilde{Y}_{H_2O} >$, (k) $< \tilde{Y}_{C_2H_2} >$ and (l) $< \tilde{Y}_{CH_4} >$ on the cross-sectional plane at $y = 0.1m$ for Case1.

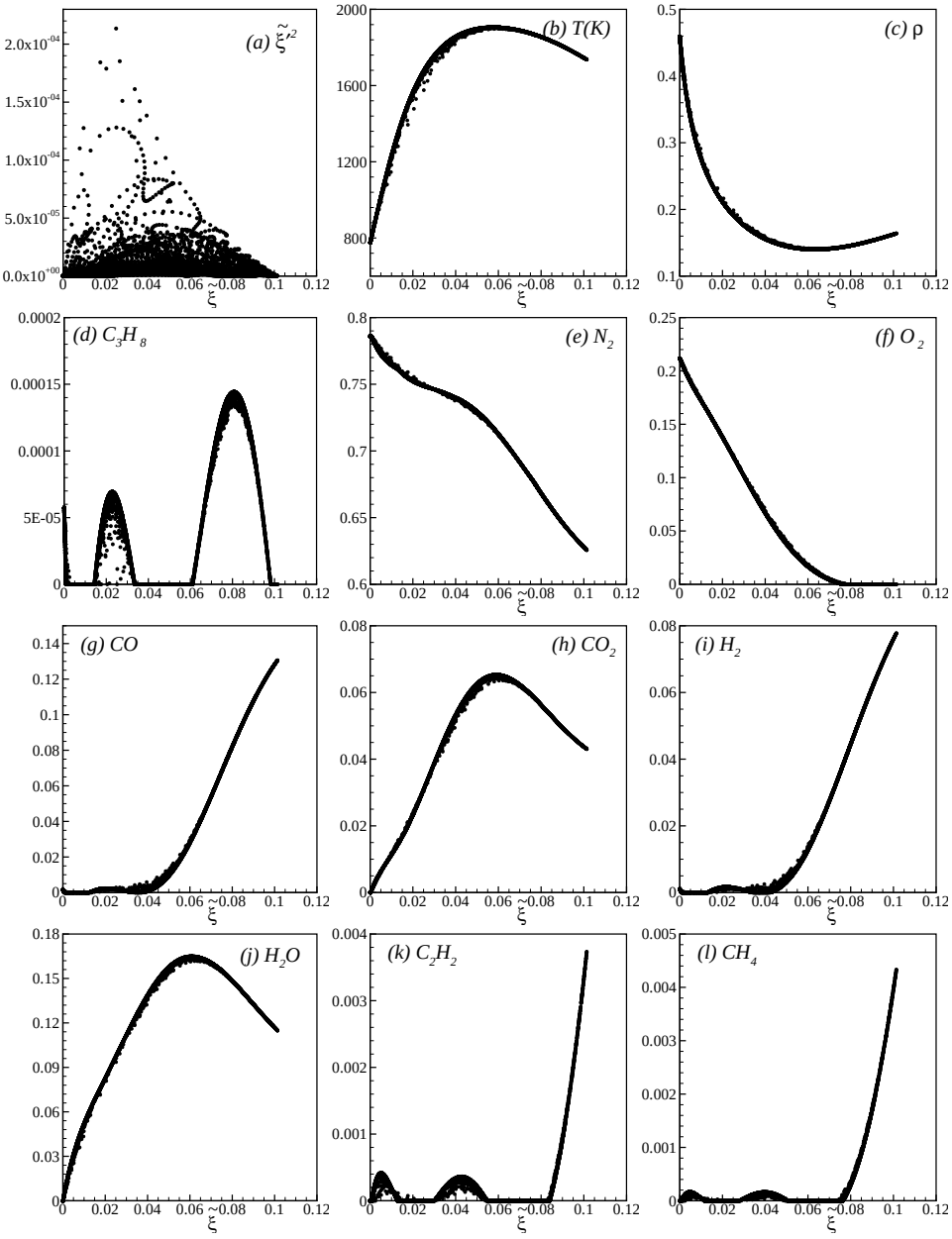

Figure 3.19: Scatter plots of the instantaneous values of (a) $\tilde{\xi}''^2$, (b) $\tilde{T}(K)$, (c) $\tilde{\rho}$ (d) $\tilde{Y}_{C_3H_8}$, (e)$\tilde{Y}_{N_2}$, (f) $\tilde{Y}_{O_2}$, (g) $\tilde{Y}_{CO}$, (h) $\tilde{Y}_{CO_2}$, (i) $\tilde{Y}_{H_2}$, (j) $\tilde{Y}_{H_2O}$, (k) $\tilde{Y}_{C_2H_2}$ and (l) $\tilde{Y}_{CH_4}$ on the cross-sectional plane at $y = 0.3m$ for Case1.

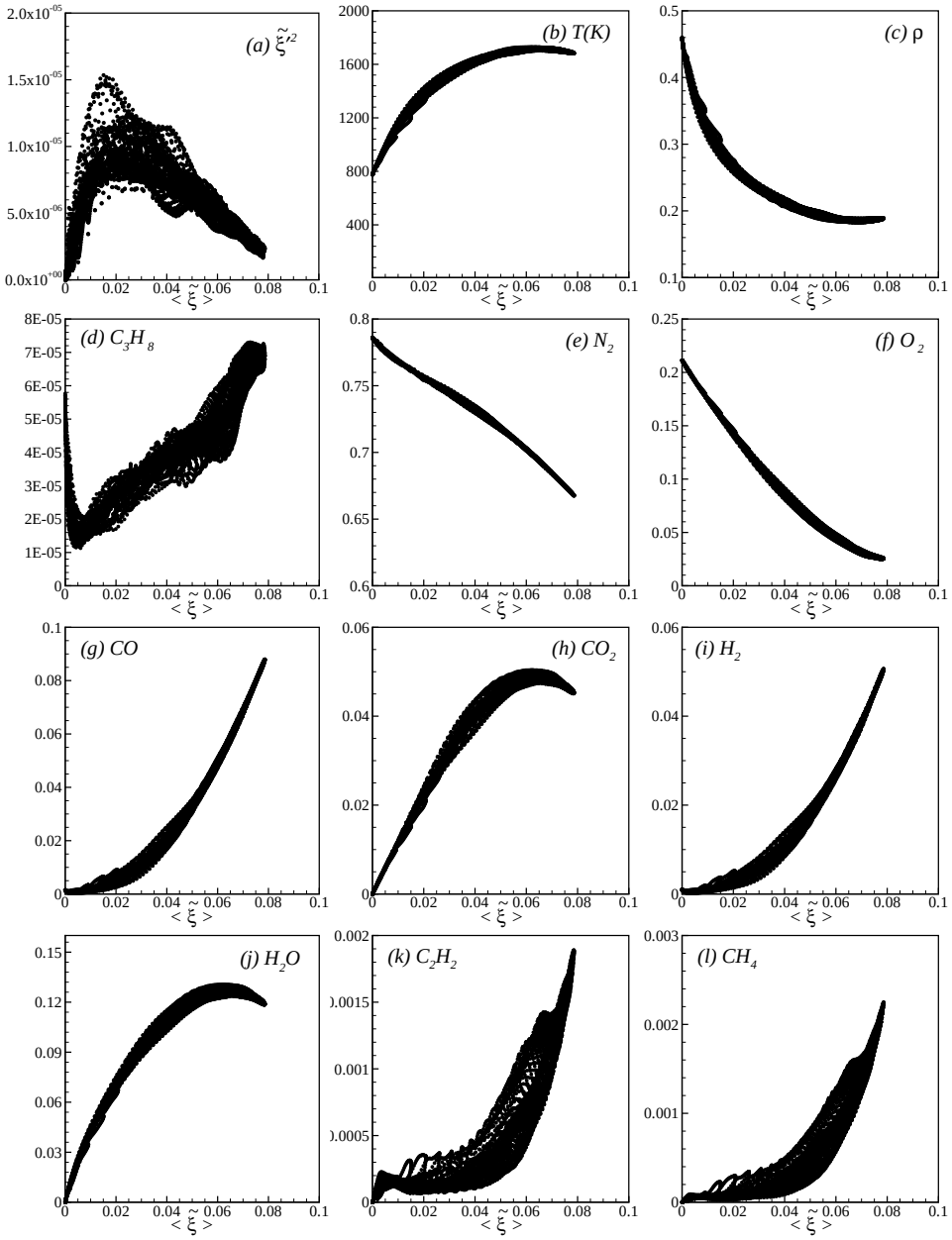

Figure 3.20: Scatter plots of mean values of (a) $< \tilde{\xi}''^2 >$, (b) $< \tilde{T}(K) >$, (c) $< \tilde{\rho} >$, (d) $< \tilde{Y}_{C_3H_8} >$, (e)$< \tilde{Y}_{N_2} >$, (f) $< \tilde{Y}_{O_2} >$, (g) $< \tilde{Y}_{CO} >$, (h) $< \tilde{Y}_{CO_2} >$, (i) $< \tilde{Y}_{H_2} >$, (j) $< \tilde{Y}_{H_2O} >$, (k) $< \tilde{Y}_{C_2H_2} >$ and (l) $< \tilde{Y}_{CH_4} >$ on the cross-sectional plane at $y = 0.3m$ for Case1.

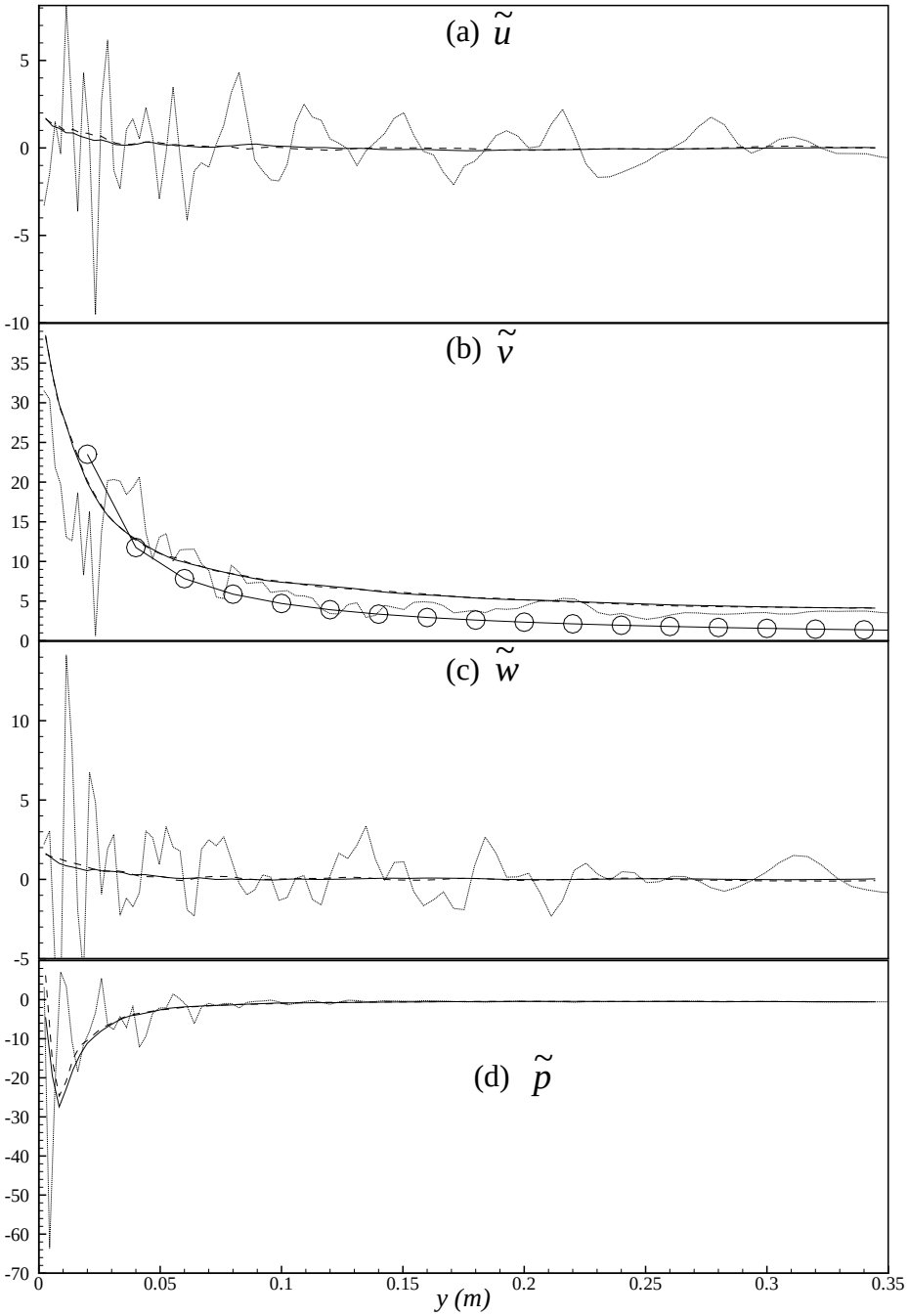

Figure 3.21: Centerline profiles of the velocity components, (a) $\tilde{u}$, (b) $\tilde{v}$, (c) $\tilde{w}$ and (d) pressure, $\tilde{p}$. Solid line, time mean (Case1); Dashed line, time mean (Case2); Dotted line, Favre averaged (Case1); Solid line with circle, mean axial velocity of an axisymmetric fully developed turbulent flow.

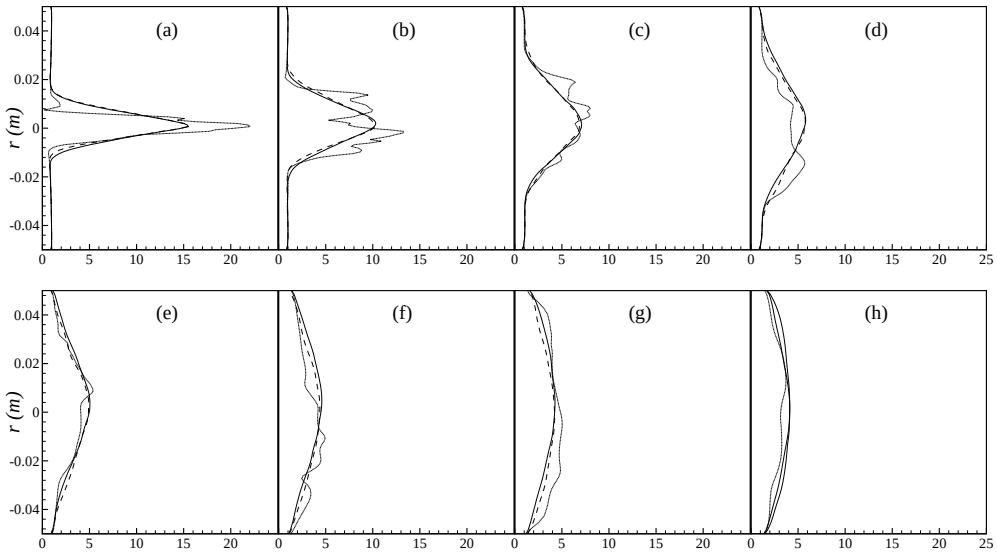

Figure 3.22: Radial profiles of the axial velocity component, $\tilde{v}$, at (a) $y = 0.025m$, (b) $y = 0.05m$, (c) $y = 0.1m$, (d) $y = 0.15m$, (e) $y = 0.2m$, (f) $y = 0.25m$, (g) $y = 0.3m$, and (h) $y = 0.35m$. For legend, see Fig. 3.21

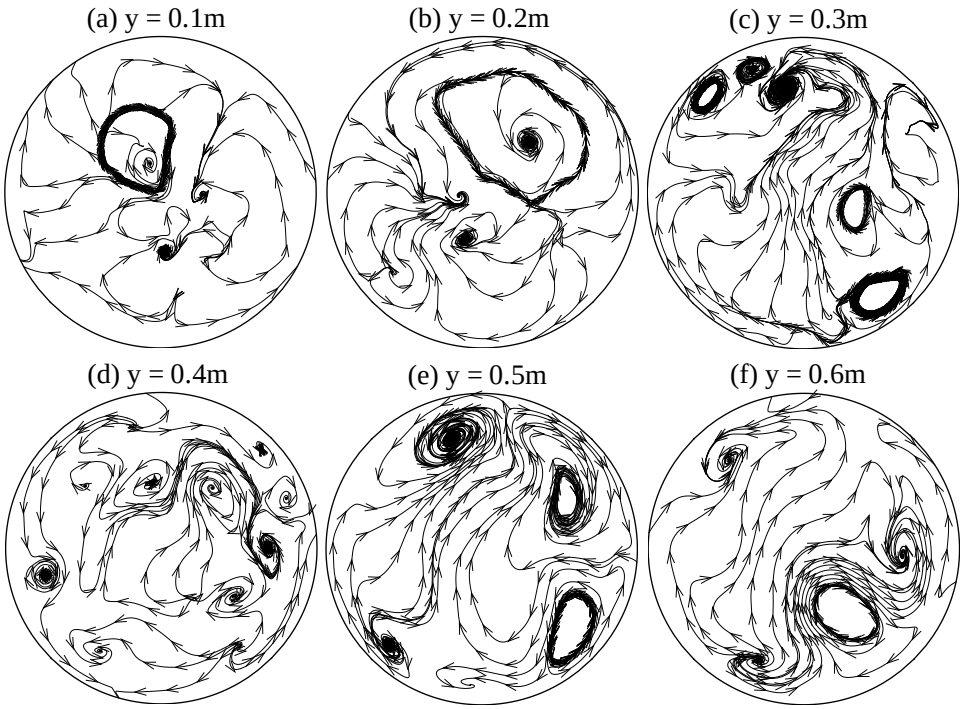

Figure 3.23: Instantaneous plot of streamlines for Case1 at different cross-sectional positions: (a) $y = 0.1m$, (b) $y = 0.2m$, (c) $y = 0.3m$, (d) $y = 0.4m$, (e) $y = 0.5m$, and (b) $y = 0.6m$.

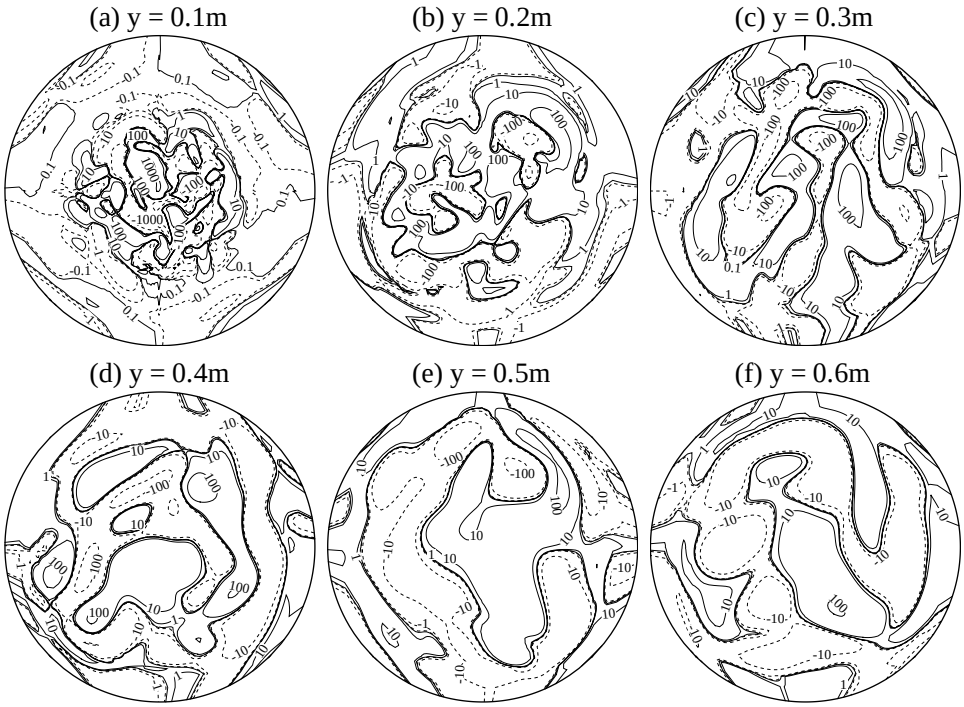

Figure 3.24: Instantaneous plot of vortex for Case1 at different cross-sectional positions: (a) $y = 0.1m$, (b) $y = 0.2m$, (c) $y = 0.3m$, (d) $y = 0.4m$, (e) $y = 0.5m$, and (b) $y = 0.6m$; dashed lines represent contour with negative values.

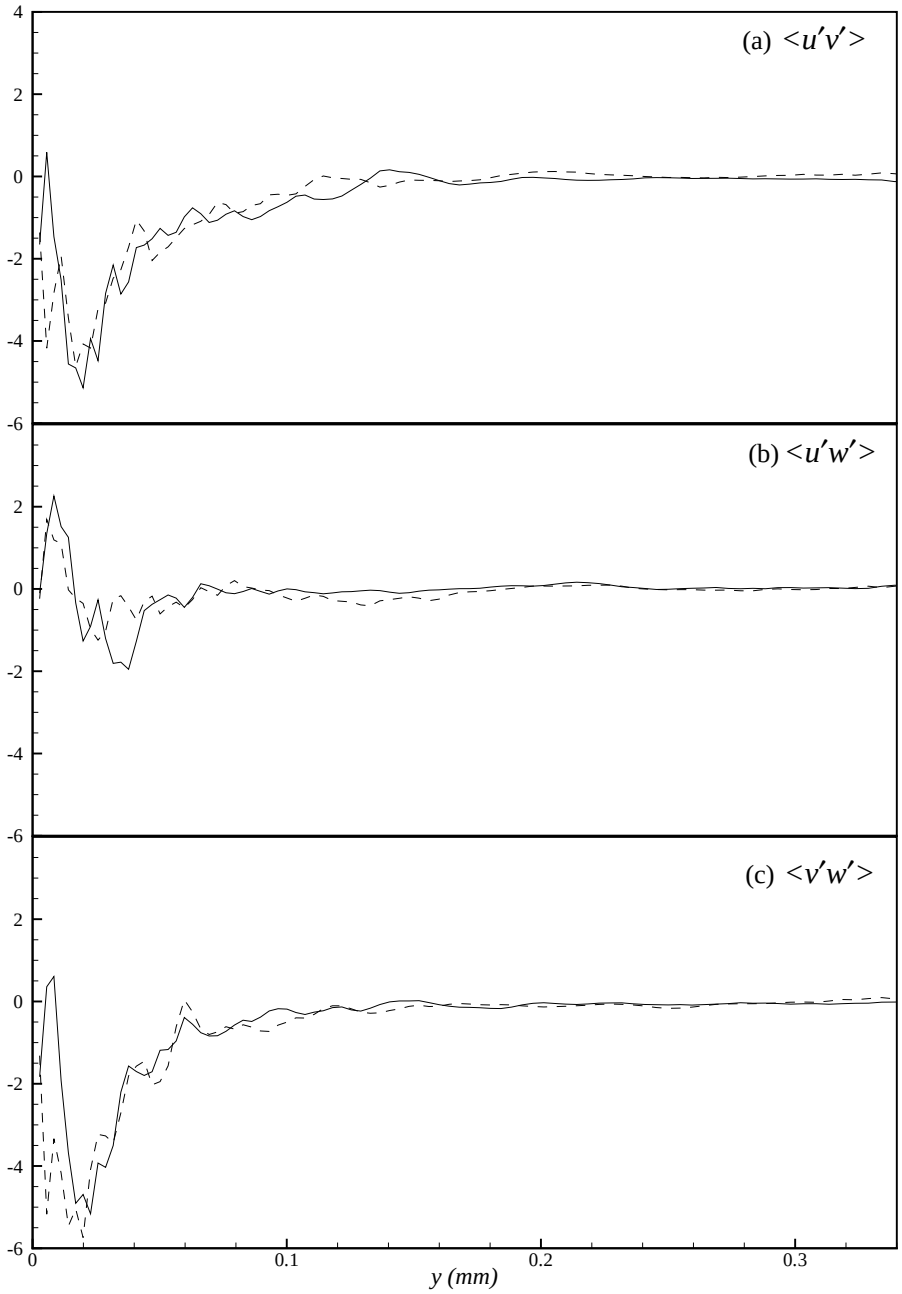

Figure 3.25: Profiles of the mean turbulence shear stresses along the axial direction. Solid line, Case1; Dashed line, Case2.

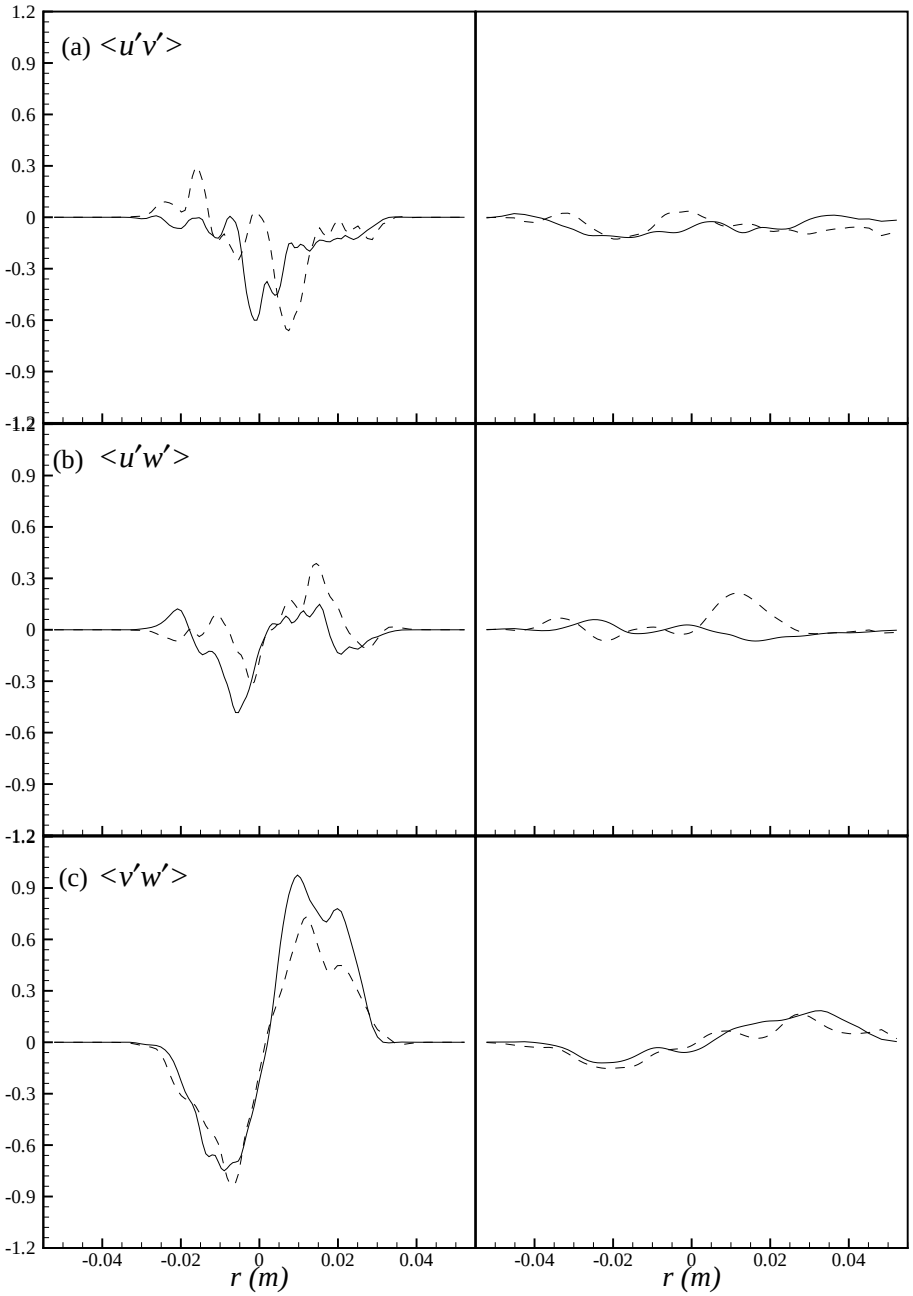

Figure 3.26: Profiles of the mean turbulence shear stresses along the radial direction at $y = 0.1m$ (left column) and $y = 0.3m$ (right column). Solid line, Case1; Dashed line, Case2.

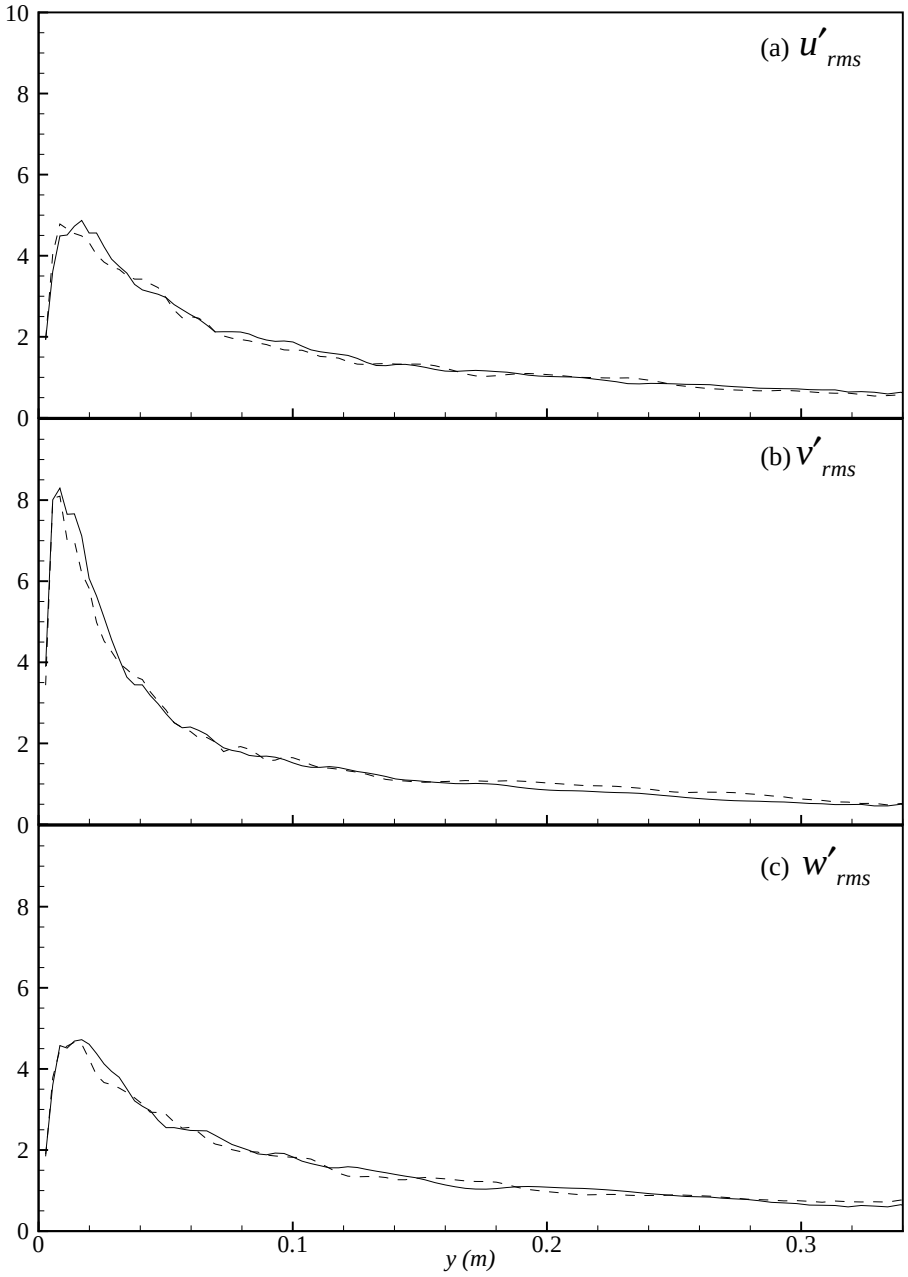

Figure 3.27: Root mean square (rms) of the fluctuations u', v', w' along the axial direction. Solid line, Case1; Dashed line, Case2.

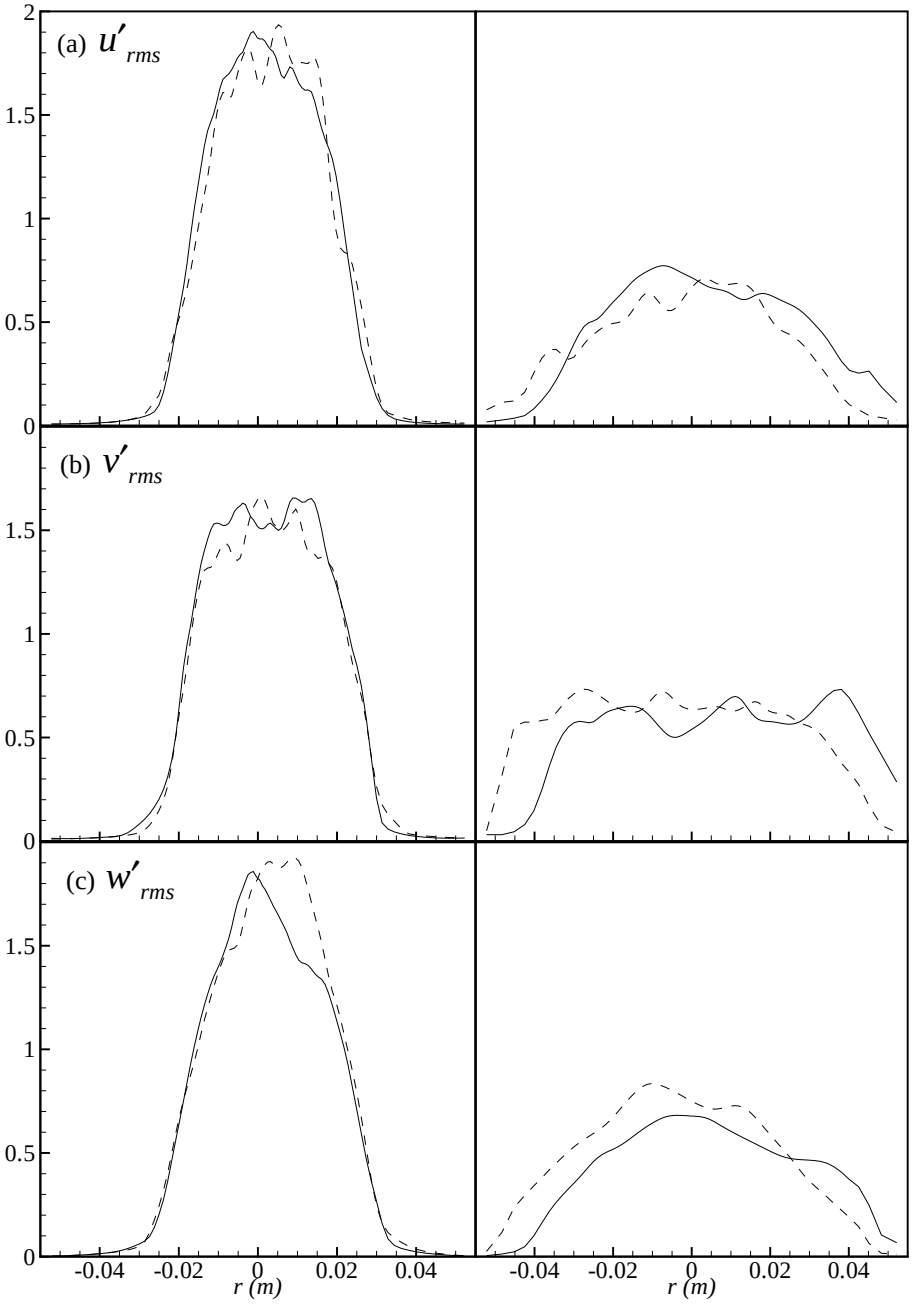

Figure 3.28: Root mean square (rms) of the fluctuations u', v', w' along the radial direction at $y = 0.1m$ (left column) and $y = 0.3m$ (right column). Solid line, Case1; Dashed line, Case2.

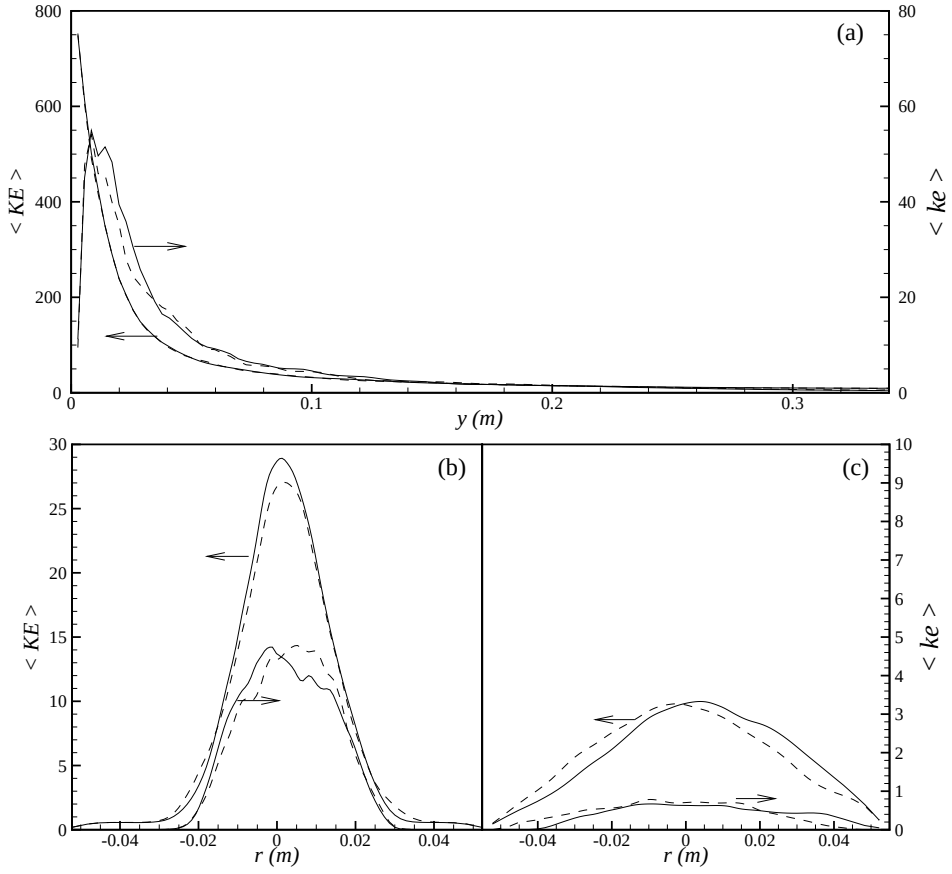

Figure 3.29: Mean and turbulent kinetic energy along (a) the axial direction, and the radial direction at (b) $y = 0.1m$ and (c) $y = 0.3m$. Solid line, Case1; Dashed line, Case2.

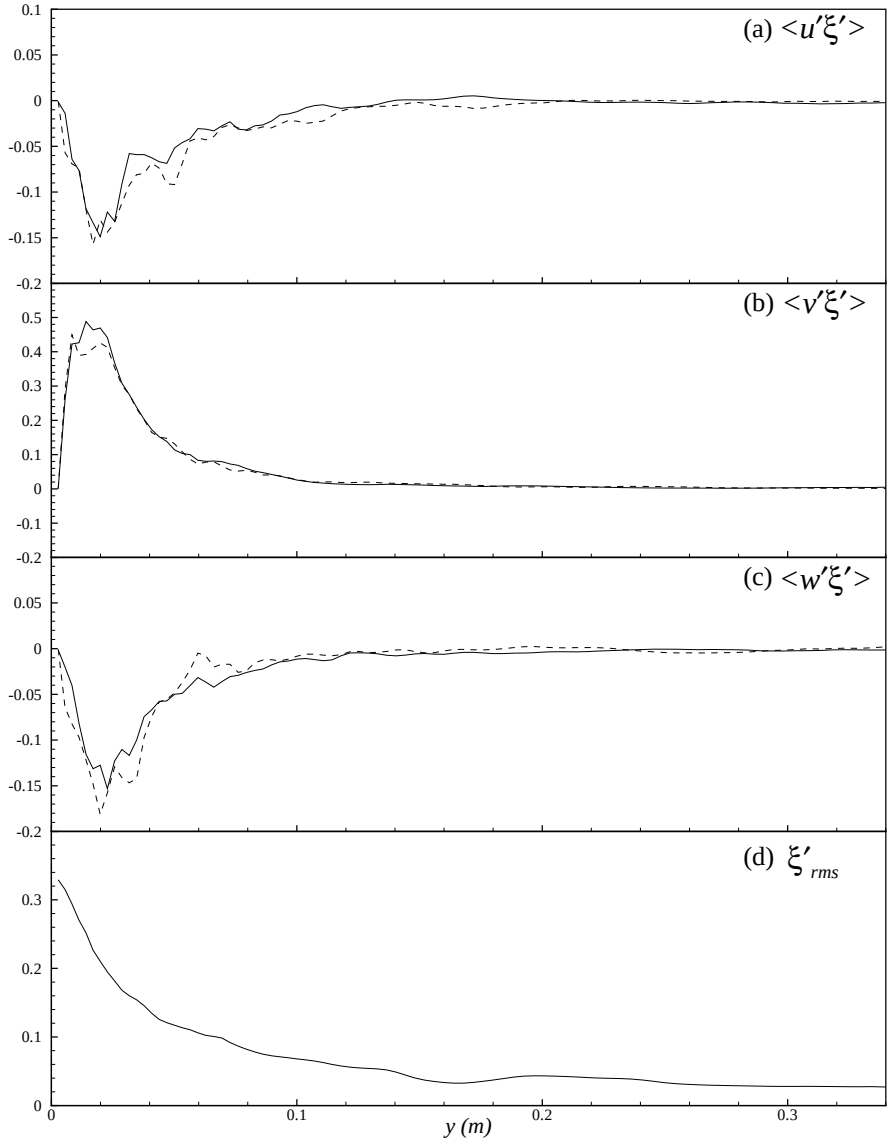

Figure 3.30: Profiles of the mean mixture fraction fluxes along the axial direction. Solid line, Case1; Dashed line, Case2.

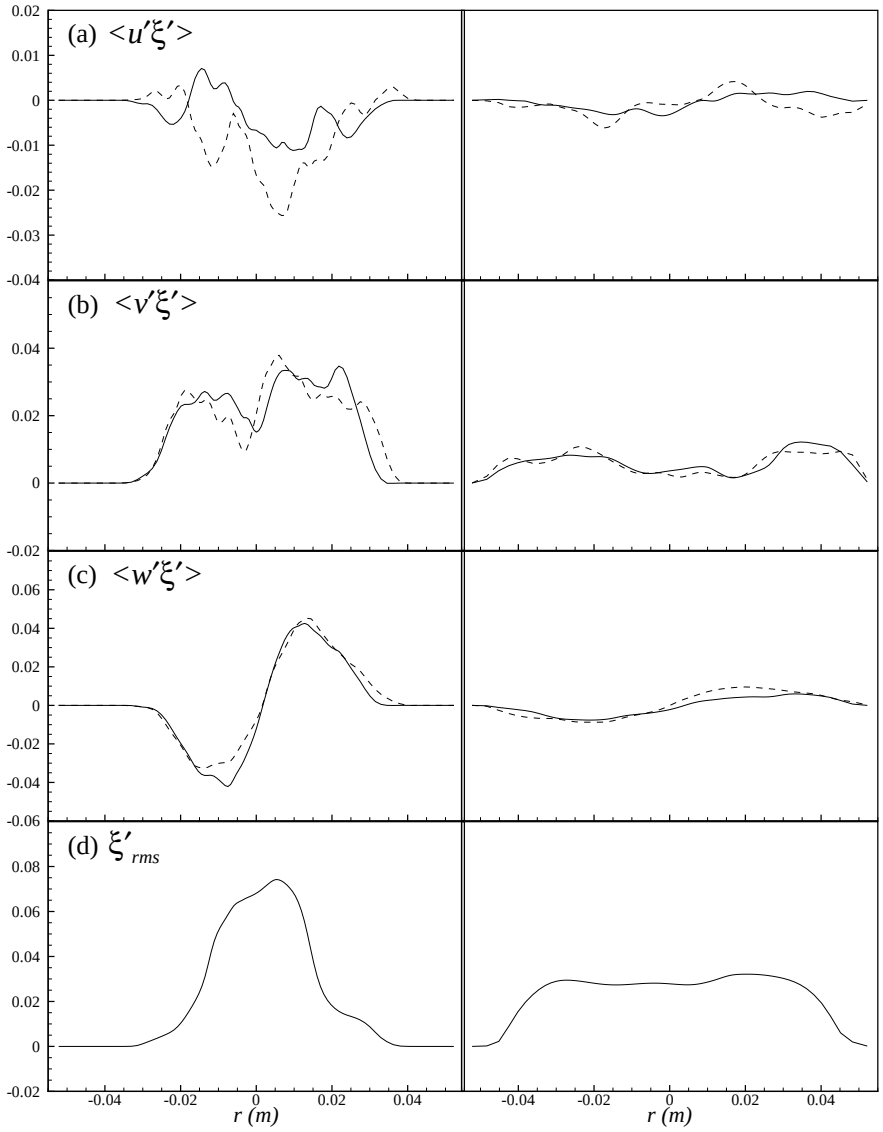

Figure 3.31: Profiles of the mean mixture fraction fluxes along the radial direction at $y = 0.1m$ (left column) and $y = 0.3m$ (right column). Solid line, Case1; Dashed line, Case2.

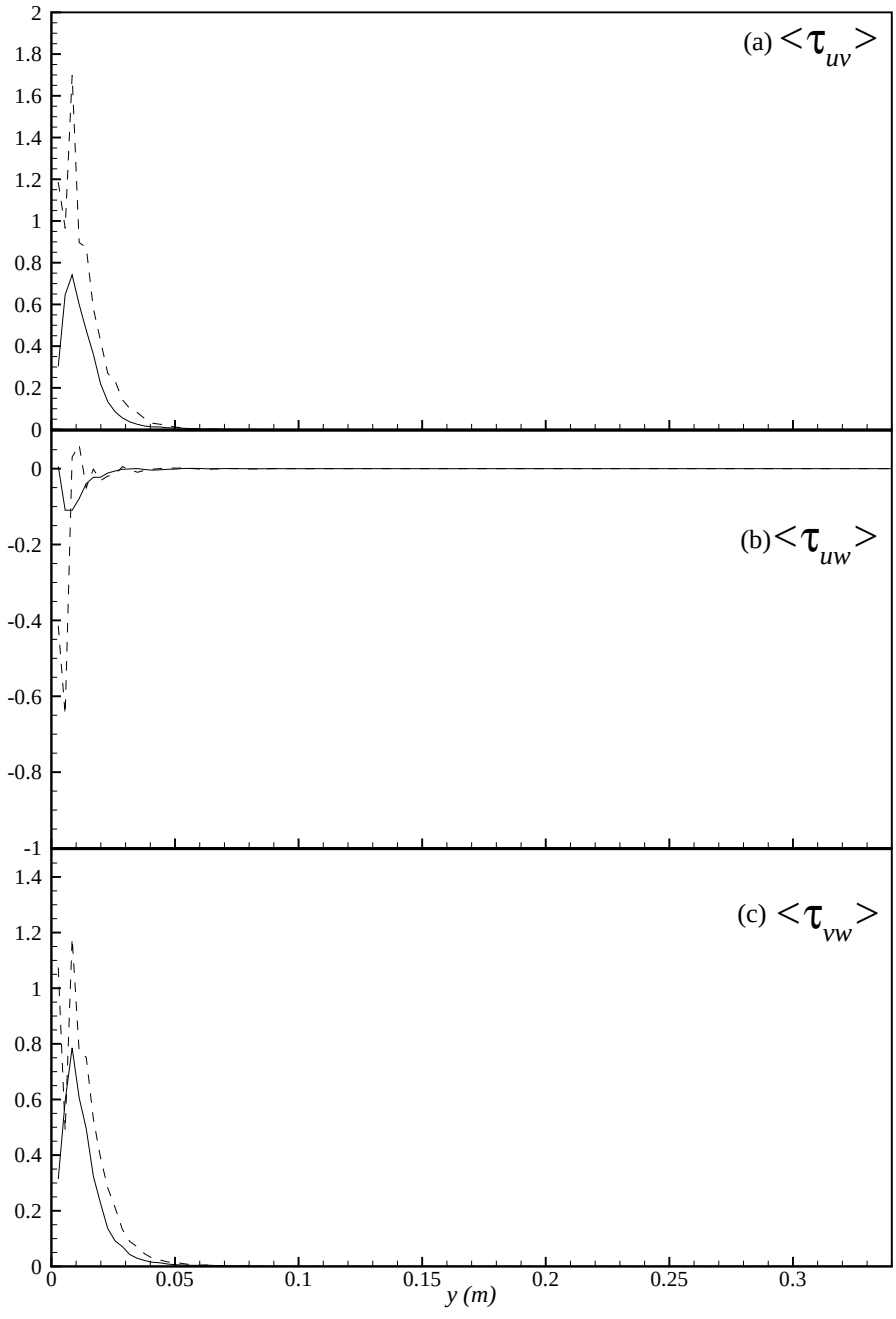

Figure 3.32: Profiles of the mean sub-grid scale shear stresses along the axial direction. Solid line, Case1; Dashed line, Case2.

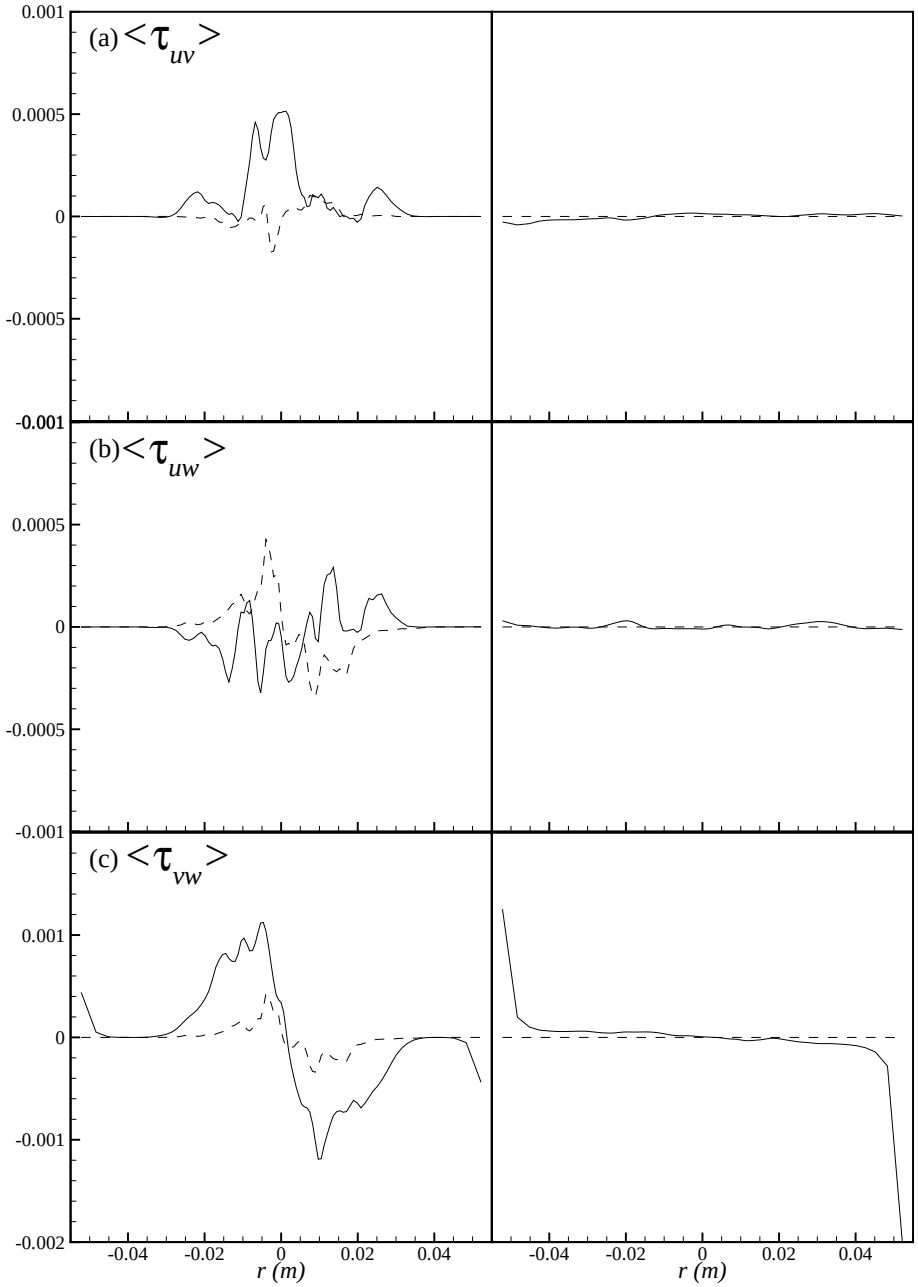

Figure 3.33: Profiles of the mean sub-grid scale shear stresses along the radial direction at $y = 0.1m$ (left column) and $y = 0.3m$ (right column). Solid line, Case1; Dashed line, Case2.

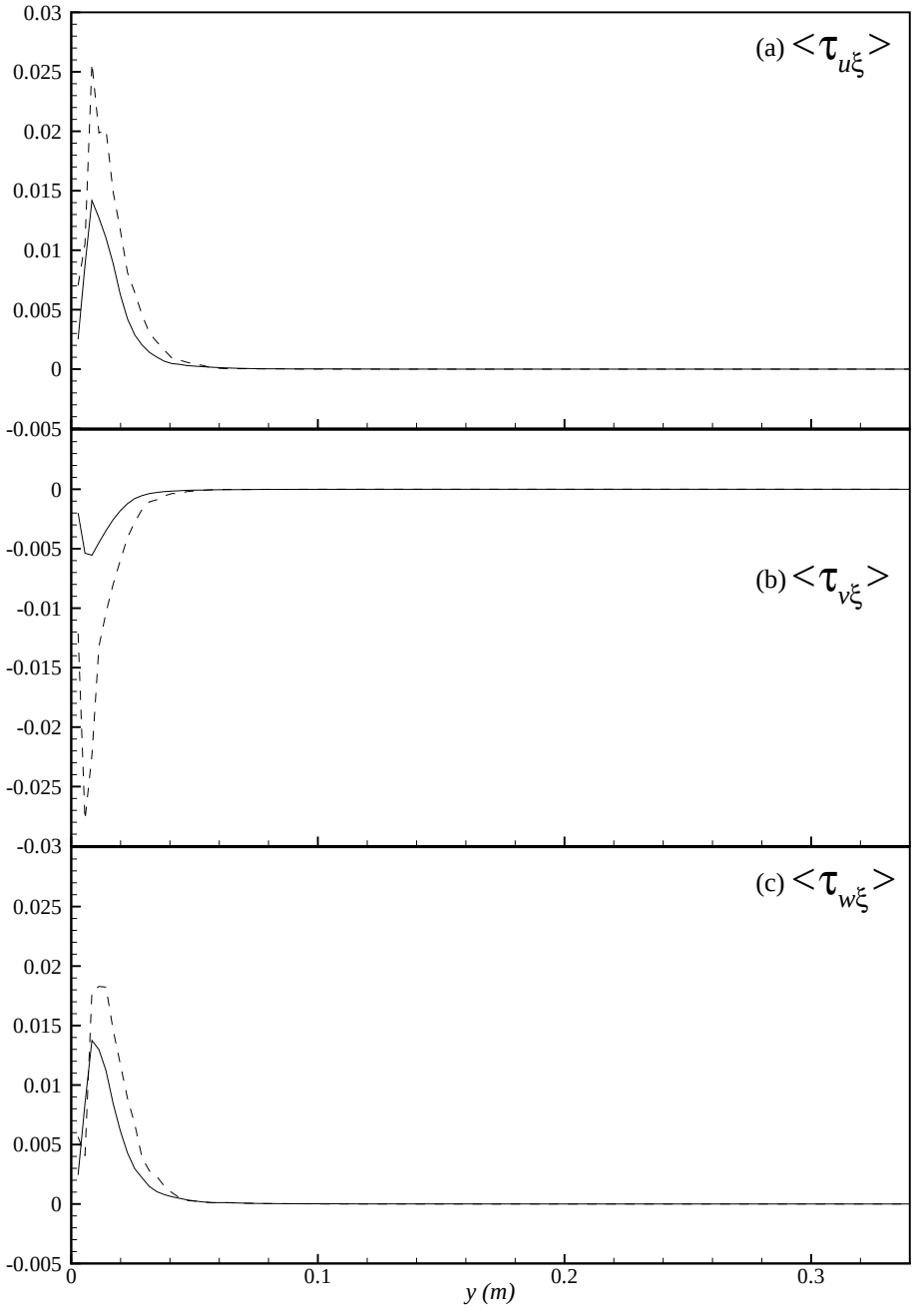

Figure 3.34: Profiles of the mean sub-grid scale mixture fraction fluxes along the axial direction. Solid line, Case1; Dashed line, Case2.

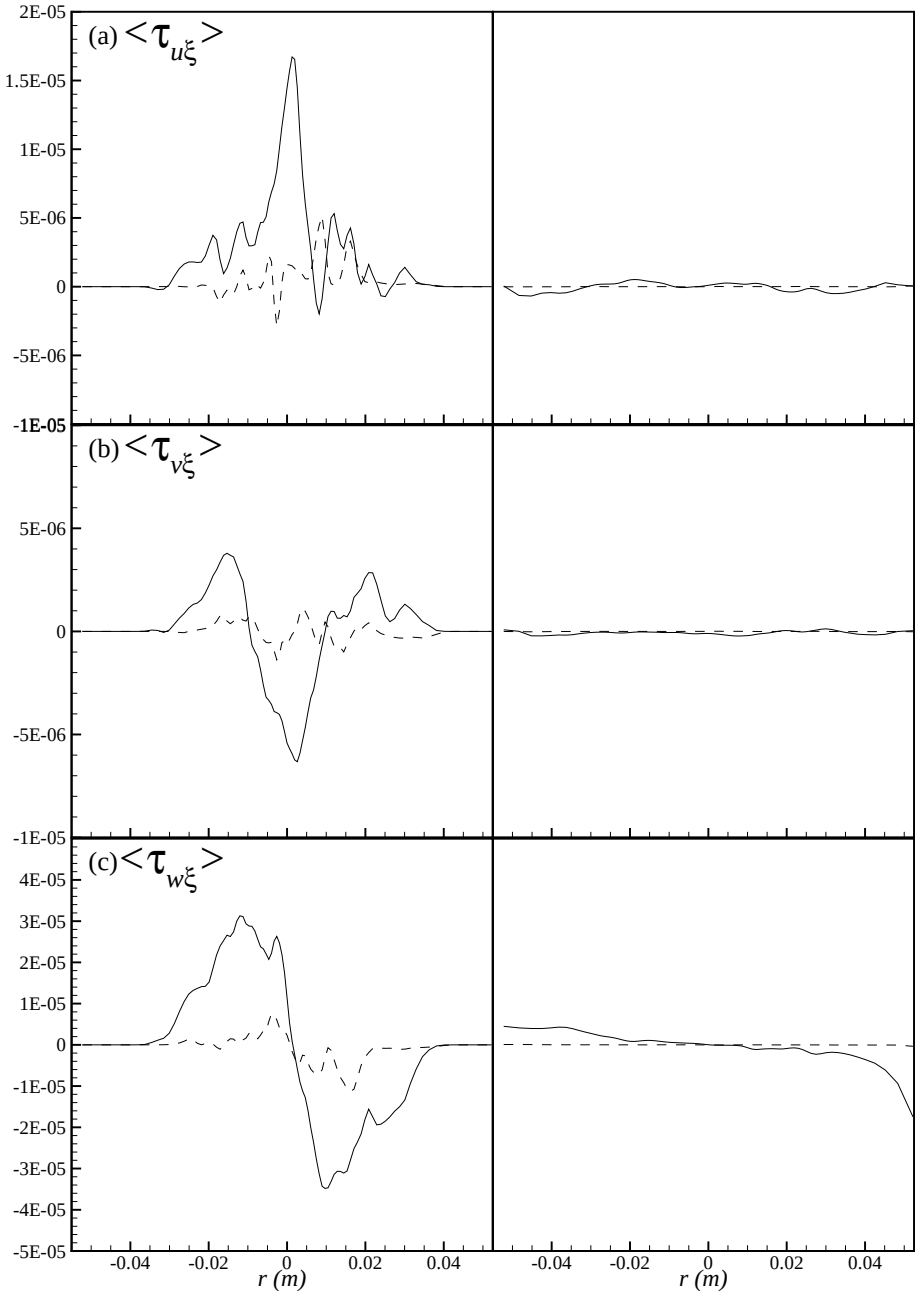

Figure 3.35: Profiles of the mean sub-grid scale mixture fraction fluxes the radial direction at $y = 0.1m$ (left column) and $y = 0.3m$ (right column). Solid line, Case1; Dashed line, Case2.

Chapter 4

LES for Soot Formation in a Propane-Air Turbulent Flame

Abstract: In this chapter, the LES technique is applied to predict the soot formation in the propane-air flame inside a cylindrical combustor. A Smagorinsky model with $C_s = 0.1$ as well as a dynamic model has been employed for modelling of the sub-grid scale stresses, while the non-premixed combustion process is modelled through the conserved scalar approach with laminar flamelet model described in Chapter 3. The soot formation is included via the balance equations for soot mass fraction and soot particle number density with finite rate kinetic source terms to account for soot inception/nucleation, surface growth, agglomeration and oxidation. The computational results are compared with those of the experimental results investigated by Nishida and Mukohara [1] in co-flowing turbulent flame. Predictions by the present model are shown to be in good agreement with measured soot concentration.

4.1 Introduction

In fuel-rich combustion, enough oxygen is not present to yield a complete conversion of fuel into major combustion products such as carbon dioxide and water vapour. The combustion or pyrolysis of hydrocarbons in high temperature leads to the appearance of soot particles. Soot particles formed during combustion process significantly affect the performance and durability of many engineering systems such as gas turbines and diesel engines, see Chapter 2 for a brief review of this.

In this chapter Large Eddy Simulation technique has been applied to investi-

gate the soot formation and growth during the non-premixed propane/air turbulent combustion process within a cylindrical combustor. A Smagorinsky model with $C_s = 0.1$ as well as its dynamic calibration has been employed to model the sub-grid scale stresses. The non-premixed combustion process is modelled through the conserved scalar approach with laminar flamelet model, while the soot formation is included through the balance equations for soot mass fraction and soot particle number density. The soot reaction rate model includes soot particle inception, surface growth, particle coagulation and particle oxidation.

This chapter is structured in the following order. A brief description on the soot formation process is presented in §4.2, followed by the modelling of the soot formation and growth in §4.3. The governing filtered equations are presented in §4.4. In §4.6 the sgs modelling is presented. Results and discussion are presented in §4.7. In §4.8 a general conclusion of this chapter is made.

4.2 Brief Description on Soot Formation and Oxidation

The formation of soot particles in a flame is inherently a chemically-controlled phenomenon. A great deal of information has come from shock tubes, laminar premixed and non-premixed flames. The previous view of soot formation process can be divided into four principal sub-processes: (i) soot particle inception or nucleation, (ii) surface growth, (iii) particle coagulation, and (iv) particle oxidation. These sub-processes can occur simultaneously or varying degrees for individual process depending on the specific combustion environment. Kennedy [38] and Haynes and Wagner [100] offer a good review of these issues. A brief description of soot formation process is given below.

4.2.1 Soot Particle Inception or Nucleation

Particle inception is the initial stage of formation of the smallest soot particles from relatively low molecular weight (gaseous) hydrocarbons. These smallest particles have sizes of the order of about 1 nm and masses of about 1000 atomic mass units. Though the actual mechanics behind the formation of soot particles from a com-

bustion of gaseous mixture are not well understood, it is generally accepted that the presence of high level intermediate combustion/pyrolysis products, particularly acetylene (C_2H_2) via Polycyclic Aromatic Hydrocarbons (PAHs), is closely associated with the nucleation of soot particles. The choice of acetylene (C_2H_2) as the crucial feature of the soot formation process is strongly supported by experimental evidence, for example, see Harris and Weiner [101]. The PAH hypothesis is the most generally accepted based on the numerous experimental and modelling studies.

The starting point for the PAH route is the formation of the first aromatic ring, followed by the formation of large PAHs through the "H-abstraction-C_2H_2-addition" (HACA) mechanism. The HACA mechanism occurs by way of a two-step process which involves the hydrogen abstraction to activate aromatics, followed by subsequent acetylene addition. Some of the large PAHs have stable structures at high temperature which are known as "islands of stability" that allow more and more aromatics ring to be added via HACA. At a certain size, some PAH species begin to stick to each other during collision, while individual PAHs keep increasing in size at the same time via HACA. This combined growth by molecular chemical reactions and physical collisions leads to the appearance of solid particles.

4.2.2 Soot Surface Growth

The soot surface growth process follows the soot particle inception and occurs through the addition of acetylene (C_2H_2) to the already formed particles and PAH coagulation. It is generally accepted that the major growth species in hydrocarbon flames is acetylene, although PAHs may also play a role. Surface growth process leads to an increase of the total mass of soot particles in flames but the number of particles remains unchanged.

4.2.3 Soot Particle Coagulation

Once the initial soot particles are formed through the inception and surface growth process, the physical process of collisions between these particles leads to the formation of larger spheroid soot particles. This process is known as soot coagulation which occurs simultaneously with surface growth processes. This process of coag-

ulation does not increase the mass of soot present, but reduces the overall number of particles with each particle carrying more mass. Particle coagulation is usually classified as coalescent growth and agglomeration into fractal aggregates. In coalescent growth process, particles are usually assumed to be spherical and two particles collide and merge together to form a new single spherical particle. On the other hand, in agglomeration soot particles stick to each other forming a chain-like structure.

4.2.4 Soot Particle Oxidation

Oxidation of soot particle occurs at the particle surface with oxygen molecule and OH radical to form CO and CO_2. Soot particle oxidation is an inverse process of surface growth that changes the mass of solid soot particles back into gas-phase species. It is the only process that reduces the total amount of soot present in flames.

4.3 Modelling of Soot Formation and Growth

In the present work, the soot formation and growth mechanism within the flame are modelled via the solution of the two conservation equations for soot mass fraction and soot particle number density. These equations can be written as

$$\frac{\partial(\rho\phi)}{\partial t} + \frac{\partial(\rho u_j \phi)}{\partial x_j} = \frac{\partial}{\partial x_j}\left(\Gamma \frac{\partial \phi}{\partial x_j}\right) + \rho S(\phi), \tag{4.1}$$

where ϕ represents the soot mass fraction, $Y_{c(s)}$, and/or the soot particle number density, N.

A simplified reaction mechanism of Leung *et al.* [47] for soot formation, later used by Fairweather *et al* [2], has been used in the present work. The instantaneous rates of formation of soot mass fraction, $Y_{c(s)}$, per unit volume are therefore expressed as Fairweather *et al* [2],

$$\begin{aligned}\rho S(Y_{c(s)}) = r_i M_{c(s)} + r_{ii} M_{c(s)} [C(s)]^{1/3} [\rho N]^{1/6} \\ - r_{iii} M_{c(s)} [C(s)]^{2/3} [\rho N]^{1/3},\end{aligned} \tag{4.2}$$

where $[C(s)] = \rho Y_{c(s)}/M_{c(s)}$ and $[\rho N] = \rho N$; and the terms on the right hand side

represent respectively the processes of nucleation, surface growth and oxidation. The formation of soot particle number density, N, can be expressed as

$$\rho S(N) = r_{iv} - r_v[C(s)]^{1/6}[\rho N]^{11/6}, \tag{4.3}$$

where the terms on the right hand side represent the processes of nucleation and coagulation respectively.

In equations (4.2) and (4.3), the individual reaction rates, r_s, are taken as

$$r_i = k_i[C_2H_2], \tag{4.4}$$

$$r_{ii} = k_{ii}A^{1/2}[C_2H_2], \tag{4.5}$$

$$r_{iii} = k_{iii}A[O_2], \tag{4.6}$$

$$r_{iv} = 2N_A r_i / C_{min}, \tag{4.7}$$

$$r_v = 2C_a \left(\frac{6M_{c(s)}}{\pi\rho_{c(s)}}\right)^{1/6} \left(\frac{6kT}{\rho_{c(s)}}\right)^{1/2}, \tag{4.8}$$

where the parameter, A, has the expression as

$$A = 2C_a \left(\frac{6M_{c(s)}}{\pi\rho_{c(s)}}\right)^{2/3}. \tag{4.9}$$

In the above expressions, $\rho_{c(s)} = 2000\ Kg/m^3$ is the soot density, $C_{min} = 100$ is the number of carbon atoms in the incipient carbon particle, $C_a = 9$ is an agglomeration rate constant, $M_{c(s)} = 12.011\ kg/kmol$ is the molar mass of soot, $N_A = 6.022 \times 10^{26}\ particles/kmol$ is the Avogadros' number, $k = 1.381 \times 10^{-23}$ J/K is the Boltzmann constant. All the rate constants, k_s, are given in Table 4.1 as used by Fairweather *et al* [2].

4.4 Spatial and Favre Filtering for LES

As the flame is associated with the large density variations. Application of the Favre-filtered function, defined in equation (3.43) of Chapter 3, is needed to get the soot mass fraction and particle number density equations for LES. Applying the

Favre-filtered function to the conservation equations for soot mass fraction and soot particle number density (4.1) gives

$$\frac{\partial(\bar{\rho}\tilde{\phi})}{\partial t} + \frac{\partial(\widetilde{\bar{\rho}u_j\phi})}{\partial x_j} = \frac{\partial}{\partial x_j}\left(\Gamma\frac{\partial\tilde{\phi}}{\partial x_j}\right) + \bar{\rho}\tilde{S}(\tilde{\phi}). \tag{4.10}$$

The source terms in conservation equations (4.10) for soot mass fraction and particle number density are now written respectively as,

$$\begin{aligned}\bar{\rho}\tilde{S}(\tilde{Y}_{c(s)}) = \tilde{r}_i M_{c(s)} + \tilde{r}_{ii} M_{c(s)}^{2/3}\bar{\rho}^{1/2}\tilde{Y}_{c(s)}^{1/3}\tilde{N}^{1/6} \\ -\tilde{r}_{iii} M_{c(s)}^{1/3}\bar{\rho}\tilde{Y}_{c(s)}^{2/3}\tilde{N}^{1/3}\end{aligned} \tag{4.11}$$

and

$$\bar{\rho}\tilde{S}(\tilde{N}) = \tilde{r}_{iv} - \tilde{r}_v M_{c(s)}^{-1/6}\bar{\rho}^2\tilde{Y}_{c(s)}^{1/6}\tilde{N}^{11/6}. \tag{4.12}$$

In equations (4.11) and (4.12), the SGS correlations among the reaction rates, density, the soot mass fraction, and the soot particle number density are neglected.

The reaction rates, r_s, given in (4.4)-(4.8) are functions of temperature and gaseous concentrations, which in turn can be expressed as a function of mixture fraction through the flamelet concept. The five rate terms are shown in Fig. 4.2. In Fig. 4.3 the variation of these five rate terms with the variation of mixture fraction variance, ξ'^2, are presented. This figure shows that the peak value of the reaction rates decreases in magnitude and also shifts towards the larger values of the mixture fraction. The Favre-averaged reaction rates, $\tilde{r}_s$, may therefore be determined by

$$\tilde{r}_s(\tilde{\xi}) = \int_0^1 r_s(\xi)\tilde{P}(\xi)d\xi, \tag{4.13}$$

where $\tilde{P}(\xi)$ is the β-pdf (probability density function), given in (3.73) of Chapter 3, constructed from the predicted values of the conserved scalar, $\tilde{\xi}$, and the sub-grid scalar variance, $\tilde{\xi}_{sgs}^{\prime 2}$. Due to the high peak appeared in the reaction rates, it is convenient to use a piece-wise polynomial fitting approach for the best data fitting of the reaction rates. Thus, a piece-wise polynomial fitting approach is used to integrate the β-pdf, which is described in the following section.

With the spherical particle assumption, the soot particle diameter can be ob-

tained by the following relation (Leung *et al* [47]),

$$\tilde{d}_{c(s)} = \left(\frac{6}{\pi} \frac{1}{\rho_{c(s)}} \frac{\tilde{Y}_{c(s)}}{\tilde{N}} \right)^{1/3}. \tag{4.14}$$

The soot concentration, $W_{c(s)}$ (g/Nm^3), is calculated per unit volume at the Normal Temperature and Pressure (N. T. P) from the following relation:

$$W_{c(s)} = \tilde{Y}_{c(s)} \times 10^6 \times \frac{M_{c(s)}}{22.41}. \tag{4.15}$$

The fraction of gas occupied by solid soot particles represented by the soot volume fraction, $\tilde{f}_v$, which will be needed for the radiative calculations, can be derived from,

$$\tilde{f}_v = \frac{\bar{\rho}\tilde{Y}_{c(s)}}{\rho_{c(s)}}. \tag{4.16}$$

4.5 Piece-Wise Integration of the Sub-grid β-pdf

For the piece-wise polynomial fitting, the relationship between the reaction rates, r_s, and the mixture fraction, ξ, are split into m polynomials with each polynomial having degree n in the conserved scalar, which are as follows:

$$\begin{aligned}
r_s^{(1)}(\xi) &= \sum_{i=0}^{n} a_i^{(1)} \xi^i \quad \text{valid for } 0 = l_0 < \xi < l_1 \\
&\cdots \qquad \cdots \\
r_s^{(k)}(\xi) &= \sum_{i=0}^{n} a_i^{(k)} \xi^i \quad \text{valid for } l_{k-1} < \xi < l_k \\
&\cdots \qquad \cdots \\
r_s^{(m)}(\xi) &= \sum_{i=0}^{n} a_i^{(m)} \xi^i \quad \text{valid for } l_{m-1} < \xi < l_m = 1
\end{aligned} \tag{4.17}$$

which enable us to express $r(\xi)$ over the whole integration interval $0 < \xi < 1$ as a sum of the m polynomials in the following way:

$$\begin{aligned} r_s(\xi) &= r_s^{(1)}(\xi) \cdots + r_s^{(k)}(\xi) \cdots + r_s^{(n)}(\xi) \\ &= \sum_{k=1}^{m} r_s^{(k)}(\xi), \end{aligned} \tag{4.18}$$

Therefore, the expression (4.13) can be rewritten as the sum of the m integrals as,

$$\tilde{r}_s(\tilde{\xi}) = \sum_{k=1}^{m} \int_{l_{k-1}}^{l_k} r_s^{(k)}(\xi)\tilde{P}(\xi)d\xi, \tag{4.19}$$

The interval $l_{k-1} < \xi < l_k$ over which the integration of $r_s^{(k)}(\xi)$ is carried out, is only a part of the interval $0 < \xi < 1$ which appears in the expression of the β-function, so that the incomplete β-function (see Press *et al* [102]) needs to be introduced which is,

$$I_x(r,s) = \frac{\beta_x(r,s)}{\beta(r,s)} = \frac{1}{\beta(r,s)} \int_0^x \xi^{r-1}(1-\xi)^{s-1}d\xi, \tag{4.20}$$

where the parameters, r and s; and the function, $\beta(r,s)$, are given in (3.74) and (3.75) of Chapter 3 respectively.

The general integral for the interval $l_{k-1} < \xi < l_k$ is given by,

$$\begin{aligned} \tilde{r}_s^{(k)}(\tilde{\xi}) &= \int_{l_{k-1}}^{l_k} r_s^{(k)}(\xi)\tilde{P}(\xi)d\xi \\ &= \frac{\Gamma(r+s)}{\Gamma(r)} \sum_{i=0}^{n} a_i^{(k)} \frac{\Gamma(r+i)}{\Gamma(r+s+i)} \left(I_{l_k}(r+i,s) - I_{l_{k-1}}(r+i,s)\right) \end{aligned} \tag{4.21}$$

Therefore, the expression (4.19) can be rewritten in terms of the incomplete β-function as,

$$\tilde{r}_s(\tilde{\xi}) = \sum_{k=1}^{m} \frac{\Gamma(r+s)}{\Gamma(r)} \sum_{i=0}^{n} a_i^{(k)} \frac{\Gamma(r+i)}{\Gamma(r+s+i)} \left(I_{l_k}(r+i,s) - I_{l_{k-1}}(r+i,s)\right) \tag{4.22}$$

where the coefficients $a_0^{(k)}$, $a_1^{(k)}$, ..., $a_n^{(k)}$ are obtained from the polynomial fitting

of k-th piece of the reaction rates against the mixture fraction. For each piece, the degree of the polynomial, $n = 6$, is taken for the best fitting.

4.6 Sub-Grid Scale Modelling

An application of the density weighted filter to the convection term in the governing equation (4.10) of soot formation introduces the unknown term, $\widetilde{\bar{\rho}u_j\phi}$, leaving this equation unclosed. This unknown term is defined as Germano [80] by

$$\widetilde{\bar{\rho}u_j\phi} = \bar{\rho}\tilde{u}_j\tilde{\phi} + J_j^{sgs}, \tag{4.23}$$

where J_j^{sgs} is unknown and referred to as sub-grid scale fluxes for soot mass fraction or soot particle number density respectively. This unknown must be modelled.

Like the modelling of sub-grid scale mixture fraction fluxes (described in Chapter 3), a gradient model introduced by Schmidt and Schumann [82] is used for modelling the sub-grid scale soot mass fraction or soot particle number density fluxes, J_j^{sgs}, which is of the form

$$J_j^{sgs} = -\bar{\rho}\Gamma_{sgs}\frac{\partial\tilde{\phi}}{\partial x_j} = -\frac{\bar{\rho}\nu_{sgs}}{\sigma_{sgs}}\frac{\partial\tilde{\phi}}{\partial x_j}, \tag{4.24}$$

where σ_{sgs} is the sub-grid scale Prandtl/Schmidt number which takes a value of 0.7 in this computation.

4.7 Results and Discussion

In this section we now present the computational results. The average time step, dt, used in the computation is at the order of 10^{-6}. The time averaged results presented here are calculated by using the relation (3.82) given in Chapter 3. As in Chapter 3, the results are obtained for two cases, Smagorinsky constant, C_s, of 0.1 (Case1) and dynamically calibrated C_s (Case2). The model parameters are summarised in Table 3.1 of Chapter 3. The solid lines indicate Case1 and the dashed lines represent Case2.

In Chapter 3, it was found that most of the quantities were dominated in the

upstream region of the computational domain. So, to save computational cost, the results presented in this chapter are obtained for a short computational domain. A schematic of this short domain of the cylindrical combustor is shown in Fig. 4.1, which shows that the length of the combustor is taken as $0.35m$. It is also worth to mention here that we have reproduced the results presented in Chapter 3 in the short domain and found unchanged results.

4.7.1 Reaction Rates for Soot Formation

Instantaneous and mean results of the five reaction rates (a) $\tilde{r}_i$, (b) $\tilde{r}_{ii}$, (c) $\tilde{r}_{iii}$, (d) $\tilde{r}_{iv}$ and (e) $\tilde{r}_v$ on the horizontal midplane of the combustor, obtained in Case1, are plotted in the Figs. 4.4 and 4.5 respectively. From these figures, the distribution of the instantaneous as well as the mean values of the reaction rates on the horizontal midplane of the combustor can be visualised clearly. The reaction rates (a) $\tilde{r}_i$, (b) $\tilde{r}_{ii}$ and (d) $\tilde{r}_{iv}$, have similar distribution but different in magnitudes, and they all depend on the concentration of C_2H_2 (see Figs. 3.10(h) and 3.11(h) of Chapter 3) and the flame temperature (see Fig. 3.6 of Chapter 3). The reaction rate, $\tilde{r}_{iii}$, plotted in frame (c), however depends on both the O_2 concentration and the temperature and has the maximum value at the flame front. The reaction rate for coagulation, $\tilde{r}_v$, plotted in frame (e), is a function of temperature only, and that is why it is distributed like the flame temperature.

In Fig. 4.6 mean values of the first three reaction rates, $\tilde{r}_i$, $\tilde{r}_{ii}$ and $\tilde{r}_{iii}$, for soot formation are depicted along (a) the axial direction, and the radial direction at the three different cross-sectional positions of (b) $y = 0.1m$, (c) $y = 0.2m$, and (d) $y = 0.3m$, while the mean values of the rates for soot particle number density, $\tilde{r}_{iv}$ and $\tilde{r}_v$, along the axial and radial directions are presented in Fig. 4.7. In both figures the reaction rates are presented for both the Case1 and Case2. As the reaction rates, $< \tilde{r}_i >$, $< \tilde{r}_{ii} >$ and $< \tilde{r}_{iv} >$, are mainly a function of the C_2H_2 concentration, both the axial and radial profiles of these reaction rates shown in Figs. 4.6 and 4.7 are similar to the shape of the axial and radial profile of the C_2H_2 concentration (frame (h) of Figs. 3.12, 3.13 and 3.14 of Chapter 3). On the other hand the axial and radial profiles of reaction rate for oxidation, $\tilde{r}_{iii}$, plotted in Fig. 4.6, is similar to the axial and radial profiles of O_2 concentration (frame (c) of Figs. 3.12,3.13 and

3.14 of Chapter 3) because of its dependence on the O_2 concentration as well as the temperature. Similar profile like temperature can be found in the axial and radial profiles of the reaction rate for particle coagulation, $\tilde{r}_v$, depicted in Fig. 4.7 as it is a function of the temperature only. The above results confirm that the reaction rates, $\tilde{r}_i$, $\tilde{r}_{ii}$ and $\tilde{r}_{iv}$, are dominated by the concentration of C_2H_2 while the third reaction rate, $\tilde{r}_{iii}$, is dominated by the O_2 concentration although all these reaction rates are a function of the flame temperature through their nonlinear reaction rate constants, k_s.

Comparing the results, presented in Figs. 4.6 and 4.7, between Case1 and Case2, we have found a very similar level of the mean reaction rates.

4.7.2 Soot Concentrations and Particle Number Density

In Figs. 4.8 and 4.9, respectively the instantaneous and mean values of the (a) soot concentration, $\tilde{W}_{C(S)}$, (b) soot volume fraction, $\tilde{f}_v$, (c) particle number density, $\tilde{N}$, and (d) soot particle diameter, $\tilde{d}_{c(s)}$, are plotted on the horizontal midplane of the combustor. These plots show a clear visualisation of how these quantities are distributed on this plane.

Fig. 4.8(a) shows that the instantaneous soot concentration is high in the region where the instantaneous reaction rates, $\tilde{r}_i$ and $\tilde{r}_{ii}$ (frame (a) and (b) of Fig. 4.4), were found high. In the flame front region, where the high level of the instantaneous reaction rate, $\tilde{r}_{iii}$, was predicted, the level of the instantaneous soot concentration is predicted low because of the reaction rate, $\tilde{r}_{iii}$, is associated with the oxidation of the soot particle. From Fig. 4.8(c), it can be seen that the instantaneous soot particle number density is predicted high, like the reaction rate, $\tilde{r}_{iv}$, in the region where the instantaneous soot concentration was also predicted high. As the particle coagulation reduces the number of the particle, the soot particle number density can be found low where the reaction rate, $\tilde{r}_{iv}$, which is associated with the particle coagulation and plotted in Fig 4.4(e), is found to be high. The mean plot of these properties (see Fig. 4.9) also follow the similar trend.

Mean soot concentration, $< \tilde{W}_{C(S)} >$, within the flame along the axial direction is shown in frame (a) of Fig. 4.10 and compared against the experimental findings of Nishida and Mukohara [1]. In frames (b)-(d) of Fig. 4.10, mean soot concentration,

$< \tilde{W}_{C(S)} >$, along the radial direction is presented at three different cross-sectional positions of (b) $y = 0.1m$, (c) $y = 0.2m$ and (d) $y = 0.3m$ and comparisons with those of the experimental measurements also given. The predictions of soot concentration are presented per unit volume at Normal Temperature and Pressure (N. T. P). In the present model, soot formation and growth are associated with the levels of C_2H_2, while oxidation is associated with the levels of O_2 in the flame.

In Fig. 4.10 (a), the initial increase in the axial mean soot concentration can be attributed to an increase in the flame temperature (see Fig. 3.8(a)), which also promotes the fuel pyrolysis to produce unburned hydrocarbon, C_2H_2, (see Fig. 3.12(h) of Chapter 3). At the downstream region, at about $0.25 < y(m) < 0.35$, the soot concentration decreases gradually. The decrease likely results from the combined effects of the high temperature and the high levels of O_2 predicted in that region (see Figs. 3.8(a) and 3.12(c) of Chapter 3), which promotes the soot oxidation. The concentration of soots in the axial direction is slightly under-predicted compared with the experiment, this might be the cause of an slightly over-prediction of the temperature and O_2 and under-prediction of C_2H_2, as already mentioned that the soot production is directly linked with C_2H_2, O_2 and T.

The radial profiles of $< \tilde{W}_{C(S)} >$ plotted in Fig. 4.10(b)-(c) show the peaks and the decaying trends from the peak levels are well predicted in the model. The radial peak soot concentrations are achieved just inside the location of peak temperature within the flame. Along the radial direction, near the centreline of the combustor an under-prediction in the radial mole fraction of C_2H_2 (see Figs. 3.13(h) and 3.14(h) of Chapter 3) corresponds to an under-prediction in the radial mean soot concentration. Towards the combustor wall, where the soot burn-out takes place due to the high levels of O_2 (see Figs. 3.13(c) and 3.14(c) of Chapter 3), an over-prediction of C_2H_2 leads to an over-prediction of mean soot concentration.

The axial and radial profiles of soot volume fraction, $\tilde{f}_v$, are plotted in Figs. 4.11. Both the axial and radial plots have the same trend as soot concentration presented in Figs. 4.10. Appearance of the concave shape near the inlet in the axial profile is due to the density used to calculate the soot volume fraction (relation (4.16)). Note that these results are required for the radiation calculations described in Chapter 6.

The predicted mean soot particle number density along the axial direction is plotted in Fig. 4.12(a) and along the radial direction it is plotted in Fig. 4.12 at the

different cross-sectional positions, (b) $y = 0.1m$, (c) $y = 0.2m$ and (d) $y = 0.3m$. It should be noted that the experimental results of the soot particle number density are not available in Nishida and Mukohara [1], therefore it is not possible for us to make a comparison against the experiment. However, the axial prediction of $< \tilde{N} >$ shows that it initially grows from the inlet and reaches the peak level at the middle zone of the combustor, it then decreases towards the downstream. The trends of $< \tilde{N} >$ appear to correspond the prediction of the soot concentration (shown in Fig. 4.10(a)), and this is expected, because the high density of the soot particle number causes the high prediction of the soot concentration, and vice-versa. The radial distributions of $< \tilde{N} >$ in Figs. 4.12(b)-(d) again show the similar trends with the concentration of soot presented in Figs. 4.10(b)-(d).

To have an idea about the soot particle size distribution in the flame, the axial profile of mean soot particle diameter, $\tilde{d}_{c(s)}$, is depicted in Fig. 4.13(a) while the radial profiles are plotted at the different cross-sectional positions: (b) $y = 0.1m$, (c) $y = 0.2m$ and (d) $y = 0.3m$. In Fig. 4.13(a), the axial profile shows that the soot particle diameter initially decreases up to the axial distance $y = 0.05$ where the flame is dominated by the fuel stream. Then, it is increasing, due to the soot surface growth and coagulation process, along the centerline of the combustor and having the largest soot particle diameter around the region of highest soot concentration. The soot particle size then decreases towards the outlet region where the soot burn-out takes place. Radial profiles plotted in Fig. 4.13(b-d) show that the peak value of the soot particle diameter is found at the centre of the combustor and it decreases towards the combustor wall having its minimum value in the flame front region, where oxidation is likely to be occurred. These figures show that the average soot particle diameter lies between about 5 and $30nm$ which is significant for the propane-air combustion.

Comparing the axial profiles of all the mean soot quantities, presented in frame (a) of Figs. 4.10-4.13, between Case1 and Case2, it is observed that higher value of C_s upto an axial distance $y = 0.05m$ in Case2 leads to a slightly lower prediction in all the mean soot quantities in this region. However, towards the downstream a very similar results are found in both Case1 and Case2. The radial profiles of all the above quantities also indicate that the choice of sub-grid scale model is uninfluenced, whether it is a constant valued Smagorinsky model or a dynamic model.

4.7.3 Scatter Plots of Reaction Rates

The results presented in this section are obtained for Case1.

In Fig. 4.14 and 4.15, scatter plots of the instantaneous and mean values of the five reaction rates: (a) $\tilde{r}_i$, (b) $\tilde{r}_{ii}$, (c) $\tilde{r}_{iii}$, (d) $\tilde{r}_{iv}$ and (e) $\tilde{r}_v$ on the horizontal midplane of the combustor are presented respectively. The scatter plots of the instantaneous values of the five reaction rates, $\tilde{r}_s$, on the cross-sectional plane of the combustor at $y = 0.1$ and $y = 0.3$ are shown in Figs. 4.16 and 4.18 respectively. The corresponding time averaged values are plotted respectively in Figs. 4.17 and 4.19.

Scatter plots of both the instantaneous (Fig. 4.14) and mean (Fig. 4.15) values of the reaction rates, $\tilde{r}_s$, on the horizontal midplane show that the values scattered more for smaller values of the mixture fraction for which the mixture fraction variance was found relatively high (see frame (a) of Figs. 3.15 and 3.16 in Chapter 3). This can be justified from Fig. 4.3 where the peak value of the reaction rates decreased in magnitude and also shifted to larger values of the mixture fraction as the mixture fraction variance increases. Similar trend is also found in the scatter plots of these reaction rates, $\tilde{r}_s$, on the different cross-sectional planes, presented in Figs. 4.16-4.19. Moreover, the difference in magnitude of the reaction rates at the peak region between the instant and mean results is casued by the slightly different values of the mixture fraction variance obtained at this region, for example, see in Figs. 3.17(a) and 3.18(a). Also the mean results of the reaction rates show more scattered because of the same reason.

Instantaneous scatter plots of (a) the soot concentration, $\tilde{W}_{c(s)}$, and (b) the soot particle number density, $\tilde{N}$, versus the mixture fraction, $\tilde{\xi}$, and the temperature, $\tilde{T}(K)$, are shown in Fig. 4.20 and Fig. 4.21 respectively. Scatter plots of the soot concentration, $\tilde{W}_{c(s)}$, versus the mixture fraction, $\tilde{\xi}$, show that the soot concentration is maximum for mixture fraction at about 0.1 due to the higher reaction rates found in that region (see Fig. 4.14). The peak soot concentration in the scatter plots of soot concentration versus temperature is found at the temperature around $1750K$ which is the average maximum temperature of the flame (see Fig. 3.8 of Chapter 3). These plots also show that the particle number density is high in the region where the soot concentration is maximum which is expected.

4.7.4 Resolved and Sub-grid Scale Fluxes

The mean values of the soot mass fraction fluxes (a) $< u'Y'_{c(s)} >$, (b) $< v'Y'_{c(s)} >$ and (c) $< w'Y'_{c(s)} >$; and the soot particle number density fluxes (a) $< u'N' >$, (b) $< v'N' >$ and (c) $< w'N' >$, are depicted respectively in Figs. 4.22 and 4.24 along the centerline direction, while along the radial direction these results are plotted respectively in Figs. 4.23 and 4.25 at the different cross-sectional positions of $y = 0.1m$ (left column), $y = 0.2m$ (middle column) and $y = 0.3m$ (right column).

Fig. 4.22 shows that the levels of the centreline soot mass fraction fluxes are high at the downstream region which is found due to the higher level of soot mass fraction predicted in this region. Similarly, the centreline soot particle number density fluxes plotted in Fig. 4.24 are predicted relatively high in the middle zone of the combustor where the soot particle number density were also predicted high. From these results it can also be noted that the soot mass fraction fluxes are dominated by the production of high level of the soot mass fraction and its number density, hence their fluctuations, rather than the turbulence intensity. The radial profiles (Figs. 4.23 and 4.25) show that both the soot mass fraction fluxes and soot particle number density fluxes are high around the centreline and disappear at the combustor wall region. Comparing the predicted fluxes between Case1 and Case2, some variations can be found, but they are very small in magnitude.

In Figs. 4.26 and 4.28, respectively the mean values of the sub-grid scale soot mass fraction fluxes (a) $< \tau_{uY_{c(s)}} >$, (b) $< \tau_{vY_{c(s)}} >$ and (c) $< \tau_{wY_{c(s)}} >$; and soot particle number density fluxes (a) $< \tau_{uN} >$, (b) $< \tau_{vN} >$ and (c) $< \tau_{wN} >$, are presented along the centerline, while these results are shown along the radial direction in Figs. 4.27 and 4.29 respectively at the different cross-sectional positions of $y = 0.1m$ (left column), $y = 0.2m$ (middle column) and $y = 0.3m$ (right column).

In both Figs. 4.26 and 4.28, it can be seen that in the upstream region where the turbulent intensity was found high (see Fig. 3.25 of Chapter 3), the sub-grid scale contributions to the soot mass fraction as well as the soot particle number density fluxes are predicted to be maximum. This prediction is unlike the resolved scale fluxes which were dominated by the higher level of soot production. These sub-grid scale contributions are negligible and almost vanish beyond the region $y = 0.15m$ of the combustor. On the centreline, the sub-grid scale soot mass fraction fluxes,

$< \tau_{uY_{c(s)}} >$ and $< \tau_{wY_{c(s)}} >$, and soot particle number density fluxes, $< \tau_{uN} >$ and $< \tau_{wN} >$, have similar magnitudes that differ in the radial direction. As is to be expected, the levels of the sub-grid scale fluxes are very much lower than those of the resolved scale fluxes. Comparison between the sub-grid scale fluxes in Case1 and Case2 shows that Case2 produces higher levels of these fluxes in the upstream region where the value of C_s in Case2 (Fig 3.5) was found higher than 0.1 used in Case1. Towards the downstream both the predictions agree very well.

4.8 Conclusion

Large Eddy Simulation technique has been applied to investigate the soot formation and growth during the non-premixed propane/air turbulent combustion process within a cylindrical combustor. In LES a constant valued Smagorinsky model as well as a dynamic model is taken into account for modelling the sub-grid scale stresses. The non-premixed combustion process is modelled through the conserved scalar approach with laminar flamelet model, while the soot formation is included through the balance equations for soot mass fraction and soot particle number density. A simplified reaction model for soot formation and growth has been applied which includes soot particle inception, surface growth, particle coagulation and particle oxidation.

The computational results of soot concentration have been compared with the experimental data obtained by Nishida and Mukohara [1] in the turbulent co-flowing propane and preheated air combustion, where a good agreement is achieved. Comparing the predicted results with experimental measurements, it can be noted that the LES together with the present soot model is capable enough to predict soot formation in the turbulent co-flowing propane-air flame. However, the present results suggest that the prediction of soot levels could be improved if the accuracy in the prediction of O_2, C_2H_2 and temperature levels were increased.

It can be found that the resolved scale fluxes are dominated by the production of high level of soot mass fraction and its number density, while the sgs scale fluxes are dominated by the turbulence intensity.

The predicted results are almost unaffected by the choice of the sub-grid scale modelling, whether it is a constant valued Smagorinsky model or a dynamic model.

However, in the upstream region, higher value of dynamic C_s than the constant C_s leads to a higher prediction in sub-grid scale quantities.

Table 4.1: Rate constants, as $AT^b e^{-E/RT}$, for soot formation model (units used are kg, m, s, kmol and K).

Rate Constant	A	b	E/R
k_i	1.00×10^4	0.0	21100
k_{ii}	1.20×10^4	0.0	12100
k_{iii}	7.15×10^2	0.5	19680

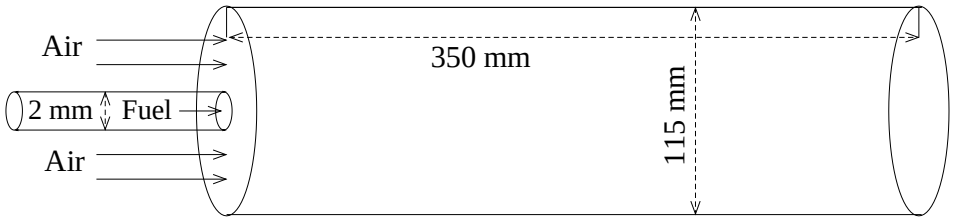

Figure 4.1: A schematic of the cylindrical combustor with short computational domain.

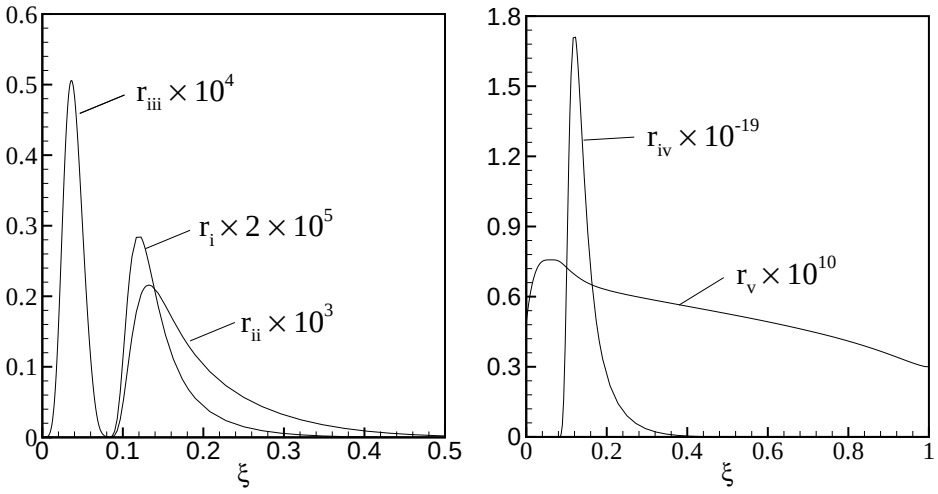

Figure 4.2: Dependence of the instantaneous rate terms, r_s, on the mixture fraction, ξ.

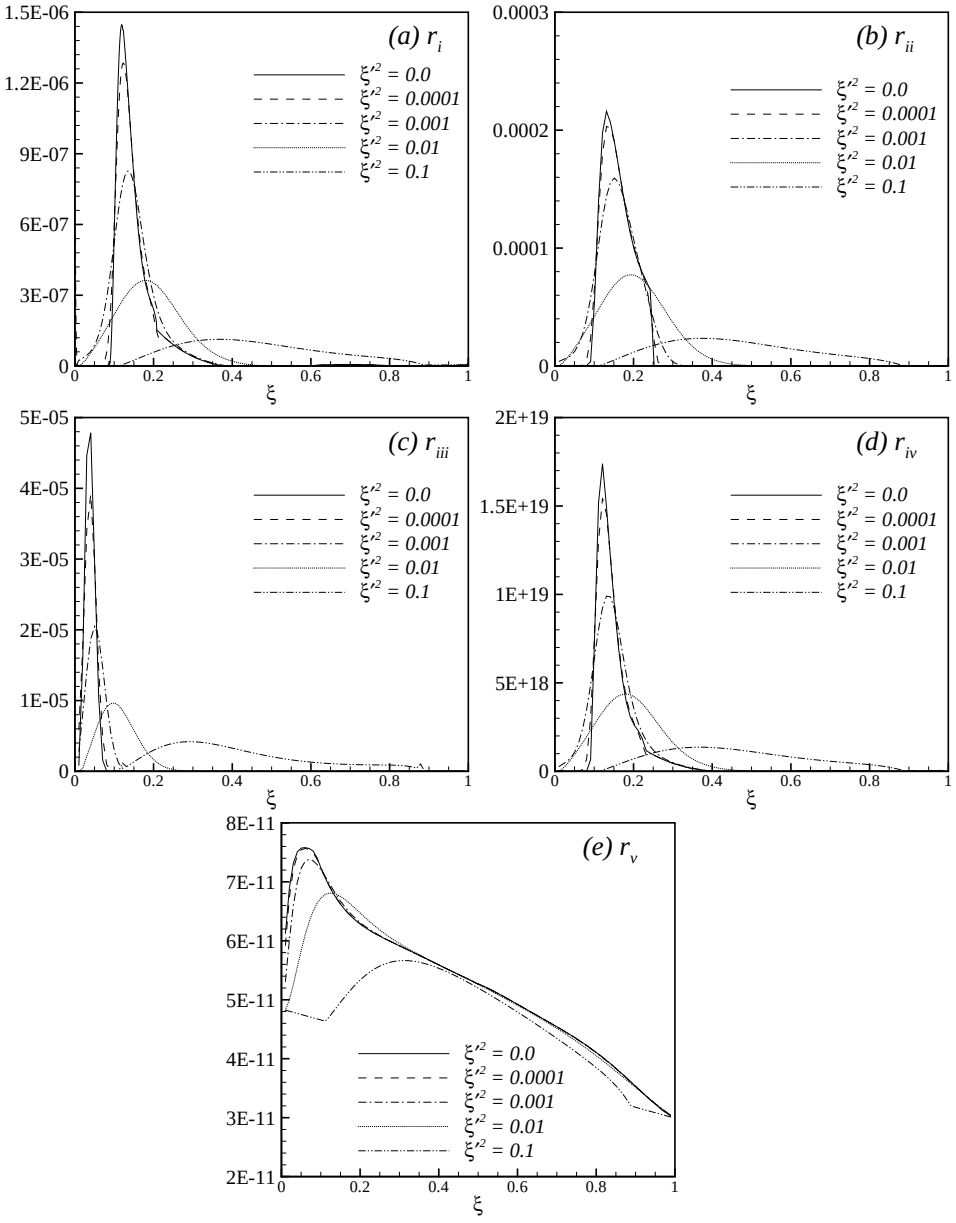

Figure 4.3: Dependence of the instantaneous rate terms, r_s, on the mixture fraction, ξ, and the mixture fraction variance, ξ'^2.

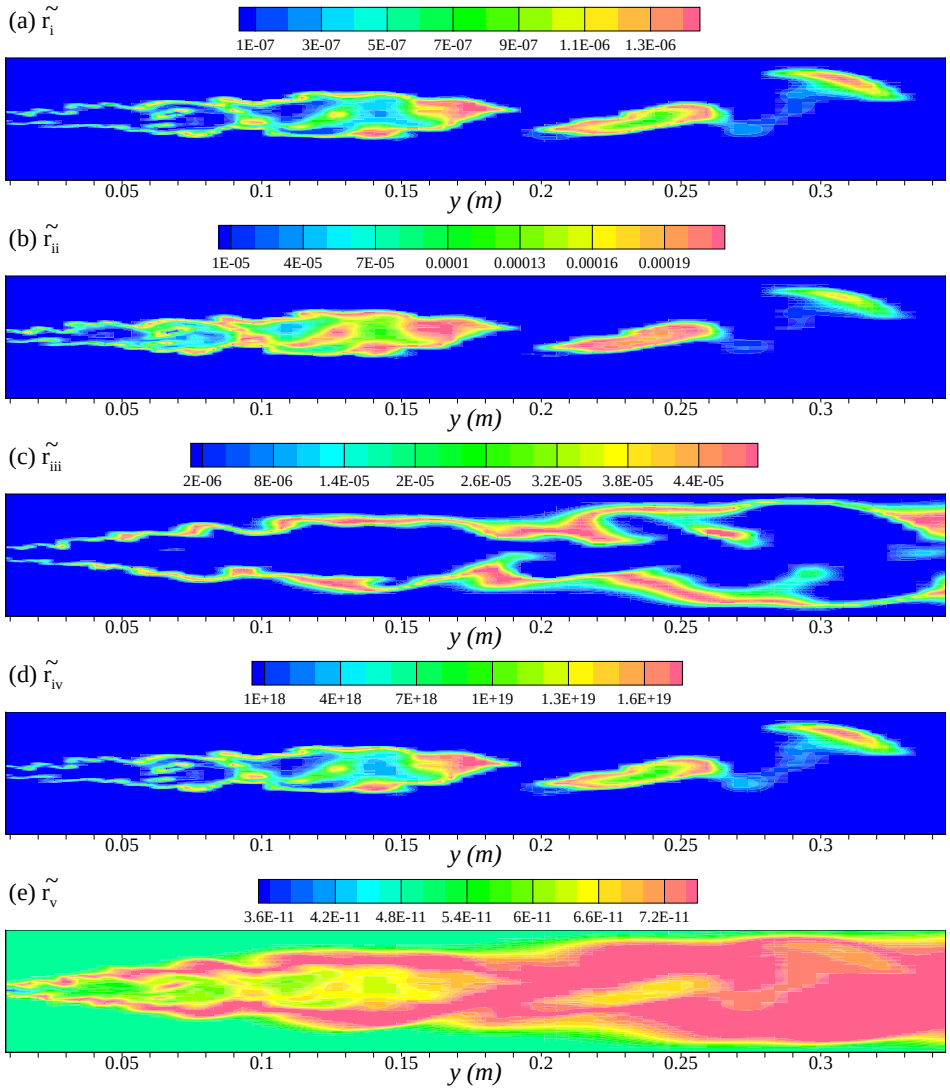

Figure 4.4: Instantaneous values of the reaction rates: (a) $\tilde{r}_i$, (b) $\tilde{r}_{ii}$, (c) $\tilde{r}_{iii}$, (d) $\tilde{r}_{iv}$ and (e) $\tilde{r}_v$ on the horizontal mid-plane of the combustor for Case1.

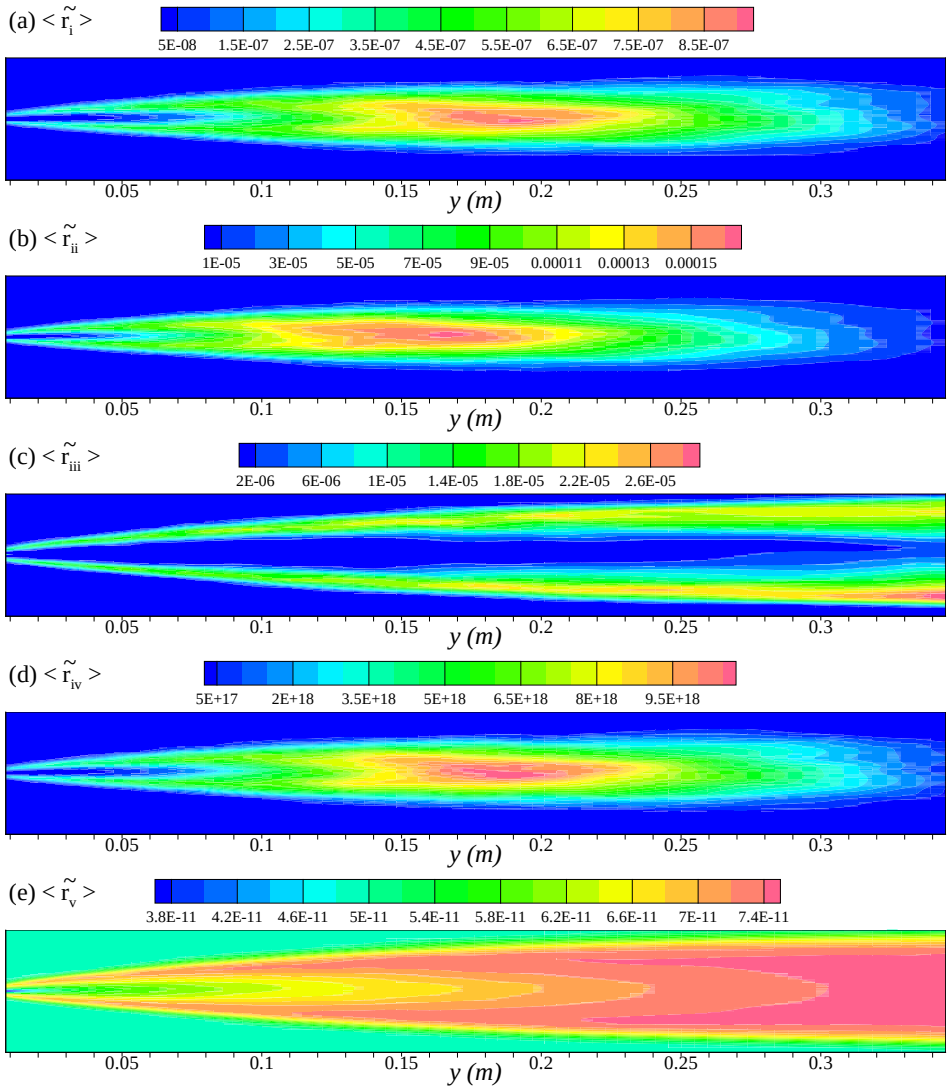

Figure 4.5: Mean reaction rates: (a) $< \tilde{r}_i >$, (b) $< \tilde{r}_{ii} >$, (c) $< \tilde{r}_{iii} >$, (d) $< \tilde{r}_{iv} >$ and (e) $< \tilde{r}_v >$ on the horizontal mid-plane of the combustor for Case1.

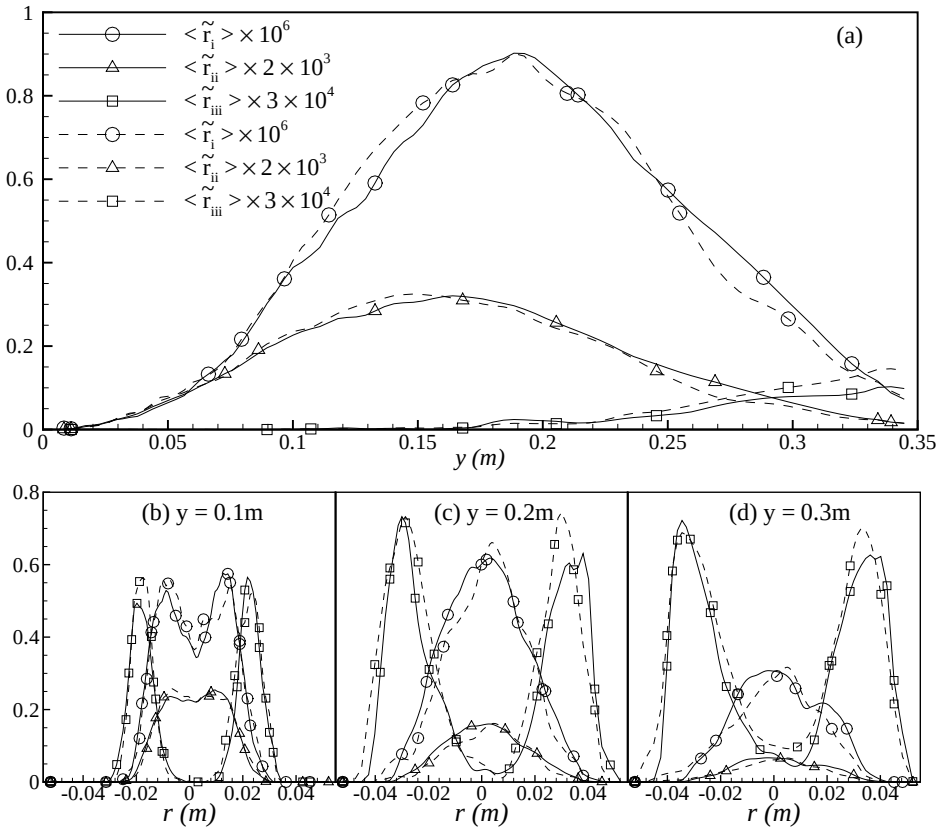

Figure 4.6: Mean values of the reaction rates for soot formation and oxidation along (a) axial direction, and the radial direction at the different cross-sectional positions: (b) $y = 0.1m$, (c) $y = 0.2m$ and (d) $y = 0.3m$.

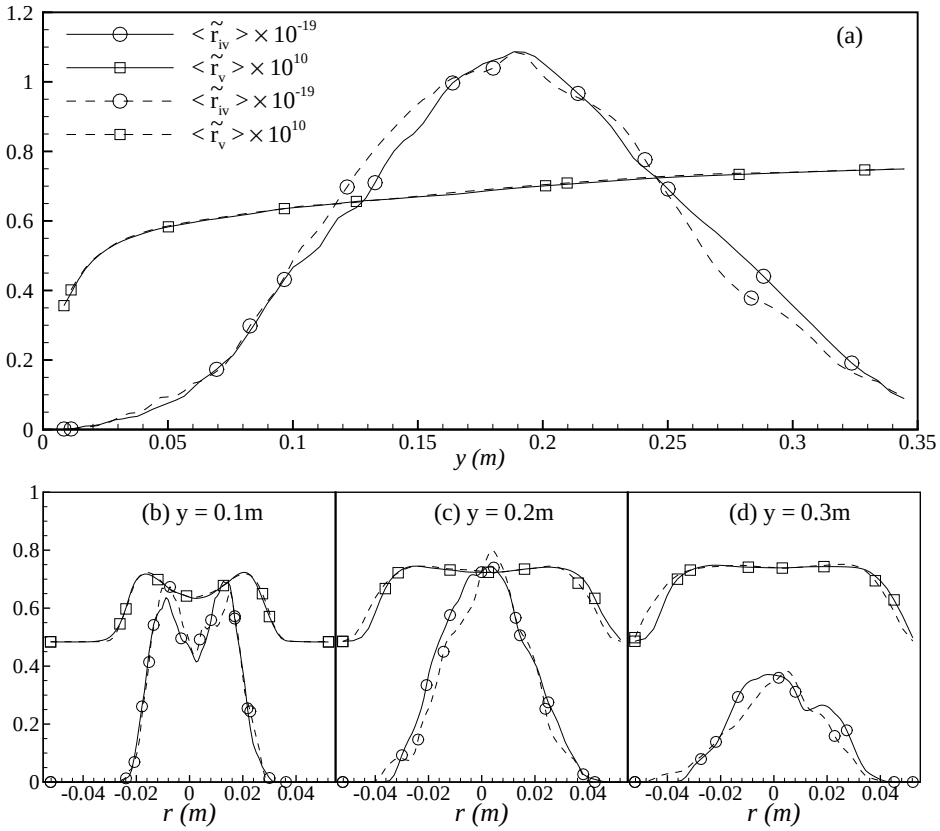

Figure 4.7: Mean values of reaction rates for soot particle number density along (a) the axial direction, and the radial direction at the different cross-sectional positions: (b) $y = 0.1m$, (c) $y = 0.2m$ and (d) $y = 0.3m$.

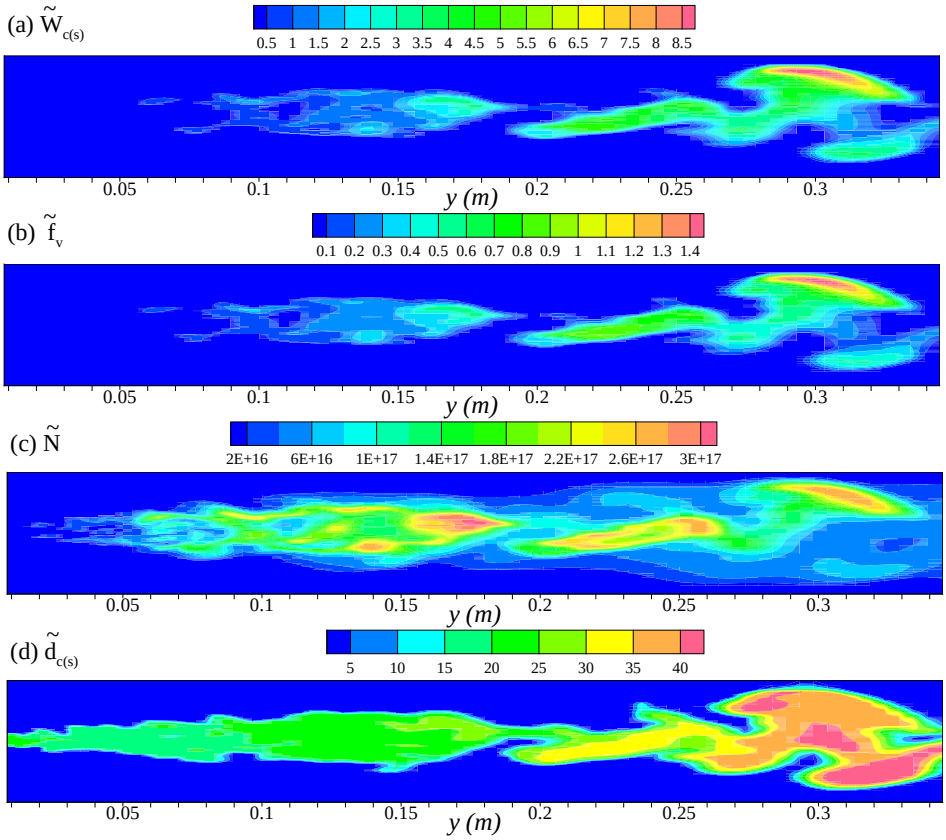

Figure 4.8: Instantaneous values of the (a) soot concentration, $\tilde{W}_{c(s)}$, (b) soot volume fraction, $\tilde{f}_v$, (c) soot particle number density, $\tilde{N}$, and (d) soot particle diameter, $\tilde{d}_{c(s)}$, on the horizontal mid-plane of the combustor for Case1.

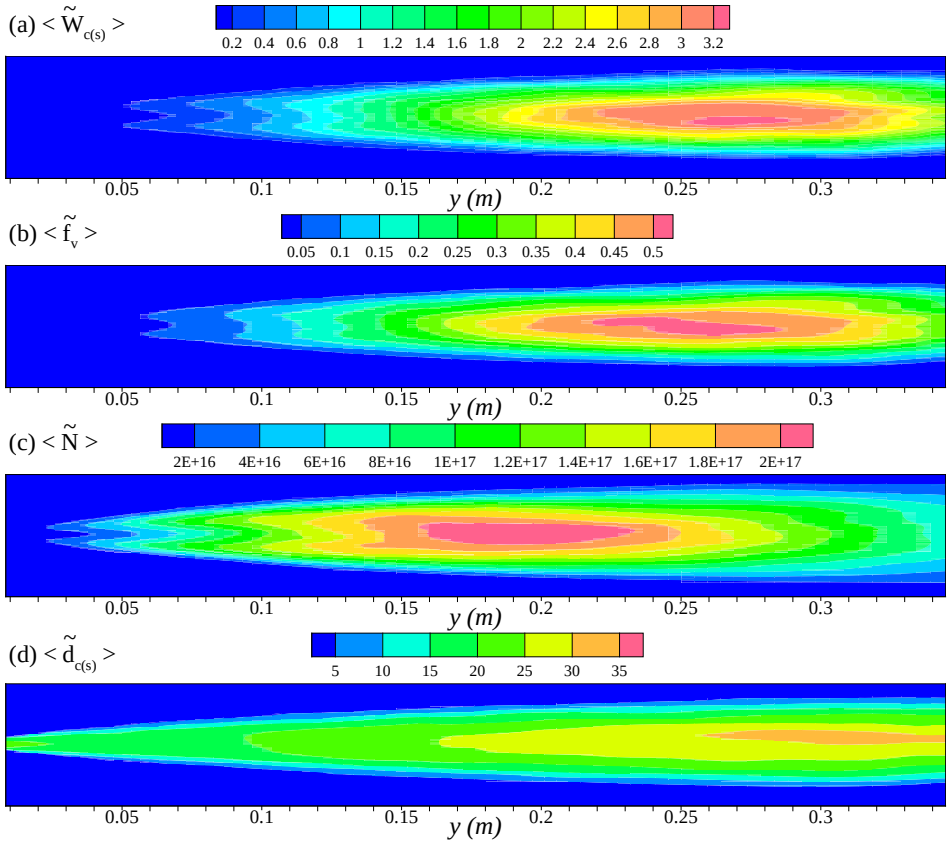

Figure 4.9: Mean values of the (a) soot concentration, $< \tilde{W}_{c(s)} >$, (b) soot volume fraction, $< \tilde{f}_v >$, (c) soot particle number density, $< \tilde{N} >$, and (d) soot particle diameter, $< \tilde{d}_{c(s)} >$, on the horizontal mid-plane of the combustor for Case1.

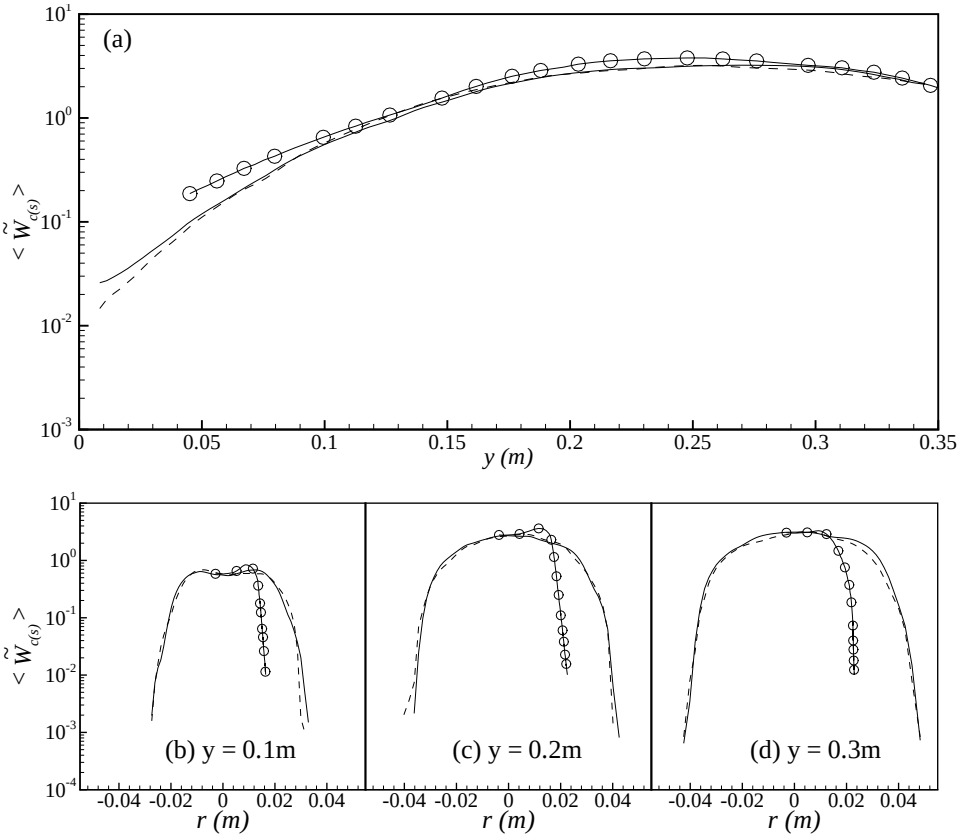

Figure 4.10: Mean soot concentration, $< \tilde{W}_{c(s)} > (g/Nm^3)$, with the experimental data along the (a) axial direction, and radial direction at the different cross-sectional positions: (b) $y = 0.1m$, (c) $y = 0.2m$ and (d) $y = 0.3m$.

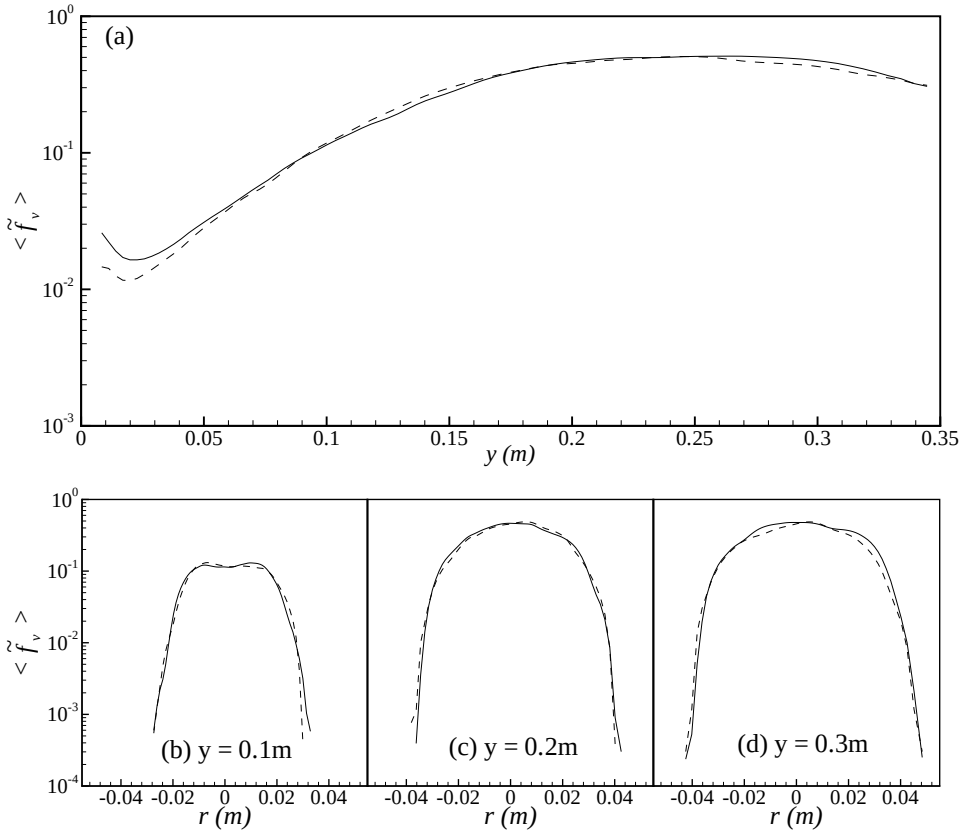

Figure 4.11: Mean soot volume fraction, $< \tilde{f}_v >$ (ppm), along the (a) axial direction, and radial direction at the different cross-sectional positions: (b) $y = 0.1m$, (c) $y = 0.2m$ and (d) $y = 0.3m$.

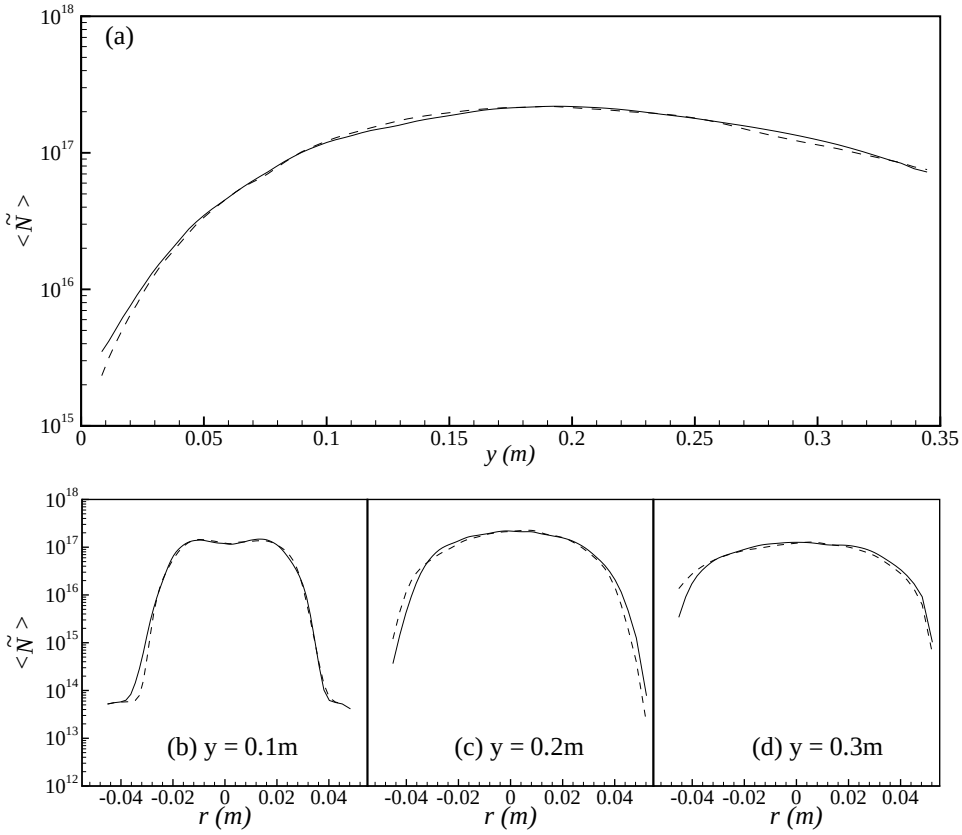

Figure 4.12: Mean soot particle number density, $< \tilde{N} >$ ($particles/m^3$), along the (a) axial direction, and radial direction at the different cross-sectional positions: (b) $y = 0.1m$, (c) $y = 0.2m$ and (d) $y = 0.3m$.

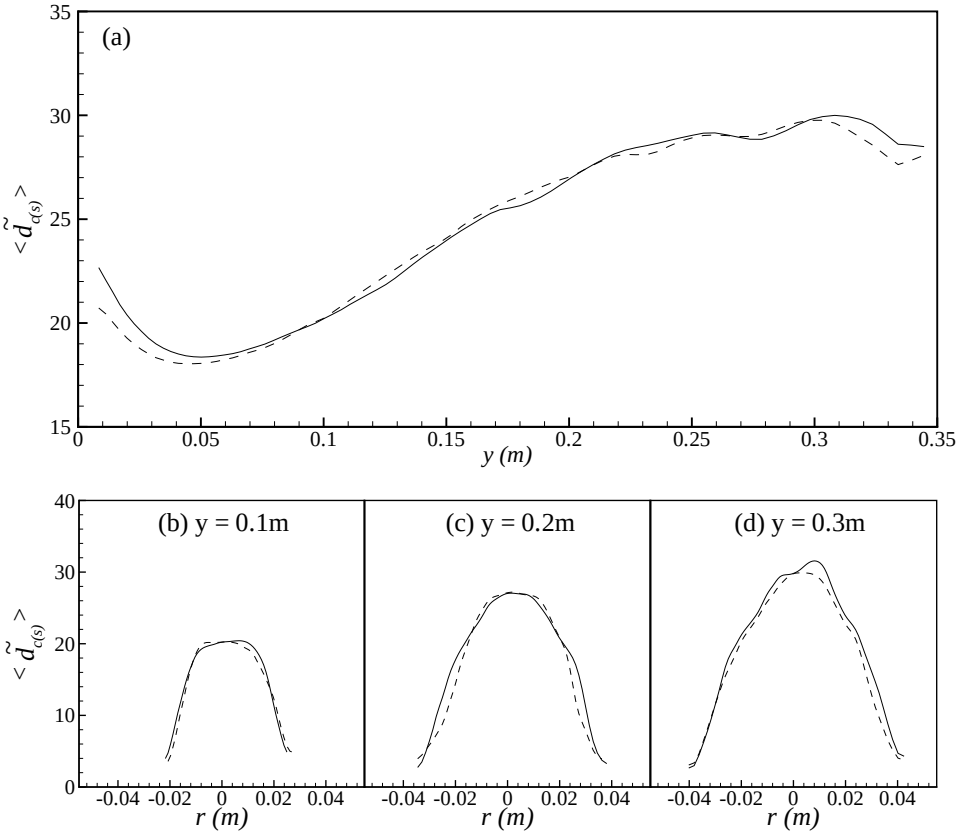

Figure 4.13: Mean soot particles diameter, $< \tilde{d}_{c(s)} >$ (nm) along the (a) axial direction, and radial direction at the different cross-sectional positions: (b) $y = 0.1m$, (c) $y = 0.2m$ and (d) $y = 0.3m$.

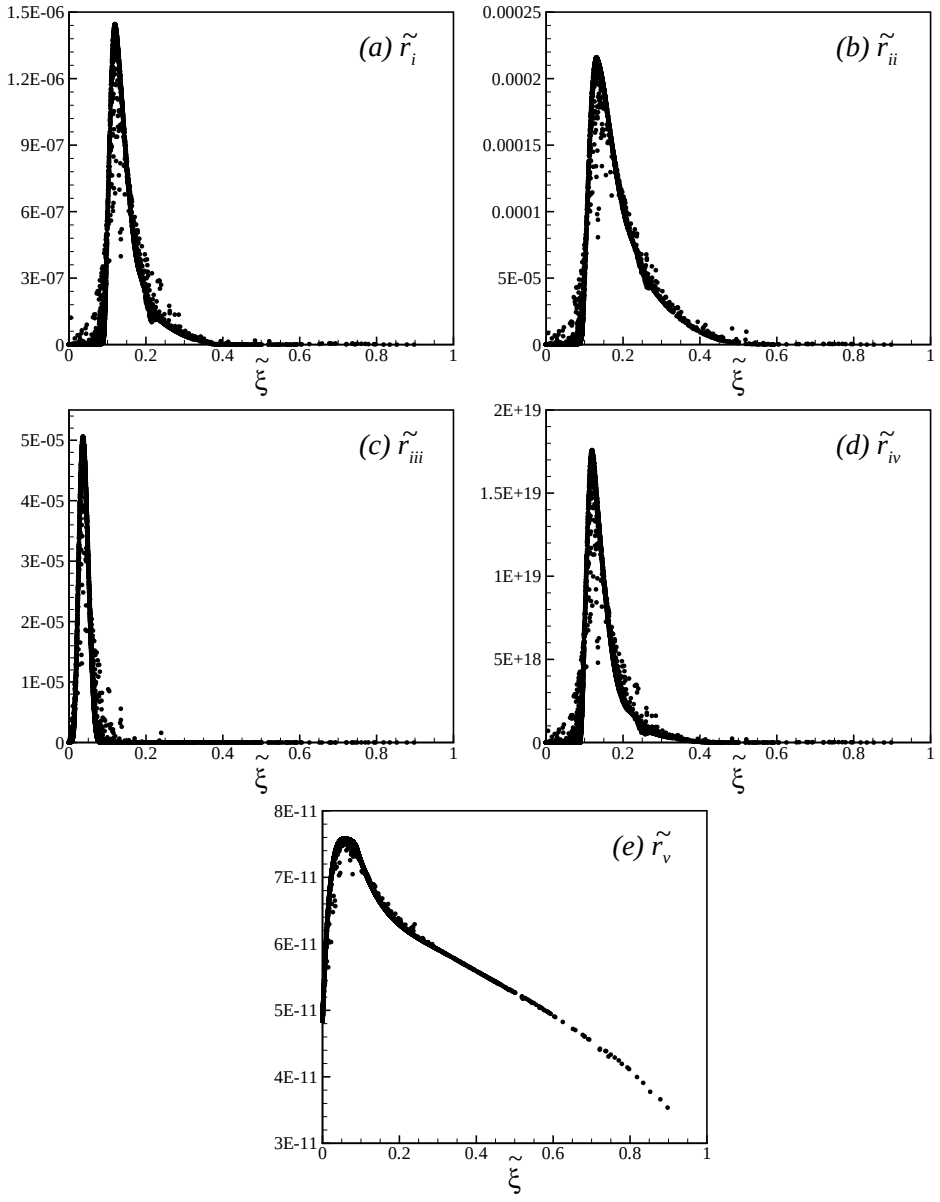

Figure 4.14: Scatter plots of the instantaneous values of the reaction rates: (a) $\tilde{r}_i$, (b) $\tilde{r}_{ii}$, (c) $\tilde{r}_{iii}$, (d) $\tilde{r}_{iv}$ and (e) $\tilde{r}_v$ on the horizontal midplane of the combustor for Case1.

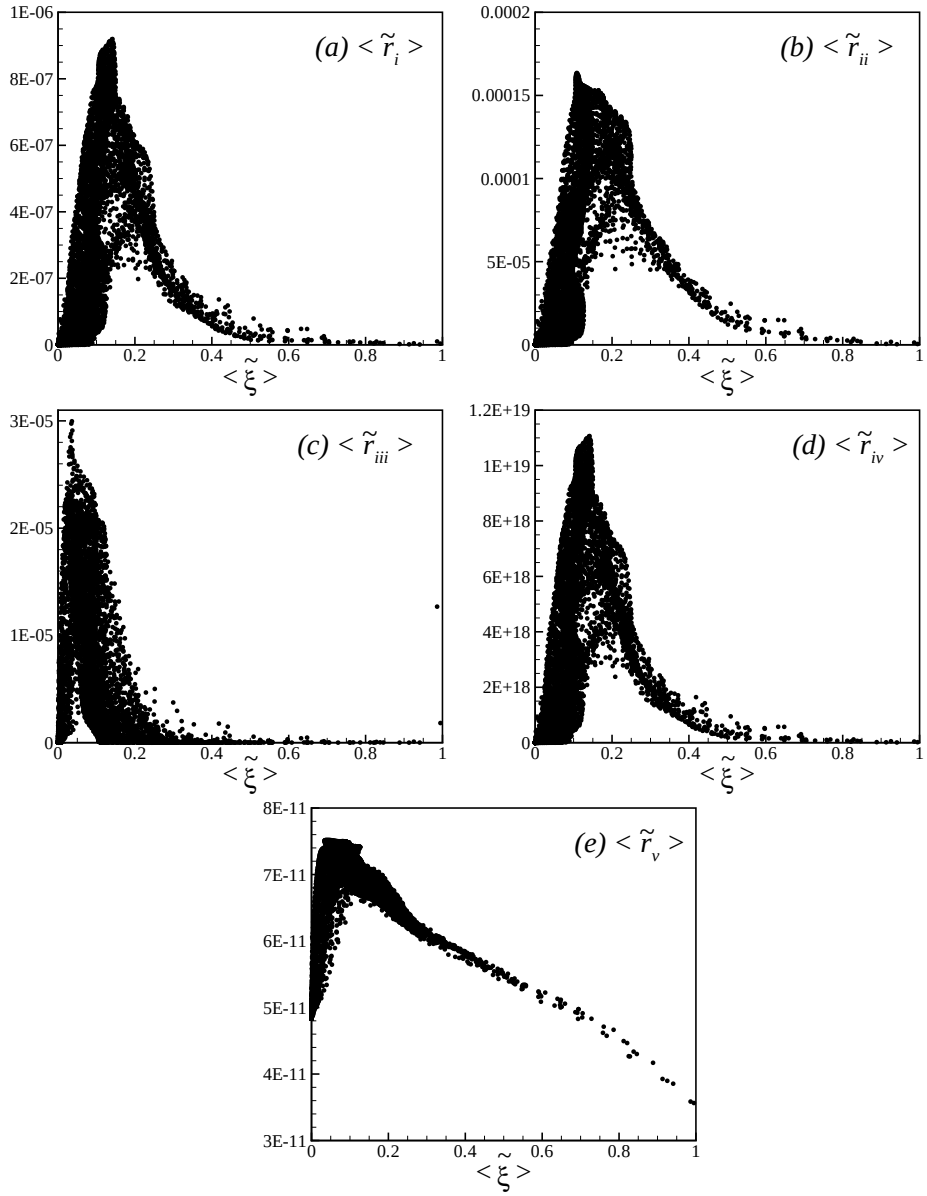

Figure 4.15: Scatter plots of the mean reaction rates: (a) $< \tilde{r}_i >$, (b) $< \tilde{r}_{ii} >$, (c) $< \tilde{r}_{iii} >$, (d) $< \tilde{r}_{iv} >$ and (e) $< \tilde{r}_v >$ on the horizontal midplane of the combustor for Case1.

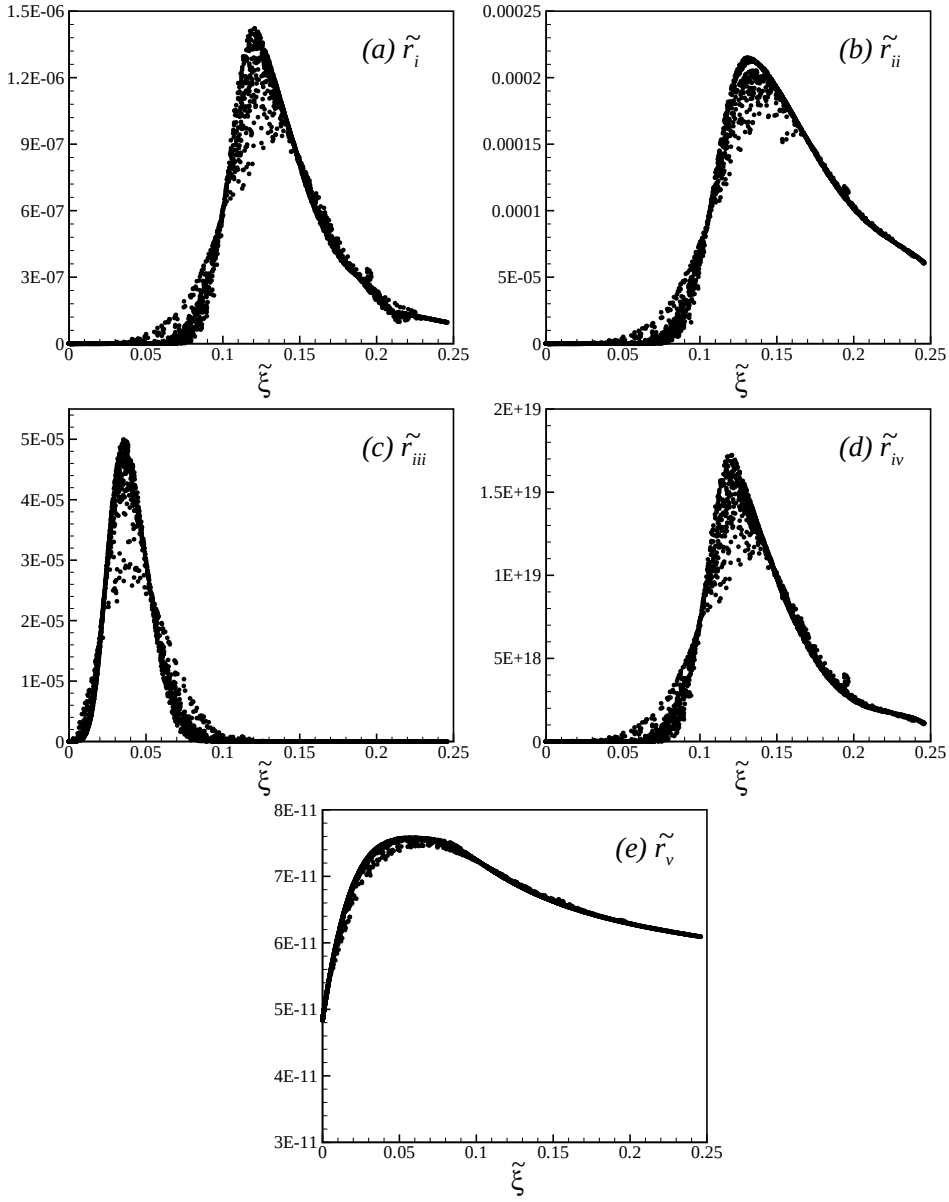

Figure 4.16: Scatter plots of the instantaneous values of the reaction rates: (a) $\tilde{r}_i$, (b) $\tilde{r}_{ii}$, (c) $\tilde{r}_{iii}$, (d) $\tilde{r}_{iv}$ and (e) $\tilde{r}_v$ on the cross-sectional position at $y = 0.1m$ for Case1.

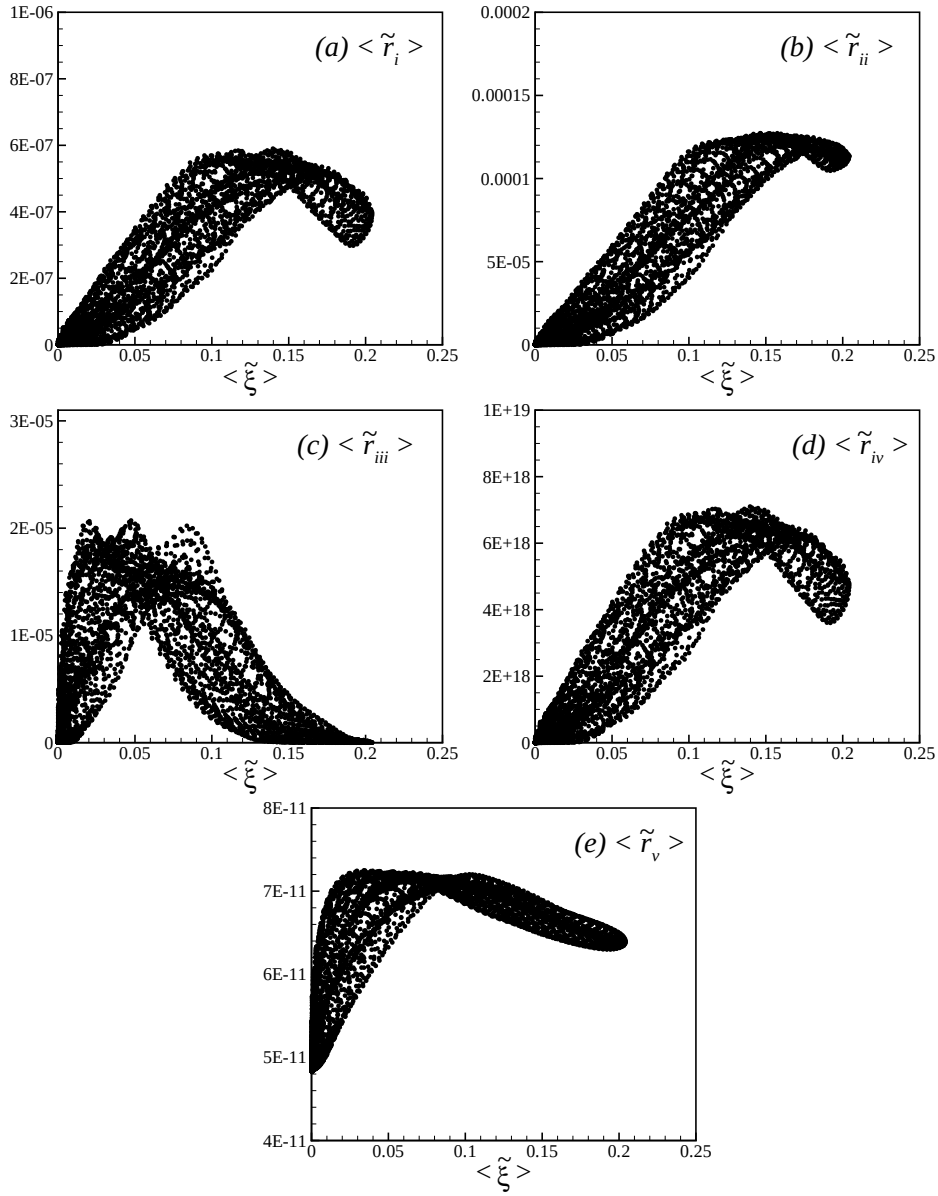

Figure 4.17: Scatter plots of the mean reaction rates: (a) $< \tilde{r}_i >$, (b) $< \tilde{r}_{ii} >$, (c) $< \tilde{r}_{iii} >$, (d) $< \tilde{r}_{iv} >$ and (e) $< \tilde{r}_v >$ on the cross-sectional position at $y = 0.1m$ for Case1.

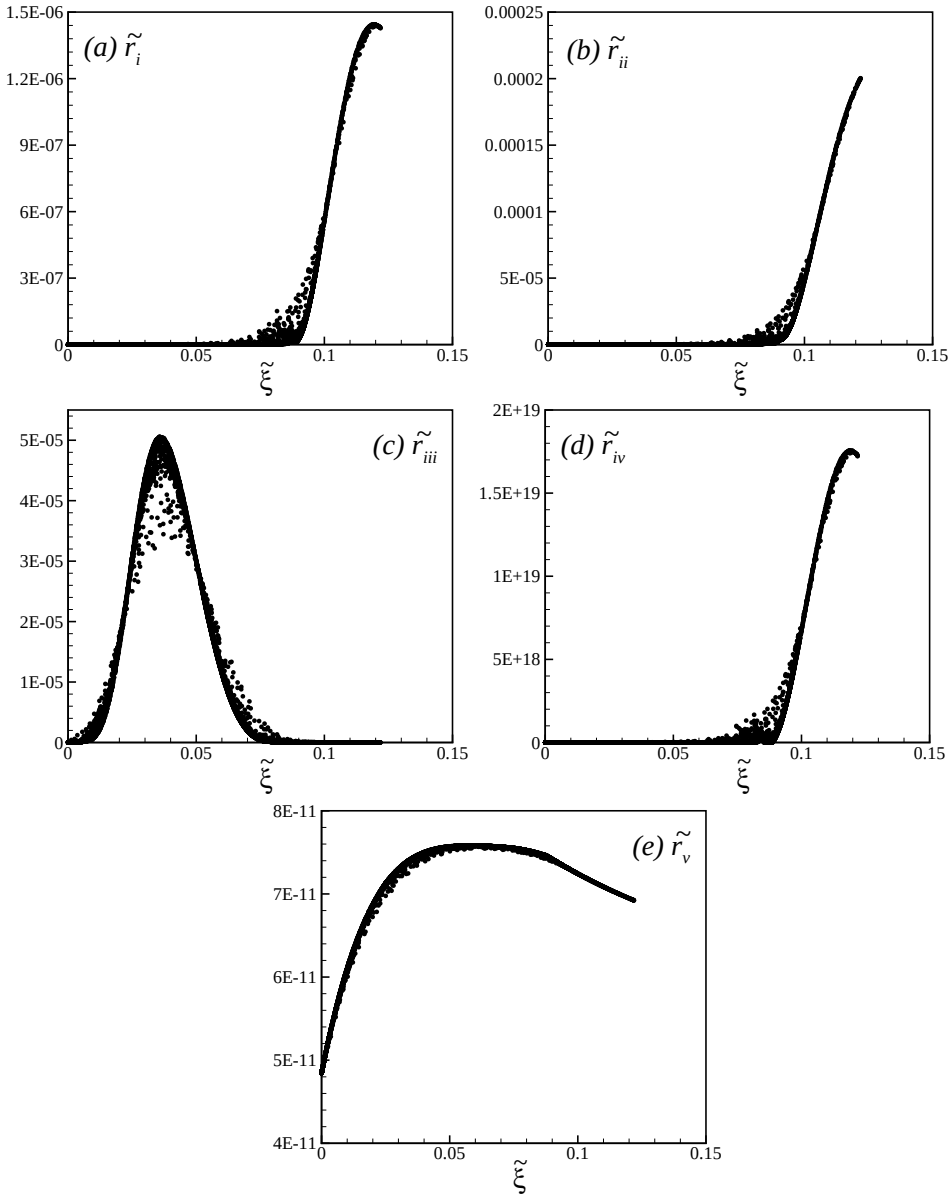

Figure 4.18: Scatter plots of the instantaneous values of the reaction rates: (a) $\tilde{r}_i$, (b) $\tilde{r}_{ii}$, (c) $\tilde{r}_{iii}$, (d) $\tilde{r}_{iv}$ and (e) $\tilde{r}_v$ on the cross-sectional position at $y = 0.3m$ for Case1.

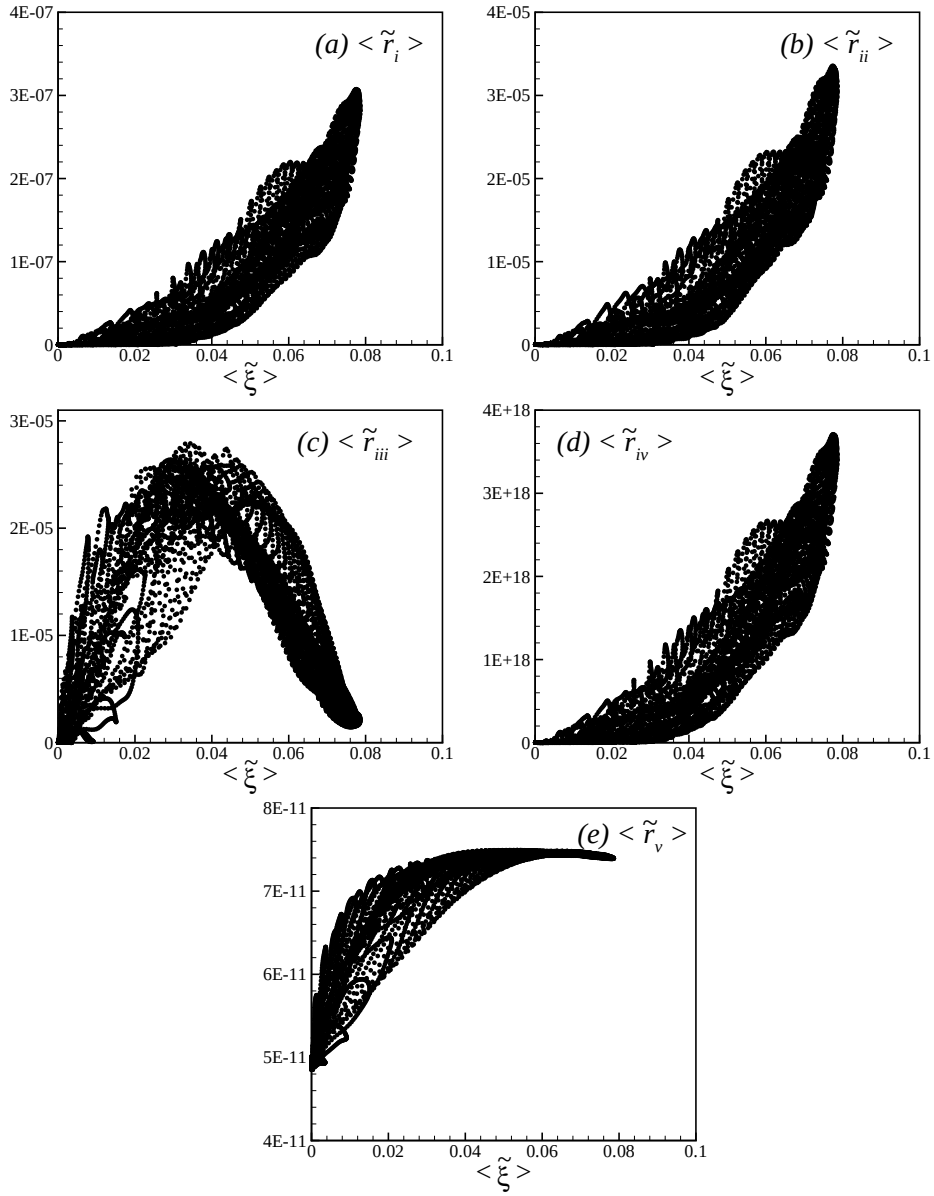

Figure 4.19: Scatter plots of mean reaction rates: (a) $< \tilde{r}_i >$, (b) $< \tilde{r}_{ii} >$, (c) $< \tilde{r}_{iii} >$, (d) $< \tilde{r}_{iv} >$ and (e) $< \tilde{r}_v >$ on the cross-sectional position at $y = 0.3m$ for Case1.

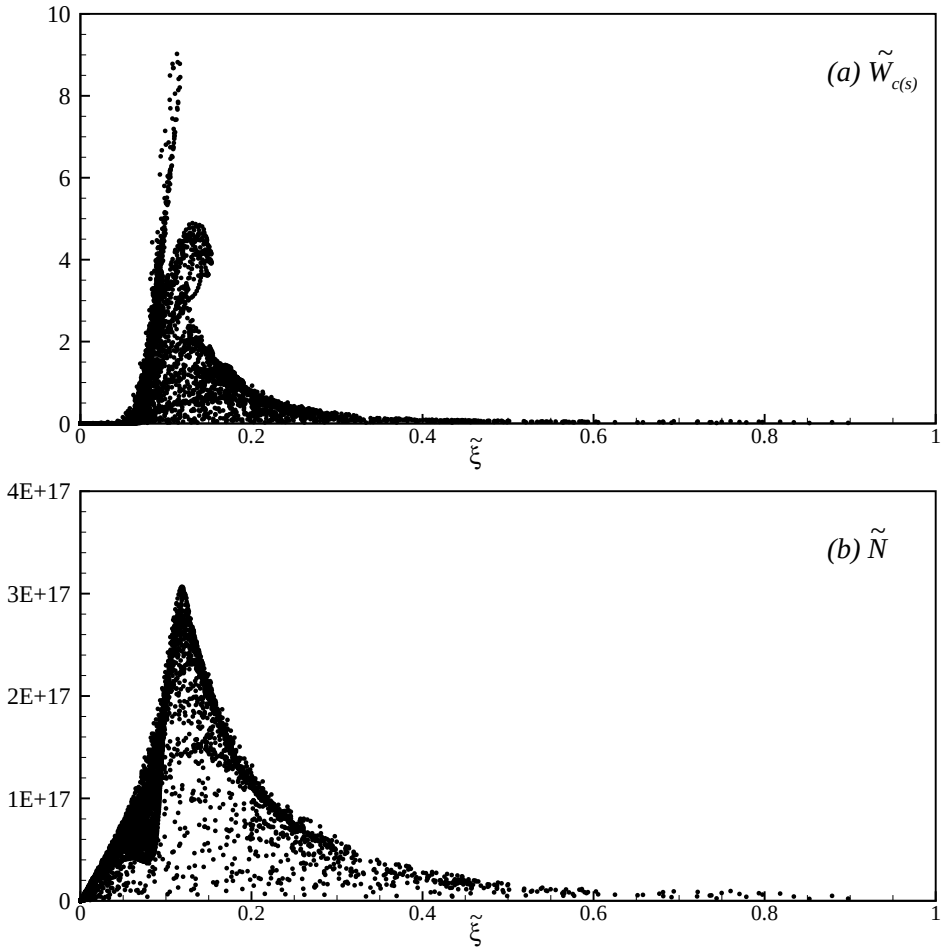

Figure 4.20: Scatter plots of the instantaneous values of (a) the soot concentration, $\tilde{W}_{c(S)}$, and (b) the soot particle number density, $\tilde{N}$, against the mixture fraction, $\tilde{\xi}$, on the horizontal midplane of the combustor for Case1.

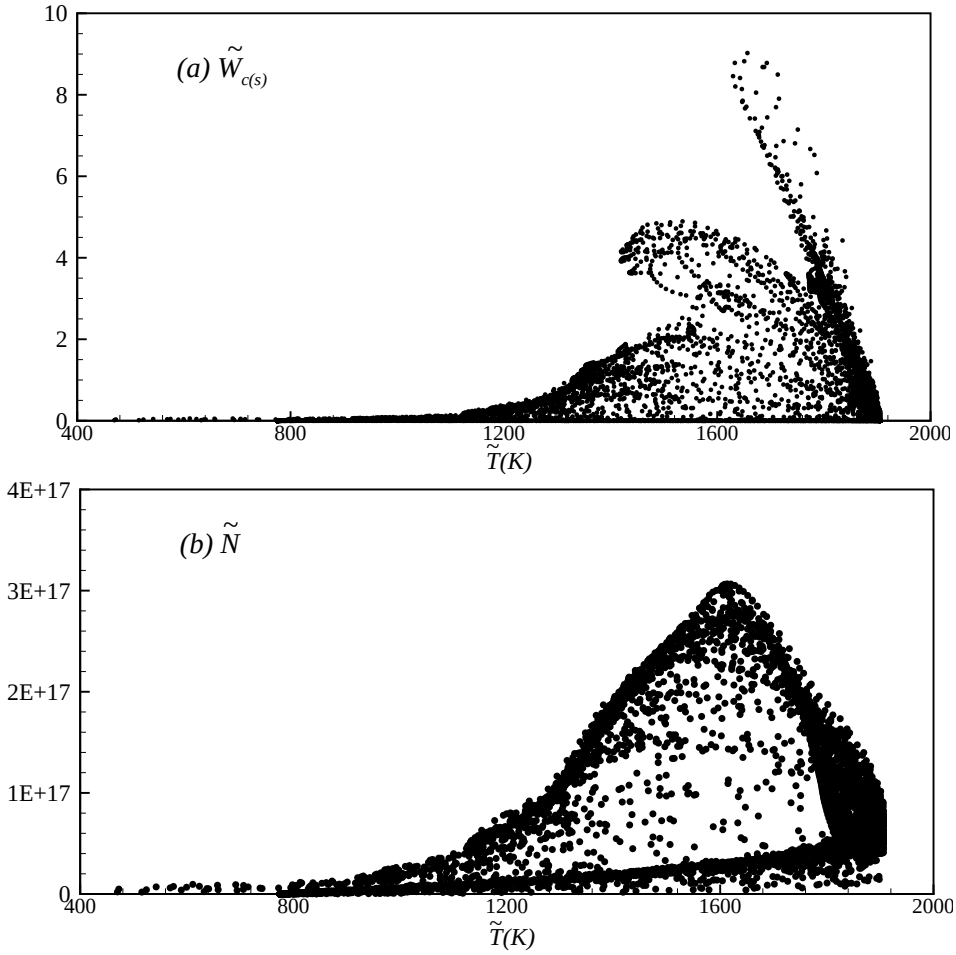

Figure 4.21: Scatter plots of the instantaneous values of (a) the soot concentration, $\tilde{W}_{c(S)}$, and (b) the soot particle number density, $\tilde{N}$, against the temperature, $\tilde{T}(K)$, on the horizontal midplane of the combustor for Case1.

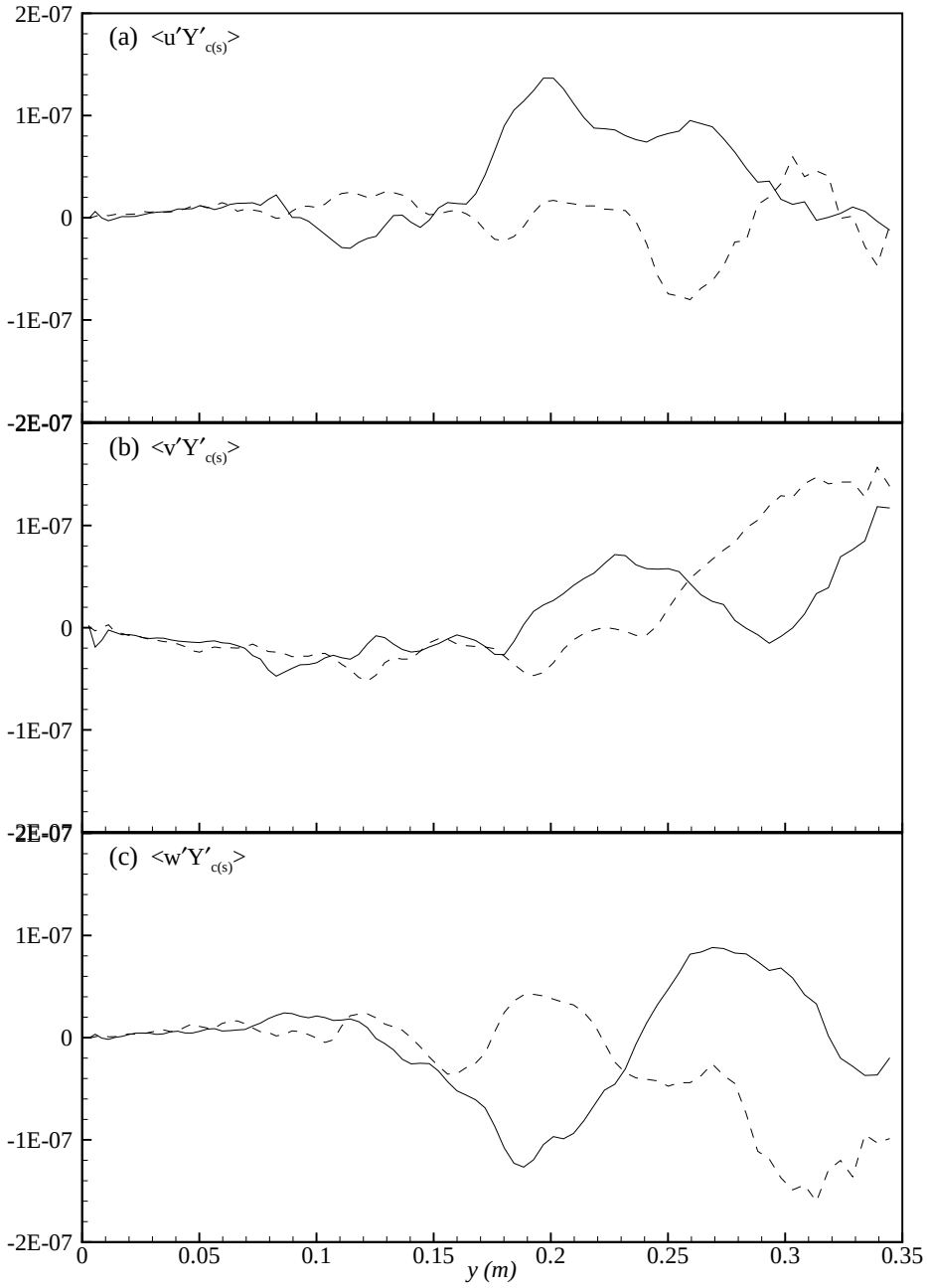

Figure 4.22: Profiles of the mean soot mass fraction fluxes, (a) $< u'Y'_{c(s)} >$, (b) $< v'Y'_{c(s)} >$ and (c) $< w'Y'_{c(s)} >$, along the axial direction.

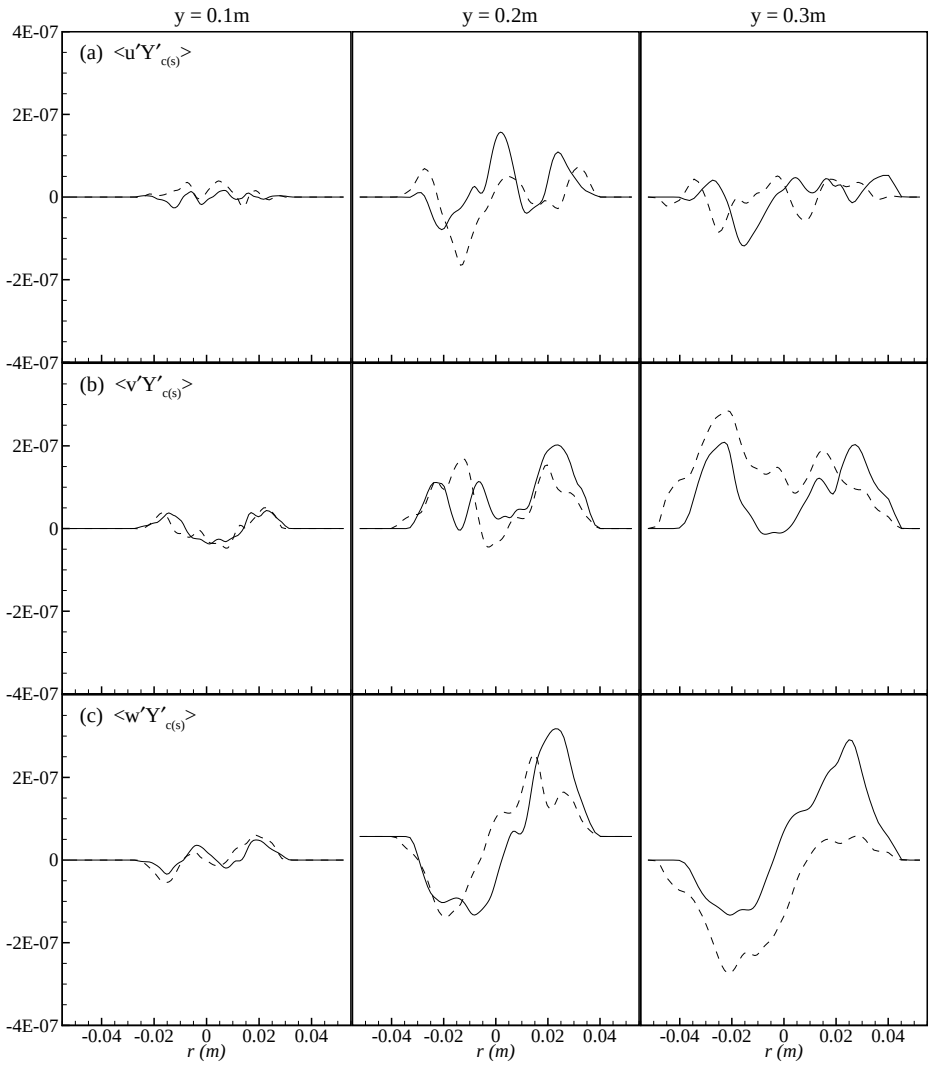

Figure 4.23: Profiles of the mean soot mass fraction fluxes, (a) $< u'Y'_{c(s)} >$, (b) $< v'Y'_{c(s)} >$ and (c) $< w'Y'_{c(s)} >$, along the radial direction at the different cross-sectional positions: $y = 0.1m$ (left column), $y = 0.2m$ (middle column), and $y = 0.3m$ (right column).

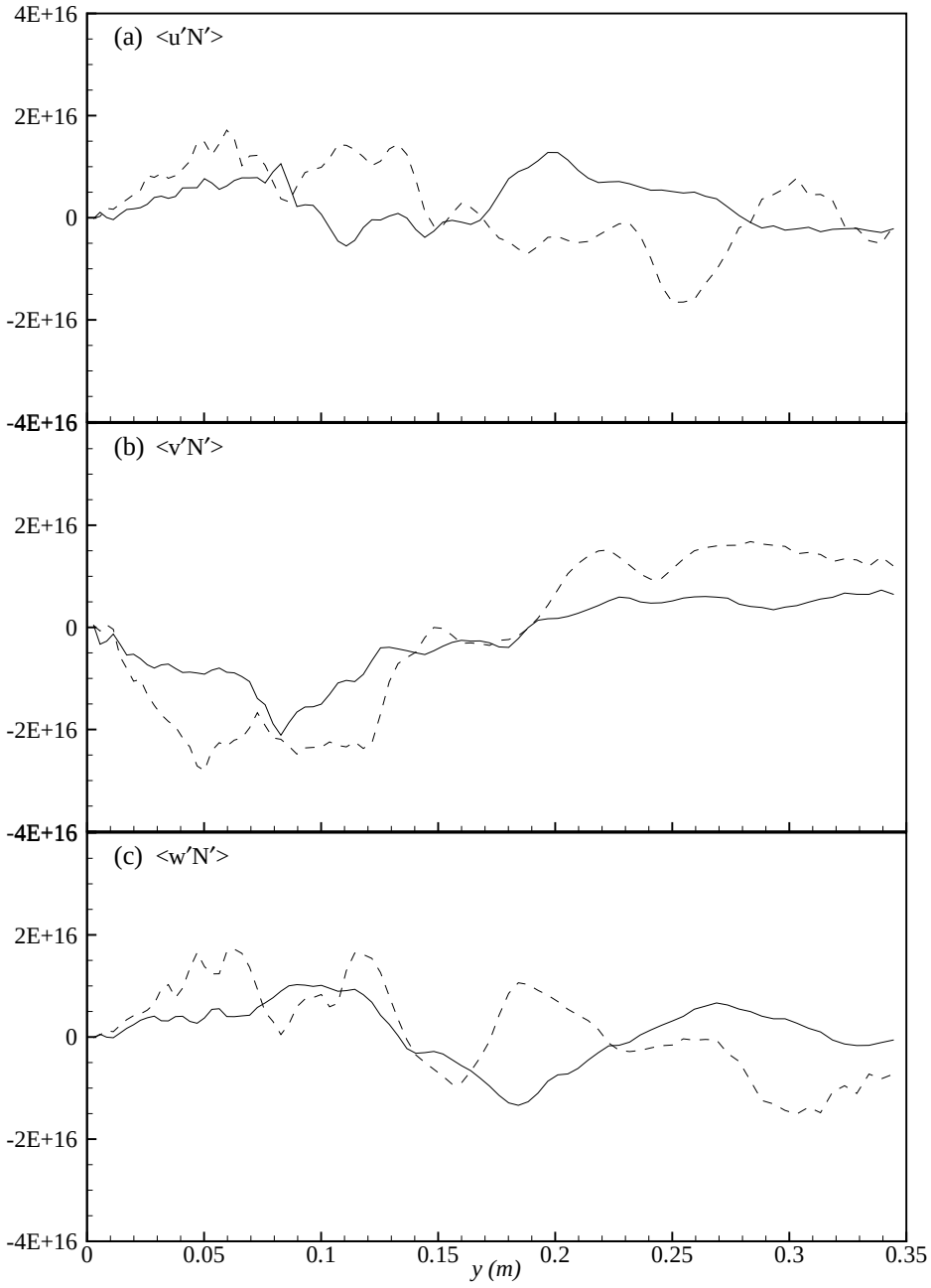

Figure 4.24: Profiles of the mean soot particle number density fluxes, (a) $< u'N' >$, (b) $< v'N' >$ and (c) $< w'N' >$, along the axial direction.

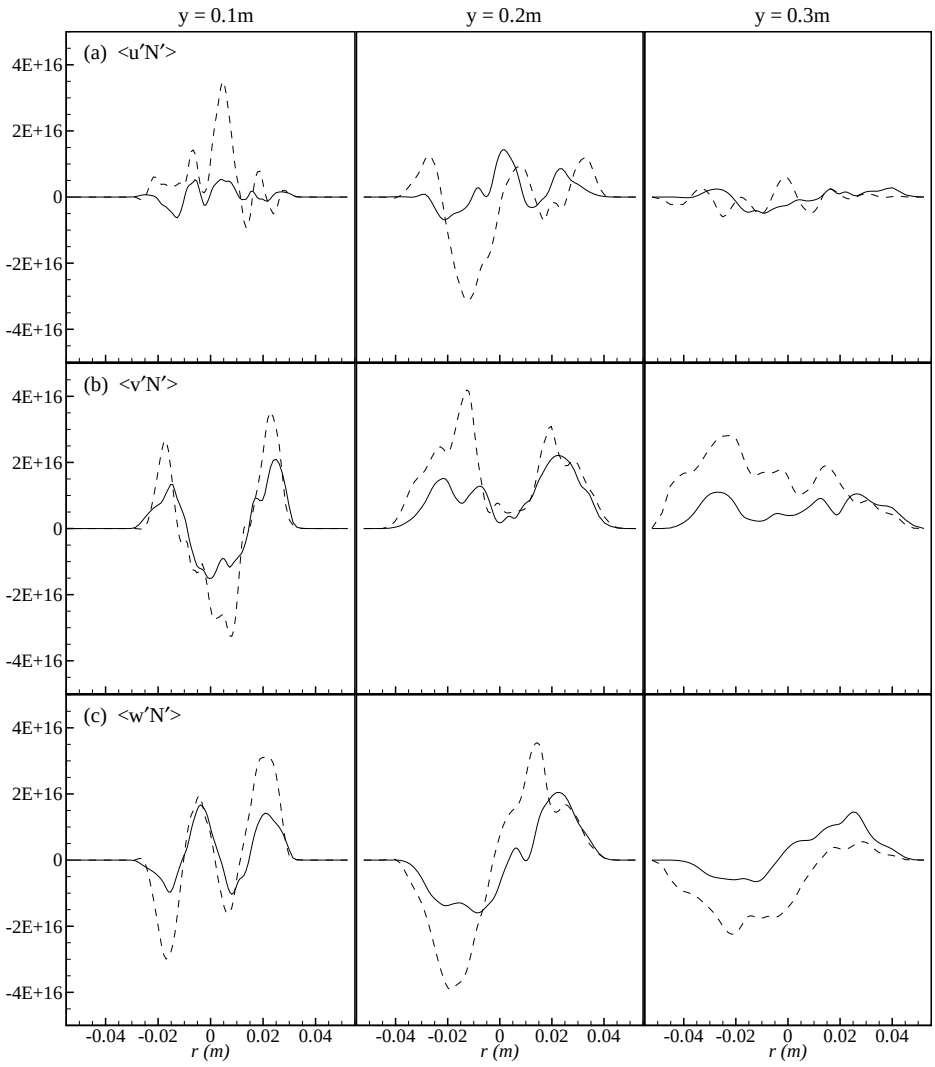

Figure 4.25: Profiles of the mean soot particle number density fluxes, (a) $< u'N' >$, (b) $< v'N' >$ and (c) $< w'N' >$, along the radial direction at the different cross-sectional positions: $y = 0.1m$ (left column), $y = 0.2m$ (middle column), and $y = 0.3m$ (right column).

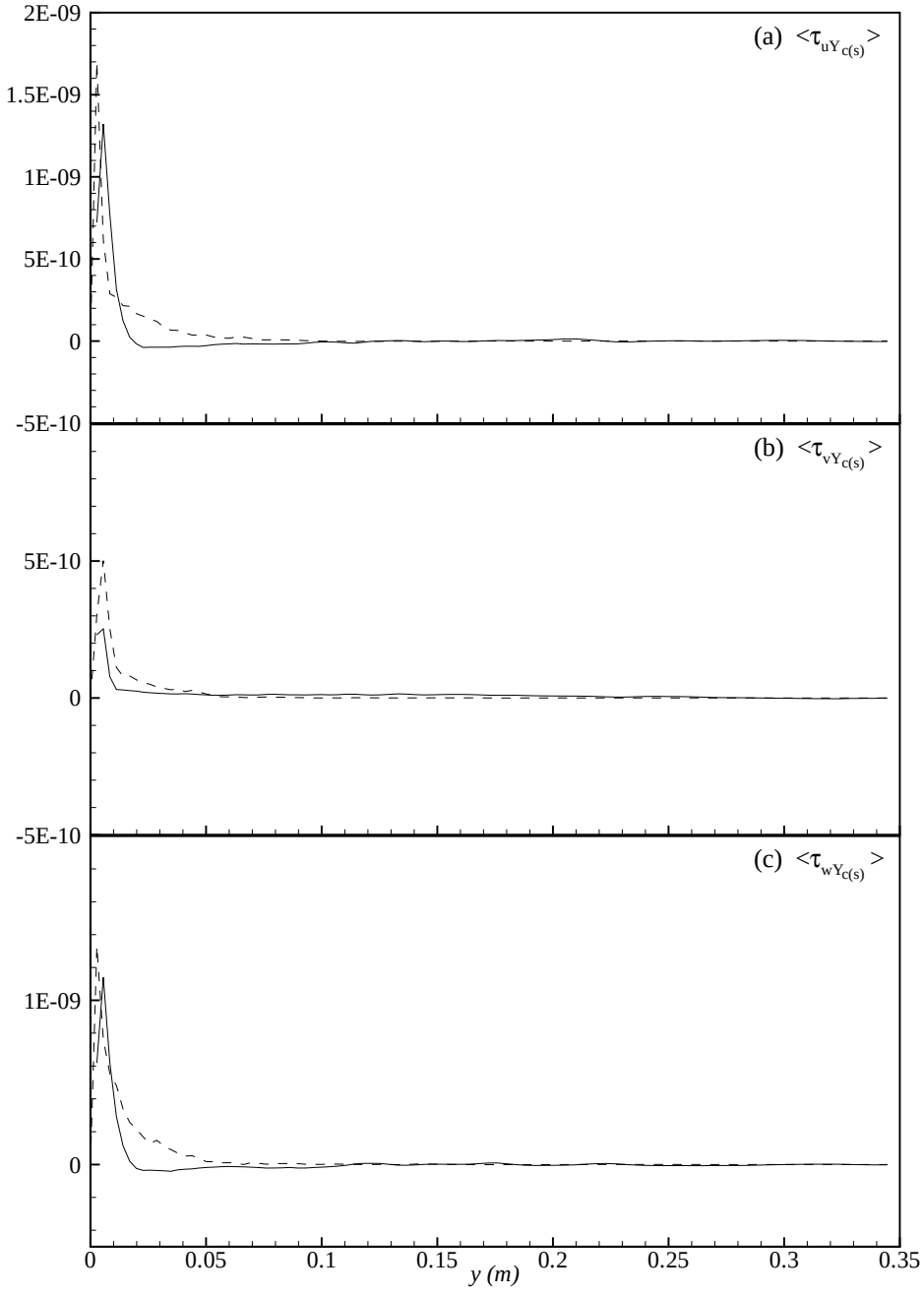

Figure 4.26: Profiles of the mean sub-grid scale soot mass fraction fluxes, (a) $<\tau_{uY_{c(s)}}>$ (b) $<\tau_{vY_{c(s)}}>$ and (c) $<\tau_{wY_{c(s)}}>$, the axial direction.

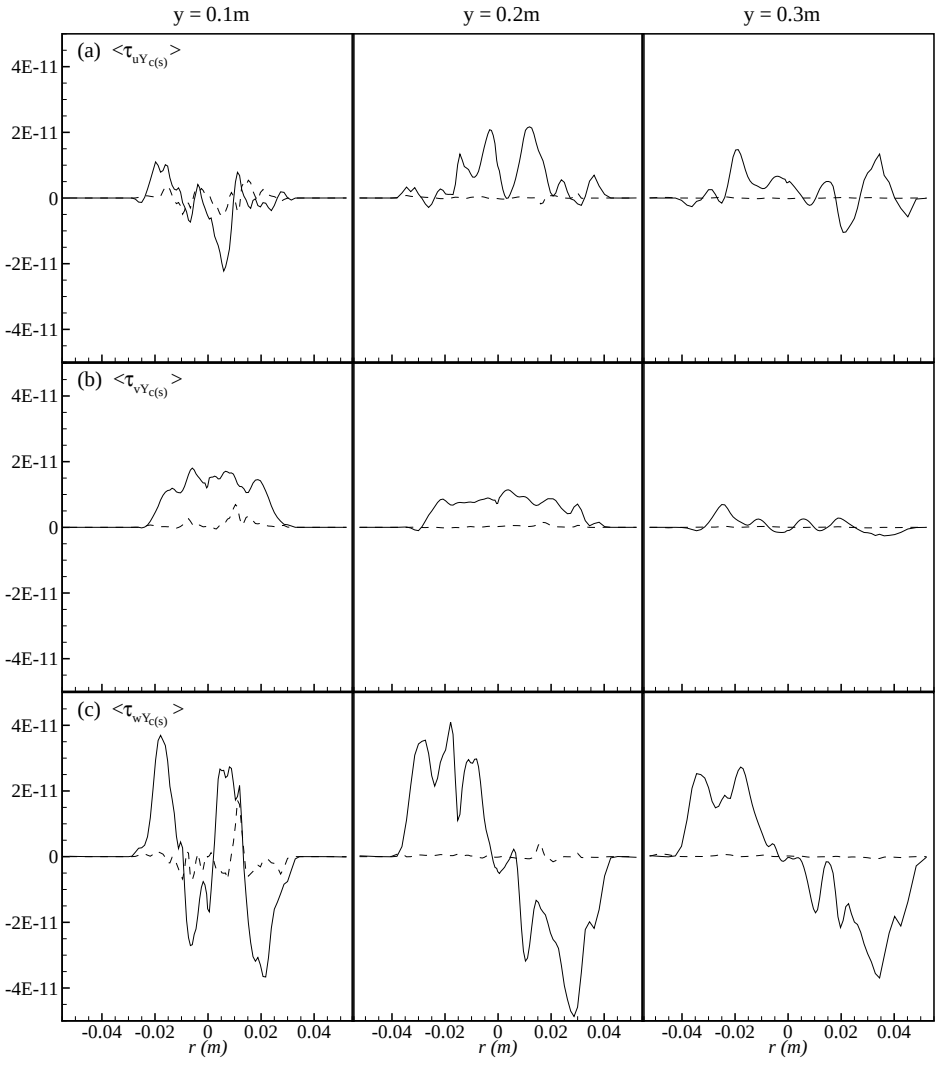

Figure 4.27: Profiles of the mean sub-grid scale soot mass fraction fluxes, (a) $< \tau_{uY_{c(s)}} >$ (b) $< \tau_{vY_{c(s)}} >$ and (c) $< \tau_{wY_{c(s)}} >$, along the radial direction at the different cross-sectional positions: $y = 0.1m$ (left column), $y = 0.2m$ (middle column), and $y = 0.3m$ (right column).

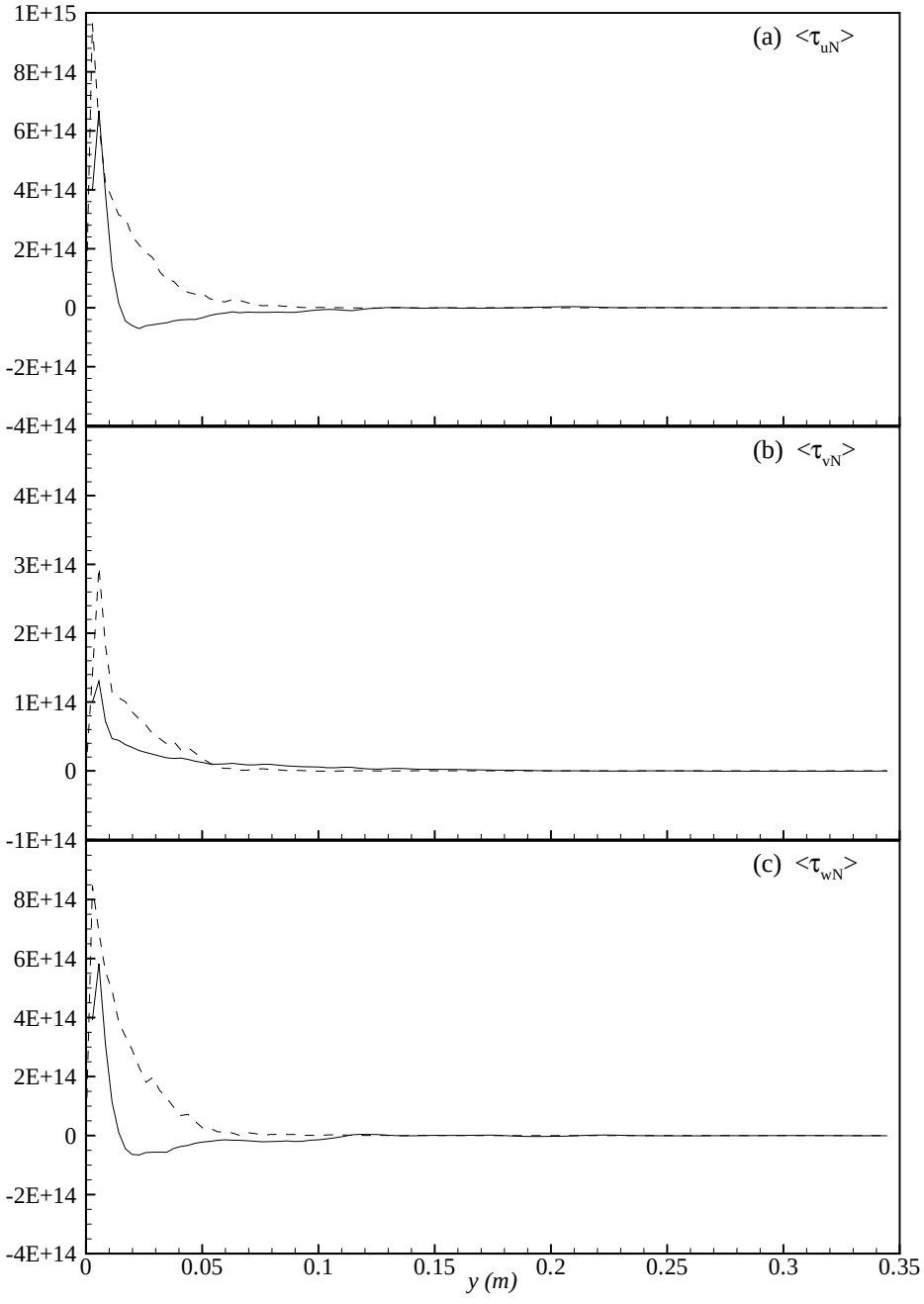

Figure 4.28: Profiles of the mean sub-grid scale soot particle number density fluxes, (a) $< \tau_{uN} >$, (b) $< \tau_{vN} >$ and (c) $< \tau_{wN} >$, along the axial direction.

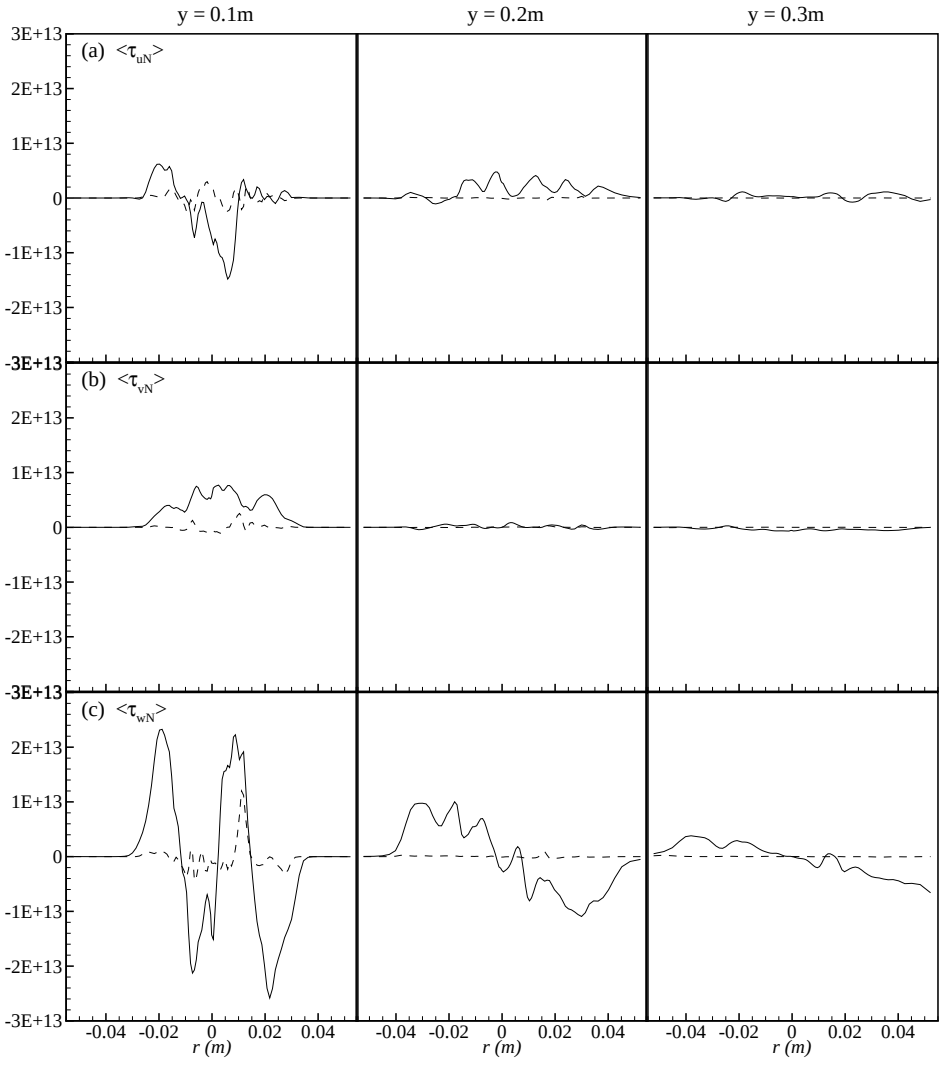

Figure 4.29: Profiles of the mean sub-grid scale soot particle number density fluxes, (a) $< \tau_{uN} >$, (b) $< \tau_{vN} >$ and (c) $< \tau_{wN} >$, along the radial direction at the different cross-sectional positions: $y = 0.1m$ (left column), $y = 0.2m$ (middle column), and $y = 0.3m$ (right column).

Chapter 5

LES for NO Prediction in a Propane-Air Turbulent Flame

Abstract: The formation of the nitric oxide (NO) in a non-premixed propane-air turbulent combustion process inside a cylindrical combustor is investigated. The non-premixed combustion process is modelled via the conserved scalar approach with the laminar flamelet model, described in Chapter 3. The NO formation is modelled through the extended Zeldovich (thermal) reaction mechanism. A transport equation for NO mass fraction is coupled with the flow and the composition fields and solved using the Large Eddy Simulation (LES) technique. In LES the governing equations are filtered using a spatial filtering approach to separate the flow field into large scale eddies and small scale eddies. The large scale eddies are resolved explicitly while the small scale eddies are modelled via Smagorinsky model with constant C_s as well as its dynamic version, described in Chapter 3.

5.1 Introduction

The formation of Nitrogen Oxides (NO_x) can not be avoided in any combustion process, which is formed as an undesired product and is a contributor to air pollution and health problems. Due to the increasing concerns over the environmental pollution, it is essential to understand the NO_x formation mechanisms in a combustion process and the development of their reduction technologies for efficient design of combustion devices. But, one of the great challenges in predicting the formation of the NO_x in a combustion process is the chemical time-scale, which is slow. A brief review on this is given in Chapter 2.

NO_x is used to refer to the nitric oxide, NO, and the nitrogen oxide, NO_2. Typically 95% of the total NO_x emissions is nitric oxide, NO, which is the primary form in combustion products. The nitric oxide, NO, is subsequently oxidized to NO_2 in the atmosphere.

Large Eddy Simulation technique has been applied to investigate the NO production in the non-premixed propane-air turbulent combustion process within a cylindrical combustor. The unresolved small scale eddies are modelled via Smagorinsky model with constant C_s as well as a dynamic model, described in Chapter 3. The non-premixed combustion process is modelled through the conserved scalar approach with the laminar flamelet model, described in Chapter 3, while the NO production mechanism is modelled through a balance equation for NO mass fraction. The extended Zeldovich (thermal) reaction mechanism is taken into account to model the NO production.

This chapter is structured in the following order. A brief description on the nitric oxide, NO, formation mechanism and the modelling of its formation are presented in §5.2 and §5.3 respectively. The governing equation for LES is presented in §5.4. In §5.5 the sgs modelling is presented. Results and discussion are presented in §5.6. Finally, in §5.7 a general conclusion of this chapter is given.

5.2 Nitric Oxide (NO) Formation Mechanism

There are four different routes or mechanisms in the formation of NO_x, which were identified by Bowman [49]. These are the thermal NO route, the prompt NO route, the N_2O (nitrous oxide) route, and the fuel-bound nitrogen route. Brief description of these different routes are given below:

Thermal NO is formed by the high-temperature oxidation of atmospheric nitrogen. Thermal NO, also well-known as $Zeldovich - NO$ after the introduction of this mechanism by Zeldovich [50], is enhanced by presence of superequilibrium O and OH and is very sensitive to temperature.

The prompt NO mechanism, also known as $Fenimore - NO$ as it was postulated by Fenimore [51]. In the prompt NO mechanism, hydrocarbon radicals attack the molecular nitrogen, producing atomic nitrogen, which are subsequently oxidized to NO.

The N_2O route is analogous to the thermal route in that the O atom attacks the molecular nitrogen. However, with the presence of a third body, N_2O is formed and this subsequently reacts with O atoms to reduce NO. The N_2O route is unimportant at ambient pressure.

The fuel-bound NO_x is produced by nitrogen species contained in certain fuels reacting with air during combustion.

The relative contribution from the different routes depends on fuel type, temperature, pressure and residence time as described by Bartok *et al.* [103]. An extensive explanation on these NO_x formation mechanism can be found in the book written by Warnatz *et al* [69].

5.3 Nitric Oxide (NO) Prediction Model

In a non-premixed combustion process a high temperature occurs at the stoichiometric interface where the thermal reaction mechanism of NO dominates its formation. So, the maximum flame temperature is the most important parameter that determines the potential for NO formation. The high NO levels that occur in practical systems can only be reduced by reducing the thermal NO formation. In the present NO formation model, the extended Zeldovich (thermal) reaction mechanism proposed by Zeldovich [50], is taken into account through the solution of a transport equation for NO mass fraction (see equation (5.8)). The extended Zeldovich reaction mechanism has the following three reactions;

$$N_2 + O \xrightarrow{k_1} NO + N, \tag{5.1}$$

$$O_2 + N \xrightarrow{k_2} NO + O, \tag{5.2}$$

$$OH + N \xrightarrow{k_3} NO + H, \tag{5.3}$$

According to the above reactions, the formation rate of NO is

$$\frac{d[NO]}{dt} = k_1[N_2][O] + k_2[O_2][N] + k_3[OH][N], \tag{5.4}$$

and the rate for nitrogen atoms is

$$\frac{d[N]}{dt} = k_1[N_2][O] - k_2[O_2][N] - k_3[OH][N]. \tag{5.5}$$

Assuming a quasi steady state assumption of the nitrogen atoms, i.e., $\frac{d[N]}{dt} \approx 0$, yields the rate of formation of NO as

$$r_{NO} = \frac{d[NO]}{dt} = 2k_1[N_2][O], \tag{5.6}$$

where $[N_2] = \rho Y_{N_2}/M_{N_2}$, $[O] = \rho Y_O/M_O$; $M_{N_2} = 28\ kg/kmol$ and $M_O = 16\ kg/kmol$ are the molar mass of N_2 and O respectively. The reaction rate, k_1, based on Baulch *et al.* [104; 105] is taken as

$$k_1 = 4.1 \times 10^{10} exp\left(-\frac{318}{RT}\right). \tag{5.7}$$

where $R = 8.314472 J.K^{-1}.mol^{-1}$ is the universal gas constant.

The transport equation for NO is written as

$$\frac{\partial(\rho Y_{NO})}{\partial t} + \frac{\partial(\rho u_j Y_{NO})}{\partial x_j} = \frac{\partial}{\partial x_j}\left(\Gamma \frac{\partial Y_{NO}}{\partial x_j}\right) + \rho S(Y_{NO}), \tag{5.8}$$

where Y_{NO} is the mass fraction of NO.

The source term, $\rho S(Y_{NO})$, for the formation of NO mass fraction per unit volume is therefore expressed as

$$\rho S(Y_{NO}) = M_{NO} r_{NO}, \tag{5.9}$$

where M_{NO} is the molecular weight of NO.

5.4 Spatial and Favre Filtering for LES

As the flame is associated with large density variations, an application of Favre-Filtered function, defined in equation (3.43) of Chapter 3, is essential to get the NO mass fraction equation for LES. Employing the Favre-filtered function, the

conservation equation for NO mass fraction becomes

$$\frac{\partial(\bar{\rho}\tilde{Y}_{NO})}{\partial t} + \frac{\partial(\bar{\rho}\widetilde{u_j Y}_{NO})}{\partial x_j} = \frac{\partial}{\partial x_j}\left(\Gamma \frac{\partial \tilde{Y}_{NO}}{\partial x_j}\right) + \bar{\rho}\tilde{S}(\tilde{Y}_{NO}), \tag{5.10}$$

where the instantaneous source term, $\bar{\rho}\tilde{S}(\tilde{Y}_{NO})$, is written as

$$\bar{\rho}\tilde{S}(\tilde{Y}_{NO}) = M_{NO}\tilde{r}_{NO}, \tag{5.11}$$

The NO production rate, r_{NO}, is a function of the flame temperature and the concentrations of N_2 and O (see equations (5.6) and (5.7)), which in turn can be expressed as a function of mixture fraction through the flamelet concept. The instantaneous r_{NO} is shown in Fig. 5.1. The variation of the NO production rate with the variation of the mixture fraction variance, ξ'^2, is presented in Fig. 5.2. This figure shows that the peak value of the the NO production rate decreases in magnitude and also shifts to larger values of the mixture fraction. The Favre-averaged NO production rate, $\tilde{r}_{NO}$, for NO formation may therefore be determined by

$$\tilde{r}_{NO}(\tilde{\xi}) = \widetilde{\frac{d[NO]}{dt}}(\tilde{\xi}) = \int_0^1 r_{NO}\tilde{P}(\xi)d\xi, \tag{5.12}$$

where $\tilde{P}(\xi)$ is the β-pdf, given in equation (3.73) of Chapter 3, constructed from predicted values of the conserved scalar, $\tilde{\xi}$, and the sub-grid scalar variance, $\tilde{\xi}''^2$. The high peak in NO production rate, r_{NO}, suggests the use of piece-wise polynomial fitting approach for the best data fitting. Therefore, a piece-wise polynomial fitting approach is applied to integrate the β-pdf, which is described in §4.5 of Chapter 4.

5.5 Sub-Grid Scale Modelling

An application of the density weighted filter to the convection term in the governing equation of NO mass fraction (equation (5.10)) introduces the unknown term, $\bar{\rho}\widetilde{u_j Y}_{NO}$, leaving this equation unclosed. This unknown term is defined as Germano [80], by

$$\bar{\rho}\widetilde{u_j Y}_{NO} = \bar{\rho}\tilde{u}_j\tilde{Y}_{NO} + J_j^{sgs}, \tag{5.13}$$

where J_j^{sgs} is unknown and referred to the sub-grid scale fluxes for NO mass fraction. This unknown must be modelled.

Similar to the modelling of sub-grid scale mixture fraction fluxes (described in Chapter 3), the sub-grid scale fluxes for the mass fraction of NO are modelled as,

$$J_j^{sgs} = -\bar{\rho}\Gamma_{sgs}\frac{\partial \tilde{Y}_{NO}}{\partial x_j} = -\frac{\bar{\rho}\nu_{sgs}}{\sigma_{sgs}}\frac{\partial \tilde{Y}_{NO}}{\partial x_j}, \tag{5.14}$$

where σ_{sgs} is the sub-grid scale Prandtl/Schmidt number which takes a value of 0.7 in the present computation. The above gradient model was introduced by Schmidt and Schumann [82].

5.6 Results and Discussion

The computational results of this chapter have now been presented. Again to save computational cost, the results presented in this chapter are simulated for a short computational domain. A schematic of this short domain of the cylindrical combustor is shown in Fig. 4.1. The average time step, dt, used in the computation is at the order of 10^{-6}. The time averaged results presented here are calculated by using the relation (3.82) given in Chapter 3.

As in Chapter 3 and Chapter 4, the results of this chapter are also obtained for two different sgs cases, Smagorinsky model with $C_s = 0.1$ (Case1) and a dynamic model for C_s (Case2). The solid lines indicate Case1 and the dashed lines represent Case2. The model parameters are summarised in Table 3.1 of Chapter 3.

5.6.1 Production Rate, Source and Mole fraction of NO

In Fig. 5.3 the computationally predicted instantaneous results of the (a) temperature, $\tilde{T}(K)$, (b) NO production rate, $\tilde{r}_{NO}$, (c) NO source, $\bar{\rho}\tilde{S}(\tilde{Y}_{NO})$, and (d) mass fraction of NO, $\tilde{Y}_{NO}$, on the horizontal midplane of the combustor are plotted. These results are obtained in Case1. The contour plots give a clear visualisation of the distribution of the above results.

Near the inlet when the gaseous fuel gets initially contact with the air stream coming from both sides of the centreline of the combustor, the combustion takes

place and the temperature increases (see frame (a)). The flame then diffuses and travels towards the outlet of the combustor. A higher colour contour level can be seen around the centreline of the combustor where combustion occurs at the stoichiometric condition. Frame (b) shows that at the vicinity of the stoichiometric interface the production rate of NO as well as the prediction of NO source (frame (c)) increases, which again leads to an increase in the prediction of the mass fraction of NO (frame (d)).

In Fig. 5.4 the time averaged results of the (a) temperature, $< \tilde{T}(K) >$, (b) NO production rate, $< \tilde{r}_{NO} >$, (c) NO source, $< \bar{\rho}\tilde{S}(\tilde{Y}_{NO}) >$, and (d) mass fraction of NO, $< \tilde{Y}_{NO} >$, on the horizontal midplane of the combustor are plotted. The solid lines shown on the contour plots represent the locus of the stoichiometric mixture fraction. These contour plots, obtained in Case1, clearly show that the production of NO is highly dependent on both the flame temperature (frame (a)) and the concentration of N_2 (Fig. 3.11(b) of Chapter 3). The mass fraction of NO reaches the maximum level at the stoichiometric zone, again this prediction confirms the earlier observation on the instantaneous results.

Mean axial and radial profiles of the NO production rate, $< \tilde{r}_{NO} >$, are depicted in Fig. 5.5. Axial profile on the centerline of the combustor, plotted in Fig. 5.5(a), shows that the rate is zero upto the axial distance $y = 0.1$, where the fuel stream dominates, afterwards the rate increases and gets its maximum at the outlet of the combustor. From the radial profile of the NO production rate, plotted in Fig. 5.5(b-d), it can be seen that the peak values are predicted in between the centerline and the combustor wall where the temperature has also its maximum, which can clearly be seen from the instantaneous and mean plot of the NO production rate presented respectively in Figs. 5.3 and 5.4.

Axial and radial profiles of the mean NO source, $< \bar{\rho}\tilde{S}(\tilde{Y}_{NO}) >$, and mean mass fraction of NO, $< \tilde{Y}_{NO} >$, are presented in Figs. 5.6 and 5.7 respectively. Axial (Fig. 5.6(a)) and radial (Fig. 5.6(b-d)) profiles of NO source have the similar pattern as $< \tilde{r}_{NO} >$, because the NO source is dominated by the NO production rate (Fig. 5.5). Predicted axial profile of the NO mass fraction (Fig. 5.7(a)) increases gradually as the flame temperature increases and achieves a peak level at the outlet of the combustor where both the maximum temperature (Fig. 3.8(a) of Chapter 3) and the maximum concentration of N_2 (Fig. 3.12(b) of Chapter 3) are recorded.

This is simply because the present NO formation model includes the Zeldovich or thermal reaction mechanism in which the NO production rate is highly dependent on the temperature and reactants (N_2 and O_2). The radial profiles (Figs. 5.7(b-d)) of the NO mass fraction show that the NO production level decreases along the radial direction because of the temperature near the combustor wall which is very low although the N_2 level is predicted high in this region.

Comparison between Case1 and Case2 shows that Case2 produces slightly low levels of the mean NO mass fraction in the upstream region, while towards the downstream both predictions gradually converge together.

5.6.2 Scatter Plots of the NO Production Rate and Mass fraction

The following scatter results are obtained in Case1.

In Fig.5.8, the scatter plots of the (a) instantaneous and (b) mean values of the NO production rate, $\tilde{r}_{NO}$, on the horizontal midplane of the combustor are presented. While the scatter plots of the (a) instantaneous and (b) mean values of the NO production rate on the cross-sectional plane of the combustor at $y = 0.1$ and $y = 0.3$ are shown in Figs. 5.9 and 5.10 respectively.

For the values of mixture fraction where the mixture fraction variance was found relatively concentrated (see frame (a) of Figs. 3.15 and 3.16 in Chapter 3), both the instantaneous and mean values in the scatter plots of NO production rate, $\tilde{r}_{NO}$, are found more scattered. As already seen in the Fig. 5.2 that the peak value of the the NO production rate decreased in magnitude for the higher values of mixture fraction variance.

Instantaneous scatter plots of the NO mass fraction, $\tilde{Y}_{NO}$, versus (a) the mixture fraction, $\tilde{\xi}$, and (b) the temperature, $\tilde{T}(K)$, on the horizontal midplane of the combustor are depicted in Fig. 5.11. This instantaneous scatter plots of the NO mass fraction versus mixture fraction, plotted in frame (a), shows that it is maximum at the mixture fraction value of about 0.05 where the NO production rate (see Fig. 5.8) is high. From frame (b) it can be seen again that the NO mass fraction is maximum at the temperature of about $1900K$ which was the maximum instant temperature in the flame (see Fig. 3.6 of Chapter 3). This is significant as the NO

production mechanism used in the present model is highly dependent on the flame temperature.

5.6.3 Resolved and Sub-Grid Scale Fluxes

The mean NO mass fraction fluxes, (a) $< u'Y'_{NO} >$, (b) $< v'Y'_{NO} >$ and (c) $< w'Y'_{NO} >$, are depicted in Fig. 5.12 along the axial direction on the centerline, and these fluxes are plotted along the radial direction at three different cross-section positions of $y = 0.1m$ (left column), $y = 0.2m$ (middle column) and $y = 0.3m$ (right column) in Fig. 5.13.

In Fig. 5.12, the levels of the centreline NO mass fraction fluxes are found high at the upstream because of the turbulence. Downstream of the inlet, where the fuel gets its first contact with the air, combustion takes place and the flow becomes highly turbulent, which leads to the high level of the NO mass fraction fluxes. The NO mass fraction flux with the axial velocity component, $< v'Y'_{NO} >$, has the largest value compared to the other two, this is expected as the axial velocity, hence its fluctuation, is higher than that of the radial components. The magnitudes of all the fluxes decrease towards the downstream region where the turbulence intensity is seen to be low. The radial profiles (Fig. 5.12(b-d)) show that the NO mass fraction fluxes are higher around the centreline and disappear at the combustor wall region. Similar levels but some variation can be found between the fluxes in Case1 and Case2, although the variation is very small in magnitude.

In the Fig. 5.14, the mean values of the sub-grid scale NO mass fraction fluxes, (a) $< \tau_{uY_{NO}} >$, (b) $< \tau_{vY_{NO}} >$ and (c) $< \tau_{wY_{NO}} >$, are plotted along the axial direction on the centerline, while the radial profiles of these sgs fluxes are presented in Fig. 5.15 at three different cross-sectional positions of $y = 0.1m$ (left column), $y = 0.2m$ (middle column) and $y = 0.3m$ (right column).

In the upstream region the turbulent intensity was found high, hence the sub-grid scale contributions to the NO mass fraction fluxes are predicted to be maximum. These contributions are negligible and almost vanish beyond the region $y = 0.05m$ of the combustor. On the centreline the sub-grid scale NO mass fraction fluxes, $< \tau_{uY_{NO}} >$ and $< \tau_{wY_{NO}} >$, have similar magnitudes that differ in the radial direction. As is to be expected, the levels of the sub-grid scale NO mass fraction

fluxes are very much lower than those of the resolved scale fluxes. Comparing the sgs fluxes between Case1 and Case2, it is found that Case2 produces higher peak in the upstream. This higher peak is due to the higher levels of dynamic C_s in the upstream. Towards the downstream of the combustor both cases produce same results although radial profiles show higher prediction in case1 but negligibly small in magnitude.

5.7 Conclusion

Large Eddy Simulation technique has been applied to investigate the NO production in the non-premixed propane/air turbulent combustion process within a cylindrical combustor. The Smagorinsky model with $C_s = 0.1$ and a dynamic model have been employed for modelling of the sub-grid scale stresses. The non-premixed combustion process is modelled through the conserved scalar approach with the laminar flamelet model, while the NO production mechanism is modelled through a balance equation for NO mass fraction. The extended Zeldovich (thermal) reaction mechanism is taken into account to model the NO production.

It was not possible to compare the computational results of the NO mass fraction with experimental data, as Nishida and Mukohara [1] did not perform any measurements on the NO mass fraction. However, the present results of NO clearly agree well with the principle and reaction mechanism of the extended Zeldovich (thermal) used for modelling NO. The NO mass fraction is predicted high in the high temperature zone.

It has also been found that the sub-grid scale contribution to the prediction of NO mass fraction is dominated by the intensity of the turbulence.

The results are almost uninfluenced by the choice of sub-grid scale models although slightly lower prediction of NO mass fraction is found with dynamic C_s in the upstream. However, dynamic C_s produces a higher levels of the sub-grid scale quantities in the upstream region.

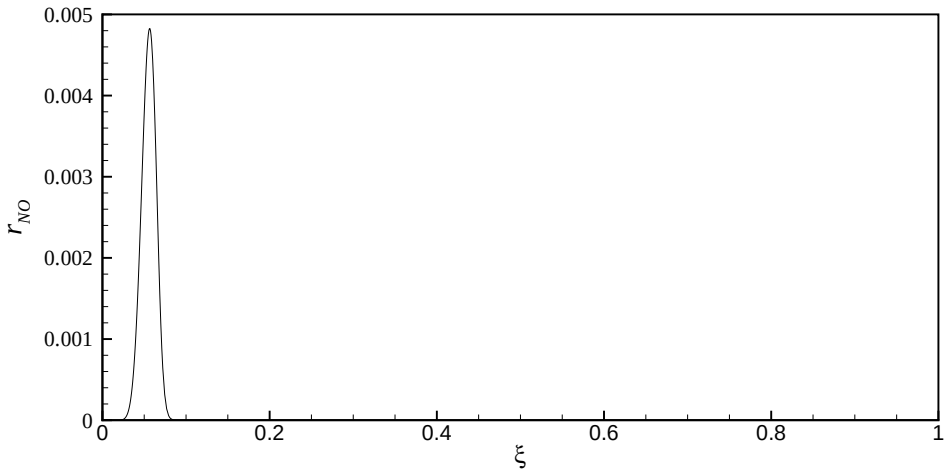

Figure 5.1: Dependence of the instantaneous NO production rate on the mixture fraction.

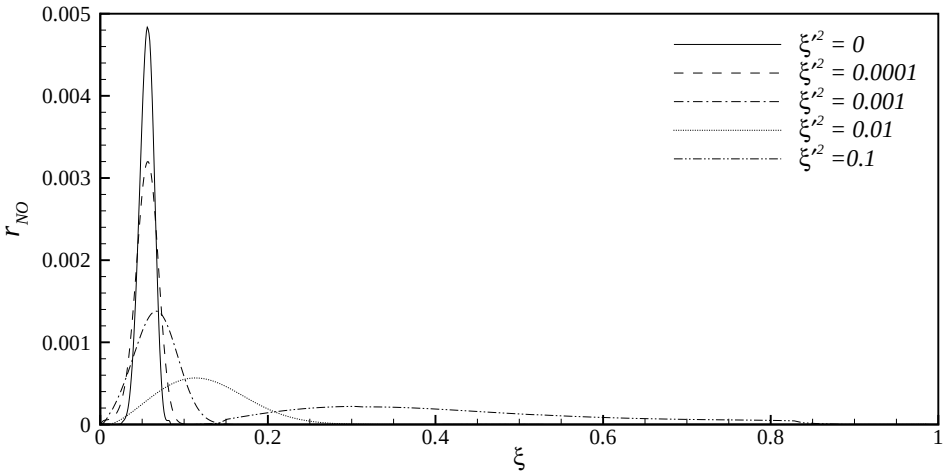

Figure 5.2: Dependence of the instantaneous NO production rate on the mixture fraction and mixture fraction variances.

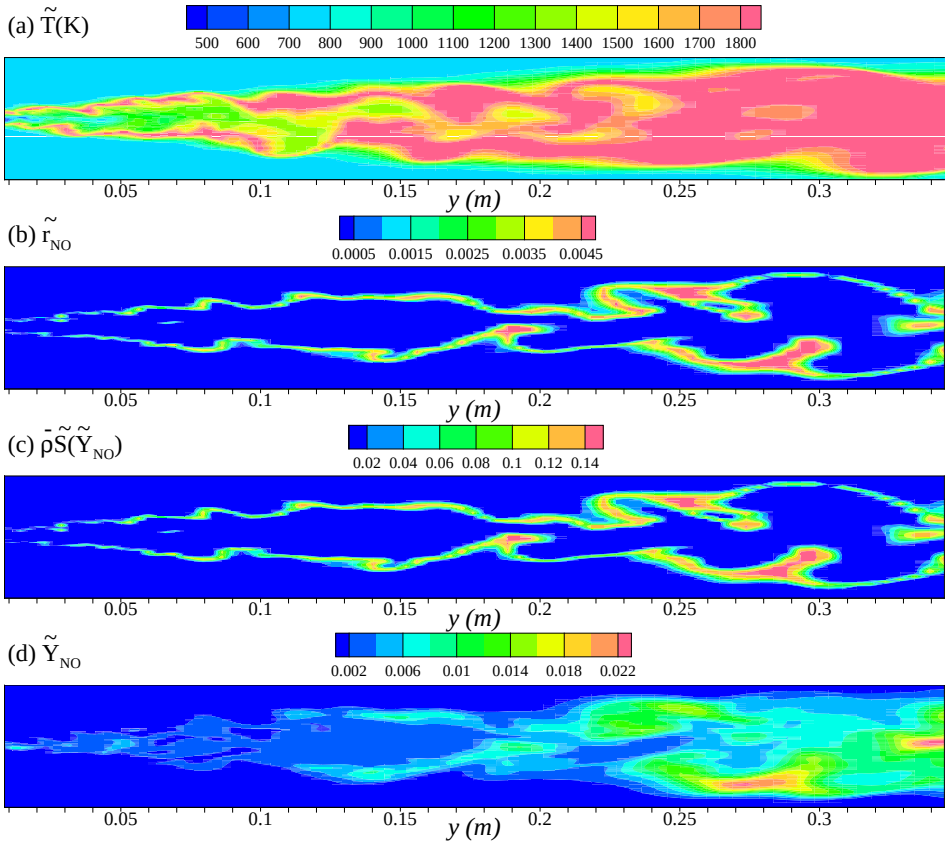

Figure 5.3: The instantaneous plot of the (a) temperature, $\tilde{T}(K)$, (b) NO production rate, $\tilde{r}_{NO}$, (c) source term for NO formation, $\bar{\rho}\tilde{S}(\tilde{Y}_{NO})$, and (d) NO mass fraction, $\tilde{Y}_{NO}$ on the horizontal mid-plane of the combustor, for Case1.

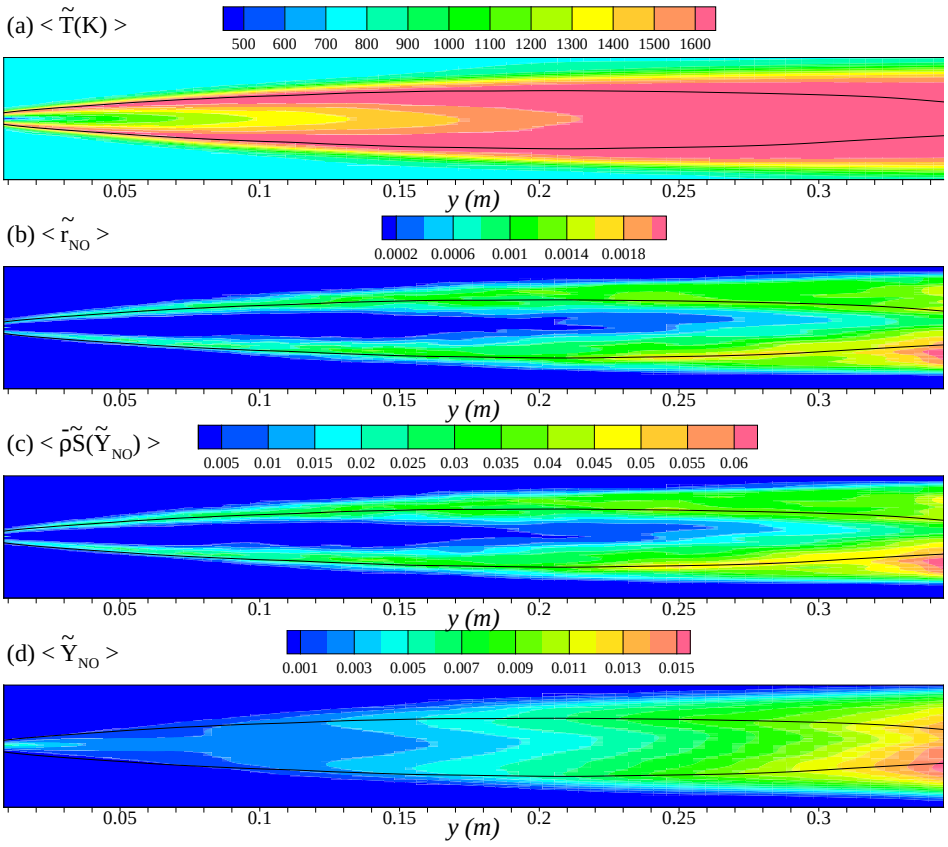

Figure 5.4: The mean values of the (a) temperature, $< \tilde{T}(K) >$, (b) NO production rate, $< \tilde{r}_{NO} >$, (c) source term for NO formation, $< \bar{\rho}\tilde{S}(\tilde{Y}_{NO}) >$, and (d) NO mass fraction, $< \tilde{Y}_{NO} >$ on the horizontal mid-plane of the combustor, for Case1.

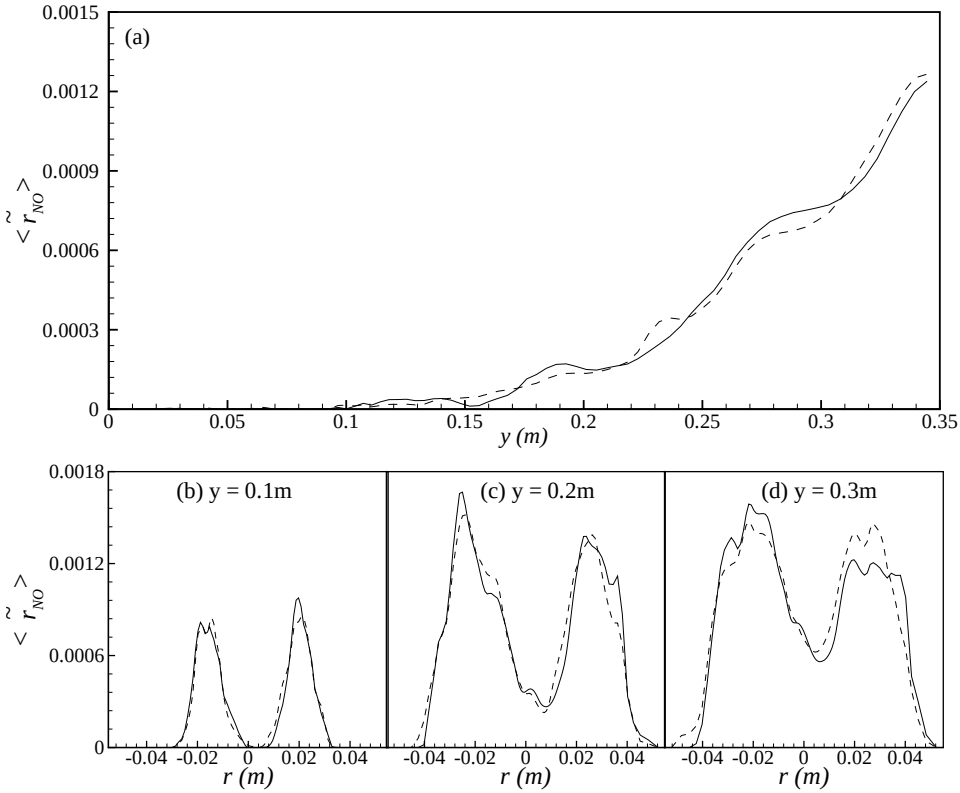

Figure 5.5: Mean values of NO production rate, $< \tilde{r}_{NO} >$, along the (a) axial direction and radial direction at the different cross-section positions: (b) $y = 0.1m$, (c) $y = 0.2m$, (d) $y = 0.3m$ of the combustor.

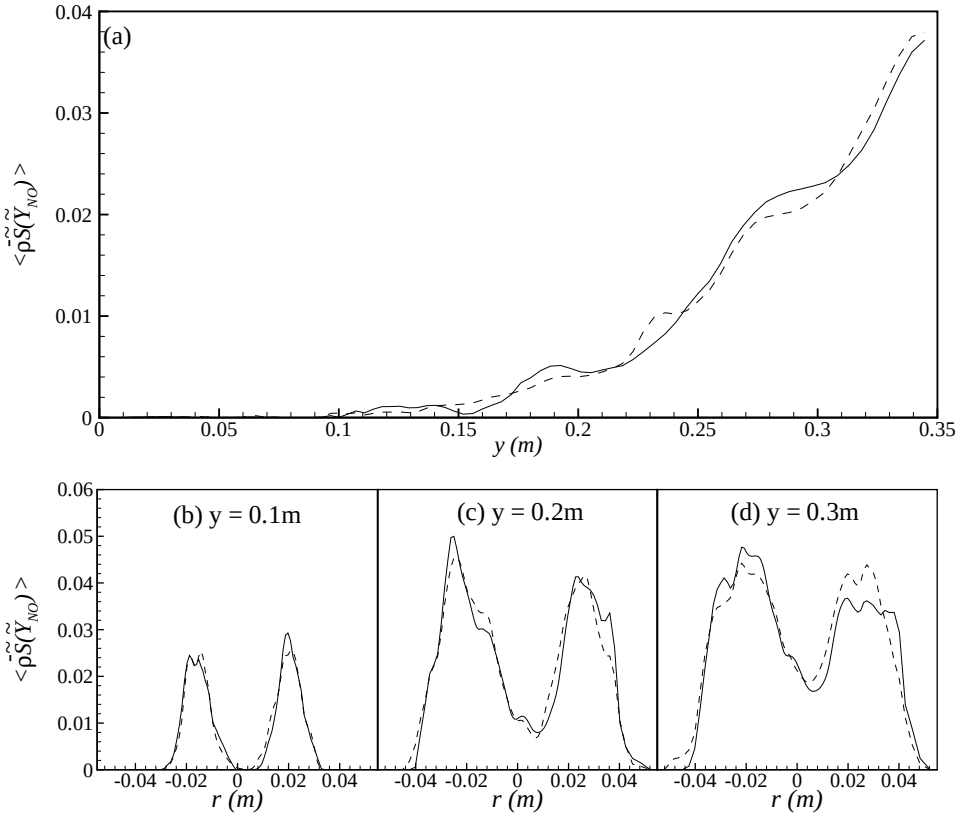

Figure 5.6: Mean values of source term for NO formation, $< \bar{\rho}\tilde{S}(\tilde{Y}_{NO}) >$, along the (a) axial direction and radial direction at the different cross-section positions: (b) $y = 0.1m$, (c) $y = 0.2m$, (d) $y = 0.3m$ of the combustor.

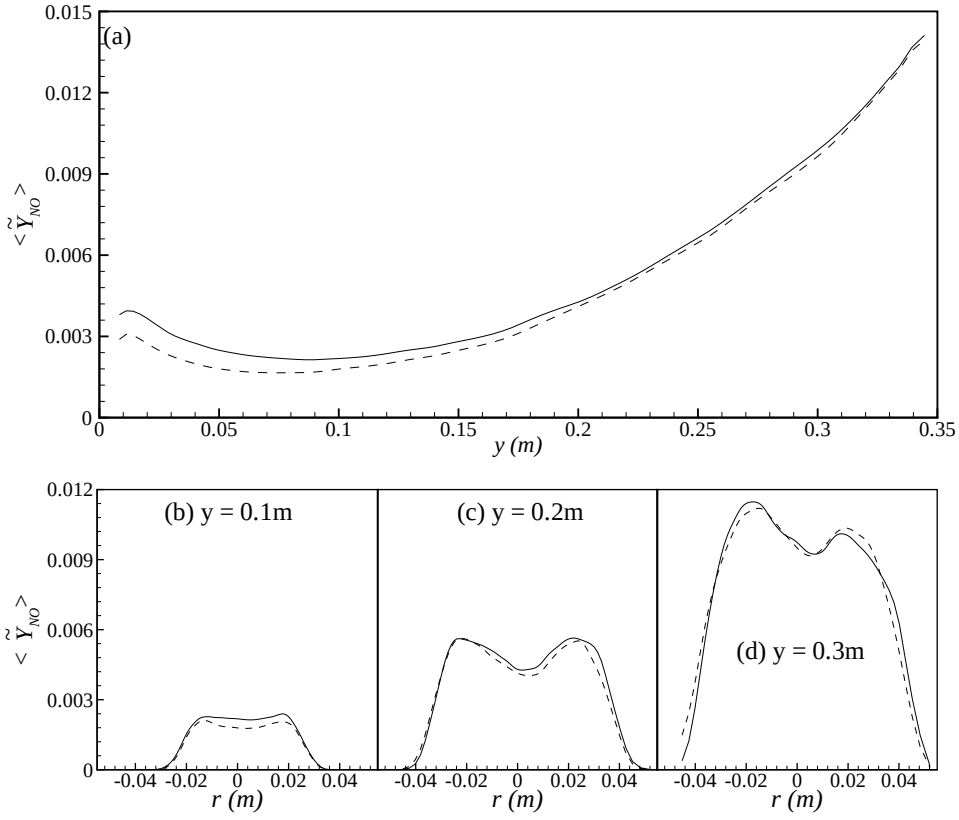

Figure 5.7: Mean values of the NO mass fraction, $< \tilde{Y}_{NO} >$, along the (a) axial direction and radial direction at the different cross-section positions: (b) $y = 0.1m$, (c) $y = 0.2m$, (d) $y = 0.3m$ of the combustor.

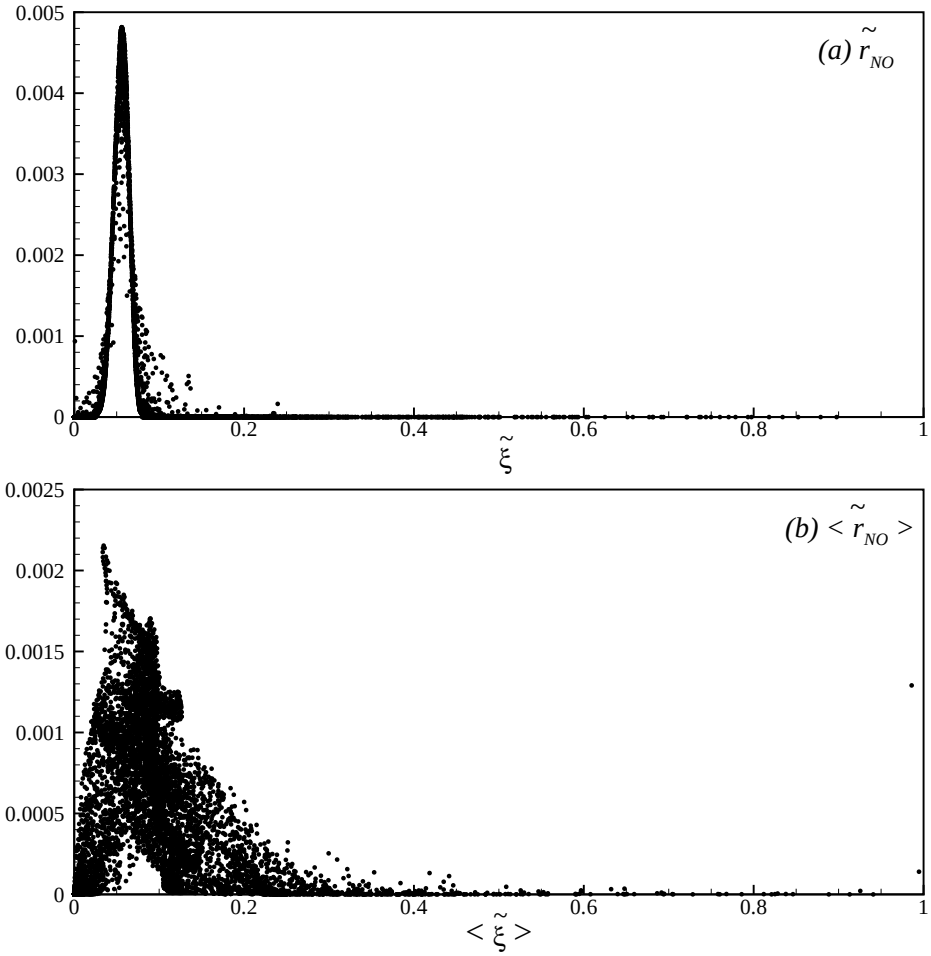

Figure 5.8: Scatter plots of the NO production rate: (a) instantaneous, $\tilde{r}_{NO}$, and (b) mean, $< \tilde{r}_{NO} >$, on the horizontal midplane of the combustor, for Case1.

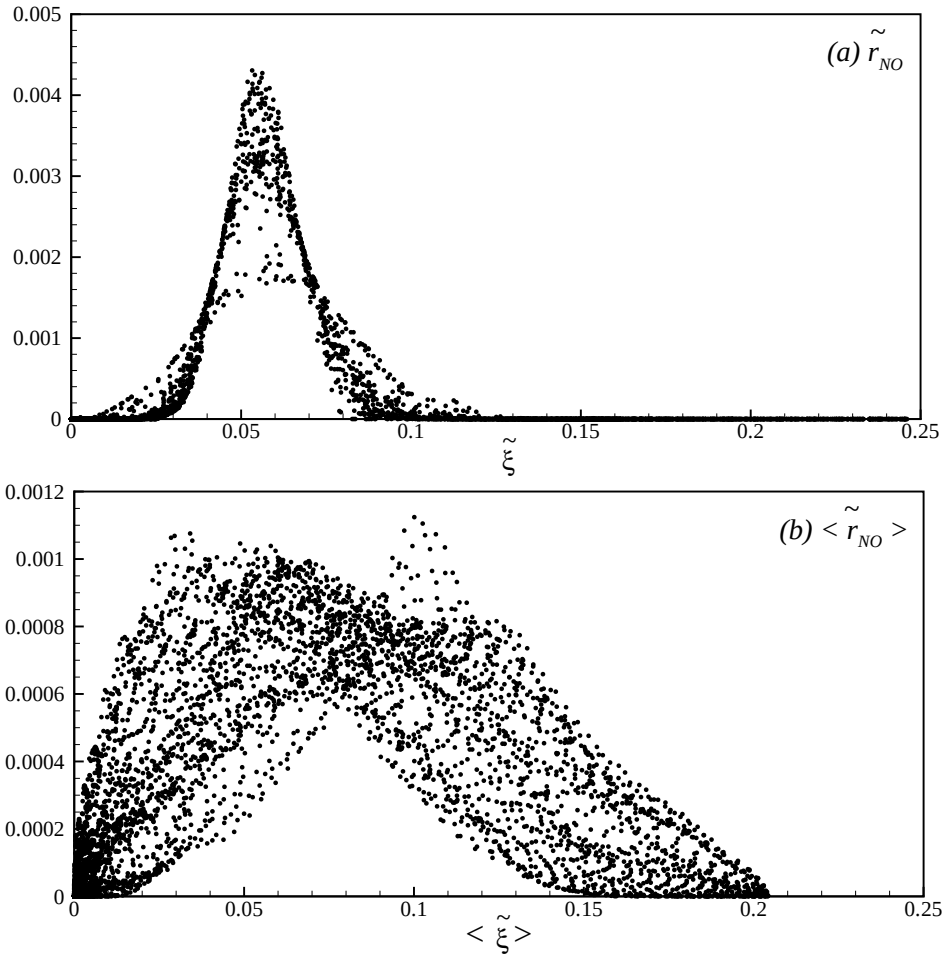

Figure 5.9: Scatter plots of NO production rate: (a) instantaneous, $\tilde{r}_{NO}$ and (b) mean, $< \tilde{r}_{NO} >$, on the cross-sectional plane at $y = 0.1m$ of the combustor, for Case1.

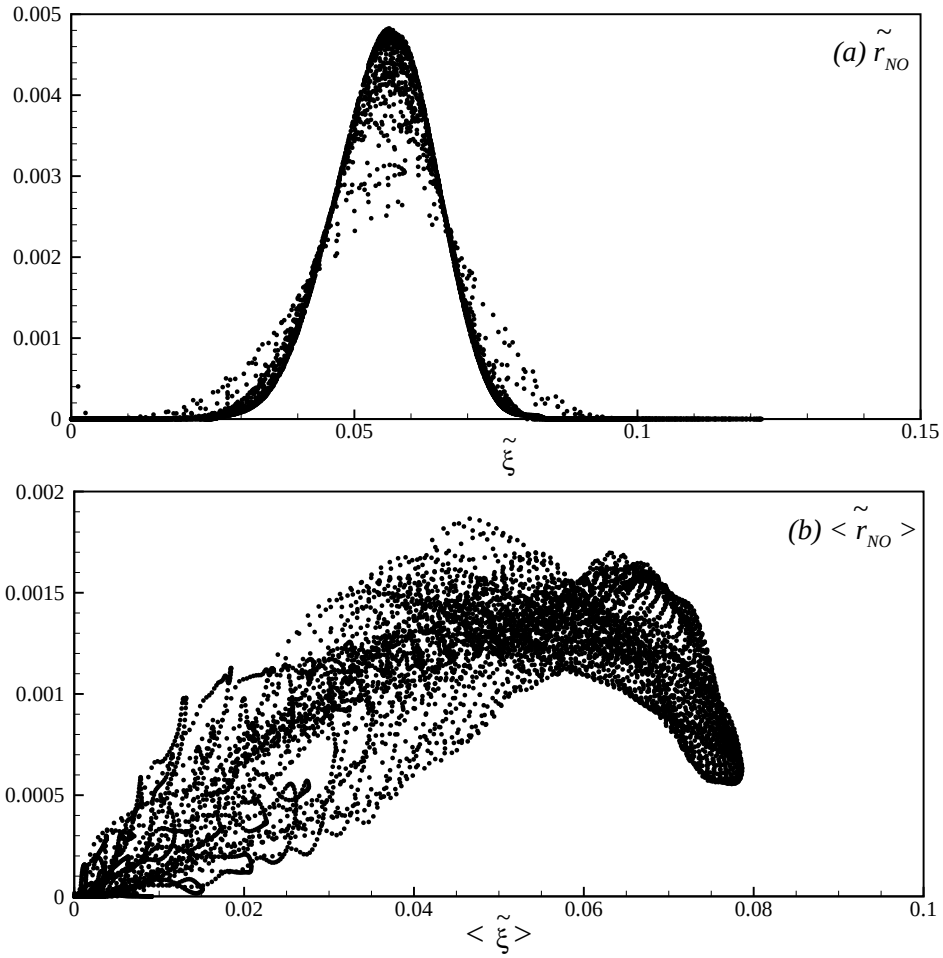

Figure 5.10: Scatter plots of the NO production rate: (a) instantaneous, $\tilde{r}_{NO}$, and (b) mean, $< \tilde{r}_{NO} >$, on the cross-sectional plane at $y = 0.3m$ of the combustor, for Case1.

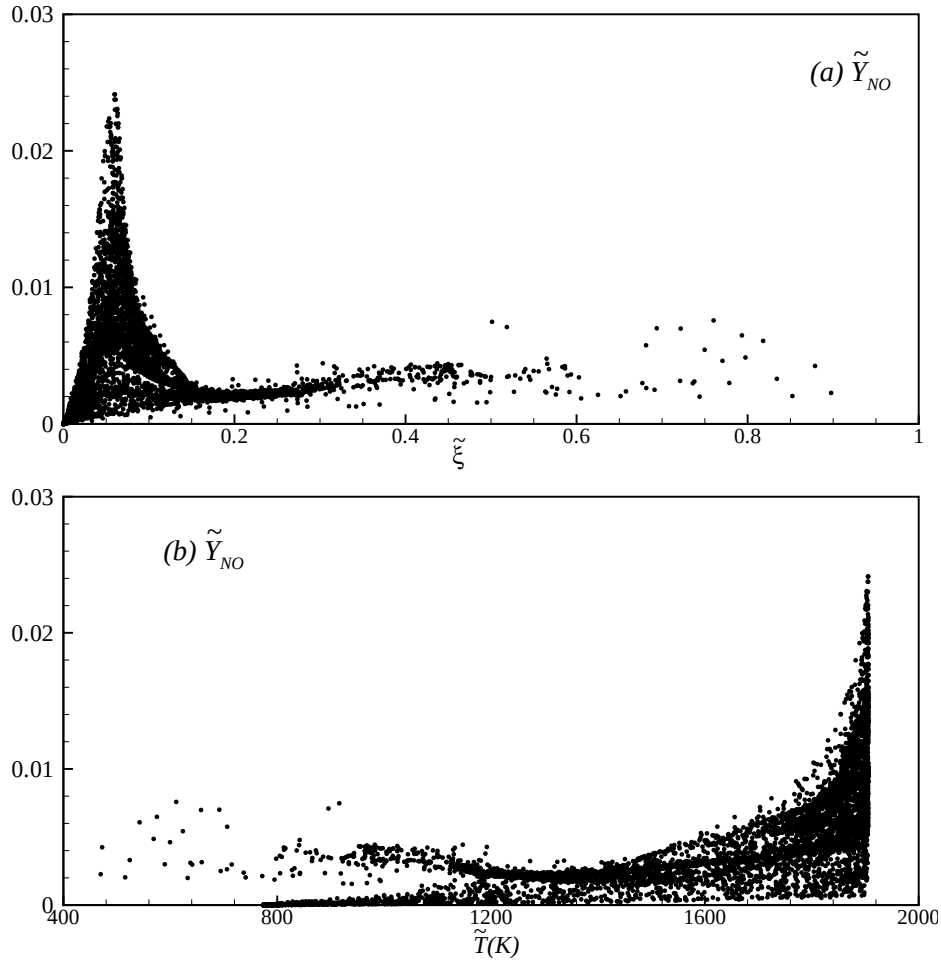

Figure 5.11: Scatter plots of the instantaneous values of NO mass fraction, $\tilde{Y}_{NO}$, versus (a) the mixture fraction, $\tilde{\xi}$, and (b) the temperature, $\tilde{T}(K)$, on the horizontal midplane of the combustor, for Case1.

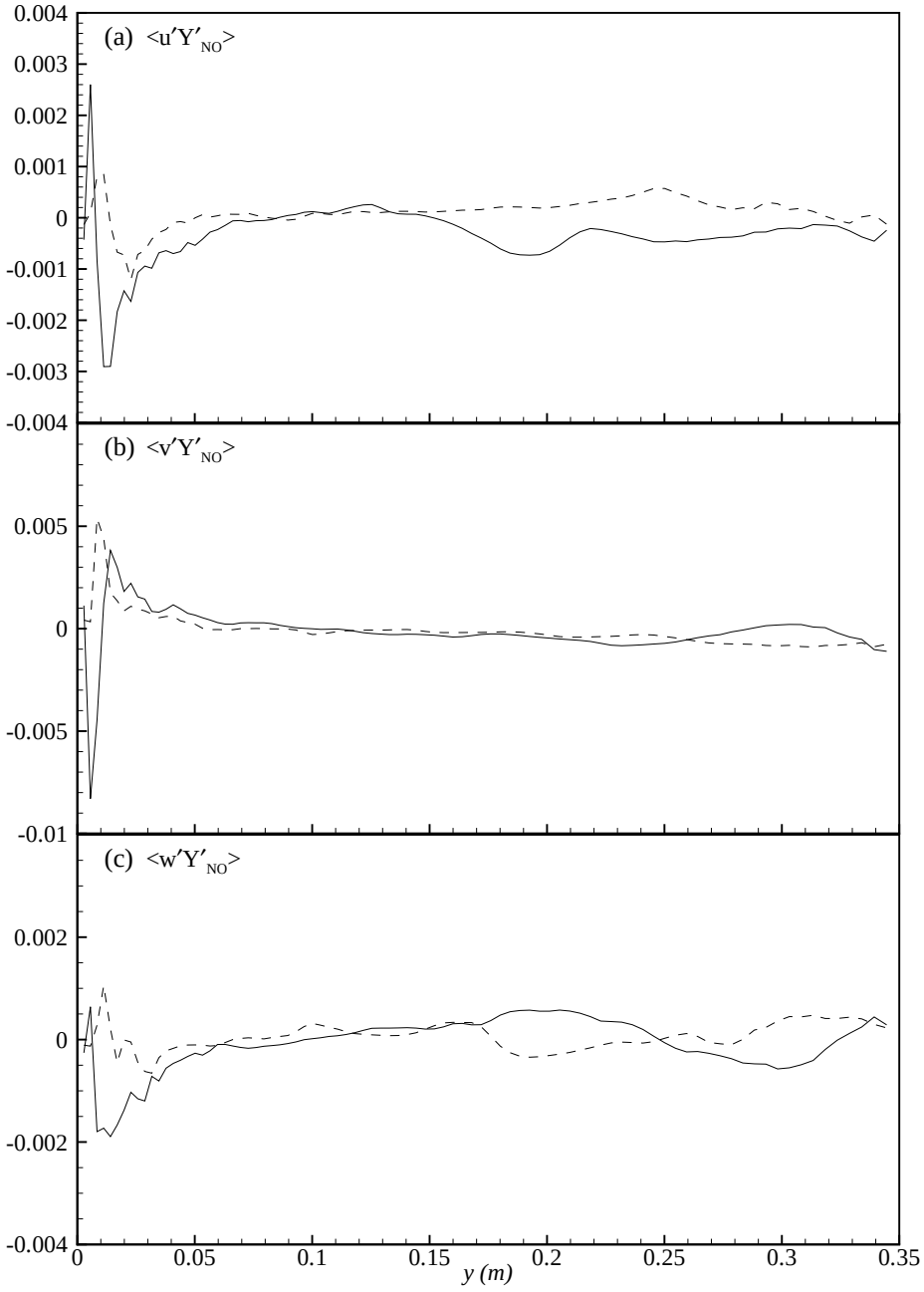

Figure 5.12: Profiles of the mean NO mass fraction fluxes, (a) $< u'Y'_{NO} >$, (b) $< v'Y'_{NO} >$ and (c) $< w'Y'_{NO} >$, along the axial direction.

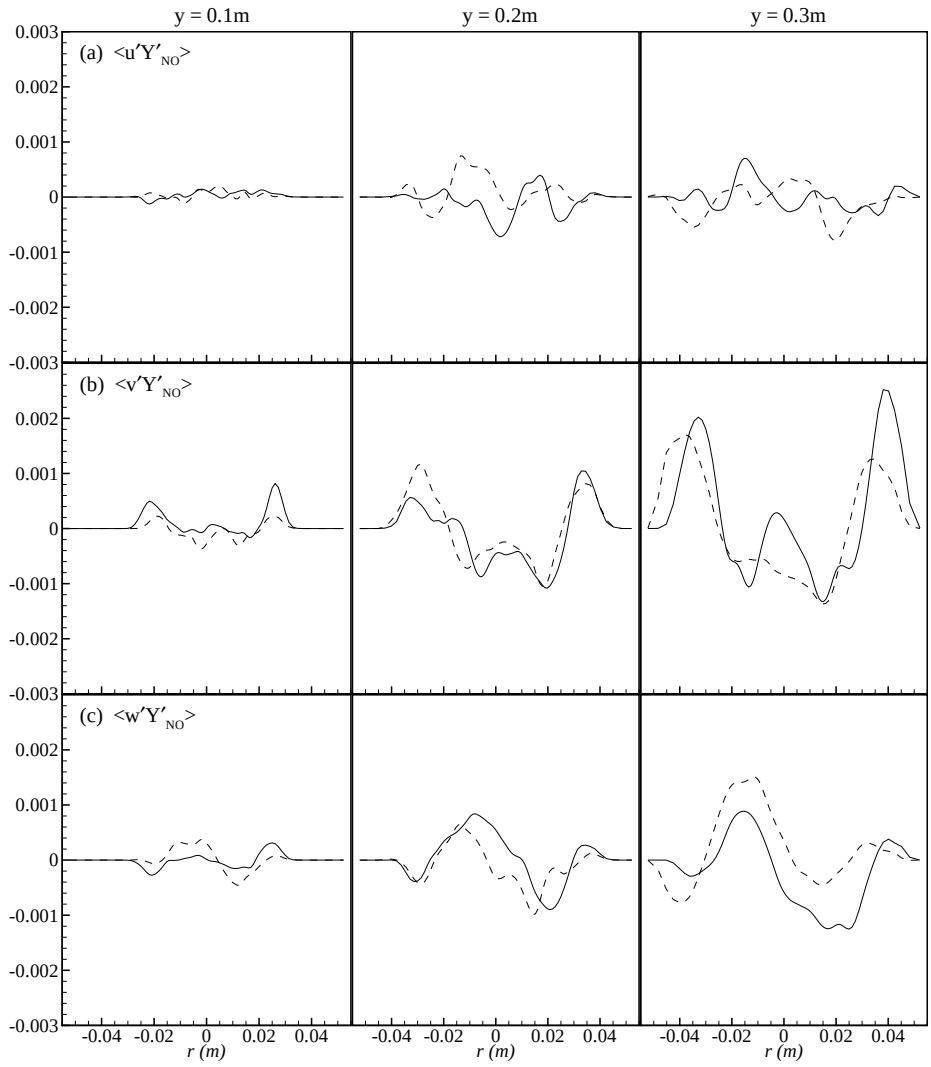

Figure 5.13: Profiles of the mean NO mass fraction fluxes, (a) $< u'Y'_{NO} >$, (b) $< v'Y'_{NO} >$ and (c) $< w'Y'_{NO} >$, along the radial direction at the different cross-sectional positions: $y = 0.1m$ (left column), $y = 0.2m$ (middle column), and $y = 0.3m$ (right column).

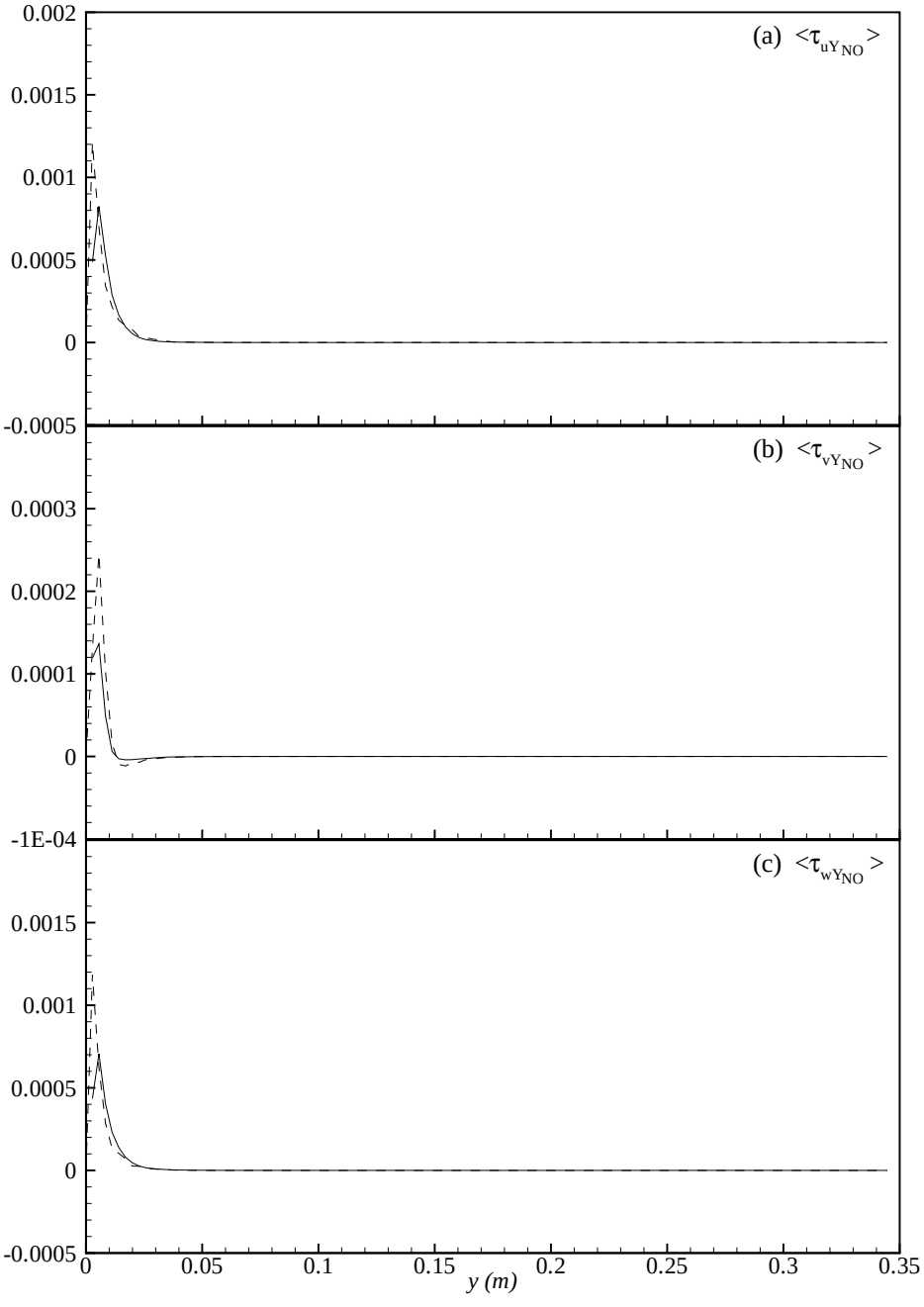

Figure 5.14: Profiles of the mean sub-grid scale NO mass fraction fluxes, (a) $<\tau_{uY_{NO}}>$, (b) $<\tau_{vY_{NO}}>$ and (c) $<\tau_{wY_{NO}}>$, along the axial direction.

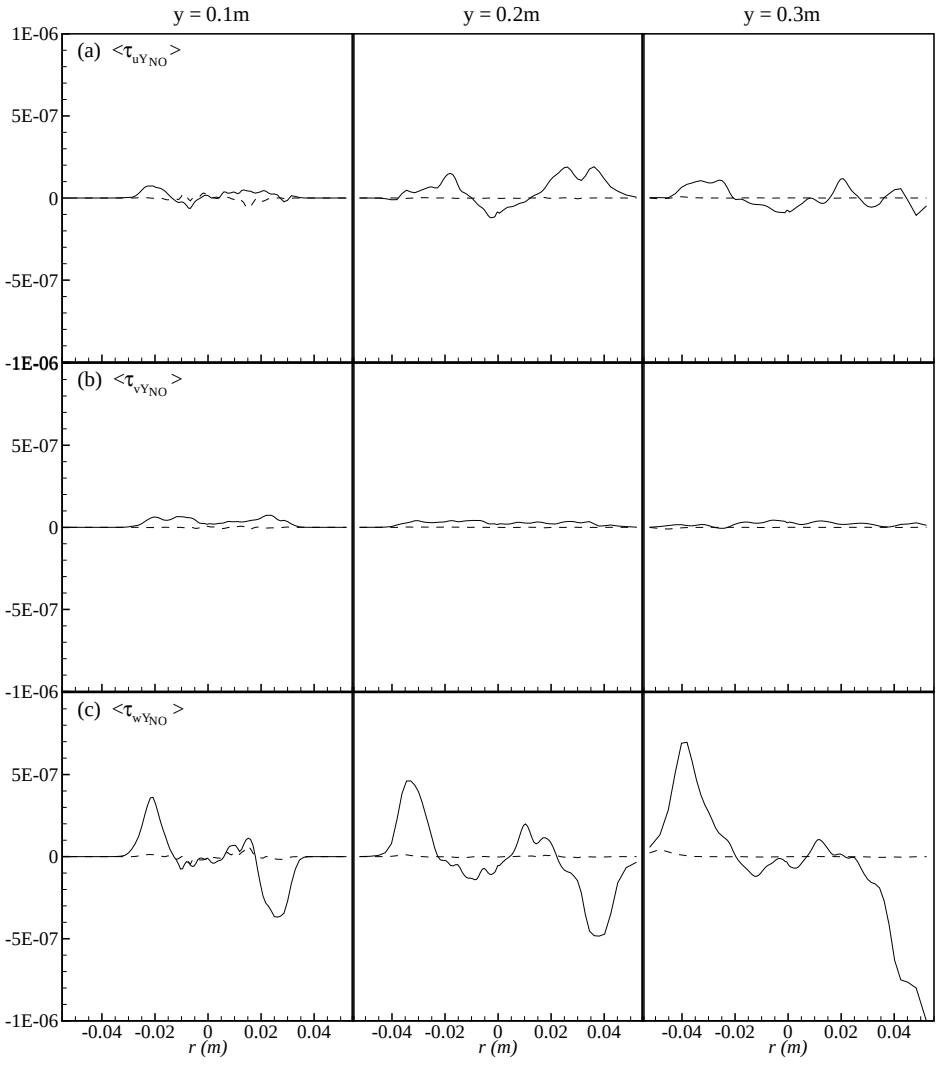

Figure 5.15: Profiles of the mean sub-grid scale NO mass fraction fluxes, (a) $< \tau_{uY_{NO}} >$, (b) $< \tau_{vY_{NO}} >$ and (c) $< \tau_{wY_{NO}} >$, along the radial direction at the different cross-sectional positions: $y = 0.1m$ (left column), $y = 0.2m$ (middle column), and $y = 0.3m$ (right column).

Chapter 6

Radiative Heat Transfer from a Non-Premixed Propane-Air Flame

Abstract: The Discrete Ordinates Method (DOM/S_n) with Large Eddy Simulation (LES) is employed to investigate the radiative heat transfer in the flame inside the three-dimensional cylindrical combustor studied in Chapters 3-5. Both the luminous, which is due to the appearance of soot particles in the flame, and the non-luminous, which is due to hot products of combustion (mainly carbon dioxide (CO_2) and water vapour (H_2O)), radiations have been considered in this study. The radiation is modelled through the Radiative Transfer Equation (RTE), which is the steady state representation of radiative heat transfer/flux. The RTE is solved using the Discrete Ordinates Method (DOM/S_n) which has been combined with the LES of the flow, temperature, combustion species and soot formation. The LES results used in this chapter are obtained only for Smagorinsky model with $C_s = 0.1$. The effect of scattering is ignored as it is found that the absorption dominates the medium. Assessments of the various orders of DOM are made, and the effects of various wall emissivity on the prediction of radiative transfer are analysed.

6.1 Introduction

In most combustion devices such as furnaces, gas turbines, internal combustions engines, burners, etc., a large portion of the total heat flux/transfer occurs mainly by radiation from the flame. In fuel-rich combustion, the ratio of fuel to air is high and mixing of fuel and air is inadequate which leads to the production of solid soot particles and the radiation occurs in both non-luminous and luminous flame.

The radiation emitted from non-luminouss flame depends on the hot combustion products, mainly carbon dioxide (CO_2) and water vapour (H_2O). On the other hand, the luminous radiation is mainly for the appearance of soot particles in the flame. For an efficient design of a combustion system with less pollutant emissions, it is essential to predict the wall temperature accurately, which in turn depends on the accurate prediction of the radiative heat transfer. Therefore, an adequate treatment of thermal radiation is essential to develop a mathematical model for the combustion processes.

In this chapter, we investigate the radiative heat transfer in the co-flowing non-premixed propane-air flame inside the three-dimensional cylindrical combustor considered in Chapters 3-5. Both the luminous and non-luminous radiataion are considered, which are modelled through the Radiative Transfer Equation (RTE). The RTE is then solved using the Discrete Ordinates Method (DOM/S_n) combining with the LES of the flow, temperature, combustion species and soot formation.

This chapter is organised in the following order. The Radiative Transfer Equation and its Discrete Ordinates representation are presented in §6.2 and §6.3 respectively. The description on the combination of DOM with LES is given in §6.4, followed by the sgs modelling in §6.5. The absorption and scattering coefficients are described, respectively, in §6.6 and §6.7. In §6.8 and §6.9, the radiation modelling and important radiation quantities are given respectively. Results and discussion are presented in §6.10 which is followed by a general conclusion of this chapter in §6.11.

6.2 Radiative Transfer Equation

The balance of radiative energy passing in a specified direction $\hat{s}$ through a small differential volume in an absorbing-emitting and scattering grey medium can be written as,

$$(\hat{s}.\nabla)I(\mathbf{r},\hat{s}) = -(\kappa_a+\sigma)I(\mathbf{r},\hat{s}) + \kappa_a I_b(\mathbf{r}) + \frac{\sigma}{4\pi}\int_{\Omega'=4\pi} I(\mathbf{r},\hat{s}')\Phi(\hat{s}'\rightarrow\hat{s})d\Omega' \,, \tag{6.1}$$

where Ω is the solid angle, $I(\mathbf{r}, \hat{s})$ is the radiative intensity which is a function of position, $\mathbf{r} = (x, y, z)$, and the directions, $\hat{s}$ and $\hat{s}'$; $I_b(\mathbf{r})$ is the blackbody radiative intensity at the temperature of the medium, T, defined as $\frac{s_b T^4}{\pi}$, where $s_b = 5.67 \times 10^{-8} W/m^2 K^4$ is the Stefan-Boltzmann constant; κ_a and σ are the absorption and the scattering coefficients respectively; $\Phi(\hat{s}' \rightarrow \hat{s})$ is the scattering phase function which determines the probability of the radiative energy transfer from the incoming ($\hat{s}'$) to the outgoing ($\hat{s}$) directions.

In equation (6.1), the term on the left hand side represents the gradient of the radiative intensity in the specified direction, $\hat{s}$, and the three terms on the right hand side represent changes of the radiative intensity due to absorption and out-scattering, emission, and in-scattering, respectively.

If the wall bounding the medium is assumed to be gray and emits and reflects diffusely, the radiative boundary condition for the RTE (equation (6.1)) is taken as

$$I(\mathbf{r}_w, \hat{s}) = \varepsilon_w I_{bw}(\mathbf{r}_w) + \frac{1 - \varepsilon_w}{\pi} \int_{\mathbf{n}.\hat{\mathbf{s}}'<\mathbf{0}} I(\mathbf{r}_w, \hat{s}')|\mathbf{n}.\hat{s}'|d\Omega' \,, \tag{6.2}$$

where $I_{bw}(\mathbf{r}_w)$ is the black body intensity of the wall; ε_w is the wall emissivity; and $\mathbf{n}$ represents the outward unit normal vector on the wall.

6.3 Discrete Ordinates Method (DOM)

The Discrete Ordinates Method (DOM), introduced by Chandrasekhar [55], is a numerical technique by which the Radiative Tranfer Equation (RTE) is transformed into a set of simultaneous partial differential equations based on a discrete representation of the directional variation of the radiative intensity. In the DOM, the radiative transfer equation (6.1) is solved for the set of M discrete directions $\hat{s}_m$, m=1,2,3,....M, spanning the total solid angle range of 4π. The integrals over the solid angle are approximated by numerical quadratures, that is,

$$\int_{\Omega'=4\pi} I(\mathbf{r}, \hat{s}')\Phi(\hat{s}' \rightarrow \hat{s})d\Omega' = \sum_{m'=1}^{M} \omega_{m'} I_{m'} \Phi(m, m') \,, \tag{6.3}$$

where M is the total number of discrete ordinates transmitted from each computational control volume and related to n, the order of S_n approximation, through the relation $M = n(n+2)$ and $\omega_{m'}$ are the quadrature weights corresponding to the direction $\hat{s}_{m'}$.

The discrete ordinates representation of the RTE is written as

$$\alpha_m \frac{\partial I_m}{\partial x} + \beta_m \frac{\partial I_m}{\partial y} + \gamma_m \frac{\partial I_m}{\partial z} + (\kappa_a + \sigma) I_m = \kappa_a I_b + \frac{\sigma}{4\pi} \sum_{m'=1}^{M} \omega_{m'} I_{m'} \Phi(m, m') \ , \quad (6.4)$$

$$m = 1, 2, ..., M$$

where I_m is the directional radiative intensity along the direction $\hat{s}_m$; the subscripts m and m' denote the outgoing and the incoming directions respectively. The representation of incoming and outgoing directions is shown in Fig. 6.1. α_m, β_m and γ_m are the direction cosines of the discrete direction $\hat{s}_m$ along the coordinates. In Table 6.1, which can be found in Fiveland [60] and Modest [106], only positive values of the direction cosines and the associated weights are given, which cover one eighth of the total directions and of the range of solid angles, 4π, as the three-dimensional geometry in Cartesian coordinates has eight corners.

In equation (6.4), the phase function $\Phi(m, m')$ represents the fraction of the energy scattered into the outgoing direction $\hat{s}_m$ from the incoming direction $\hat{s}_{m'}$ which can be expressed as a Legendre series (Chu and Churchill [107]) as,

$$\Phi(m, m') = \sum_{n=0}^{N} (2n+1) a_n P_n(\cos\Theta) \ , \quad (6.5)$$

where $P_n(\cos\Theta)$ is the Legendre polynomials and $\cos\Theta$ can be defined as

$$\cos\Theta = \alpha_m \alpha_{m'} + \beta_m \beta_{m'} + \gamma_m \gamma_{m'} \ . \quad (6.6)$$

which measures the angle Θ between the incident and outgoing beams.

To solve the discrete ordinates representation of RTE (equation (6.4)), the boundary condition given in equation (6.2) can be rewritten in the discrete ordinates form

as

$$I_m = \varepsilon_w I_{bw} + \frac{1-\varepsilon_w}{\pi} \sum_{\substack{m'=1 \\ \alpha_{m'}<0}}^{M} \omega_{m'} |\alpha_{m'}| I_{m'} \qquad : x = -L_x/2\,, \tag{6.7}$$

$$I_m = \varepsilon_w I_{bw} + \frac{1-\varepsilon_w}{\pi} \sum_{\substack{m'=1 \\ \alpha_{m'}>0}}^{M} \omega_{m'} |\alpha_{m'}| I_{m'} \qquad : x = L_x/2\,, \tag{6.8}$$

$$I_m = \varepsilon_w I_{bw} + \frac{1-\varepsilon_w}{\pi} \sum_{\substack{m'=1 \\ \beta_{m'}<0}}^{M} \omega_{m'} |\beta_{m'}| I_{m'} \qquad : y = 0\,, \tag{6.9}$$

$$I_m = \varepsilon_w I_{bw} + \frac{1-\varepsilon_w}{\pi} \sum_{\substack{m'=1 \\ \beta_{m'}>0}}^{M} \omega_{m'} |\beta_{m'}| I_{m'} \qquad : y = L_y\,, \tag{6.10}$$

$$I_m = \varepsilon_w I_{bw} + \frac{1-\varepsilon_w}{\pi} \sum_{\substack{m'=1 \\ \gamma_{m'}<0}}^{M} \omega_{m'} |\gamma_{m'}| I_{m'} \qquad : z = -L_z/2\,, \tag{6.11}$$

$$I_m = \varepsilon_w I_{bw} + \frac{1-\varepsilon_w}{\pi} \sum_{\substack{m'=1 \\ \gamma_{m'}>0}}^{M} \omega_{m'} |\gamma_{m'}| I_{m'} \qquad : z = L_z/2\,. \tag{6.12}$$

where $I_{bw} = \frac{s_b T_w^4}{\pi}$ is the black body intensity of the combustor walls at wall temperature, T_w.

6.4 Combination of DOM with LES

Employing the Favre-filtered function (equation (3.43) of Chapter 3) to the radiative transfer equation (discrete ordinates representation), the filtered equation for the radiative heat transfer can be written as follows:

$$\alpha_m \frac{\partial \bar{I}_m}{\partial x} + \beta_m \frac{\partial \bar{I}_m}{\partial y} + \gamma_m \frac{\partial \bar{I}_m}{\partial z} + \overline{(\kappa_a + \sigma) I_m} = \overline{\kappa_a I_b} + \overline{\frac{\sigma}{4\pi} \sum_{m'=1}^{M} \omega_{m'} I_{m'} \Phi(m, m')}\,, \tag{6.13}$$

In the computational domain, the inlet and outlet boundaries are considered to be open and set to be black body absorption i.e., the emissivity of the open boundary

is taken as $\varepsilon_w = 1$, (Zheng *et al* [108], Ruan *et al* [109]), for which the radiation coming from the upstream of the inlet and downstream of the outlet do not affect the internal thermal field. According to this assumption, the filtered boundary conditions for the RTE now become,

$$\bar{I}_m = \varepsilon_w \bar{I}_{bw} + \frac{1-\varepsilon_w}{\pi} \sum_{\substack{m'=1 \\ \alpha_{m'}<0}}^{M} \omega_{m'} |\alpha_{m'}| \bar{I}_{m'} \qquad : x = -L_x/2 \,, \quad (6.14)$$

$$\bar{I}_m = \varepsilon_w \bar{I}_{bw} + \frac{1-\varepsilon_w}{\pi} \sum_{\substack{m'=1 \\ \alpha_{m'}>0}}^{M} \omega_{m'} |\alpha_{m'}| \bar{I}_{m'} \qquad : x = L_x/2 \,, \quad (6.15)$$

$$\bar{I}_m = \bar{I}_{bw} \qquad : y = 0 \,, \quad (6.16)$$

$$\bar{I}_m = \bar{I}_{bw} \qquad : y = L_y \,, \quad (6.17)$$

$$\bar{I}_m = \varepsilon_w \bar{I}_{bw} + \frac{1-\varepsilon_w}{\pi} \sum_{\substack{m'=1 \\ \gamma_{m'}<0}}^{M} \omega_{m'} |\gamma_{m'}| \bar{I}_{m'} \qquad : z = -L_z/2 \,, \quad (6.18)$$

$$\bar{I}_m = \varepsilon_w \bar{I}_{bw} + \frac{1-\varepsilon_w}{\pi} \sum_{\substack{m'=1 \\ \gamma_{m'}>0}}^{M} \omega_{m'} |\gamma_{m'}| \bar{I}_{m'} \qquad : z = L_z/2 \,. \quad (6.19)$$

where $\bar{I}_{bw} = \frac{s_b \tilde{T}_w^4}{\pi}$ is the black body intensity of the combustor walls at wall temperature, $\tilde{T}_w$. In the present computation, the wall temperature, $\tilde{T}_w$, is considered as the reference room temperature.

6.5 Sub-Grid Scale Modelling

Due to the nonlinear correlations between the turbulence and radiation, some unknown terms like $\overline{(\kappa_a + \sigma) I_m}$, $\overline{\kappa_a I_b}$, etc., appear in the radiative transfer equation (6.13). Neglecting the sub-grid scale turbulence-radiation interaction, these unknown terms can be expressed as,

$$\overline{(\kappa_a + \sigma) I_m} = (\bar{\kappa}_a + \bar{\sigma}) \bar{I}_m, \;\; \overline{\kappa_a I_b} = \bar{\kappa}_a \bar{I}_b, \;\; \text{etc.} \quad (6.20)$$

6.6 Absorption Coefficients

Absorption coefficients of both the non-luminous and luminous flame radiations are described below.

6.6.1 Non-Luminous Flame

Non-luminous radiation is assumed to occur due to the hot products of combustion mainly carbon dioxide (CO_2) and water vapour (H_2O). Thus, the absorption coefficient for CO_2 and H_2O is expressed as Magnussen and Hjertager [43] and Kaplan *et al* [63] by

$$\bar{\kappa}_a = 0.1 \left(\tilde{Y}_{CO_2} + \tilde{Y}_{H_2O} \right) \ m^{-1}, \tag{6.21}$$

where $\tilde{Y}_{CO_2}$ and $\tilde{Y}_{H_2O}$ are the mole fractions of CO_2 and H_2O respectively.

6.6.2 Luminous Flame

If the scattering particles are extremely small (*e.g.* soot particles, whose diameters are ranging between $5nm$ and $80nm$, see in Fig. 4.13 in Chapter 4), the size parameter becomes very close to zero which reduces Mie scattering to Rayleigh scattering. Therefore, the absorption coefficient for the small particles reduce to (Modest [106], DesJardin [110])

$$\kappa_a = C_0 \frac{f_v}{\lambda} \tag{6.22}$$

with

$$C_0 = \frac{36\pi nk}{(n^2 - k^2 + 2)^2 + 4n^2k^2} \tag{6.23}$$

where f_v is the soot volume fraction, λ is the wavelength of light inside the combustor, n and k are the real and imaginary component of the complex soot index of refraction , $m = n - ik$, which depends on the local composition of hydrogen to carbon atom concentrations in the soot in addition to wavelength. This refraction indices of soot for propane flame has been investigated by Dalzell and Sarofim [111], Felske *et al* [112] and Koylu and Faeth [113].

With the simple $1/\lambda$ wavelength dependence, the Plank-mean absorption coef-

ficient can be obtained as (Modest [106]):

$$\kappa_a = 3.83 C_0 f_v T / C_2, \tag{6.24}$$

where $C_2 = 1.4388 cmK$ is the Plank function constant.

After studying the available experimental data, Siegel [114] has shown that the coefficient C_0 is 4.9 for propane soot. Moreover, to facilitate calculations of C_0, Chang and Charalampopoulos [115] provided the following polynomial expression for the real and imaginary part of the refraction index that are valid for the wavelength range $0.4\mu m \leq \lambda \leq 30.0\mu m$:

$$n = 1.811 + 0.1263 ln\lambda + 0.027 ln^2\lambda + 0.0417 ln^3\lambda \tag{6.25}$$

and

$$k = 0.5821 + 0.1213 ln\lambda + 0.2309 ln^2\lambda - 0.01 ln^3\lambda \tag{6.26}$$

In combustion applications, the soot particles are irradiated by light of approximately $3\mu m$ wavelength (Modest [106]), which gives the soot refractive index from equations (6.25) and (6.26) as $n = 2.04$ and $k = 0.98$ respectively and the corresponding value of the constant C_0 is calculated from (6.23) as 5.27. Using this value of C_0 the absorption coefficient from (6.24) becomes

$$\kappa_a = 1401.82 f_v T. \tag{6.27}$$

The overall filtered absorption coefficient for the luminous flame has been calculated as a sum of the individual absorption coefficients for the mixture of CO_2 and H_2O, and the soot as

$$\bar{\kappa}_a = 0.1 \left(\tilde{Y}_{CO_2} + \tilde{Y}_{H_2O} \right) + 1401.82 \tilde{f}_v \tilde{T} \quad m^{-1}. \tag{6.28}$$

6.7 Scattering Coefficient

As already mentioned, the soot particles are generally small and spherical, ranging in size between $5nm$ and $80nm$ and which in combustion applications are irradiated by light of approximately $\lambda = 3\mu m$ (Modest [106]). Therefore, the size parameter

$x = \frac{2\pi a}{\lambda} \rightarrow 0$ (a is the particle diameter) reduces Mie scattering to Rayleigh scattering. In Rayleigh scattering, the efficiency factors for scattering and absorption are given respectively as follows:

$$Q_{sca} = \frac{8}{3}\left|\frac{m^2-1}{m^2+2}\right|^2 x^4 \tag{6.29}$$

and

$$Q_{abs} = -4Im\left(\frac{m^2-1}{m^2+2}\right)x. \tag{6.30}$$

Due to the fact that $x^4 \ll x$, the scattering may be neglected. This fact can clearly be demonstrated from Fig. 6.2, where the axial profiles of these scattering and absorption efficiency factors are presented, respectively in frame (a) and (b), which are obtained using the above relations (6.29-6.30) together with the use of the soot particle diameter presented in Fig. 4.13(a) of Chapter 4. This figure shows that the order of absorption efficiency is $O(10^{-2})$ while the scattering efficiency has a order of $O(10^{-6})$, which suggests that the scattering may be neglected. Moreover, some experimental measurements also confirm that the scattering may indeed be neglected (see Modest [106]). Suydam [116] investigated the scattering and absorption of light by soot particles. He concluded that, of the total extinction cross section, about 93% arises from absorption and only 7% from scattering.

6.8 Radiation Modelling

For the radiation modelling, it is considered that the cylindrical combustor contains an absorbing-emitting and radiatively grey medium which means that the emissivity and the absorptivity do not depend on the wavelength. Discussion in §6.7 suggests that the medium is highly dominated by the absorption and the scattering effect is negligibly small. Moreover, the scattering is not an important issue for combustion gases (and soot particles), as mentioned by Viskanta and Menguc [117]. Therefore, we have neglected the effect of scattering in the present study, i.e., we take $\sigma = 0$. According to these, the RTE equation (6.13) can be rewritten as,

$$\alpha_m \frac{\partial \bar{I}_m}{\partial x} + \beta_m \frac{\partial \bar{I}_m}{\partial y} + \gamma_m \frac{\partial \bar{I}_m}{\partial z} = \bar{\kappa}_a \bar{I}_b - \bar{\kappa}_a \bar{I}_m. \tag{6.31}$$

6.9 Important Radiation Quantities

The radiative heat flux vectors, $\bar{\mathbf{q}}$, can be calculated from

$$\bar{\mathbf{q}} = \int_{4\pi} \bar{I}\hat{s}d\Omega \approx \sum_{m=1}^{M} \omega_m \bar{I}_m \hat{s}_m. \tag{6.32}$$

The net wall radiative heat fluxes, $\bar{\mathbf{q}}_n$, are defined as

$$\bar{\mathbf{q}}_n = \varepsilon_w \left(\bar{\mathbf{q}}_{in} - \pi \bar{I}_{bw} \right). \tag{6.33}$$

where $\bar{\mathbf{q}}_{in}$ is the incoming radiative heat flux.

The magnitude of the radiative heat fluxes, for example on yz plane, can be obtained from

$$|\bar{\mathbf{q}}| = \left(\bar{q}_y^2 + \bar{q}_z^2 \right)^{1/2}. \tag{6.34}$$

The divergence of the radiative heat fluxes, $\nabla.\bar{\mathbf{q}}$, which determines the net energy loss or gain due to the radiation, can be calculated from the following relation

$$\nabla.\bar{\mathbf{q}} = 4\pi\bar{\kappa}_a\bar{I}_b - \int_{4\pi} \bar{\kappa}_a \bar{I} d\Omega. \tag{6.35}$$

Another important radiation quantity is the incident radiation, $\bar{G}_r$, which is calculated as

$$\bar{G}_r = \int_{4\pi} \bar{I} d\Omega \approx \sum_{m=1}^{M} \omega_m \bar{I}_m. \tag{6.36}$$

6.10 Results and Discussion

The radiation results for both the luminous and non-luminous flames presented in this section are obtained considering the open inlet and outlet boundary and set to be black body absorption i.e., the emissivity of the both open boundary is taken as, $\varepsilon_w = 1.0$, for which the radiation coming from the upstream of the inlet and downstream of the outlet do not affect the internal thermal field (Zhang *et al* [108], Ruan *et al* [109]). The combustor wall temperature is kept fixed at the reference room temperature (like as Desjardin and Frankel [48]). A short domain of the cylindrical

combustor is considered for the radiation calculation and a schematic of this short computational domain is already shown in Fig. 4.1 of Chapter 4.

6.10.1 Luminous Results

In Fig. 6.3 the incident radiation for various orders of DOM (S_n) is presented to show the effects of the order of approximations of DOM, where the wall emissivity is kept at $\varepsilon_w = 0.5$ for all the approximations. The incident radiation is an important radiation property related to the radiative energy density, by which the total radiation energy is stored in each computational node. In Fig. 6.3(a) the axial profiles on the centerline of the combustor are shown whereas the radial profiles at the different cross-sectional positions are plotted in Fig. 6.3(b-d). It can be seen from Fig. 6.3(a-d) that the incident radiation obtained by using the lower order approximation, S_2, of the DOM diverges a little bit from those with the higher order approximations. The higher order approximations (S_4, S_6 and S_8) converge together.

The effect of wall emissivity, which is defined as the ratio of the radiation emitted by the wall to the radiation emitted by the black body, on the incident radiation, $\bar{G}_r$, is shown in Fig. 6.4. The results are plotted for the different values of wall emissivity, $\varepsilon_w = 0.1, 0.2, 0.3, 0.5, 0.9$ with the S_6 approximation. The axial profiles along the centerline are plotted in frame (a), while the radial profiles at the different cross-sectional positions are presented in frames (b) $y = 0.1m$, (c) $y = 0.2m$ and (d) $y = 0.3m$. Fig. 6.4(a-d) shows that the low wall emissivity leads to a higher value in the entire incident radiation. With the increasing values of the wall emissivity the incident radiation decreases, as low wall emissivity reduces the heat loses by the radiation to the surroundings, so more energy is re-radiated into the combustor which in turn increases the entire incident radiation and vice-versa.

Furthermore, from Figs. 6.3(a) and 6.4(a), the axial profile along the centerline shows that the incident radiation increases towards the downstream of the combustor as the soot volume fraction profile (see Fig. 4.11(a) of Chapter 4) increases, which is significant and consistent with the temperature profile (see Fig. 3.8(a) of Chapter 3). The peak value of the incident radiation is found at the location where the peak value of temperature as well as the soot volume fraction were achieved. From the peak level, the incident radiation decreases rapidly towards the outlet de-

spite the slowly decreasing in temperature and soot volume fraction profiles in this region. The reason behind this slight inconsistency is due to the consideration of the open outlet boundary with the reference room temperature at the high temperature region.

In Figs. 6.3 and 6.4, the radial profiles of the entire incident radiation, plotted in frames (b) and (c) which are closed to the inlet, show that the peak values of the incident radiation are predicted around the center of the combustor. But at the downstream region (frame (d)) the peak value is shifted towards the combustor wall because of the high level of soot volume fraction as well as absorption coefficient predicted in this location which can clearly be seen in frames (d) and (e) of Fig. 6.5. In addition, it can also be seen from all the radial profiles that the incident radiation decreases towards the combustor wall having its minimum value at the wall.

In Fig. 6.5(a-d) instantaneous results of the temperature, mole fractions of CO_2 and H_2O, and soot volume fraction, $\tilde{f}_v$, are plotted respectively on the horizontal midplane of the combustor. The black body radiation, $\bar{I}_b$, is a function of temperature and absorption coefficient, where the absorption coefficient for the luminous flame is again a function of mole fractions, $\tilde{Y}_{CO_2}$ and $\tilde{Y}_{H_2O}$, soot volume fraction and temperature. Thus, these results are required as an input for the radiation sources.

The absorption coefficient, $\bar{\kappa}_a$, plotted in Fig. 6.5(e) shows that it is high in the region where the soot volume fraction as well as the temperature is large, clearly dominating by the soot volume fraction as well as the temperature rather than the mole fractions of CO_2 and H_2O, which proves the fact that the soot is the highly dominant element of the absorbing-emitting medium.

The results of the other radiation quantities are depicted in Fig. 6.5(f-j) on the horizontal midplane of the combustor. The total radiative intensity, $\bar{I}$, plotted in frame (f), shows that it is maximum at the region where the absorption coefficient, $\bar{\kappa}_a$, is maximum. Similar pattern but different magnitude can be found in the incident radiation, $\bar{G}_r$, depicted in frame (g), as this is obtained by summing over the total radiation multiplied by the weight factors in each direction. The radiative heat flux vector, $\bar{\mathbf{q}}$, presented in frame (h), shows that the radiation transport is directed from the sooting region where the values of the absorption coefficient, $\bar{\kappa}_a$, found maximum. In frame (i) the magnitude of the radiative heat flux, $|\bar{\mathbf{q}}|$, shows again clearly that the radiative heat flux is maximum where the soot volume fraction as

well as the absorption coefficient is maximum. As the length of each radiative heat flux vectors is directly proportional to its magnitude, these plots also show that the strongest radiative flux is emanating from the sooting region. An important quantity of the radiation transport is the divergence of the radiative heat flux, $\nabla.\bar{\mathbf{q}}$, which measures the net energy loss or gain due to the radiation, is depicted in frame (j), showing a massive amount of net energy gain due to the radiation in the highly sooting region.

The quantities plotted in Fig. 6.5(a-j) on the horizontal midplane are also plotted at the different cross-sectional positions, $y = 0.1m$ (left column), $y = 0.2m$ (middle column) and $y = 0.3m$ (right column), in Fig. 6.6(a-j). From all these cross-sectional plots, it is clear that all the radiation properties attain maximum in the region where the absorption coefficient as well as the soot volume fraction are maximum. As the absorption coefficient is dominated mostly by the soot volume fraction, so the radiation properties are also dominated by the presence of soot in the flame.

The net radiative heat fluxes, $\bar{\mathbf{q}}_n(kWm^{-2})$, on the four boundary walls: (a) $z = -L_z/2$, (b) $z = L_z/2$, (c) $x = -L_x/2$ and (d) $x = L_x/2$ of the combustor are presented in Fig. 6.7. The dashed lines in these figures indicate the negative contour. At the center of the downstream region of the wall, $z = -L_z/2$, no heat gain/loss can be found but at the same location of the opposite wall, $z = L_z/2$, the wall gains heat by the radiative transfer, however, these two opposite walls lose heat. The other opposite walls, $x = -L_x/2$ and $x = L_x/2$, lose heat at every location and this heat loss is found to be high at the downstream. The maximum heat loss by the radiative transfer can be found on the wall, $x = L_x/2$, at the downstream region.

6.10.2 Non-Luminous Results

To compare the effects of radiative heat transfer between the luminous and non-luminous flame, we present the results for non-luminous flame in Figs. 6.8-6.12 in a similar fashion as shown for the luminous flame.

The incident radiation, $\bar{G}_r$, for different S_n approximations with the fixed wall emissivity of $\varepsilon_w = 0.5$ as well as for different wall emissivity, ε_w, with the S_6 approximation are presented respectively in Figs. 6.8 and 6.9. Fig. 6.8(a-d) shows

that both the axial and radial profiles of the incident radiation predicted with the lower order approximation (S_2) diverges from those predicted with the higher order approximations i.e., S_4, S_6 and S_8, while the higher order approximations converge together. Similar to the results for the luminous flame, both the axial and radial profiles of the incident radiation, presented in Fig. 6.9(a-d), show that the value of the incident radiation increases with the decreasing value of the wall emissivity. The shape of the axial profiles (frame (a) of both the Figs. 6.8 and 6.9) are similar to those of the luminous flame, however, the peak value of all the radial profiles is found around the center of the combustor which is a little unlikely that the radial profiles for the luminous flame. The incident radiation in the non-luminous flame is found lower than that of the luminous flame because of the lower level of the absorption coefficient found in the non-luminous flame.

The instantaneous values of (a) the temperature, the mole fractions of (b) CO_2 and (c) H_2O, (d) the absorption coefficient ($\bar{\kappa}_a$), (e) total radiation ($\bar{I}$), (f) the incident radiation ($\bar{G}_r$), (g) the radiative heat flux vector ($\bar{\mathbf{q}}$), (h) magnitude of the heat flux ($|\bar{\mathbf{q}}|$) and (i) the divergence of the radiative heat flux ($\nabla.\bar{\mathbf{q}}$) are plotted on the horizontal midplane in Fig. 6.10 while the above quantities at different cross-sectional positions, $y = 0.1m$ (left column), $y = 0.2m$ (middle column) and $y = 0.3m$ (right column), are presented in Fig. 6.11(a-i). The absorption coefficient, $\bar{\kappa}_a$, in Figs. 6.10(d) and 6.11(d), shows that it is higher in the region where the temperature as well as the mole fractions of CO_2 and H_2O, has higher values. Thus it is clear that the radiation in the non-luminous flame is highly dominated by the CO_2 and H_2O gases.

The other radiation properties such as total radiation ($\bar{I}$), incident radiation ($\bar{G}_r$), magnitude of radiative heat flux ($|\bar{\mathbf{q}}|$) and divergence of the radiative heat flux ($\nabla.\bar{\mathbf{q}}$) are found maximum at the region where the absorption coefficient ($\bar{\kappa}_a$) and the temperature are maximum. Thus, the radiation properties for the non-luminous flame are dominated by the absorption coefficient as well as the flame temperature.

The net wall radiative heat fluxes, $\bar{\mathbf{q}}_n(kWm^{-2})$, on the four boundary walls: (a) $z = -L_z/2$, (b) $z = L_z/2$, (c) $x = -L_x/2$ and (d) $x = L_x/2$ of the combustor are presented in Fig. 6.12. The dashed lines in these figures again indicate the negative contour. These figures show that all the combustor walls lose heat by the radiative heat transfer and these heat loses can be found high at the downstream. The amount

of heat loses from the non-luminous flame is found to be higher than those of the luminous flame.

6.11 Conclusion

The Discrete Ordinates Method (DOM/S_n) with the Large Eddy Simulation (LES) has been employed to investigate the radiative heat transfer for the luminous as well as the non-luminous flame in the three-dimensional cylindrical combustor. The absorption coefficient for the luminous flame, expressed in equation (6.28), has been calculated as a function of the mole fractions of CO_2 and H_2O, the soot volume fraction ($\tilde{f}_v$) and the temperature, while for the non-luminous flame, given in equation (6.21), it is a function of mole fractions of CO_2 and H_2O only. The scattering coefficient, described in §6.7, was negligible compared to the absorption coefficient and thus the scattering effects were neglected in the present study.

The instantaneous values of the total radiation, incident radiation, radiative heat flux, and the divergence of heat flux for both the non-luminous and luminous flame have been obtained and presented. For both the luminous and non-luminous flame, the above radiation properties are found to be dominated by the absorption coefficient. Due to the high absorption coefficient predicted in the luminous flame, these radiation properties are found higher than those for the non-luminous flame.

The net wall radiative heat fluxes are also calculated. For the luminous flame, the combustor walls lose heat at most places but gain heat at a particular location of one wall in the downstream region whereas for the non-luminous flame, all the walls lose heat by the radiative heat transfer.

It should be noted here that the amount of heat losses must be taken into account for the accurate prediction of the flame temperature and combustion species, and this can be done by coupling the divergence of the radiative heat fluxes, $\nabla.\bar{\mathbf{q}}$, with the overall energy conservation equation.

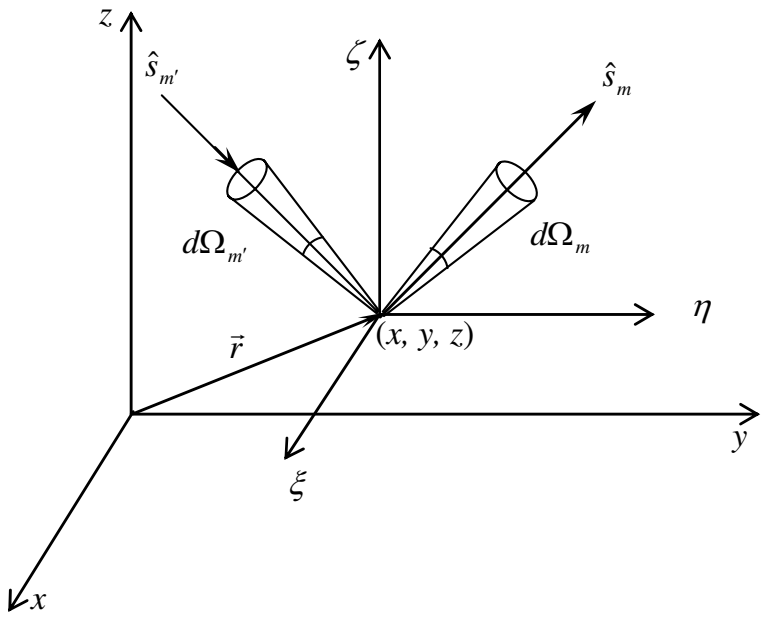

Figure 6.1: Representation of the angular coordinates and the solid angles ($d\Omega_m, d\Omega_{m'}$) along the incoming ($\hat{s}_{m'}$) and outgoing ($\hat{s}_m$) directions.

Table 6.1: Discrete ordinates for the S_n approximations for the first quadrant.

S_n	Ordinates			Weights
	α_m	β_m	γ_m	ω_m
S_2	0.5773503	0.5773503	0.5773503	1.5707963
S_4	0.2958759	0.2958759	0.9082483	0.5235987
	0.2958759	0.9082483	0.2958759	0.5235987
	0.9082483	0.2958759	0.2958759	0.5235987
S_6	0.1838670	0.1838670	0.9656013	0.1609517
	0.1838670	0.6950514	0.6950514	0.3626469
	0.1838670	0.9656013	0.1838670	0.1609517
	0.6950514	0.1838670	0.6950514	0.3626469
	0.6950514	0.6950514	0.1838670	0.3626469
	0.9656013	0.1838670	0.1838670	0.1609517
S_8	0.1422555	0.1422555	0.9795543	0.1712359
	0.1422555	0.5773503	0.8040087	0.0992284
	0.1422555	0.8040087	0.5773503	0.0992284
	0.1422555	0.9795543	0.1422555	0.1712359
	0.5773503	0.1422555	0.8040087	0.0992284
	0.5773503	0.5773503	0.5773503	0.4617179
	0.5773503	0.8040087	0.1422555	0.0992284
	0.8040087	0.1422555	0.5773503	0.0992284
	0.8040087	0.5773503	0.1422555	0.0992284
	0.9795543	0.1422555	0.1422555	0.1712359

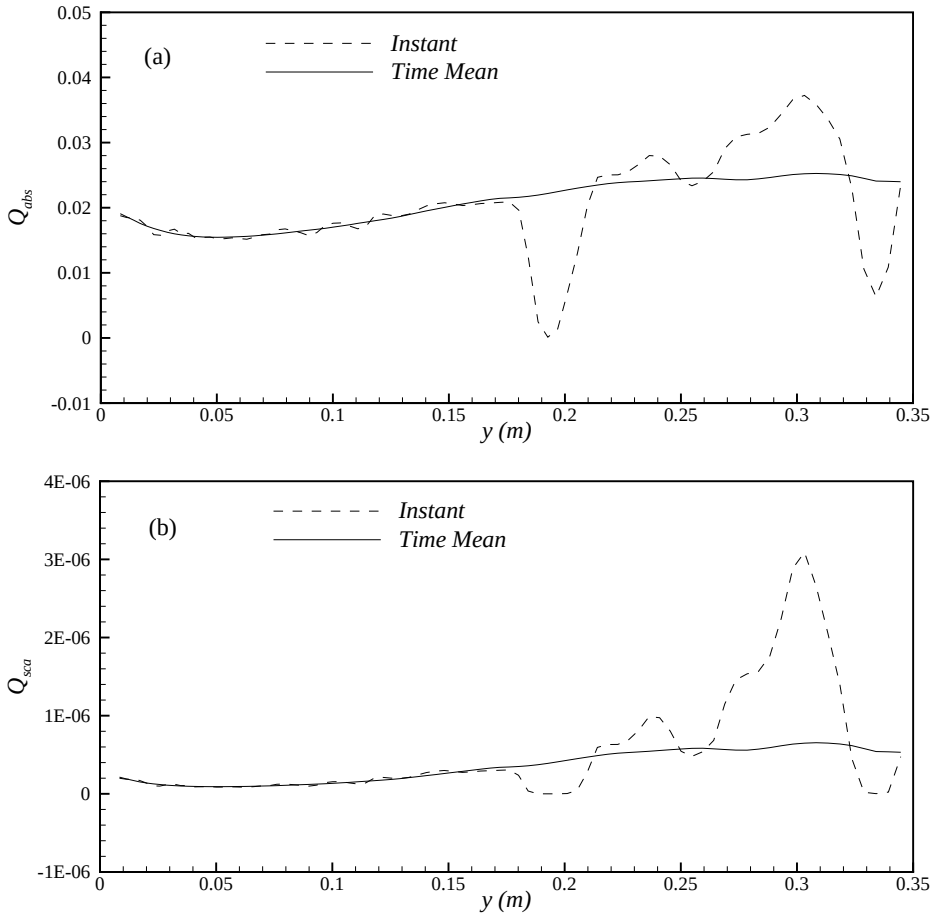

Figure 6.2: A comparison between the (a) absorption and (b) scattering efficiencies.

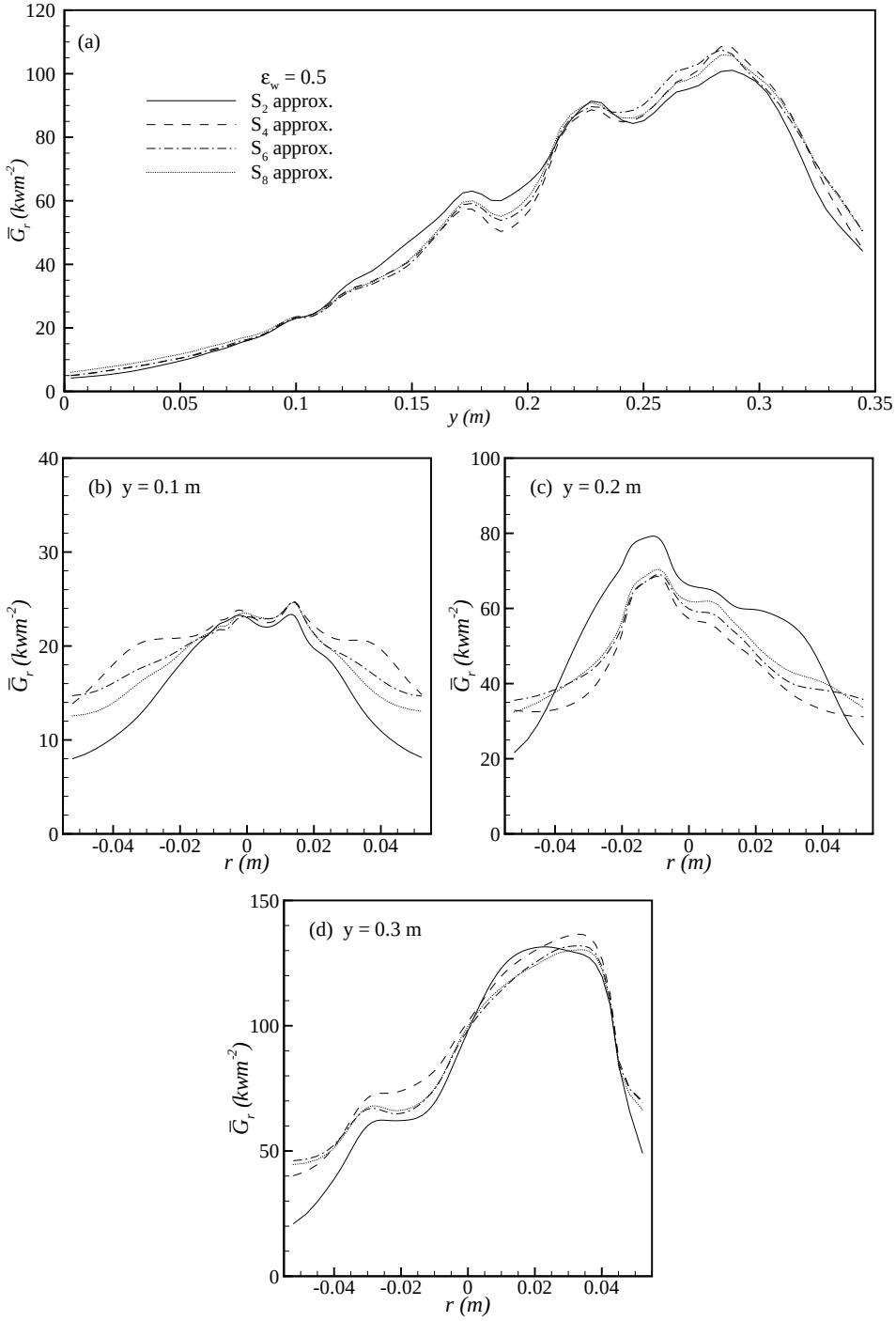

Figure 6.3: Incident radiation, $\bar{G}_r(kWm^{-2})$, for the luminous flame along (a) the axial direction, and the radial direction at the different cross-sectional positions: (b) $y = 0.1m$, (c) $y = 0.2m$ and (d) $y = 0.3m$ for the different S_n approximations taking the wall emissivity, $\varepsilon_w = 0.5$.

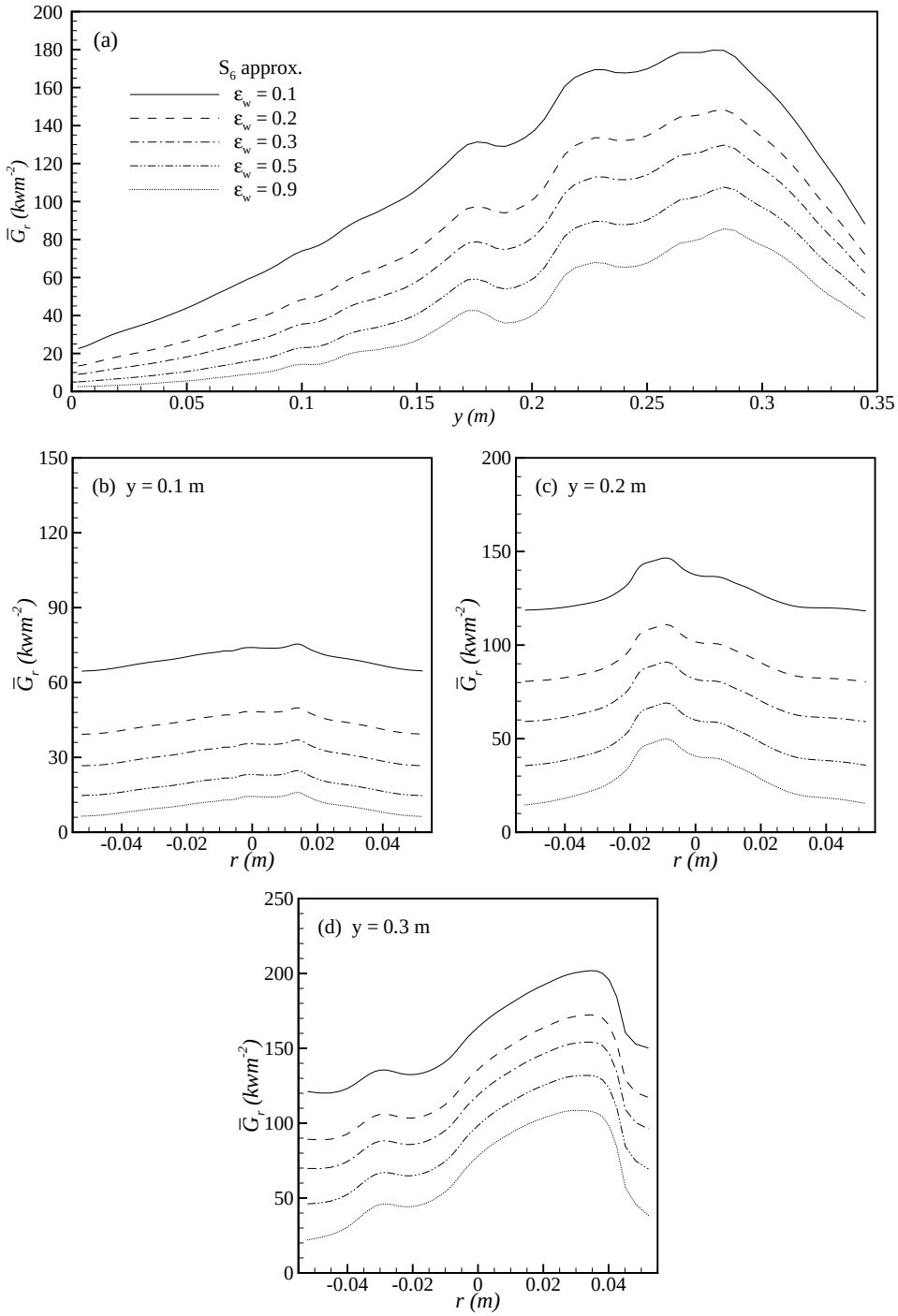

Figure 6.4: Incident radiation, $\bar{G}_r(kWm^{-2})$, for the luminous flame along (a) the axial direction, and the radial direction at the different cross-sectional positions: (b) $y = 0.1m$, (c) $y = 0.2m$, (d) $y = 0.3m$ for the different wall emissivity, ε_w.

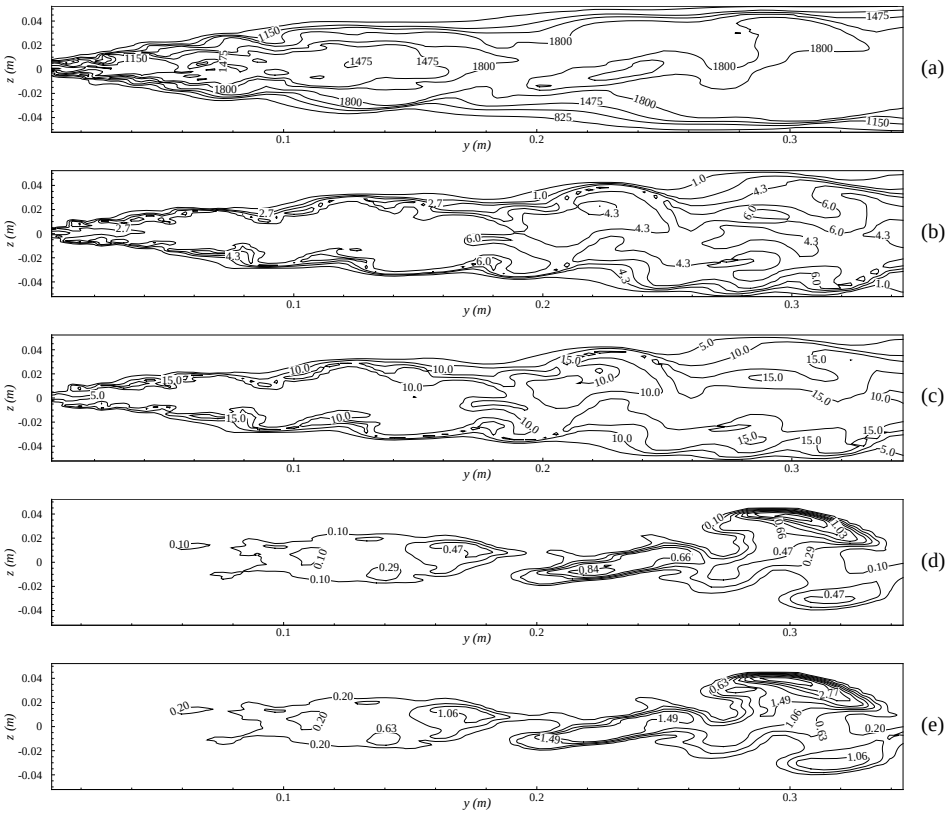

Figure 6.5: Instantaneous contour plots of (a) $\tilde{T}(K)$, (b) $\tilde{Y}_{CO_2} \times 10^{-2}$, (c) $\tilde{Y}_{H_2O} \times 10^{-2}$, (d) $\tilde{f}_v(ppm)$, (e) $\bar{\kappa}_a(m^{-1})$, (f) $\bar{I}(kWm^{-2})$, (g) $\bar{G}_r(kWm^{-2})$, (h) $\bar{\mathbf{q}}$, (i) $|\bar{\mathbf{q}}|(kWm^{-2})$ and (j) $\nabla.\bar{\mathbf{q}}(kWm^{-3})$ for the luminous flame on the horizontal mid-plane of the combustor.

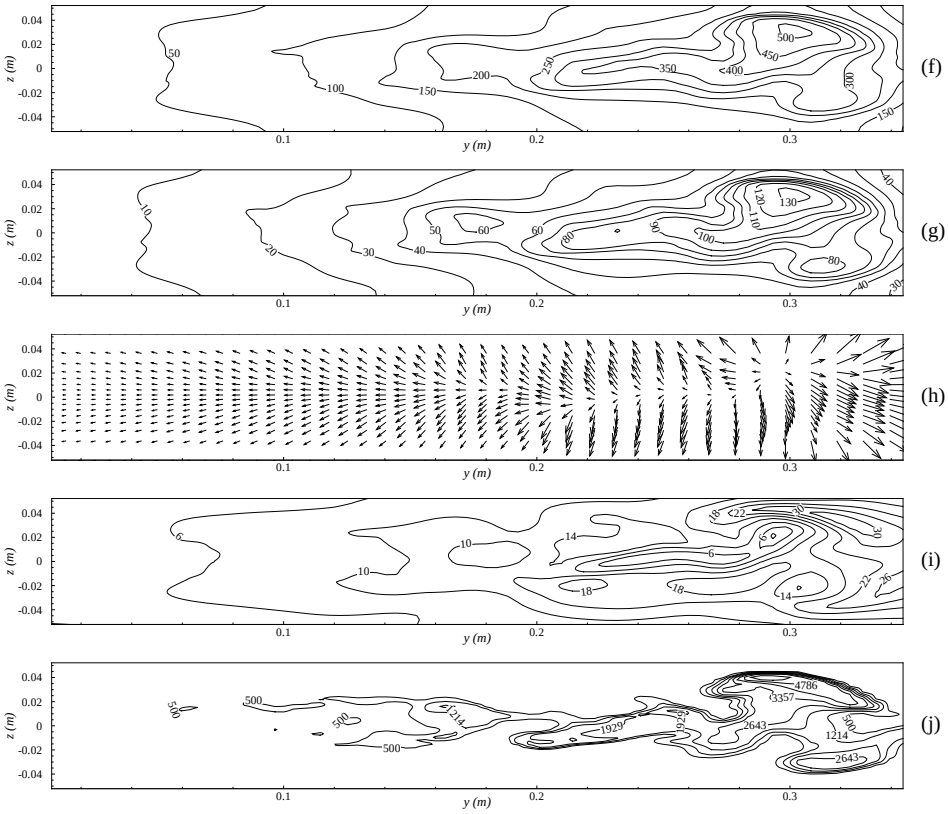

Figure 6.5: (continued)

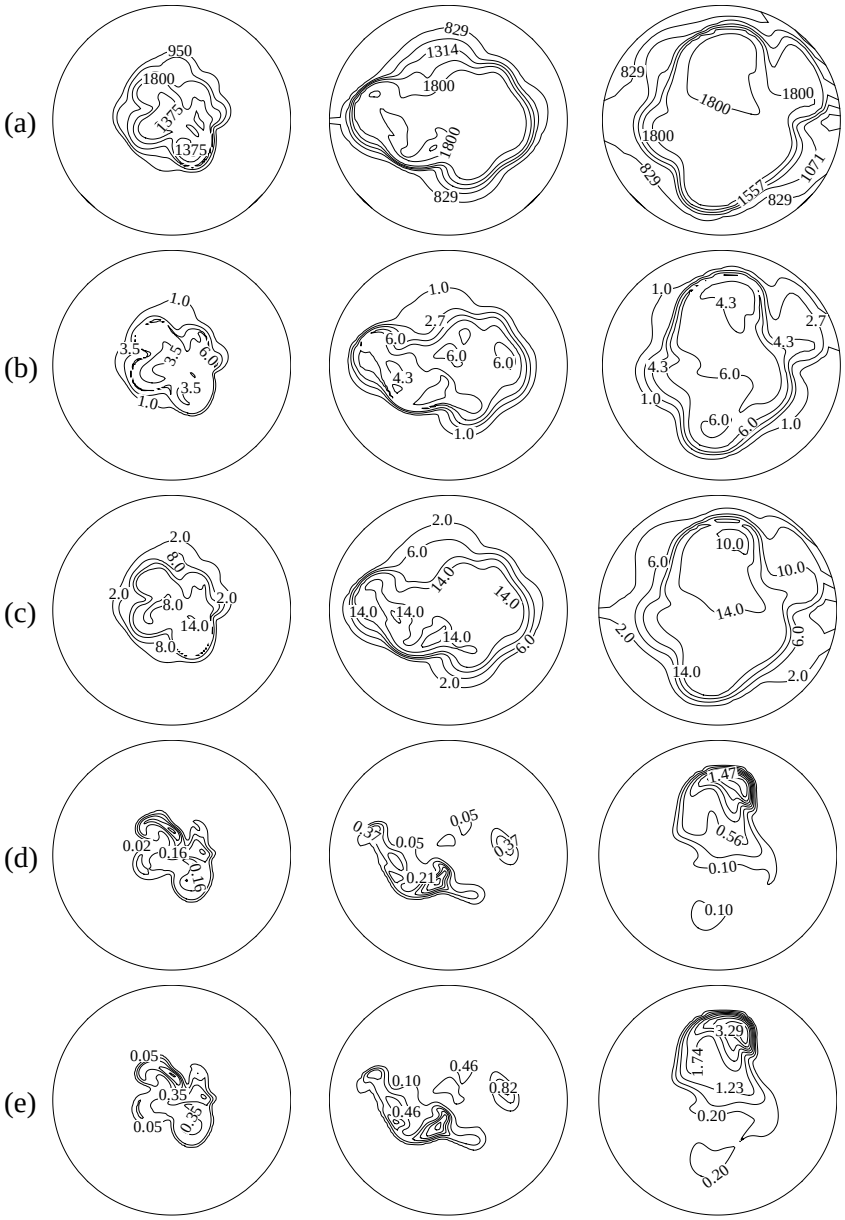

Figure 6.6: Instantaneous contour plots of (a) $\tilde{T}(K)$,(b) $\tilde{Y}_{CO_2} \times 10^{-2}$, (c) $\tilde{Y}_{H_2O} \times 10^{-2}$, (d) $\tilde{f}_v(ppm)$, (e) $\bar{\kappa}_a(m^{-1})$, (f) $\bar{I}(kWm^{-2})$,(g) $\bar{G}_r(kWm^{-2})$, (h) $\bar{\mathbf{q}}$, (i) $|\bar{\mathbf{q}}|(kWm^{-2})$ and (i) $\nabla.\bar{\mathbf{q}}(kWm^{-3})$ for the luminous flame at the different cross-sectional positions: $y = 0.1m$ (left column), $y = 0.2m$ (middle column) and $y = 0.3m$ (right column) of the combustor.

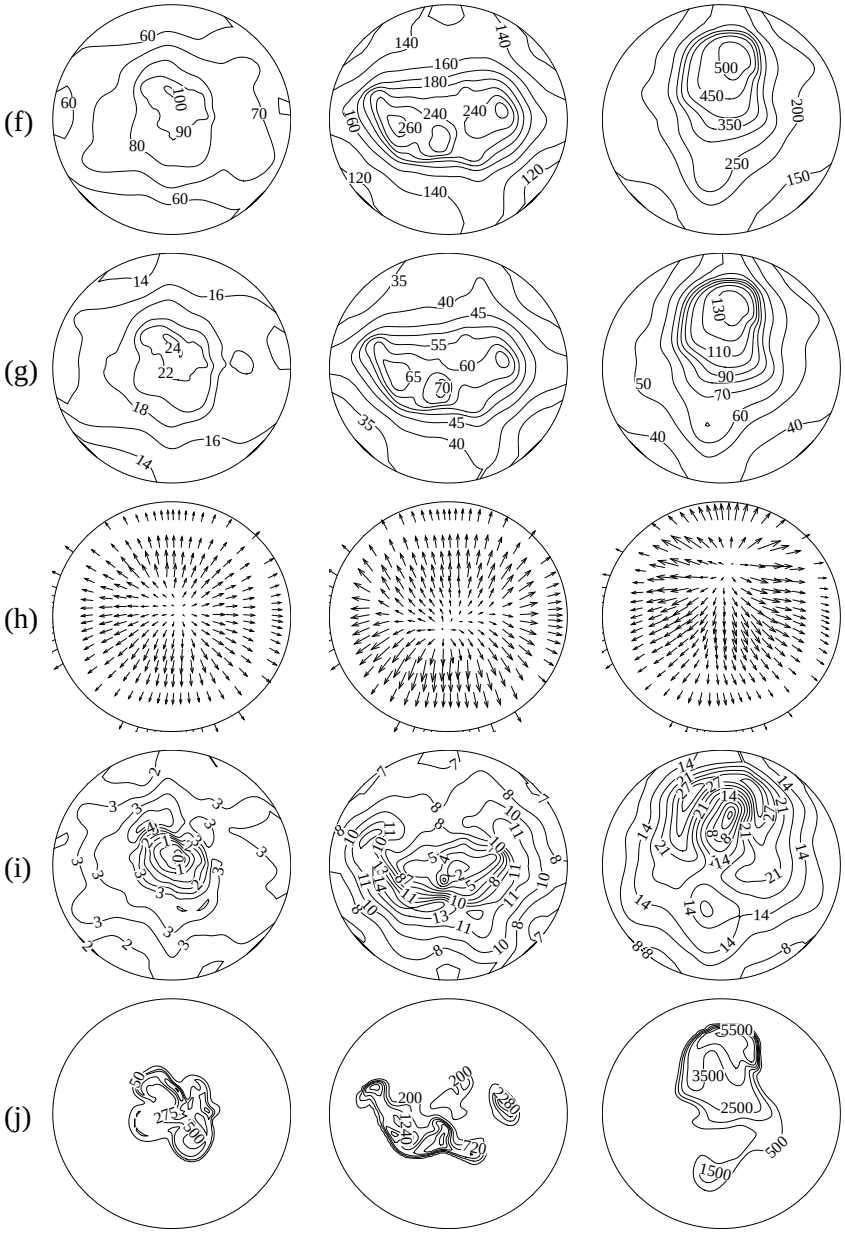

Figure 6.6: (continued)

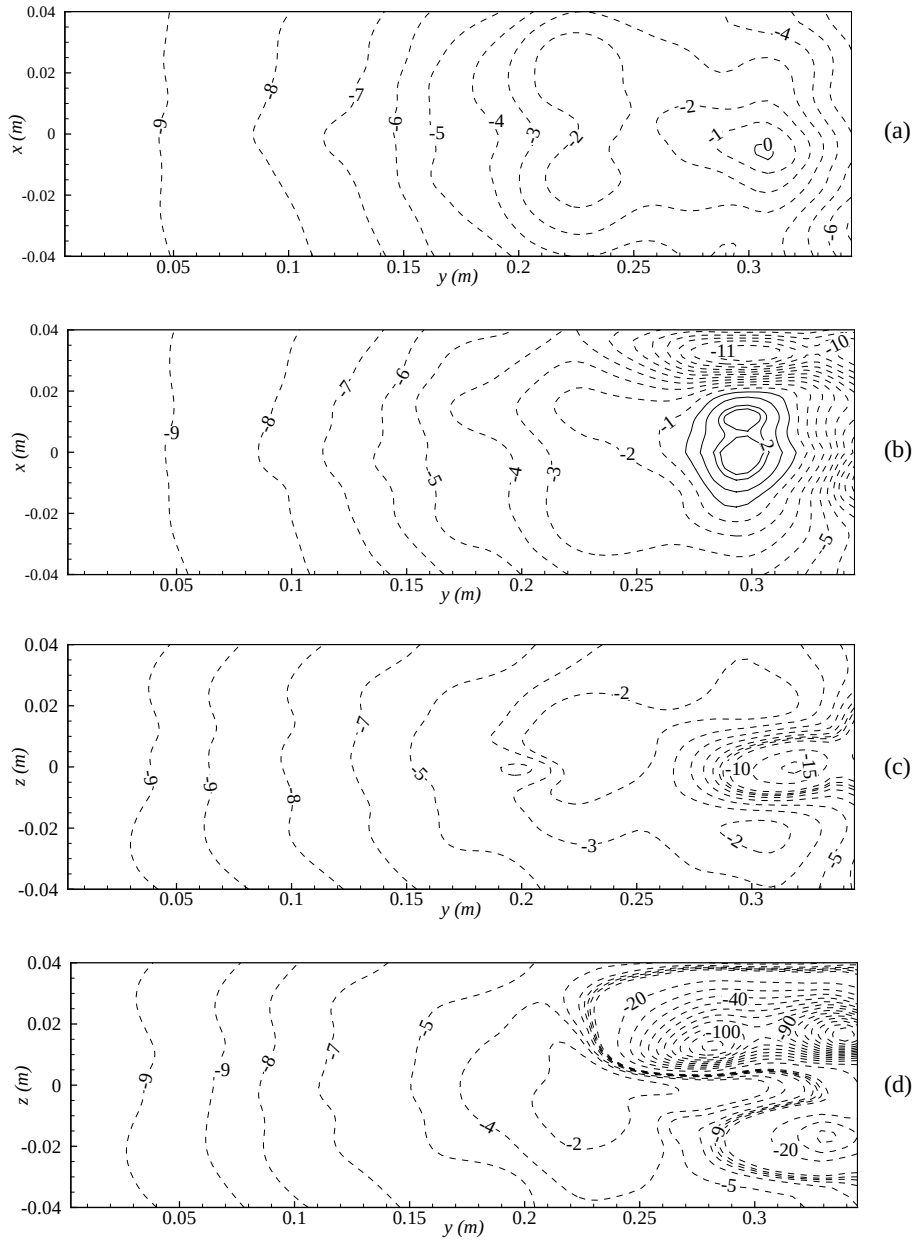

Figure 6.7: The net radiative heat fluxes, $\bar{\mathbf{q}}_n(kWm^{-2})$, for the lumonous flame on the walls of the combustor: (a) $z = -L_z/2$, (b) $z = L_z/2$, (c) $x = -L_x/2$ and (d) $x = L_x/2$.

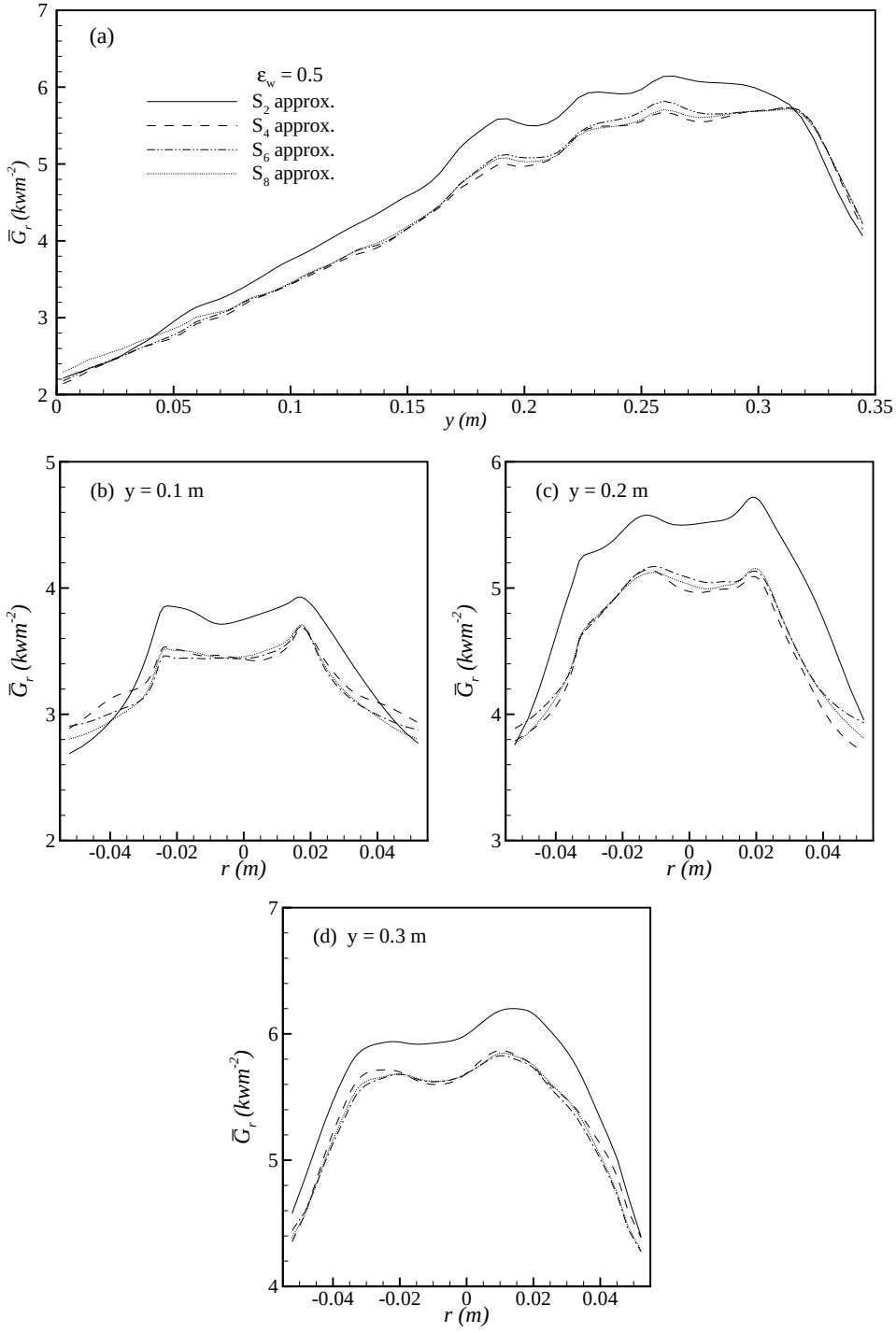

Figure 6.8: Incident radiation, $\bar{G}_r(kWm^{-2})$, for the non-luminous flame along (a) the axial direction, and the radial direction at the different cross-sectional positions: (b) $y = 0.1m$, (c) $y = 0.2m$ and (d) $y = 0.3m$ for the different S_n approximations taking the wall emissivity, $\varepsilon_w = 0.5$.

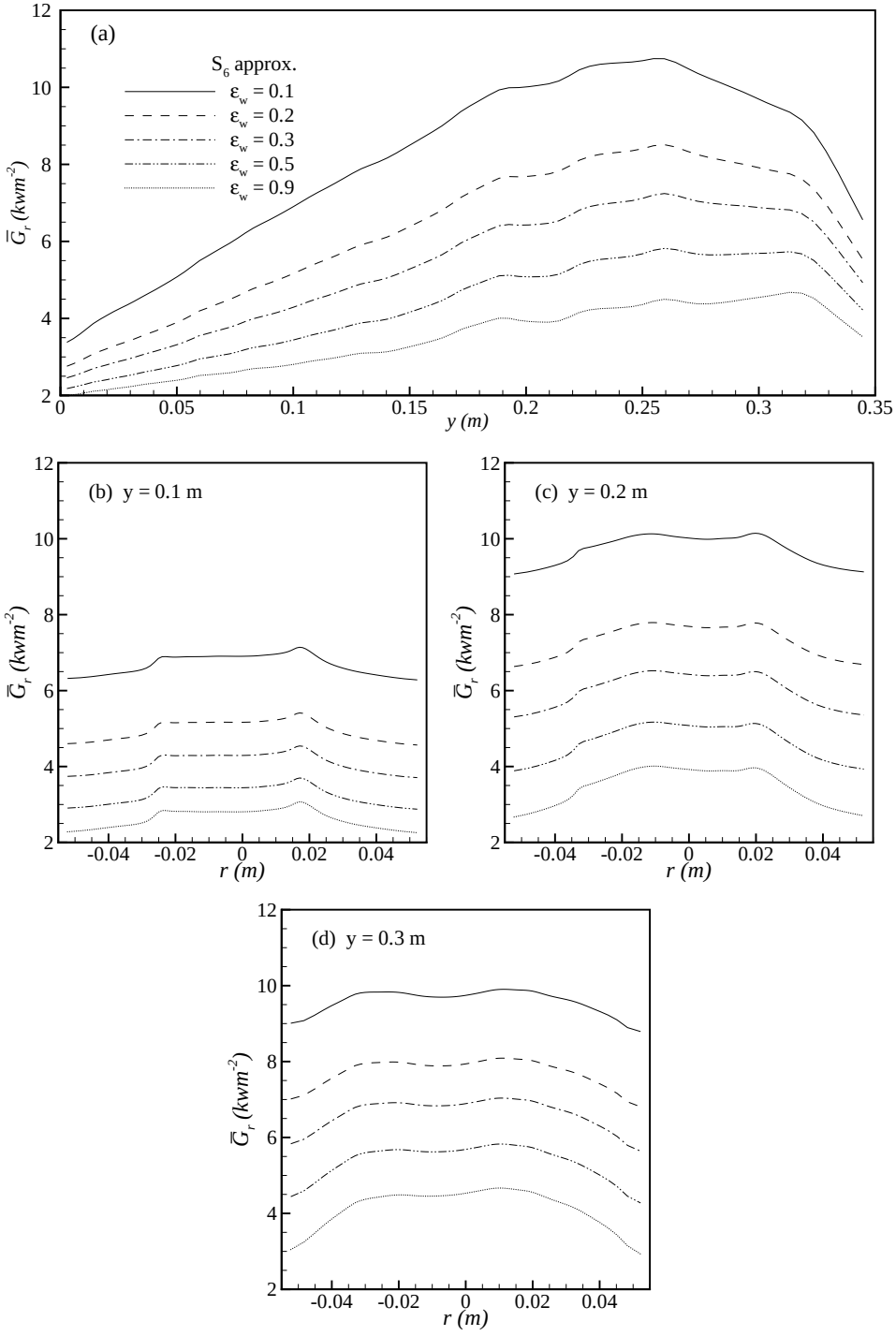

Figure 6.9: Incident radiation, $\bar{G}_r(kWm^{-2})$, for the non-luminous flame along (a) the axial direction, and the radial direction at the different cross-sectional positions: (b) $y = 0.1m$, (c) $y = 0.2m$, (d) $y = 0.3m$ for the different wall emissivity, ε_w.

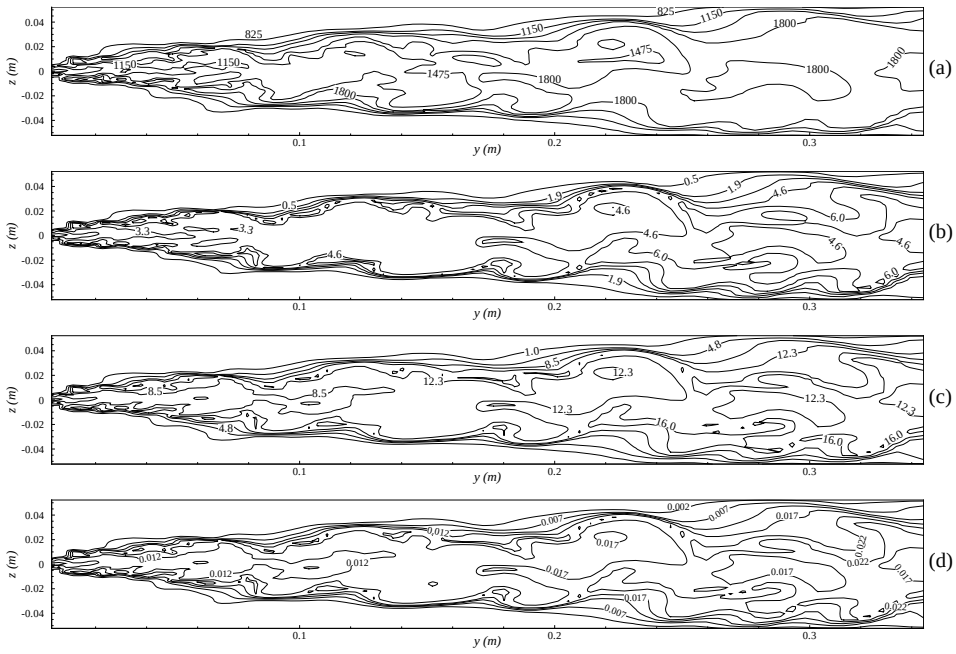

Figure 6.10: Instantaneous contour plots of (a) $\tilde{T}(K)$, (b) $\tilde{Y}_{CO_2} \times 10^{-2}$, (c) $\tilde{Y}_{H_2O} \times 10^{-2}$, (d) $\bar{\kappa}_a(m^{-1})$, (e) $\bar{I}(kWm^{-2})$, (f) $\bar{G}_r(kWm^{-2})$, (g) $\bar{\mathbf{q}}$, (h) $|\bar{\mathbf{q}}|(kWm^{-2})$ and (i) $\nabla.\bar{\mathbf{q}}(kWm^{-3})$ for the non-luminous flame on the horizontal mid-plane of the combustor.

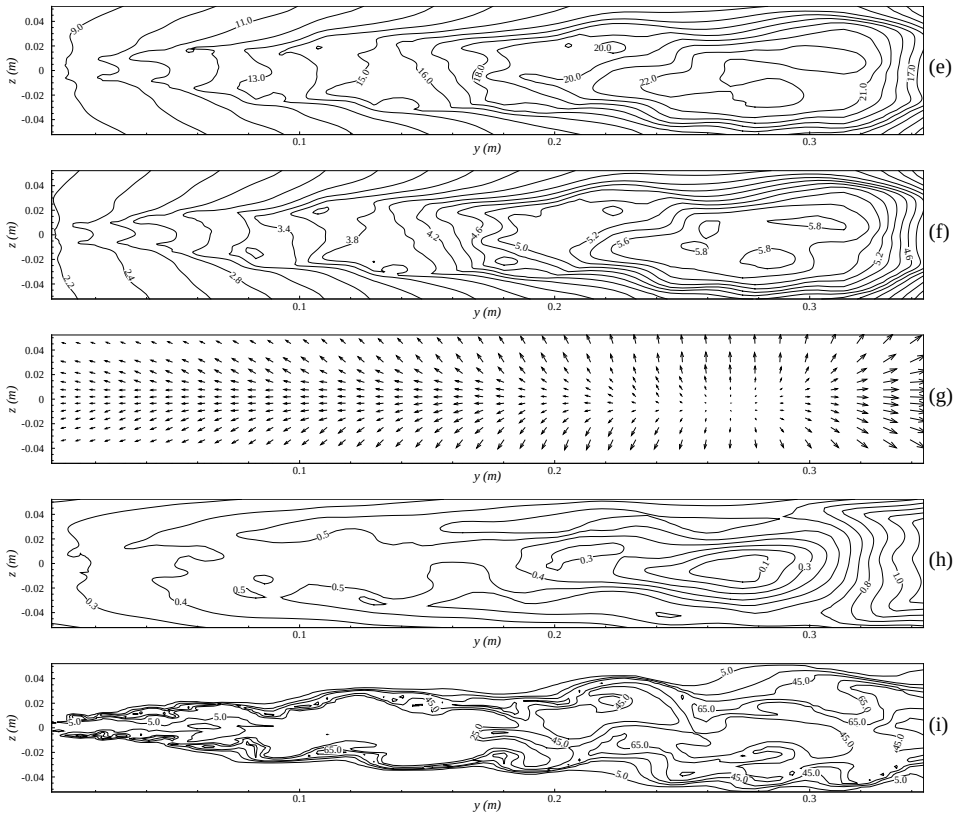

Figure 6.10: (continued)

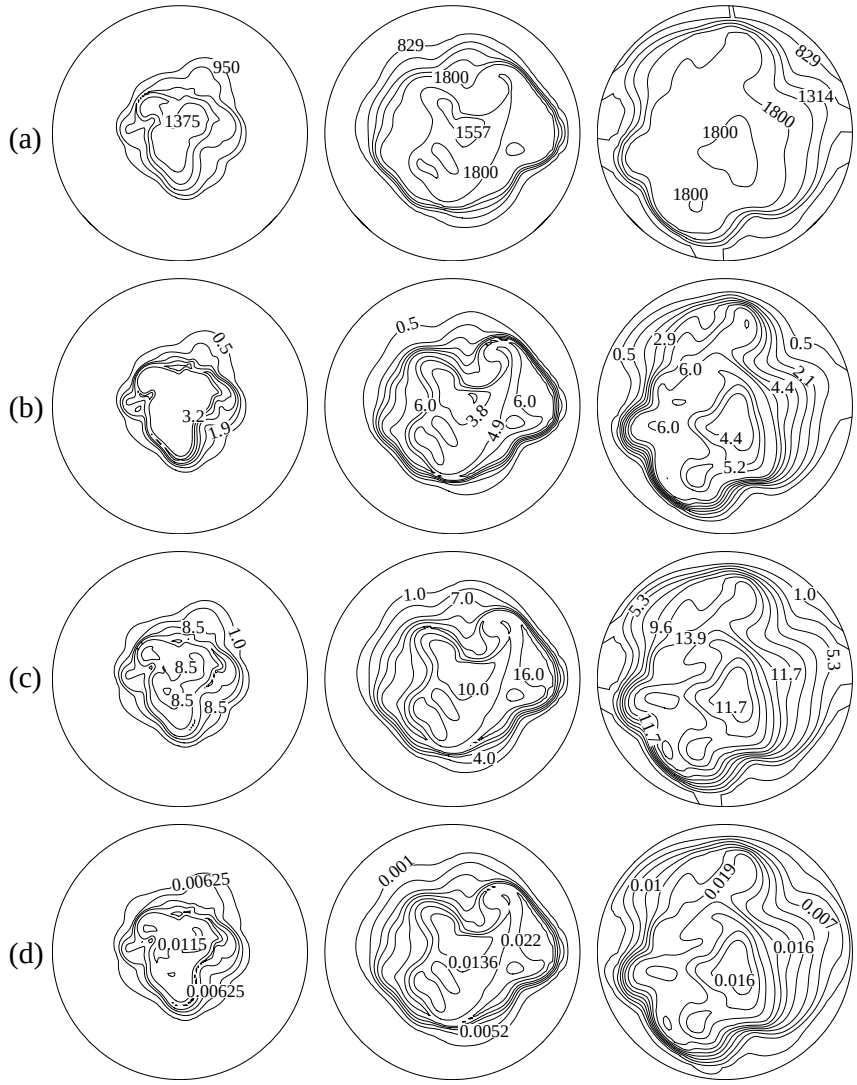

Figure 6.11: Instantaneous contour plots of (a) $\tilde{T}(K)$, (b) $\tilde{Y}_{CO_2} \times 10^{-2}$, (c) $\tilde{Y}_{H_2O} \times 10^{-2}$, (d) $\bar{\kappa}_a(m^{-1})$, (e) $\bar{I}(kWm^{-2})$, (f) $\bar{G}_r(kWm^{-2})$, (g) $\bar{\mathbf{q}}$, (h) $|\bar{\mathbf{q}}|(kWm^{-2})$ and (i) $\nabla.\bar{\mathbf{q}}(kWm^{-3})$ for the non-luminous flame at different cross-sectional positions: $y = 0.1m$ (left column), $y = 0.2m$ (middle column) and $y = 0.3m$ (right column) of the combustor.

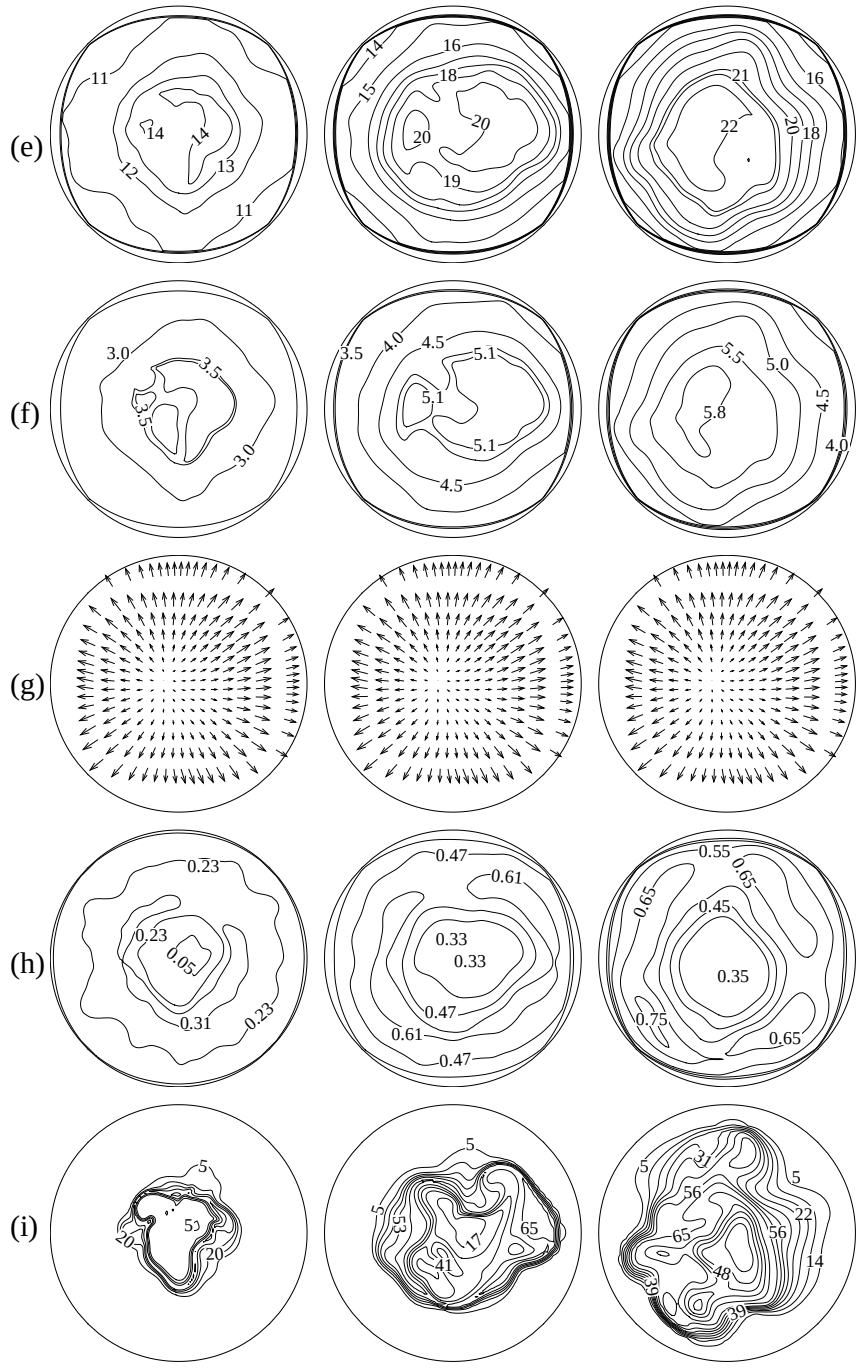

Figure 6.11: (continued)

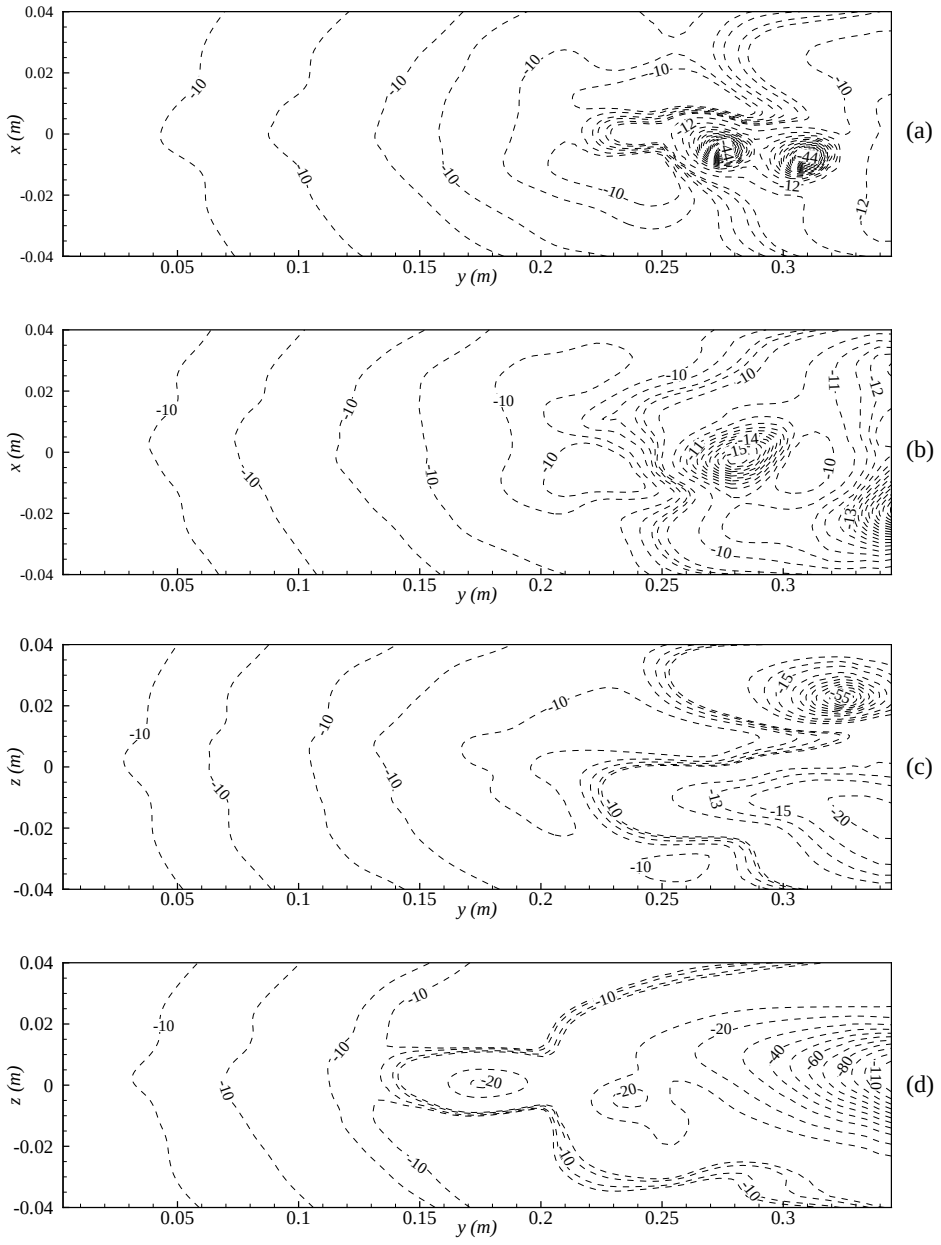

Figure 6.12: The net radiative heat fluxes, $\bar{\mathbf{q}}_n(kWm^{-2})$, for the non-luminous flame on the walls of the combustor: (a) $z = -L_z/2$, (b) $z = L_z/2$, (c) $x = -L_x/2$ and (d) $x = L_x/2$.

Chapter 7

Conclusions and Recommendations for Future Research

In this chapter, the findings of the present study have been summarised and some suggestions for the future work are made.

7.1 Conclusions

Large Eddy Simulation technique has been applied to analyse the turbulent flow, species concentrations with temperature, soot formation and growth, NO_x formation, and radiative heat transfer in the non-premixed propane/air combustion process within a cylindrical combustor. In LES, a Smagorinsky model with $C_s = 0.1$ as well as a dynamic model is employed for the modelling of sub-grid scale stresses, while the non-premixed combustion process is modelled via conserved scalar approach with laminar flamelet model. The soot formation is included into the non-premixed combustion process through the balance equations for soot mass fraction and soot particle number density with finite rate kinetic source terms to account for soot inception/nucleation, surface growth, agglomeration and oxidation. In the NO formation model, the extended Zeldovich (thermal) reaction mechanism is taken into account through a transport equation for NO mass fraction. The radiation is modelled through the Radiative Transfer Equation (RTE), which is the steady state representation of radiative heat transfer/flux. The RTE is solved using the Discrete Ordinates Method (DOM/S_n) which has been combined with the LES of the flow, temperature, combustion species and soot formation. The findings of this study are summarised chapter-wise.

In Chapter 3, the predicted mean temperature and species concentrations results along both the axial and radial directions have been compared with the experimental data investigated by Nishida and Mukohara [1] in the turbulent co-flowing propane and preheated air combustion, where a good agreement is achieved both quantitatively and qualitatively, although they appear to show some disagreements with the experimental results at some locations. The possible reasons of this have been discussed in the results and discussion section of Chapter 3. Most of the results are almost uninfluenced by the choice of the sub-grid scale models, whether it is a Smagorinsky model with constant C_s of 0.1 or a dynamic model. However, the mole fraction, $< \tilde{Y}_{O_2} >$, is predicted better in a dynamic model which in turn leads to a slightly better prediction in $< \tilde{Y}_{CO_2} >$ and $< \tilde{Y}_{H_2O} >$ by this model. It is also observed that the sub-grid scale quantities are predicted higher by the dynamic model in the upstream region where the value of dynamic C_s is found higher than the constant C_s of 0.1.

In Chapter 4, the computational results of soot concentration have also been compared with the experimental data obtained by Nishida and Mukohara [1], where a good agreement is achieved. However, the present results suggest that the prediction of soot levels could be improved if the accuracy in the prediction of O_2, C_2H_2 and temperature levels were increased. It has been found that the resolved scale fluxes are dominated by the production of high level of soot mass fraction and its number density, while the sub-grid scale fluxes are dominated by the turbulence intensity. We have again observed that the predicted results are almost unaffected by the choice of the sub-grid scale modelling. But, in the upstream region, higher value of dynamic C_s than the constant C_s leads to a higher prediction in sub-grid scale quantities.

In Chapter 5, no comparison between the predicted results of the NO mass fraction and experimental data is possible, as Nishida and Mukohara [1] did not perform any measurements on the NO mass fraction. However, the present results of NO clearly agree well with the principle and reaction mechanism of the extended Zeldovich (thermal) used for modelling NO. The NO mass fraction is predicted high in the high temperature zone. The sub-grid scale contributions to the prediction of NO mass fraction is found to be dominated by the intensity of the turbulence. Again, the results are almost uninfluenced by the choice of sub-grid scale models

although slightly lower prediction of NO mass fraction is found with dynamic C_s in the upstream. Dynamic C_s also produces a higher levels of the sub-grid scale quantities in the upstream region.

In Chapter 6, the instantaneous values of the total radiation, incident radiation, radiative heat flux, and the divergence of heat flux for both the non-luminous and luminous flames have been obtained and presented. For both the luminous and non-luminous flames, the above radiation properties are found to be dominated by the absorption coefficient. Due to the high absorption coefficient predicted in the luminous flame than the non-luminous flame, these radiation properties are found higher than those for the non-luminous flame. From the net wall radiative heat fluxes it is observed that for the luminous flame, the combustor walls lose heat at most places but gain heat at a particular location of one wall in the downstream region whereas for the non-luminous flame, all the walls lose heat by the radiative heat transfer.

7.2 Future Research

The application of LES in the modelling of turbulent reacting flows is a relatively recent development. Therefore, much remains to be done in this area. In the present conserved scalar methodology, the effect of strain or flame stretch is not included and therefore further development incorporating the effect of flame stretch is needed for the study of local extinction. A stretched laminar flamelet model of Liew *et al* [118] may be used to incorporate the effects of flame stretch into the present model, but the computation would become more expensive.

To get the filtered source terms for soot mass fraction and soot particle number density, the interaction between turbulence and soot chemistry is neglected in this study. Therefore, future work is required to incorporate the turbulence fluctuations in soot mass fraction and soot particle number density.

In the present study, the sub-grid scale turbulence-radiation interactions are neglected in the modelling of the nonlinear correlations between turbulence and radiation. So future studies are required to incorporate those interactions and to investigate their effects.

The divergence of the radiative heat fluxes, $\nabla.\bar{\mathbf{q}}$, which determines the amount

of heat loss/gain due to the radiation, must be coupled with the overall energy conservation equation for the accurate prediction of the flame temperature, which in turn improve the prediction of combustion species and soot formation in the flame. Further study is required to investigate this effect on the temperature, combustion species and soot formation in the flame, which again would deserve a massive amount of computing resources.

References

[1] O. Nishida, S. Mukohara, Characteristics of Soot Formation and Decomposition in Turbulent Diffusion Flames, *Combustion and Flame* 47 (1982) 269–279.

[2] M. Fairweather, W. P. Jones, H. S. Ledin, R. P. Lindstedt, Predictions of Soot Formation in Turbulent, Non-Premixed Propane Flames, in: *24th Symposium (International) on Combustion*, The Combustion Institute, 1992, pp. 1067–1074.

[3] S. Vedal, Ambient Particles and Health: Lines that Divide, *Journal of the Air and Waste Management Association* 47 (1997) 551–581.

[4] O. Reynolds, On the Dynamical Theory of Incompressible Viscous Fluids and the Determination of the Criterion, *Philosophical Transactions of the Royal Society of London A* 186 (1895) 123–164.

[5] N. Branley, *Large Eddy Simulation of Non-Premixed Turbulent Flames*, PhD thesis, Department of Chemical engineering and Chemical Technology, Imperical College London (1999).

[6] L. Vervisch, T. Poinsot, Direct Numerical Simulation of Non-Premixed Turbulent Flames, *Annual Review of Fluid Mechanics* 30 (1998) 655–691.

[7] R. S. Rogallo, P. Moin, Numerical Simulation of Turbulent Flows, *Annual Review of Fluid Mechanics* 16 (1984) 99–137.

[8] P. Moin, Towards Large Eddy and Direct Simulation of Complex Turbulent Flows, *Computer Methods in Applied Mechanics and Engineering* 87 (1991) 329–334.

[9] J. Smagorinsky, General Circulation Experiments with the Primitive

Equations-I. The Basic Experiment, *Monthly Weather Review* 91(3) (1963) 99–164.

[10] D. K. Lilly, The Representation of Small-Scale Turbulence in Numerical Simulation Experiments, in: *Proceedings of the IBM Scientific Computing Symposium on Environmental Sciences*, New York, 1967, pp. 195–210.

[11] J. W. Deardorff, A Numerical Study of Three-Dimensional Turbulent Channel Flow at Large Reynolds Numbers, *Journal of Fluid Mechanics* 41(2) (1970) 453–480.

[12] K. Akselvoll, P. Moin, Large-Eddy Simulation of Turbulent Confined Coannular Jets, *Journal of Fluid Mechanics* 315 (1996) 387–411.

[13] W. P. Jones, M. Wille, Large-Eddy Simulation of a Plane Jet in a Cross-Flow, *International Journal of Heat and Fluid Flow* 17 (1996) 296–306.

[14] L. L. Yuan, R. L. Street, J. H. Ferziger, Large-Eddy Simulations of a Round Jet in Crossflow, *Journal of Fluid Mechanics* 379 (1999) 71–104.

[15] L. di Mare, W. P. Jones, LES of Turbulent Flow Past a Swept Fence, *International Journal of Heat and Fluid Flow* 24 (2003) 606–615.

[16] M. Lesieur, O. Metais, New Trends in Large-Eddy Simulations of Turbulence, *Annual Review of Fluid Mechanics* 28 (1996) 45–82.

[17] P. Moin, Progress in Large Eddy Simulation of Turbulent Flows, Techical report, AIAA 97-0749 (1997).

[18] M. Lesieur, O. Metais, P. Comte, *Large-Eddy Simulations of Turbulence*, Cambridge University Press, 2005.

[19] F. Gao, E. E. O'Brien, A Large-Eddy Simulation Scheme for Turbulent Reacting Flows, *Physics of Fluids A* 5(6) (1993) 1282–1284.

[20] P. E. DesJardin, S. H. Frankel, Large Eddy Simulation of a Nonpremixed Reacting Jet: Application and Assessment of Subgrid-Scale Combustion Models, *Physics og Fluids* 10(9) (1998) 2298–2314.

[21] N. Branley, W. P. Jones, Large Eddy Simulation of a Turbulent Non-premixed Flame, *Combustion and Flame* 127 (2001) 1914–1934.

[22] F. di Mare, W. P. Jones, K. R. Menzies, Large Eddy Simulation of a Model Gas Turbine Combustor, *Combustion and Flame* 137 (2004) 278–294.

[23] N. Peters, *Turbulent Combustion*, Cambridge University Press, 2000.

[24] H. Pitsch, Large-Eddy Simulation of Turbulent Combustion, *Annual Review of Fluid Mechanics* 38 (2006) 453–482.

[25] J. J. Riley, Review of Large-Eddy Simulation of Non-Premixed Turbulent Combustion, *Journal of Fluids Engineering* 128 (2006) 209–215.

[26] N. Peters, Laminar Diffusion Flamelet Models in Non-Premixed Turbulent Combustion, *Progress in Energy and Combustion Science* 10 (1984) 319–339.

[27] A. W. Cook, J. J. Riley, G. Kosaly, A Laminar Flamelet Approach to Subgrid-Scale Chemistry in Turbulent Flows, *Combustion and Flame* 109 (1997) 332–341.

[28] A. Yu. Klimenko, Multicomponent Diffusion of Various Admixtures in Turbulent Flow, *Fluid Dynamics* 25 (1990) 327–334.

[29] R. W. Bilger, Conditional Moment Closure for Turbulent Reacting Flow, *Physics of Fluids A* 5(2) (1993) 436–444.

[30] N. S. A. Smith, Conditional Moment Closure of Mixing and Reaction in Turbulent Non Premixed Combustion, Center for Turbulent Research, Annual Research Briefs, (1996) 85–99.

[31] S. H. Kim, H. Pitsch, Conditional Filtering Method for Large-Eddy Simulation of Turbulent Nonpremixed Combustion, *Physics of Fluids* 17 (2005) 105103.

[32] A. R. Kerstein, A Linear-Eddy Model of Turbulent Scalar Transport and Mixing, *Combustion Science and Technology* 60 (1988) 391–421.

[33] A. R. Kerstein, Linear-Eddy Modeling of Turbulent Transport. II: Application to Shear Layer Mixing, *Combustion and Flame* 75 (1989) 397–413.

[34] A. R. Kerstein, Linear-Eddy Modelling of Turbulent Transport. Part 3. Mixing and Differential Molecular Diffusion in Round Jets, *Journal of Fluid Mechanics* 216 (1990) 411–435.

[35] A. R. Kerstein, Linear-Eddy Modelling of Turbulent Transport. Part 4. Structure of Diffusion Flames, *Combustion Science and Technology* 81 (1992) 75–96.

[36] A. W. Cook, J. J. Riley, A Subgrid Model for Equilibrium Chemistry in Turbulent Flows, *Physics of Fluids* 6(8) (1994) 2868–2870.

[37] P. J. Colucci, F. A. Jaberi, P. Givi, Filtered Density Function for Large Eddy Simulation of Turbulent Reacting Flows, *Physics of Fluids* 10(2) (1998) 499–515.

[38] I. M. Kennedy, Models of Soot Formation and Oxidation, *Progress in Energy and Combustion Science* 23 (1997) 95–132.

[39] M. J. Zimberg, S. H. Frankel, J. P. Gore, Y. R. Sivathanu, A Study of Coupled Turbulent Mixing, Soot Chemistry, and Radiation Effects Using Linear Eddy Model, *Combustion and Flame* 113 (1998) 454–469.

[40] S. J. Brookes, J. B. Moss, Predictions of Soot and Thermal Radiation Properties in Confined Turbulent Jet Diffusion Flames, *Combustion and Flame* 116 (1999) 486–503.

[41] Z. Wen, S. Yun, M. J. Thomson, M. F. Lightstone, Modeling Soot Formation in Turbulent Kerosene/Air Jet Diffusion Flames, *Combustion and Flame* 135 (2003) 323–340.

[42] R. Said, A. Garo, R. Borghi, Soot Formation Modeling for Turbulent Flames, *Combustion and Flame* 108 (1797) 71–86.

[43] B. F. Magnussen, B. H. Hjertager, On Mathematical Modeling of Turbulent Combustion with Special Emphasis on Soot Formation and Combustion, in:

Sixteenth Symposium (International) on Combustion, The Combustion Institute, Pittsburgh, 1976, pp. 719–729.

[44] B. F. Magnussen, B. H. Hjertager, J. G. Olsen, D. Bhaduri, Effects of Turbulent Structure and Local Concentrations on Soot Formation and Combustion in C_2H_2 Diffusion Flames, in: *Seventeenth Symposium (International) on Combustion*, The Combustion Institute, Pittsburgh, 1979, pp. 1383–1393.

[45] P. A. Tesner and T. D. Snegiriova and V. G. Knorre, Kinetics of Dispersed Carbon Formation, *Combustion and Flame* 17 (1971) 253–260.

[46] M. Fairweather, W. P. Jones, R. P. Lindstedt, Prediction of Radiative Transfer from a Turbulent Reacting Jet in a Cross-Wind, *Combustion and Flame* 89 (1992) 45–63.

[47] K. M. Leung, R. P. Lindstedt, W. P. Jones, A Simplified Reaction Mechanism for Soot Formation in Non-Premixed Flames, *Combustion and Flame* 87 (1991) 289–305.

[48] P. E. DesJardin, S. H. Frankel, Two-Dimentional Large Eddy Simulation of Soot Formation in the Near-Field of Strongly Radiating Nonpremixed Acetylene-Air Turbulent Jet Flame, *Combustion and Flame* 119 (1999) 121–132.

[49] C. T. Bowman, Control of Combustion-Generated Nitrogen Oxide Emissions: Technology Driven by Regulation, in: *24th Symposium (International) on Combustion*, The Combustion Institute, 1992, pp. 859–878.

[50] J. Zeldovich, The Oxidation of Nitrogen Combustion and Explosions, *Acta Physicochim*. URSS 21 (1946) 577–628.

[51] C. P. Fenimore, Studies of Fuel-Nitrogen Species in Rich Flame Gases, in: *17th Symposium (International) on Combustion*, The combustion institute, Philadelphia, PA, 1979, pp. 661–670.

[52] Ph. Meunier, M. Costa, M. G. Carvalho, On NO_x Emissions from Turbulent Propane Diffusion Flames, *Combustion and Flame* 112 (1998) 221–230.

[53] H. S. Kim, S. W. Baek, M. J. Yu, Formation Characteristics of Nitric Oxide in a Three-Staged Air/LPG Flame, *International Journal of Heat and Mass Transfer* 46 (2003) 2993–3008.

[54] N. Taniguchi, T. Tominaga, K. Inoue, M. Hirohata, T. Kobayashi, A Large Eddy Simulation of Non-premixed Turbulent Flame and Nitric Oxide Production, in: *4th International Symposium on Turbulence, Heat and Mass Transfer*, Begell House, Inc., 2003, pp. 1–6.

[55] S. Chandrasekhar, *Radiative Transfer*, Dover Publications, 1960.

[56] B. G. Carlson, K. D. Lathrop, Transport Theory - The Method of Discrete Ordinates, in: H. Greenspan, C. N. Kebler, D. Okrent (Eds.), *Computing Methods in Reactor Physics*, Gordon and Breach Science Publishers, New York, 1968, pp. 165–266.

[57] D. J. Hyde, J. S. Truelove, The Discrete Ordinates Approximation for Multidimensional Radiant Heat Transfer in Furnaces, *HTFS Report No. R-8502* (1977).

[58] W. A. Fiveland, A Discrete-Ordinates Method for Predicting Radiative Heat Transfer in Axisymmetric Enclosures, *ASME paper 82-HT-20* (1982).

[59] W. A. Fiveland, Discrete-Ordinates Solutions of the Radiative Transport Equations for Rectangular Enclosures, *Journal of Heat Transfer* 106 (1984) 699–706.

[60] W. A. Fiveland, Three-Dimensional Radiative Heat-Transfer Solutions by Discrete-Ordinates Method, *Journal of Thermophysics and Heat Transfer* 2 (1988) 309–316.

[61] A. S. Jamaluddin, P. J. Smith, Predicting Radiative Transfer in Axisymmetric Cylindrical Enclosures Using the Discrete Ordinates Method, *Combustion Science and Technology* 62 (1988) 173–186.

[62] A. S. Jamaluddin, P. J. Smith, Predicting Radiative Transfer in Rectangular Enclosures Using Discrete Ordinates Method, *Combustion Science and Technology* 59 (1988) 321–340.

[63] C. R. Kaplan, S. W. Baek, E. S. Oran, J. L. Ellzey, Dynamics of a Strongly Radiating Unsteady Ethylene Jet Diffusion Flame, *Combustion and Flame* 96 (1994) 1–21.

[64] N. Kayakol, N. Selçuk, I. Campbell, Ö. L. Gülder, Performance of Discrete Ordinates Method in a Gas Turbine Combustor Simulator, *Experimantal Thermal and Fluid Science* 21 (2000) 134–141.

[65] W. P. Jones, M. C. Paul, Combination of DOM with LES in a Gas Turbine Combustor, *International Journal of Engineering Science* 43 (2005) 379–397.

[66] M. C. Paul, W. P. Jones, Radiative Heat Transfer in a Model Gas Turbine Combustor, *WIT Transactions on Engineering Sciences* 53 (2006) 413–421.

[67] M. C. Paul, Performance of the Various S_n Approximations of DOM in a 3D Combustion Chamber, *ASME Journal of Heat Transfer*, To appear in September (2008).

[68] J. O. Hirschfelder, C. F. Curtiss, R. B. Bird, *The Molecular Theory of Gases and Liquids*, Wiley, New York, 1954.

[69] J. Warnatz, U. Maas, R. W. Dibble, *Combustion: Physical and Chemical Fundamentals, Modeling and Simulations, Experiments, Pollutant Formation*, Springer-Verlag, Berlin, 2001.

[70] F. M. White, *Viscous Fluid Flow*, McGraw-Hill, 1991.

[71] A. Leonard, Energy Cascade in Large-Eddy Simulations of Turbulent Fluid Flows, *Advances in Geophysics* 18(A) (1974) 237–248.

[72] M. Germano, Turbulence: the Filtering Approach, *Journal of Fluid Mechanics* 238 (1992) 325–336.

[73] S. Ghosal, P. Moin, The Basic Equations for the Large Eddy Simulation of Turbulent Flows in Complex Geometry, *Journal of Computational Physics* 118 (1995) 24–37.

[74] P. Moin, W. C. Reynolds, J. H. Ferziger, Large Eddy Simulation of Incompressible Turbulent Channel Flow, Techical report, TF-12, Department of Mechanical Engineering, Stanford University (1978).

[75] A. Favre, Statistical Equations of Turbulent Cases in Problems of Hydrodynamics and Continuum Mechanics, Techical report, Society of Industrial and Applied Mathematics, Philadelphia (1969).

[76] P. Moin, K. Squires, W. Cabot, S. Lee, A Dynamic Subgrid-Scale Model for Compressible Turbulence and Scalar Transport, *Physics of Fluids A* 3(11) (1991) 2746–2757.

[77] G. Erlebacher, M. Y. Hussaini, C. G. Speziale, T. A. Zang, Towards the Large-Eddy Simulation of Compressible Turbulent Flows, *Journal of Fluid Mechanics* 238 (1992) 155–185.

[78] H. Steiner, W. K. Bushe, Large Eddy Simulation of a Turbulent Reacting Jet with Conditional Source-Term Estimation, *Physics of Fluids* 13(3) (2001) 754–769.

[79] W. K. Bushe, H. Steiner, Conditional Moment Closure for Large Eddy Simulation of Nonpremixed Turbulent Reacting Flows, *Physics of Fluids* 11(7) (1999) 1896–1906.

[80] A. Germano, A Proposal for a Redefinition of the Turbulent Stresses in the Filtered Navier-Stokes Equations, *Physics of Fluids* 29(7) (1986) 2323–2324.

[81] M. Germano, U. Piomelli, P. Moin, W. H. Cabot, A Dynamic Subgrid-Scale Eddy Viscosity Model, *Physics of Fluids A* 3(7) (1991) 1760–1765.

[82] H. Schmidt, U. Schumann, Coherent Structure of the Convective Boundary Layer Derived from Large-Eddy Simulations, *Journal of Fluid Mechanics* 200 (1989) 511–562.

[83] J. O. Hinze, *Turbulence*, McGraw-Hill, New York, 1959.

[84] M. Wille, *Large Eddy Simulation of Jets in Cross Flows*, PhD thesis, Department of Chemical engineering and Chemical Technology, Imperical College London (1997).

[85] A. Yoshizawa, Eddy-Viscosity-Type Subgrid-Scale Model with a Variable Smagorinsky Coefficient and its Relationship with the One-Equation Model in Large Eddy Simulation, *Physics of Fluids A* 3(8) (1991) 2007–2009.

[86] S. Ghosal, T. S. Lund, P. Moin, K. Akselvoll, A Dynamic Localization Model for Large-Eddy Simulation of Turbulent Flows, *Journal of Fluid Mechanics* 286 (1995) 229–255.

[87] D. K. lilly, A Proposed Modification of the Germano Subgrid-Scale Closure Method, *Physics of Fluids A* 4(3) (1992) 633–635.

[88] R. W. Bilger, Turbulent flows with nonpremixed reactants, in: P. A. Libby, F. A. Williams (Eds.), *Turbulent Reactings Flows*, Springer-Verleg, Heidelburg, 1980, Ch. 3, pp. 65–113.

[89] S. S. Girimaji, Y. Zhou, Analysis and Modelling of Subgrid Scalar Mixing Using Numerical Data, *Physics of Fluids* 8(5) (1996) 1224–1236.

[90] C. D. Pierce, P. Moin, A Dynamic Model for Subgrid-Scale Variance and Dissipation Rate of a Conserved Scalar, *Physics of Fluids* 10(12) (1998) 3041–3044.

[91] A. W. Cook, J. J. Riley, Sub-Grid Scale Modeling of Turbulent Reacting Flows, *Combustion and flame* 112 (1998) 593–606.

[92] F. di Mare, *Large Eddy Simulation of a Gas Turbine Combustor*, PhD thesis, Department of Chemical engineering and Chemical Technology, Imperical College London (1998).

[93] C. D. Pierce, P. Moin, Methods for Generating Equilibrium Swirling Inflow Conditions, *AIAA Journal* 36(7) (1998) 1325–1327.

[94] T. Poinsot, D. Veynante, *Theoretical and Numerical Combustion*, R. T. Edwards, Inc., 2001.

[95] F. A. Williams, *Combustion Theory*, Perseus Books Publishing, L. L. C., 1985.

[96] F. A. Williams, Recent Advances in Theoretical Descriptions of Turbulent Diffusion Flames, in: S. N. B. Murthy (Ed.), *Turbulent Mixing in Non-Reactive and Reactive Flows*, Plenum Press, 1975, pp. 189–208.

[97] N. Peters, Laminar Flamelet Concepts in Turbulent Combustion, in: *Twenty-first Symposium (International) on Combustion*, The Combustion Institute, 1986, pp. 1231–1250.

[98] K. M. Leung, *Kinetic modelling of hydrocarbon flames using detailed and systemically reduced chemistry*, PhD thesis, Department of Chemical Engineering, Imperical College London (1996).

[99] H. Tennekes, J. L. Lumley, *A First Course in Turbulence*, The MIT Press, 1972.

[100] B. S. Haynes, H. G. Wagner, Soot Formation, *Progress in Energy and Combustion Science* 7 (1981) 229–273.

[101] S. J. Harris, A. M. Weiner, Determination of the rate constant for soot surface growth, *Combustion Science and Technology* 32 (1983) 267–275.

[102] W. H. Press, B. P. Flannery, S. A. Teukolsky, W. T. Vetterling, *Numerical Recipies in Fortran 77*, Cambridge University Press, 1992.

[103] W. Bartok, A. R. Crawford, A. Skopp, Control of NOX emissions from stationary sources, *Chemical Engineering Progress* 67(2) (1971) 64–72.

[104] D. L. Baulch, C. J. Cobos, R. A. Cox *et al*, Evaluated Kinetic Data for Combustion Modeling, *Journal of Physical and Chemical Reference Data* 21 (3) (1992) 411–734.

[105] D. L. Baulch, C. J. Cobos and R. A. Cox *et al*, Summary Table of Evaluated Kinetic Data for Combustion Modeling: Supplement-1, *Combustion and Flame* 98 (1994) 59–79.

[106] M. F. Modest, *Radiative heat transfer*, Academic Press, 2003.

[107] C. M. Chu, S. W. Churchill, Representation of the Angular Distribution of Radiation Scattered by a Spherical Particle, *Journal of the Optical Society of America* 45(11) (1955) 958–962.

[108] B. Zheng, C. X. Lin, M. A. Ebadian, Combined laminar forced convection and thermal radiation in a helical pipe, *International Journal of Heat and Mass Transfer* 43 (2000) 1067–1078.

[109] L. M. Ruan, L. H. Liu, H. P. Tan, The study on approximating the open bounday of two-dimension medium as one black wall, *Heat and Mass Transfer* 40 (2004) 319–324.

[110] P. E. DesJardin, *Large eddy simulation of strongly radiating non premixed turbulent jet flames*, PhD thesis, School of Mechanical Engineering, Purdue University, IN (1998).

[111] W. H. Dalzell, A. F. Sarofim, Optical Constants of Soot and Their Application to Heat-Flux Calculations, *ASME Journal of Heat Transfer* 91(1) (1969) 100–104.

[112] J. D. Felske, T. T. Charalampopoulos, H. S. Hura, Determination of Refractive Indices of Soot Particles from the Reflectivities of Compressed Soot Pellets, *Combustion Science and Technology* 37 (1984) 263–283.

[113] Ü. Ö. Köylü, G. M. Faeth, Optical Properties of Overfire Soot in Buoyant Turbulent Diffusion Flames at Long Residence Times, *Journal of Heat Transfer* 116 (1994) 152–159.

[114] R. Siegel, Radiative Behavior of a Gas Layer Seeded with Soot, NASA TN D-8278, Washington, D. C. (1976).

[115] H. Chang, T. T. Charalampopoulos, Determination of the Wavelength Dependence of Refractive Indices of Flame Soot, *Proceedings of the Royal Society of London A* 430 (1990) 577–591.

[116] B. R. Suydam, The Scattering and Absorption of Light by Soot Particles, Techical report, LA-9856-MS, http://adsabs.harvard.edu/abs/1983sals.rept.....S (1983).

[117] R. Viskanta, M. P. Mengüç, Radiation Heat Transfer in Combustion Systems, *Progress in Energy and Combustion Science* 13 (1987) 97–160.

[118] S. K. Liew, K. N. C. Bray, J. B. Moss, A Stretched Laminar Flamelet Model of Turbulent Nonpremixed Combustion, *Combustion and Flame* 56 (1984) 199–213.

[119] P. K. Sweby, High Resolution Schemes Using Flux Limiters for Hyperbolic Conservation Laws, *SIAM Journal on Numerical Analysis* 21(5) (1984) 995–1011.

[120] C. M. Rhie, W. L. Chow, Numerical Study of the Turbulent Flow Past an Airfoil with Trailing Edge Seperation, *AIAA Journal* 21(11) (1983) 1525–1532.

[121] H. A. Van Der Vorst, BI-CGSTAB: A Fast and Smoothly Converging Variant of BI-CG for the Solution of Nonsymmetric Linear Systems, *SIAM Journal on Scientific and Statistical Computing* 13(2) (1992) 631–644.

[122] J. A. Meijerink, H. A. Van Der Vorst, Guidelines for the Usage of Incomplete Decompositions in Solving Sets of Linear Equations as They Occur in Practical Problems, *Journal of Cmputational Physics* 44 (1981) 134–155.

[123] D. S. Kershaw, The Complete Cholesky-Conjugate Gradient Method for the Iterative Solution of Systems of Linear Equations, *Journal of Cmputational Physics* 26 (1978) 43–65.

[124] J. C. Chai, G. Parthasarathy, H. S. Lee, S. V. Patankar, Finite Volume Radiative Heat Transfer Procedure for Irregular Geometries, *Journal of Thermophysics and Heat Transfer* 9(3) (1995) 410–415.

[125] J. Liu, H. M. Shang, Y. S. Chen, T. S. Wang, Prediction of Radiative Transfer in General Body-Fitted Coordinates, *Numerical Heat Transfer B* 31(4) (1997) 423–439.

[126] J. F. Thompson, F. C. Thames, C. W. Mastin, Automatic Numerical Generation of Body-Fitted Curvilinear Coordinate System for Field Containing Any

Number of Arbitrary Two-Dimensional Bodies, *Journal of Computational Physics* 15 (1974) 299–319.

[127] S. V. Patankar, *Numerical Heat Transfer and Fluid Flow*, Hemisphere Publishing Corporation, 1980.

[128] J. H. Ferziger, M. Peric, *Computational Methods for Fluid Dynamics*, Springer-Verlag, 1996.

[129] C. Hrisch, *Numerical Computation of Internal and External Flows. Volume 2: Computational Methods for Inviscid and Viscous Flows*, John Willey & Sons, 1990.

Appendix A

Computational Procedures

The grid arrangement and boundary conditions along with an overview of the computational procedures employed in our simulation are presented in this chapter. The numerical solution procedure is based on a finite volume approach where Favre-filtered Navier-Stokes and transport equations are integrated over the mesh control volume. In order to facilitate calculation of flows inside the combustion chamber, the governing equations are transformed into carvilinear or body fitted coordinates. Some details of the numerical methods are described in Appendix B.

A.1 Grid Arrangement

A schematic of the flow geometry with computational domain is shown in Fig. 3.2. A curvilinear body fitted coordinate system is employed for the present simulation consisting of a total of about 1.5 million nodes inside the combustion chamber with a non-uniform mesh distributed along the three co-ordinate directions. At the centre of the combustor inlet, where the fuel is injected through a circular nozzle at a speed higher than that of the air supplied through the annulus surroundings of the cylinder inlet, a very fine mesh is required so that the steep gradients that appear in this area are adequately resolved. The mesh lines are contracted at the centre and near the inlet of the combustor, and they are expanded smoothly in all three directions outwards from the centreline and inlet. A representation of numerical grid in the horizontal mid-plane of the combustor is shown in Fig. A.1.

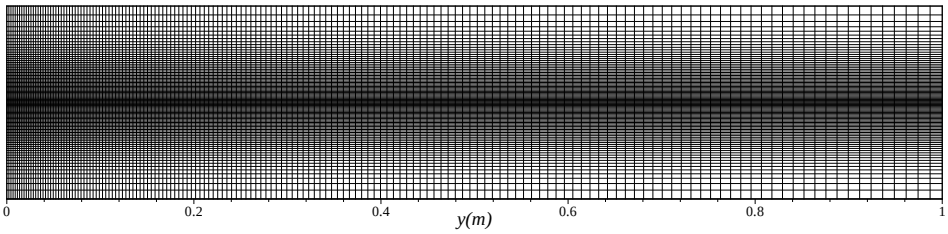

Figure A.1: Grid in the horizontal mid-plane of the combustor.

A.2 Boundary Conditions for LES

In the simulation fully-developed turbulent pipe flow profiles consisting of mean and random fluctuations were applied as the instantaneous inflow boundary conditions at the fuel nozzle, while a uniform profile is applied for the air flow. The mixture fraction at the inlet is defined as

$$\xi = \begin{cases} 1 & \text{in the fuel stream} \\ 0 & \text{in the air stream.} \end{cases} \tag{A.1}$$

The soot mass fraction and the soot particle number density are negligibly small at the inlet and set to zero. The NO mass fraction is negligibly small at the inlet and also set to zero as Fig. 5.1 of Chapter 5 shows clearly that the production rate of NO is zero at $\xi = 0.0$ and 1.0.

At the outlet boundary, a zero gradient boundary condition of the form

$$\left.\frac{\partial u_i}{\partial n}\right|_{out} = 0, \tag{A.2}$$

where $\frac{\partial}{\partial n}$ denotes the gradient taken normal to the outflow boundary, has been used, which was a sufficient condition to minimise the effects of the outlet boundary in the solutions.

A thin viscous sub-layer develops adjacent to the walls of the combustor and a prohibitively fine mesh would be required to resolve this, which turns to be a very expensive computation. To overcome this difficulty an instantaneous logarithmic-

law condition of the wall as

$$u^+ = \frac{u}{u_\tau} = \frac{1}{\kappa}\ln y^+ + A \tag{A.3}$$

is employed as a near wall condition at the surfaces of the combustor. Where $y^+ = \frac{yu_\tau}{\nu}$ is the normalised wall distance, while $\kappa \approx 0.4$ and $A \approx 5.5$ are assumed to be universal constants, and $u_\tau = \sqrt{\frac{\tau_w}{\rho}}$ is the wall friction velocity where τ_w is the wall shear stress.

A.3 Overview of the Numerical Methods for LES

The numerical solution procedure employed here is based on a finite volume approach where the Favre-filtered Navier-Stokes, the mixture fraction transport, the soot mass fraction, the soot particle number density, and the NO mass fraction equations are integrated over the mesh control volume. The in-house code LES-BOFFIN (Boundary Fitted Flow Integrator) code, initially developed at the Imperial College London, has been extended in the present model in order to solve the governing equations of the soot mass fraction, the soot particle number density and the NO mass fraction together with the Navier-Stokes and the mixture fraction equations. The code is based on a fully implicit low-Mach number formulation and is second order accurate in both space and time. The BOFFIN code has extensively been applied in the LES of reacting and non-reacting turbulent flows; for examples, see LES of a gas turbine combustor by di Mare *et al* [22], of a turbulent non-premixed flame by Branley and Jones [21], and of turbulent flow past a swept fence by di Mare and Jones [15]. Full details of the numerical method used in the BOFFIN is described in Appendix B.

An energy conserving discretisation is used for the convective terms in the momentum equations (3.45) while all other spatial derivatives in equations (3.44) and (3.45) are discretised using standard second order accurate central differences. A central differencing scheme for discretising the convection terms in the mixture fraction equation (3.46), soot mass fraction and soot number density equation (4.10) and NO mass fraction equation (5.10) may result in a violation of the extremum principles of the exact equations when cell Peclet numbers are greater than around

2. However, the mixture fraction must remain bounded between zero and unity if unphysical values of the density, temperature and species concentrations are to be avoided. In order to achieve this a Total Variation Diminishing (TVD) scheme, see Sweby [119], has been used for the convective terms in the mixture fraction equation. Time derivatives are approximated by a three-point backward difference scheme with a variable time-step. The pressure is determined by a two-step second-order time-accurate approximate factorisation method.

A co-located pressure and velocity arrangement is used and odd/even node uncoupling of the pressure and velocity fields is prevented by a pressure smoothing technique, see Rhie and Chow [120]. The system of algebraic equations resulting from the discretisation is solved using matrix pre-conditioned conjugate gradient methods; Bi-CGSTAB algorithm of Van der Vorst [121] for the velocity and scalar equations, and ICCG (1,1,1) of Meijerink and Vandervorst [122] and Kershaw [123] for the pressure. A variable time step is used in the computations to ensure that the maximum Courant number, based on the filtered velocity, lies between 0.1 and 0.2.

A.4 Discretisation of RTE in DOM

Transforming the coordinate from cartesian to general curvilinear and then integrating the transformed equation over a single control volume, ΔV, the RTE equation (6.31) can be rewritten as,

$$\sum_{i=n,e,r} \bar{I}_m^i S_m^i - \sum_{i=s,w,l} \bar{I}_m^i S_m^i = |\mathbf{J}|^P \left(\bar{\kappa}_a \bar{I}_b - \bar{\kappa}_a \bar{I}_m\right)^P . \tag{A.4}$$

where **J** is the Jacobian of the coordinate transformation, $\frac{\partial(x,y,z)}{\partial(\xi,\eta,\zeta)}$; $|\mathbf{J}|$ is the determinant of **J**; the superscripts n, s, etc., indicate that the values are taken at the northern, southern, etc., control volume surfaces respectively; and the superscript P represents the value at the central node of the control volume.

The terms S_m^i in equation (A.4) represent as,

$$S_m^i = \left(\alpha_m A_{x\xi} + \beta_m A_{y\xi} + \gamma_m A_{z\xi}\right)^i ; \quad i = n, s \tag{A.5}$$

$$S_m^i = \left(\alpha_m A_{x\eta} + \beta_m A_{y\eta} + \gamma_m A_{z\eta}\right)^i ; \quad i = e, w \tag{A.6}$$

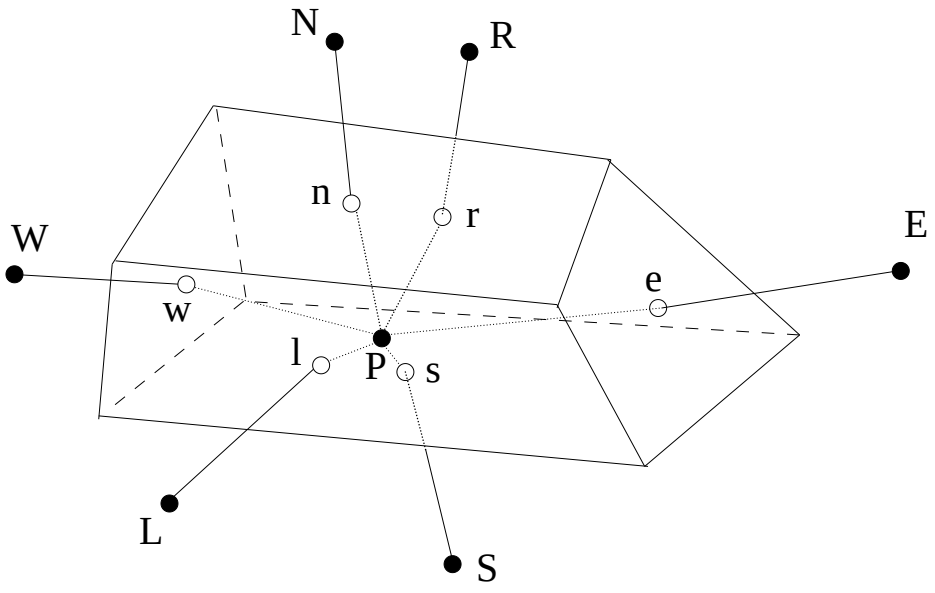

Figure A.2: A representation of control volume: hollow circles indicate the surface nodes where as solid circles indicate the node points.

$$S_m^i = (\alpha_m A_{x\zeta} + \beta_m A_{y\zeta} + \gamma_m A_{z\zeta})^i \,; \quad i = r, l \tag{A.7}$$

where $A_{x\xi}$, $A_{y\xi}$, $A_{z\xi}$, etc are the cofactors of the Jacobian $\mathbf{J}$.

To close the above system of equations, relations between the intensities on the control-volume surfaces and the nodal intensities are needed. A typical representation of control volume is given in Fig. A.2. For the complicated geometry, these closure relations are based on the step scheme, see Chai *et al* [124] and Liu *et al* [125], whereby the downstream surface intensities are set equal to the upstream nodal intensities. According to this step scheme, the discretised equation for the DOM can be rewritten as,

$$a_m^P \bar{I}_m^P = a_m^E \bar{I}_m^E + a_m^W \bar{I}_m^W + a_m^N \bar{I}_m^N + a_m^S \bar{I}_m^S + a_m^R \bar{I}_m^R + a_m^L \bar{I}_m^L + b_m^P. \tag{A.8}$$

where the intensities with subscripts E, W, etc., denote the eastern, western, etc.,

nodal intensities and the coefficients are written as,

$$a_m^P = \sum_{i=n,e,r} max(S_m^i, 0) - \sum_{i=s,w,l} max(S_m^i, 0) + |\mathbf{J}|^P \bar{\kappa}_a, \tag{A.9}$$

$$a_m^I = -min(S_m^i, 0); \quad i = n, e, r \quad \text{and} \quad I = N, E, R, \tag{A.10}$$

$$a_m^I = max(S_m^i, 0); \quad i = s, w, l \quad \text{and} \quad I = S, W, L \tag{A.11}$$

and

$$b_m^P = |\mathbf{J}|^P \bar{\kappa}_a \bar{I}_b. \tag{A.12}$$

A.4.1 Solution Algorithm and Convergent Condition for DOM

Mole fractions of CO_2 and H_2O, temperature, soot volume fraction are calculated first employing LES. Instantaneous values of these quantities are needed to obtain the radiation source terms of discrete ordinates representation of RTE and its boundary conditions. As we have neglected the scattering effects in our present study, the discretised RTE in equation (A.8) is thus uncoupled with the incoming radiative intensities and can be solved independently.

The solution is based on a control volume approach and initiated by selecting a corner of the computational domain to start integrating equation (A.8) as illustrated in Fig. A.3. In DOM, the radiative intensities at all the node points of the computational domain are calculated for each of the total M discrete directions using equation (A.8). At each iteration, the discrete equation (A.8) is solved in every direction of $\hat{s}_m$. The boundary conditions in equations (6.15)-(6.19) of Chapter 6 are also updated for the next iteration. The new solutions are then replaced by the previous iterative solutions and this process continues until the following convergent condition is satisfied

$$\underset{1 \le m \le M}{max} \left| I_m^{P(i+1)} - I_m^{P(i)} \right| \le 10^{-6}, \tag{A.13}$$

where i is the number of iteration.

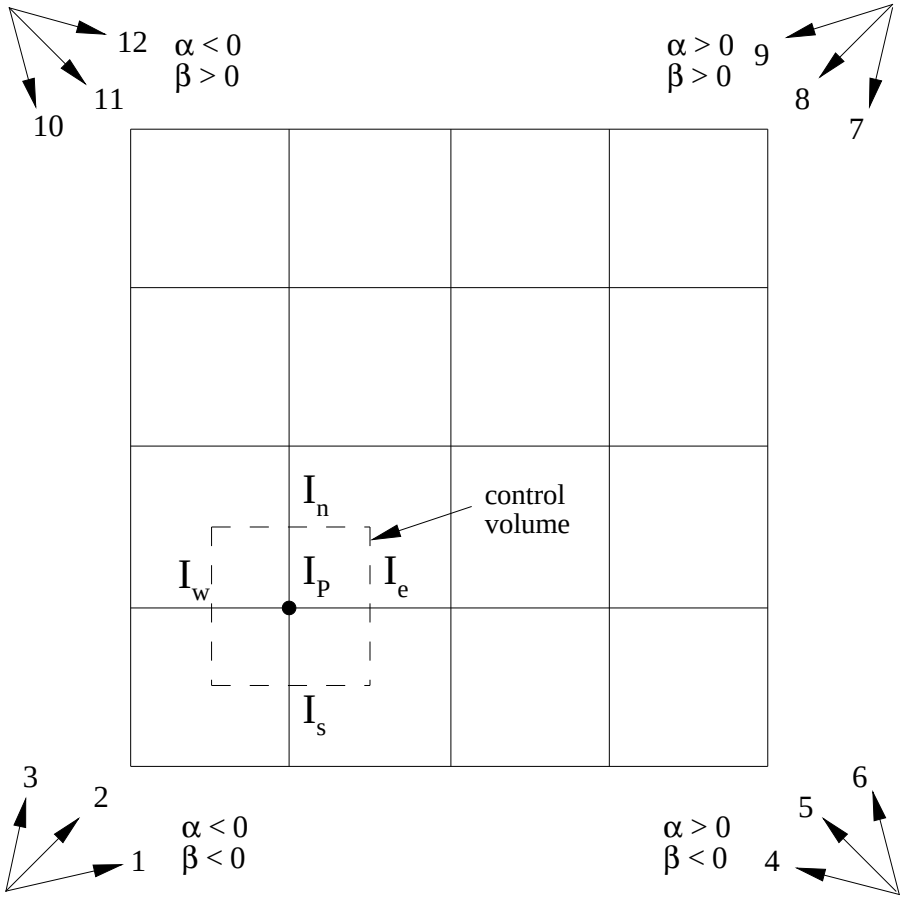

Figure A.3: A two-dimensional representative control volume and direction cosines for the S_4 approximation of DOM calculation.

Appendix B

Numerical Methods

As mentioned in Chapter A that LES-BOFFIN code, employed in our computation, uses a finite volume approach where the Favre-filtered governing equations are integrated over the mesh control volume to obtain an algebraic finite difference approximation for those partial differential transport equations. To facilitate calculation, the governing equations are transformed into carvilinear coordinates. The approach is described in this chapter. For clarity, a seperate list of symbols for this appendix is given in §B.4.

B.1 Coordinate Transformation

Thompson *et al* [126] introduced an approach where the finite difference equations are formulated in a transformed curvilinear coordinate system that coincides with the boundaries of the flow domain. In this approach, the flow domain in physical space is mapped onto a rectangular domain in computational space, as shown in Fig. B.1, where a two-dimensional case is represented for simplicity.

Fot the map $x_j \rightarrow \xi_j$, if J_{ij} represents the elements of the Jacobian matrix, **J**, of the transformation then

$$J_{ij} = \frac{\partial x_i}{\partial \xi_j}, \tag{B.1}$$

Then the determinant of the Jacobian matrix, **J**, is denoted by $|\mathbf{J}|$ and given by

$$|\mathbf{J}| = \frac{\partial x_i}{\partial \xi_j} A_{ij}, \tag{B.2}$$

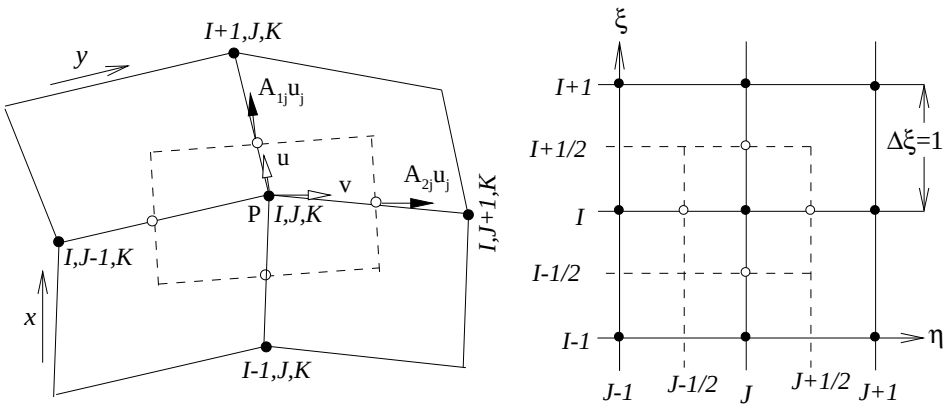

Figure B.1: Grid arrangement and notation in two-dimensional case in both physical space (left), and in computational space (right). Solid lines indicate the grid lines, dashed lines the faces of the control volume.

where A_{ij} are the elements of the cofactor matrix, $\mathbf{A}$, of the Jacobian, defined as

$$|\mathbf{A}| = |\mathbf{J}|\mathbf{J}^{-1}, \tag{B.3}$$

By applying the chain rule, the derivatives can be expressed in the transformed space in the following way:

$$\frac{\partial \phi}{\partial x_i} = \frac{\partial \phi}{\partial \xi_j}\frac{\partial \xi_j}{\partial x_i} = \frac{A_{ij}}{|\mathbf{J}|}\frac{\partial \phi}{\partial \xi_j}, \tag{B.4}$$

where ϕ is the generic variable.

The Favre-filtered transport equations (3.44)-(3.46), (4.10) and (5.10) in general curviliear co-ordinates can be written as,

continuity:

$$\frac{\partial \bar{\rho}}{\partial t} + \frac{\partial}{\partial \xi_k}\left(\frac{A_{kj}}{|\mathbf{J}|}\bar{\rho}\tilde{u}_j\right) = 0, \tag{B.5}$$

Momentum:

$$\begin{aligned}\frac{\partial(\bar{\rho}\tilde{u}_i)}{\partial t} + \frac{\partial}{\partial \xi_k}\left(\frac{A_{kj}}{|\mathbf{J}|}\bar{\rho}\tilde{u}_i\tilde{u}_j\right) &= -\frac{A_{kj}}{|\mathbf{J}|}\frac{\partial \bar{p}}{\partial \xi_k} \\ &+ \frac{\partial}{\partial \xi_k}\left[\frac{A_{kj}}{|\mathbf{J}|}\left(\mu_e\frac{A_{lj}}{|\mathbf{J}|}\frac{\partial \tilde{u}_i}{\partial \xi_l} + \mu_e\frac{A_{li}}{|\mathbf{J}|}\frac{\partial \tilde{u}_j}{\partial \xi_l}\right)\right],\end{aligned} \tag{B.6}$$

Mixture fraction or soot mass fraction or soot particle number density or NO mass fraction:

$$\frac{\partial \bar{\rho}\tilde{\phi}}{\partial t} + \frac{\partial}{\partial \xi_k}\left(\bar{\rho}\tilde{u}_j\tilde{\phi}\right) = \frac{\partial}{\partial \xi_k}\left[\frac{A_{kj}}{|\mathbf{J}|}\left(\Gamma_e \frac{A_{lj}}{|\mathbf{J}|}\frac{\partial \tilde{\phi}}{\partial \xi_l}\right)\right] + \bar{\rho}\tilde{S}(\tilde{\phi}), \tag{B.7}$$

where the source term $\bar{\rho}\tilde{S}(\tilde{\phi})$ is zero for mixture fraction equation and it is defined in equations (4.11), (4.12) and (5.11) for the soot mass fraction, soot particle number density and NO mass fraction equation respectively.

The effective viscosity, μ_e, and diffusivity, Γ_e, are respectively the sum of the molecular/turbulent and sub-grid eddy viscosity and diffusivity,

$$\mu_e = \mu + \mu_{sgs} \qquad \text{and} \qquad \Gamma_e = \Gamma + \Gamma_{sgs}. \tag{B.8}$$

The finite volume method uses the integral form of the transport equations as the starting point. Integrating the transformed equations over a single control volume, ΔV, gives,

Continuity:

$$\int_{\Delta V} \frac{\partial \bar{\rho}}{\partial t}|\mathbf{J}|dV + \int_{\Delta S} G_k n_k ds = 0, \tag{B.9}$$

Momentum:

$$\begin{aligned}\int_{\Delta V} \frac{\partial(\bar{\rho}\tilde{u}_i)}{\partial t}|\mathbf{J}|dV + \int_{\Delta S} G_k \tilde{u}_i n_k dS = &- \int_{\Delta V} A_{kj}\frac{\partial \bar{p}}{\partial \xi_k}dV \\ &+ \int_{\Delta S}\left[\mu_e\left(\frac{A_{lj}A_{kj}}{|\mathbf{J}|}\frac{\partial \tilde{u}_i}{\partial \xi_l} + \frac{A_{li}A_{kj}}{|\mathbf{J}|}\frac{\partial \tilde{u}_j}{\partial \xi_l}\right)\right] n_k dS,\end{aligned} \tag{B.10}$$

Mixture fraction or soot mass fraction or soot particle number density or NO mass fraction:

$$\int_{\Delta V} \frac{\partial \bar{\rho}\tilde{\phi}}{\partial t}|\mathbf{J}|dV + \int_{\Delta S} G_k \tilde{\phi} n_k dS = \int_{\Delta S}\left[\Gamma_e \frac{A_{lj}A_{kj}}{|\mathbf{J}|}\frac{\partial \tilde{\phi}}{\partial \xi_l}\right] n_k dS + \int_{\Delta V} \bar{\rho}\tilde{S}(\tilde{\phi})|\mathbf{J}|dV, \tag{B.11}$$

where $G_k = A_{ij}\bar{\rho}\tilde{u}_j$, are the contravariant mass fluxes. n_k is the unit normal point-

ing in the outward direction of the cell surface, ΔS, of the cell volume, ΔV. The pressure gradient term is regarded as a body force and is treated non-conservatively.

B.2 Discretisation Scheme Used in BOFFIN

The grid arrangement used in LES-BOFFIN is shown in Fig B.1, where the mesh specing is uniform i.e., $\Delta\xi = 1$. The control volume (CV) faces lie midway between nodes. According to the colocated arrangement, all the variables e.g., velocity, pressure and all transported scalar stored at the CV centres are assumed to be uniform over the CV. A linear variation of variable values between grid nodes is assumed in such a way that the value of the variables at the cell faces are obtained as averages of the values at the appropriate adjacent nodes.

In order to illustrate the discretisation scheme adopted in BOFFIN, we have considered the u-momentum equation of the Navier-Stokes equations. The convective term is approximated by,

$$\begin{aligned}\int_{\Delta S} G_k \tilde{u} n_k dS \approx & \left[G_1\tilde{u}\right]_{I+\frac{1}{2},J,K} - \left[G_1\tilde{u}\right]_{I-\frac{1}{2},J,K} \\ & + \left[G_2\tilde{u}\right]_{I,J+\frac{1}{2},K} - \left[G_2\tilde{u}\right]_{I,J-\frac{1}{2},K} \\ & + \left[G_3\tilde{u}\right]_{I,J,K+\frac{1}{2}} - \left[G_3\tilde{u}\right]_{I,J,K-\frac{1}{2}} . \end{aligned} \tag{B.12}$$

For instance, the first term of the equation (B.12), $\left[G_1\tilde{u}\right]_{I+\frac{1}{2},J,K}$, is approximated as follows:

$$\left[G_1\tilde{u}\right]_{I+\frac{1}{2},J,K} = \frac{1}{2}\left[G_1\right]_{I+\frac{1}{2},J,K}\left(\left[\tilde{u}\right]_{I,J,K} + \left[\tilde{u}\right]_{I+1,J,K}\right), \tag{B.13}$$

where a linear variation of variables between node points has been assumed, where,

$$\begin{aligned}\left[G_1\right]_{I+\frac{1}{2},J,K} = & \frac{1}{2}\left(\left[\tilde{\rho}\right]_{I,J,K} + \left[\tilde{\rho}\right]_{I+1,J,K}\right) \times \\ & \left(\left[A_{11}\tilde{u}\right]_{I+\frac{1}{2},J,K} + \left[A_{12}\tilde{v}\right]_{I+\frac{1}{2},J,K} + \left[A_{13}\tilde{w}\right]_{I+\frac{1}{2},J,K}\right), \end{aligned} \tag{B.14}$$

where the term like $[A_{11}\tilde{u}]_{I+\frac{1}{2},J,K}$ is discretised as,

$$[A_{11}\tilde{u}]_{I+\frac{1}{2},J,K} = \frac{1}{2}\left([\tilde{u}]_{I,J,K} + [\tilde{u}]_{I+1,J,K}\right) \times \left(\left[\frac{\partial y}{\partial \eta}\right]_{I+\frac{1}{2},J,K} \cdot \left[\frac{\partial z}{\partial \zeta}\right]_{I+\frac{1}{2},J,K} - \left[\frac{\partial y}{\partial \zeta}\right]_{I+\frac{1}{2},J,K} \cdot \left[\frac{\partial w}{\partial \eta}\right]_{I+\frac{1}{2},J,K}\right), \quad \text{(B.15)}$$

where, for example,

$$\left[\frac{\partial y}{\partial \eta}\right]_{I+\frac{1}{2},J,K} = \frac{1}{2}\left(\frac{[y]_{I,J+1,K} - [y]_{I,J-1,K}}{2} + \frac{[y]_{I+1,J+1,K} - [y]_{I+1,J-1,K}}{2}\right). \quad \text{(B.16)}$$

The diffusive terms are approximated in a similar manar. The cross derivative terms, arrising from the non-orthogonality of the transformed co-ordinate system are treated explicitely.

During the reacting flow calculations where a large density variation occurs, a variable time step is used at the begining of the simulations, in order to account for the large density variations properly. The time derivatives are then approximated as,

$$\tilde{\rho}\frac{\partial \tilde{\phi}}{\partial t} \approx \rho^{\star}\left[\alpha\left(\frac{\tilde{\phi}^{n+1} - \tilde{\phi}^{n}}{\Delta t}\right) - \beta\left(\frac{\tilde{\phi}^{n} - \tilde{\phi}^{n-1}}{\Delta t_0}\right)\right], \quad \text{(B.17)}$$

where Δt is the time steps at the time level $n+1$, at which the solution is sought, and Δt_0 is the time steps at the previous level, n, the most recently calculated time level. The density, $\rho^{\star}$, is evaluated by using a first order approximation as

$$\rho^{\star} \approx \frac{\rho^{n+1} + \rho^{n}}{2}. \quad \text{(B.18)}$$

The parameter α and β are given by,

$$\alpha = \frac{2 + R_t}{1 + R_t} \qquad \text{and} \qquad \beta = \frac{1}{1 + R_t}, \quad \text{(B.19)}$$

where $R_t = \frac{\Delta t}{\Delta t_0}$.

Once the flow field is established, the density varies little as the calculation proceeds, allowing the time step to be held constant. If a constant time step is used,

equation (B.17) yields,

$$\tilde{\rho}\frac{\partial\tilde{\phi}}{\partial t} \approx \rho^{\star}\left[\frac{3}{2}\left(\frac{\tilde{\phi}^{n+1}-\tilde{\phi}^{n}}{\Delta t}\right)-\frac{1}{2}\left(\frac{\tilde{\phi}^{n}-\tilde{\phi}^{n-1}}{\Delta t_0}\right)\right]. \tag{B.20}$$

The discretisation scheme described above leads to a quasi-linear system of equations for the generic variable, $\tilde{\phi}$, that can be written as,

$$a_{I,J,K}\tilde{\phi}^{n+1}_{I,J,K} = \sum_{neighbours} a_{\alpha}\tilde{\phi}^{n+1}_{\alpha} + S_{I,J,K}, \tag{B.21}$$

where $S_{I,J,K}$ represent a source term containing all terms that can not be expressed as face fluxes, and can be dependent on $\tilde{\phi}$; and a_{α} account for both the convective and diffusive terms. The summation being taken over the immediate neighbours of I, J, K (i.e., $I \pm 1$, $J \pm 1$, $K \pm 1$).

B.3 Velocity and Pressure Calculation

Once the governing equations are discretised, the pressure and velocity fields are obtained by employing a pressure correction method which is similar to the SIMPLE algorithm of Patankar [127]. This method can be illustrated as follows.

The finite difference equations (fde's), for instance, u-momentum equation to within second order accuracy can be written in the following quasi-matrix form assuming a constant time step for simplicity:

$$\mathbf{u}^{n+1} + \Delta t\mathbf{T}^{n+1}\mathbf{u}^{n+1} = -\Delta t\mathbf{D}\mathbf{p}^{n+1} - \mathbf{S}. \tag{B.22}$$

where $\mathbf{u}$ is the vector of the unknown u nodal values, $\mathbf{T}^{n+1}$ represents the coefficient matrix for the convection and diffusion terms at $n+1$, $\mathbf{D}$ arises from the discritisation of the pressure term and the sourse term $\mathbf{S}$ contains all the terms resulting from the time discretisation. The cross-derivative diffusion terms are given explicit treatment in order to reduce the calculation cost in the explicit treatment of these terms. Evaluating these cross derivatives at time level n and adding them to $\mathbf{S}$ introduces an error of $O(\Delta t^2)$ into equation (B.22). Therefore, the fde (B.22) can

be written as

$$\mathbf{u}^{n+1} + \Delta t \mathbf{T}^n \mathbf{u}^{n+1} = -\Delta t \mathbf{D}\mathbf{p}^{n+1} - \mathbf{S} + O(\Delta t^2). \tag{B.23}$$

where $\mathbf{S}$ now contains additionally those cross-derivative terms which are not included in $\mathbf{T}^n$ and treated explicitely. The tilde and bar disregarded in order to simplify the notation.

The solution to equation (B.23) onbtained by neglecting the error term $O(\Delta t^2)$ is a second order accurate approximation to $\mathbf{u}^{n+1}$, and hence a first order accurate solution of fde. In order to acheive a second order accuracy, the equation (B.22) is solved in two stages. In the first stage, a solution to (B.23) is sought. Denoting this solution as $\mathbf{u}^m$, having a corresponding pressure field $\mathbf{p}^m$, and introducing a pressure increment, $\Delta\mathbf{p}^m = \mathbf{p}^m - \mathbf{p}^n$, equation (B.23) becomes

$$\mathbf{u}^m + \Delta t \mathbf{T}^n \mathbf{u}^m + \Delta t \mathbf{D}\boldsymbol{\Delta}\mathbf{p}^m = -\Delta t \mathbf{D}\mathbf{p}^n - \mathbf{S}, \tag{B.24}$$

where m represents an intermediate time level between $n+1$, at which the solution is sought, and n, the most recent update.

Applying an approximate factorisation, equation (B.24) can be recast as

$$(\mathbf{I} + \Delta t \mathbf{T}^n)\underbrace{(\mathbf{u}^m + \Delta t \mathbf{D}\boldsymbol{\Delta}\mathbf{p}^m)}_{\mathbf{u}^*} = -\Delta t \mathbf{D}\mathbf{p}^n - \mathbf{S}. \tag{B.25}$$

A Taylor series analysis gives, $\mathbf{D}\boldsymbol{\Delta}\mathbf{p}^m \sim O(\Delta t)$. So, the error introduced by the approximate factorisation is $(\Delta t)^2 \mathbf{T}^n \mathbf{D}\boldsymbol{\Delta}\mathbf{p}^m \sim O(\boldsymbol{\Delta}\mathbf{t})^3$ and can be neglected. The equation (B.25) is then solved in two steps:

$$\mathbf{u}^* = (\mathbf{I} + \Delta t \mathbf{T}^n)^{-1}(-\Delta t \mathbf{D}\mathbf{p}^n - \mathbf{S}) \tag{B.26}$$

$$\mathbf{u}^m = \mathbf{u}^* - \Delta t \mathbf{D}\boldsymbol{\Delta}\mathbf{p}^m. \tag{B.27}$$

The vectors of unknown v and w nodal values, $\mathbf{v}$ and $\mathbf{w}$, are obtained in the similar way. However, none of these velocity fields at time level m can be obtained since $\Delta\mathbf{p}^m$ is not known.

In order to obtain the pressure increment, $\Delta\mathbf{p}^m$, the velocity fields $\mathbf{u}^m$, $\mathbf{v}^m$ and

$\mathbf{w}^m$ are subsituted into the continuity equation, which gives a Poission-type equation for the pressure increment and this will be discussed in the following subsection.

Since $\mathbf{u}^m$ is a 2nd order accurate approximation to $\mathbf{u}^{n+1}$, in the second stage, a second order accurate solution at the time level $n+1$ is obtained by rewriting the equation (B.24) for the time level $n+1$, with the coefficient matrix evaluated using values from the intermediate time level m,

$$\mathbf{u}^{n+1} + \Delta t \mathbf{T}^m \mathbf{u}^{n+1} + \Delta t \mathbf{D} \boldsymbol{\Delta} \mathbf{p}^{n+1} = -\Delta t \mathbf{D} \mathbf{p}^m - \mathbf{S}, \tag{B.28}$$

where the pressure increment, $\Delta \mathbf{p}^{n+1} = \mathbf{p}^{n+1} - \mathbf{p}^m$, is introduced. Using the approximate factorisation, equation (B.28) is written as,

$$(\mathbf{I} + \Delta t \mathbf{T}^m) \underbrace{(\mathbf{u}^{n+1} + \Delta t \mathbf{D} \boldsymbol{\Delta} \mathbf{p}^{n+1})}_{\mathbf{u}^{**}} = -\Delta t \mathbf{D} \mathbf{p}^m - \mathbf{S}. \tag{B.29}$$

Again, equation (B.29) is solved in two steps:

$$\mathbf{u}^{**} = (\mathbf{I} + \Delta t \mathbf{T}^m)^{-1} (-\Delta t \mathbf{D} \mathbf{p}^m - \mathbf{S}) \tag{B.30}$$

$$\mathbf{u}^{n+1} = \mathbf{u}^{**} - \Delta t \mathbf{D} \boldsymbol{\Delta} \mathbf{p}^{n+1}. \tag{B.31}$$

The pressure increment is again computed from the Poission-type equation which will be discussed in the next section. Variable time steps can easily accounted for by referring to equation (B.17).

B.3.1 Pressure Smoothing

As mentioned in the previous section, a Poission-like equation for the pressure increment, now defined as $\Delta p^m = p^m - p^{m-1}$, where $m-1$ indicates the most recent calculated values and m the intermediate time level at which the solution being sought, is obtained by substituting equation (B.26) in the continuity equation. For illustration purpose, considering only the flux component arised from the integra-

tion over the cell faces in the ξ direction, this substitution gives

$$\frac{\Delta t}{\alpha}\left[\frac{A_{1j}A_{kj}}{|\mathbf{J}|}\frac{\partial\Delta p^m}{\partial\xi_k}\right]_{I+\frac{1}{2},J,K} - \frac{\Delta t}{\alpha}\left[\frac{A_{1j}A_{kj}}{|\mathbf{J}|}\frac{\partial\Delta p^m}{\partial\xi_k}\right]_{I-\frac{1}{2},J,K} = \left[\rho A_{1j}u_j^{m-1}\right]_{I+\frac{1}{2},J,K} - \left[\rho A_{1j}u_j^{m-1}\right]_{I-\frac{1}{2},J,K}, \tag{B.32}$$

where u_j^{m-1} is the velocity field corresponding to the pressure field p^{m-1}. Using the central differences interpolated onto cell faces, for instance, the pressure increment's gradient at $I+\frac{1}{2}, J, K$ is approximated by

$$\left[\frac{A_{kj}}{|\mathbf{J}|}\frac{\partial\Delta p^m}{\partial\xi_k}\right]_{I+\frac{1}{2},J,K} = \frac{1}{2}\left[\frac{A_{kj}}{|\mathbf{J}|}\right]_{I+\frac{1}{2},J,K}\left(\left[\frac{\partial\Delta p^m}{\partial\xi_k}\right]_{I+1,J,K} + \left[\frac{\partial\Delta p^m}{\partial\xi_k}\right]_{I,J,K}\right), \tag{B.33}$$

where

$$\begin{aligned}\left[\frac{A_{kj}}{|\mathbf{J}|}\right]_{I+\frac{1}{2},J,K}\left[\frac{\partial\Delta p^m}{\partial\xi_k}\right]_{I,J,K} = &\left[\frac{A_{1j}}{|\mathbf{J}|}\right]_{I+\frac{1}{2},J,K}\left(\frac{\Delta p^m_{I+1,J,K}-\Delta p^m_{I-1,J,K}}{2}\right)\\ &+\left[\frac{A_{2j}}{|\mathbf{J}|}\right]_{I+\frac{1}{2},J,K}\left(\frac{\Delta p^m_{I,J+1,K}-\Delta p^m_{I,J-1,K}}{2}\right)\\ &+\left[\frac{A_{3j}}{|\mathbf{J}|}\right]_{I+\frac{1}{2},J,K}\left(\frac{\Delta p^m_{I,J,K+1}-\Delta p^m_{I,J,K-1}}{2}\right),\end{aligned} \tag{B.34}$$

The above interpolations lead to an ossilatory pressure field which is decoupled from the velocity field at even and odd grid nodes. As a remedy of this problem, the finite difference operators are redefined so that pressure increment derivatives normal to the cell faces are evaluated using values at nodes adjacent to the cell faces, and the cross derivatives interpolated from gradiants calculated at adjacent nodes, giving

$$\begin{aligned}\left[\frac{A_{kj}}{|\mathbf{J}|}\frac{\partial\Delta p^m}{\partial\xi_k}\right]_{I+\frac{1}{2},J,K,1\Delta} = &\left[\frac{A_{1j}}{|\mathbf{J}|}\right]_{I+\frac{1}{2},J,K}\left(\Delta p^m_{I+1,J,K}-\Delta p^m_{I,J,K}\right)\\ &+\left[\frac{A_{2j}}{|\mathbf{J}|}\right]_{I+\frac{1}{2},J,K}\left(\frac{\Delta p^m_{I+1,J+1,K}-\Delta p^m_{I-1,J-1,K}+\Delta p^m_{I,J+1,K}-\Delta p^m_{I,J-1,K}}{4}\right)\\ &+\left[\frac{A_{3j}}{|\mathbf{J}|}\right]_{I+\frac{1}{2},J,K}\left(\frac{\Delta p^m_{I+1,J,K+1}-\Delta p^m_{I-1,J,K-1}+\Delta p^m_{I,J,K+1}-\Delta p^m_{I,J,K-1}}{4}\right),\end{aligned} \tag{B.35}$$

where the subscript 1Δ denotes the compact stencil. It can be demonstrated that this approach is equivalent to adding a smoothing term, $\sigma(\Delta p^m)$, to the RHS of equation (B.32), of the form

$$\sigma(\Delta p^m) = \frac{\Delta t}{\alpha}\Bigg\{ \left[\frac{A_{1j}A_{kj}}{|\mathbf{J}|}\frac{\partial \Delta p^m}{\partial \xi_k}\right]_{I+\frac{1}{2},J,K} - \left[\frac{A_{1j}A_{kj}}{|\mathbf{J}|}\frac{\partial \Delta p^m}{\partial \xi_k}\right]_{I+\frac{1}{2},J,K,1\Delta} + \left[\frac{A_{1j}A_{kj}}{|\mathbf{J}|}\frac{\partial \Delta p^m}{\partial \xi_k}\right]_{I-\frac{1}{2},J,K,1\Delta} - \left[\frac{A_{1j}A_{kj}}{|\mathbf{J}|}\frac{\partial \Delta p^m}{\partial \xi_k}\right]_{I-\frac{1}{2},J,K,1\Delta}\Bigg\} \quad \text{(B.36)}$$

This smoothing term involves known and unknown components, and can be written as

$$\sigma(\Delta p^m) = \sigma(p^m) - \sigma(p^{m-1}). \quad \text{(B.37)}$$

The Rhie and Chow [120] approach is to add the unknown term, $\sigma(p^m)$, to the RHS of the equation (B.32). Adding this unknown term, the pressure increment equation becomes,

$$\begin{aligned}\frac{\Delta t}{\alpha}\left[\frac{A_{1j}A_{kj}}{|\mathbf{J}|}\frac{\partial \Delta p^m}{\partial \xi_k}\right]_{I+\frac{1}{2},J,K,1\Delta} - \frac{\Delta t}{\alpha}\left[\frac{A_{1j}A_{kj}}{|\mathbf{J}|}\frac{\partial \Delta p^m}{\partial \xi_k}\right]_{I-\frac{1}{2},J,K,1\Delta} &= \left[\rho A_{1j}u_j^{m-1}\right]_{I+\frac{1}{2},J,K} - \left[\rho A_{1j}u_j^{m-1}\right]_{I-\frac{1}{2},J,K} \\ + \frac{\Delta t}{\alpha}\Bigg\{ \left[\frac{A_{1j}A_{kj}}{|\mathbf{J}|}\frac{\partial p^{m-1}}{\partial \xi_k}\right]_{I+\frac{1}{2},J,K} - \left[\frac{A_{1j}A_{kj}}{|\mathbf{J}|}\frac{\partial p^{m-1}}{\partial \xi_k}\right]_{I+\frac{1}{2},J,K,1\Delta} \\ + \left[\frac{A_{1j}A_{kj}}{|\mathbf{J}|}\frac{\partial p^{m-1}}{\partial \xi_k}\right]_{I-\frac{1}{2},J,K} - \left[\frac{A_{1j}A_{kj}}{|\mathbf{J}|}\frac{\partial p^{m-1}}{\partial \xi_k}\right]_{I-\frac{1}{2},J,K,1\Delta}\Bigg\}.\end{aligned} \quad \text{(B.38)}$$

The compact computational stencil reduces the number of the nodes treated implicitely from 25 to 19 for each cell for the three dimensional problem. However, the implicit treatment of 19 nodes in each computational stencil is still very expensive. As in the original Rhie and Chow [120] formulation, the terms involving cross derivatives in equation (B.38), arising from the skewness of the computational mesh, are neglected to reduce the number of gridnodes involved in the solution to 7 nodes. Wille [84] showed that this approximation does not affect the formal accuracy of the solution procedure. The mass flux, for instance at $I+\frac{1}{2}, J, K$, is then

updated from

$$\left[\rho A_{1j} u_j^m\right]_{I+\frac{1}{2},J,K} = \left[\rho A_{1j} u_j^{m-1}\right]_{I+\frac{1}{2},J,K} + \frac{\Delta t}{\alpha}\left\{\left[\frac{A_{1j}A_{1j}}{|\mathbf{J}|}\frac{\partial p^{m-1}}{\partial \xi_k}\right]_{I+\frac{1}{2},J,K} - \left[\frac{A_{1j}A_{1j}}{|\mathbf{J}|}\frac{\partial p^{m-1}}{\partial \xi_k}\right]_{I+\frac{1}{2},J,K,1\Delta}\right\} + \frac{\Delta t}{\alpha}\left[\frac{A_{1j}A_{1j}}{|\mathbf{J}|}\frac{\partial \Delta p^m}{\partial \xi_k}\right]_{I-\frac{1}{2},J,K,1\Delta} \tag{B.39}$$

and the velocity field stored at the cell centres is updated from the original discrete approximation, so that

$$\left[u_j^m\right]_{I,J,K} = \left[u_j^{m-1}\right]_{I,J,K} - \frac{\Delta t}{\alpha}\left[\frac{A_{kj}}{|\mathbf{J}|}\frac{\partial \Delta p^m}{\partial \xi_k}\right]_{I,J,K}. \tag{B.40}$$

Although the mass fluxes and velocity are strongly coupled with this approach, spurious oscillation may still be developed in the velocity field but that are not sensed by the pressure field, as remarked in Wille [84].

B.3.2 The Mixture Fraction Treatment - TVD Scheme

As anticipated in Chapter A, a central scheme for discretising the convection terms in the mixture fraction equation (3.46) of Chapter 3, soot mass fraction and soot particle number density equation (4.10) of Chapter 4 and NO mass fraction equation (5.10) of Chapter 5 can not be applied, since, for these terms such scheme are known to produce unphysical 'wiggles' in solutions for the cell Peclet number, Pe_i, defind as

$$Pe_i = \frac{\rho u_i \Delta x_i}{\mu_e} \tag{B.41}$$

greater than 2, which may vary rapidly in areas where the cell Peclet number is high (Ferziger and Peric [128]). However, it is crucial to the success of the simulation that the mixture fraction must remains bounded by its physically prescribed limits between zero and unity if unphysical values of the density, temperature, species concentrations, soot mass fraction, soot particle number density and NO mass fraction are to be avoided. In order to achieve this a Total Variation Diminishing (TVD) scheme, see Sweby [119] and Hirsch [129], for the convective terms in the mixture fraction equation, has been used in the present study. The sheme is second order

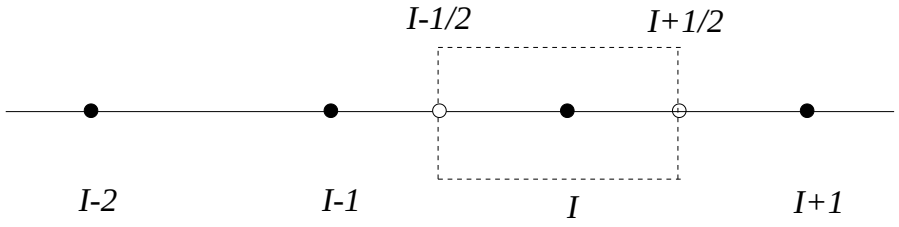

Figure B.2: 1-dimensional grid arrangement. The solid line indicates the grid lines, dashed lines indicate the bounday of the control volume.

accurate. For the illustrating purpose, the one-dimensional case with positive constant convective velocity, u, is considered. The one-dimensional mesh arrangement is shown in Fig. B.2. For a scalar, ϕ, the convective term is approximated by

$$\int_{\Delta V} u \frac{\partial \phi}{\partial x} dV \approx u \left(\phi_{I+\frac{1}{2}} - \phi_{I-\frac{1}{2}} \right). \tag{B.42}$$

The cell face values $\phi_{I+\frac{1}{2}}$ and $\phi_{I-\frac{1}{2}}$ are obtained from a first order upwind approximation to which is added a 'limited' amount of second order centred approximation,

$$\phi_{I+\frac{1}{2}} = \phi_I + \frac{\Psi_{I+\frac{1}{2}}}{2} (\phi_{I+1} - \phi_I) \tag{B.43}$$

and

$$\phi_{I-\frac{1}{2}} = \phi_{I-1} + \frac{\Psi_{I-\frac{1}{2}}}{2} (\phi_I - \phi_{I-1}). \tag{B.44}$$

The limiter Ψ is considered as a function of the ratio of the gradients of ϕ at the cell faces,

$$r_{I+\frac{1}{2}} = \left(\frac{\phi_I - \phi_{I-1}}{x_I - x_{I-1}} \right) \Big/ \left(\frac{\phi_{I+1} - \phi_I}{x_{I+1} - x_I} \right) \tag{B.45}$$

and

$$r_{I-\frac{1}{2}} = \left(\frac{\phi_{I-1} - \phi_{I-2}}{x_{I-1} - x_{I-2}} \right) \Big/ \left(\frac{\phi_I - \phi_{I-1}}{x_I - x_{I-1}} \right), \tag{B.46}$$

which provide a measure of the smoothness of the solution at these locations. In this study, the limiter is defined as

$$\Psi_{I\pm\frac{1}{2}} = max\left(0, min\left(2r_{I\pm\frac{1}{2}}, 1\right)\right). \tag{B.47}$$

The other forms of this limiter are possible, for example see Sweby [119]. The three dimensional sheme can be derived by using the above one-dimensional discretisation in each spatial direction.

B.3.3 Solution Algorithm and Convergent Condition for LES

The system of algebraic equations resulting from the discretisation are solved according to the followong algorithm:

- Compute $\mathbf{u}^*$, $\mathbf{v}^*$, $\mathbf{w}^*$ from equation (B.26) using most recently updated $\mathbf{G}^n$, ρ^n and $\mathbf{p}^n$.
- Solve for ξ^m using $\mathbf{G}^n$ and ρ^n.
  - Calculate ρ^m from ξ^m.
  - Solve for $\Delta\mathbf{p}^m$ from equation (B.38) with Rhie and Chow [120] pressure smoothing.
  - Update mass fluxes and velocities using equations (B.39) and (B.40) respectively to obtain $\mathbf{G}^m$, $\mathbf{u}^m$, $\mathbf{v}^m$ and $\mathbf{w}^m$.
- Compute $\mathbf{u}^{**}$, $\mathbf{v}^{**}$, $\mathbf{w}^{**}$ from equation (B.30) using the updated $\mathbf{G}^m$, ρ^m and $\mathbf{p}^m$.
- Solve for ξ^{n+1} using the updated $\mathbf{G}^m$ and ρ^m.
  - Calculate ρ^{n+1} from ξ^{n+1}.
  - Solve for $\Delta\mathbf{p}^{n+1}$ from equation (B.38) with Rhie and Chow [120] pressure smoothing.
  - Update mass fluxes and velocities using equations (B.39) and (B.40) respectively to obtain $\mathbf{G}^{n+1}$, $\mathbf{u}^{n+1}$, $\mathbf{v}^{n+1}$ and $\mathbf{w}^{n+1}$.

$*$ Compute the scalar ϕ^{n+1} using ρ^n and $\mathbf{G}^{n+1}$.

$*$ From ϕ^{n+1} compute density and compositions at time level $n+1$.

If necessary, the steps marked $\bullet$ can be repeated before continuing.

The maximum residuals, representing the errors associated with the entire solution procedure, are calculated within the solvers as a part of the solution procedure. For velocity, the normalised residual is,

$$||\mathbf{u}^{n+1}||^{\#} = \frac{1}{t^{\#}} \left[max \left(\rho_{ijk}^2 u_{ijk}^2 + \rho_{ijk}^2 v_{ijk}^2 + \rho_{ijk}^2 w_{ijk}^2 \right) \right], \tag{B.48}$$

where the time scale $t^{\#}$ depends on the flow under investigation and is defined using a length and a velocity scale representative of conditions at the inlet; ijk represents the location in the computational domain. In a similar way, the normalised residual for the scalar field is computed from,

$$||\phi^{n+1}||^{\#} = \frac{1}{t^{\#}} \left[max \left(\rho_{ijk}^2 \phi_{ijk}^2 \right)^{1/2} \right], \tag{B.49}$$

while the normalised residual for the pressure increment is

$$||\Delta\mathbf{p}^{n+1}||^{\#} = \frac{1}{t^{\#}} \left(\frac{1}{N_{grid}} \sum_{N_{grid}} \rho_{ijk}^2 \right)^{1/2}, \tag{B.50}$$

where N_{grid} is the total number of grid points. The momentum and transport equations are iterated until $||\mathbf{u}^{n+1}||^{\#} < 10^{-3}$ and $||\phi^{n+1}||^{\#} < 10^{-3}$ respectively. The tolerance for the pressure increment equation is reduced so that the iterative procedure does not terminate until $||\Delta\mathbf{p}^{n+1}||^{\#} < 10^{-4}$.

B.4 List of Symbols for Appendix A

Roman Symbols

a_α	coefficients in discretisation equations
$\mathbf{A}$	matrix of cofactors of Jacobian matrix
A_{ij}	elements of $\mathbf{A}$
$\mathbf{D}$	pressure term coefficient matrix
$\mathbf{G}$	mass fluxes vector
G_k	mass flux in ξ_k coordinate direction
$\mathbf{I}$	identity matrix
I, J, K	grid indexes
$\mathbf{J}$	Jacobian matrix of coordinate transformation
J_{ij}	elements of $\mathbf{J}$
m	intermediate time level
n	time level
$\mathbf{P}$	vector of nodal pressure values
Pe_i	Peclet number in x_i direction
R_t	ratio of time steps
$\mathbf{S}$	source term vector
S_α	source term in discretisation equations
t	time
$\mathbf{T}$	convective and diffusive terms coefficient matrix
u	a constant convective velocity
u_i	velocity component
$\mathbf{u}, \mathbf{v}, \mathbf{w}$	vectors of velocity components
$\mathbf{u}^\star, \mathbf{v}^\star, \mathbf{w}^\star$	vectors of intermediate velocity components
$\mathbf{u}^{\star\star}, \mathbf{v}^{\star\star}, \mathbf{w}^{\star\star}$	vectors of intermediate velocity components
x_i	physical space coordinates

Greek Symbols

α, β	parameters in time derivative discretisation
Γ	molecular diffusivity
Γ_e	effective diffusivity

Γ_{sgs}	subgrid scale eddy diffusivity
$\Delta t, \Delta t_0$	current and previous time steps
ΔV	computational cell volume
ΔS	computational cell surface
$\Delta \xi$	mesh specing in computational space
Δp	pressure increment
$\Delta \mathbf{p}$	vector of nodal pressure increments
μ	molecular viscosity
μ_e	effective viscosity
μ_{sgs}	subgrid scale eddy viscosity
ξ_i	computational space coordinates
ρ	density
σ	pressure smoothing term
ϕ	a general dependent variable
Ψ	TVD scheme limiter

Mathematical Accents

$\bar{.}$	spatial filtering
$\tilde{.}$	Favre filtering
$\|.\|$	determinant

Appendix C

Publications and Presentations

Publications

1. **Sreebash C. Paul** and Manosh C. Paul: Luminous and Non-Luminous Radiation from a Turbulent Flame. *In peparation to submit to an International Journal*.

2. **Sreebash C. Paul**, Manosh C. Paul and William P. Jones: LES for Soot Formation in a Propane-Air Turbulent Flame. *In peparation to submit to an International Journal*.

3. **Sreebash C. Paul**, Manosh C. Paul and William P. Jones: LES for NO Prediction in a Propane-Air Turbulent Flame. *In peparation to submit to an International Journal*.

4. **Sreebash C. Paul** and Manosh C. Paul: Radiative Heat Transfer during Turbulent Combustion Process. *Submitted to International Communications in Heat and Mass Transfer*.

5. **Sreebash C. Paul**, Mnaosh C. Paul and William P. Jones: Large Eddy Simulation of a Fuel-Rich Turbulent Non-Premixed Reacting Flow. *Submitted to Combustion and Flame*.

6. **Sreebash C. Paul**, Manosh C. Paul and William P. Jones: LES for Soot Formation in a Propane-Air Turbulent Flame, In *Proceedings of 5th joint ASME/JSME Fluids Engineering Conference*, San Diego, California, USA, July 30 - August 2, 2007.

7. **Sreebash C. Paul**, Manosh C. Paul and Willian P. Jones: LES for NO Prediction in a Propane-Air Turbulent Flame, In *Proceedings of 5th joint ASME/JSME Fluids Engineering Conference*, San Diego, California, USA, July 30 - August 2, 2007.

8. **Sreebash C. Paul**, Manosh C. Paul and William P. Jones: Large Eddy Simulation for Turbulent Non-Premixed Fuel-Rich Combustion in a Cylindrical Combustor. In *Proceedings of European Conference on Computational Fluid Dynamics 2006 (ECCOMAS CFD 2006)*, Egmond aan Zee, The Netherlands, 5-8 September 2006.

Conference/Seminar Presentations

1. Large Eddy Simulation for Turbulent Non-Premixed Fuel-Rich Combustion in a Cylindrical Combustor, Presented in the *European Conference on Computational Fluid Dynamics 2006 (ECCOMAS CFD 2006)*, Egmond aan Zee, The Netherlands, 5-8 September 2006

2. Large Eddy Simulation for Turbulent Fuel-Rich Non-Premixed Combustion, Presented in the Research Colloquium, Department of Mechanical Engineering, University of Glasgow, June 2006.

3. Large Eddy Simulation of Fuel-Rich Non-Premixed Combustion, Presented in the Research Colloquium, Department of Mechanical Engineering, University of Glasgow, September 2005.